Development of Novel Nanomedicines for Treatment of Primary and Metastatic Prostate Cancer

by

Omer Aydin

A dissertation submitted in partial fulfillment
of the requirements for the degree of
Doctor of Philosophy
(Biomedical Engineering)
in the University of Michigan
2016

Doctoral Committee:

Associate Professor Mohamed E.H. El-Sayed, Chair
Professor Evan T. Keller
Professor David H. Kohn
Associate Professor Kenneth M. Kozloff
Associate Professor Zhen Xu

Knowledge should mean a full grasp of knowledge:
Knowledge means to know yourself, heart and soul.
If you have failed to understand yourself,
Then all of your reading has missed its call.

-YUNUS EMRE

Dedication

This thesis is dedicated to those brave souls who have fallen martyr and given up their lives for home, democracy, and to achieve real peace in the world.

Acknowledgements

"The nature of reality is this: It is hidden, it is hidden, and it is hidden." Rumi, a Turkish Saint.

My Ph.D. experience has been a truly enriching process that has helped shape me into the well-rounded individual that I am today. The different lessons that I have learnt through all the high's and low's encountered during graduate school will forever be a part of me and help me enlighten my future life.

This thesis would not have been possible without the mentorship and support from my advisor, Dr. Mohamed ElSayed. I have learned so much about life from him that extends beyond the realms of scientific knowledge. We have shared endless hours talking about my future plans, life struggles, and personal beliefs. Walking down memory lane, I am sure that you will remember me for serving "Turkish Tea" to my lab mates during breaks and for the trouble that I created on occasion and I hope it brings a smile on your face. I would also like to thank our collaborators and my committee members namely Dr. Evan Keller, Dr. Xhen Xu, Dr. David Kohn, and Dr. Kenneth Kozloff for their valuable suggestions on my experimental plan. Further, I learned many things from their scientific prowess such as how to apply their skills to evaluate projects and data during our group discussions on the results.

My first three years in the Ph.D. program spent in the synthesis room. Here, I gained all my polymer synthesis and click chemistry knowledge under the mentorship of Dr. Yasemin Yuksel Durmaz. Her every growing enthusiasm towards science helped me stay motivated as well as her guidance both as a mentor and friend helped make my Ph.D. experience both memorable and

successful. I have always felt her support behind me in my academic life. I consider myself very lucky to have met and worked with her. You will always be my “abla” (in Turkish, it is used to address an older lady/woman out of respect). I would also like to acknowledge Dr. Gopinath Tiruchinapally who helped me in the synthesis of pH-labile cross-linkers. I would like to thank him for his time and patience in teaching me about different characterization techniques and advising me on the various synthesis tips for improving reaction efficiencies. Moreover, his contribution in the synthesis of bone-targeted tri-block copolymers helped me complete my study in a timely manner.

In addition to my committee members and our post-doctoral researchers, I would like to extend my thanks to all the former and current members of the CENT lab. Besides, making a significant impact through sharing their ideas, knowledge, and evaluable time; they have helped make my experience in Ann Arbor and at the University of Michigan a special and memorable one. Throughout my time in the BME program, I have had the priviledge to share in their expereinces as well as watch my collegues transition from being graduate student to successful Ph.Ds. The list begins with the CENT lab’s first Ph.D. student, Dr. Scott Medina, followed by Dr. Yen Lin Ling, Dr. Jack Wang, Dr. Alper Isoglu (except, he was a visiting Assistant Prof in our group), and Dr. Ibrahim Youssef. I would, especially, never forget the friendships that I developed with my labmates Sibu Kuruvilla, Neha Kaushal, and Mohamed Teiama over the last two years. I believe we have developed a truly special friendship through supporting each other both professionally and personally. I would like to extend a special thanks to Mohammed Teiama for initiating all of our fun and union times. You will never be forgotten, my dear friends.

I would like to thank all of our collaborators, Dr. Eli Vlaisavljevich and Dr. Harsha Ramaraju whom I worked closely. I always learn something new and insightful while working

with Eli. Therefore, he is my favorite researcher who I can talk all the details and novel ideas about the histotripsy project. It is clear that with his enormous research ambition and the synergy working with him, we have succeeded many milestones and established a new phenomenon regarding nanodroplet mediated histotripsy. Furthermore, I consider myself very fortunate for getting the opportunity to work closely with Harsha on the bone-targeted nanoparticle project along with Ibrahim Youssef. The enormous scientific contribution and support I received from collaborating with them help lay a strong foundation and propel the project forward. It is my honor to work with such knowledgeable and hard-working collaborators whose positive attitudes made this project both successful and enjoyable.

A special thanks to the President, Recep Tayyip Erdogan, of my home country (Turkey), who established a graduate-level fellowship program abroad to support Turkey's intellectual and research resources. Therefore, I would like to thank the Ministry of National Education (the Republic of Turkey) for awarding me a Graduate Research Fellowship in USA under the program number 1416. When I face any problem related to this fellowship I always knock the door of Turkish Education Attaché in New York to solve them. I, also would like to thank all officers and Attachés who have assisted me throughout my Ph.D. Further, I was also partially supported by Rackham Graduate School during my Ph.D., I am always thankful all their supports.

Last but not the least, I am grateful for my amazing family and will always be proud of being a member of this large family. I would like to thank my family, Osman Aydin (Dad), Aysel Aydin (Mum), Emel Aydin (Sister), and M.D. Meryem Ulku Aydin (Sister), Nihal Aygul (niece), Prof. Muharrem Ok (Uncle), Prof. Mustafa Tatci (Uncle), and all members of my large family who have encouraged, believed, supported, and prayed for me to achieve to the fullest of my ability with sound and spirit. I would like to thank "my hero", for taking me out from the deepest well

where I was stuck during the last part of my graduate life, for making the sun shine again, and helping me dream big.

All in all, I would like to thank everyone who has entered my life partially or wholly even is against or supports me. I know you are the gifts of Allah (God) so that I can find a way to reach Him.

Thank you, thank you, thank you!

Omer Aydin

August 2016

Ann Arbor, MI

Table of Contents

List of Figures

List of Tables

List of Appendices

Abstract

Prostate cancer is the 2nd most common cancer among men worldwide with an estimated 1.1 million men diagnosed with the disease in 2012 and accounting for more than 300,000 deaths in 2012. According to the GLOBOCAN 2012 report, it is estimated that prostate cancer will overtake lung cancer, which is currently the most common form of cancer affecting men globally, in the last ten years. This thesis focuses on the development of novel nanomedicine-based therapeutic approaches for focal ablation of primary prostate cancer and targeted chemotherapeutics of the treatment of metastatic prostate cancer lesions in bone.

Focal prostate cancer therapy is an effective approach that can successfully eradicate single tumor lesions. However, the focal therapy approaches have limitations with regard to treating high-volume and multi-modal tumor lesions as well as lacks the ability to selectively ablate cancer lesions. To address these therapeutic limitations, we have developed nanodroplets (average diameter ~ 200nm) encapsulating perfluorocarbons (PFC's), namely perfluoropentane (PFP) and perfluorohexane (PFH), which can rapidly expand reaching > 500 µm in < 1µsecond when exposed to therapeutic ultrasound before they collapse. The pulsating microbubbles have proved successful in mechanically fractionating neighboring cells with significantly reduced cavitation parameter thresholds. To test the tumor ablation efficiency of the different PFC (PFP or PFH)-encapsulated nanodroplets, we developed 3D-prostate cancer spheroids from PC-3 and C4-2B cancer cells using aqueous-two-phase-systems (ATPS) on an agarose 3D tumor phantom model that mimicked the cells inside a tissue extracellular-matrix. The applied treatment groups included no ND with lower-

pressure (13 MPa), no ND with high-pressure (28 MPa), PFP-loaded NDs with low-pressure (13 MPa), and PFH-loaded NDs with lower-pressure (13 MPa). During the treatments such high-pressure and low-pressure with nanodroplets, cavitation bubbles were observed at the transducer focus and cells were observed to be mechanically ruptured. After the treatments, we evaluated the ablated area of the spheroids. No nanodroplets at low-pressure could ablate less than 20 % area for both spheroid models. However, regular histotripsy with high-pressure ablated around 80 % of the spheroids. Whereas, PFP-nanodroplets with low-pressure destroyed 40 % of the spheroids, and PFH-nanodroplets could ablate almost 80 % of the spheroids. These results indicate both PFC-loaded nanodroplets significantly reduce the histotripsy threshold, and PFH-loaded nanodroplets with low-pressure can destroy cells as efficiently as high-pressure.

The current bone metastases therapy modalities are riddled with its fair share of limitations such as their inability to efficaciously deliver the therapeutic concentrations of anti-cancer agents to the target site. To address these limitations, in the second part of this dissertation we designed bone-targeted nanoparticles that can encapsulate and deliver a high dose of Cabazitaxel (CTX) to prostate cancer lesions in bone. We further studied the targeted nanoparticles internalization profile into cancer cells as well as bone cells grown in a bone-like microenvironment. The project comprised of three major aims: i) We first designed non-targeted “smart” nanoparticles containing amphiphilic triblock copolymers, poly(ethylene)-*b*-poly(acrylic acid)-*b*-poly(methyl methacrylate), that have the ability to self-assemble in an aqueous medium to form nano-sized micelles that can encapsulate anti-cancer agents like CTX in their hydrophobic core. Cross-linkage of the PAA blocks using ketal-linkers resulted in an acid-labile shell that stabilized the drug-loaded micelles at physiologic pH, but allowed selective release of the loaded cargo in acidic environments. The *in-vitro* study of the non-targeted, CTX-loaded cross-linked nanoparticles

exhibited a significantly higher therapeutic effect than free CTX without any cytotoxicity issues. Moreover, the particles did not have any biocompatibility issues based on the studies conducted such as, red blood cell hemolysis, protein adsorption, and platelet activation tests. Further, this non-targeted "smart" nanoparticle exhibited a limited macrophage uptake < 10% compared to cancer cells > 90%. ii) We conjugated the non-targeted nanoparticles with either a specific peptide sequence called pVTK or a small molecule bisphosphonate (BP) to actively target mineralizing or hydrolyzing bone surfaces in prostate cancer lesions, respectively. We characterized the size of the bone targeted particles (60-90 nm) and confirmed their binding affinity towards bone hydroxyapatite (HA) powder. Further, we examined both bone targeted nanoparticles uptake profiles into prostate cancer cell lines (PC-3 and C4-2B) and bone cell lines (MC3T3, RAW 264.7 bone macrophages, and RANKL activated RAW 264.7) on regular tissue culture plates as well as on bone-like surfaces (BLS). Results showed that increasing the number of BP-targeting copolymer in the particle formulation was able to augment the normalized particle fluorescence intensity in RAW 264.7 macrophages on regular culture plates. Additionally, the overall cellular uptake profile of bone-targeted nanoparticles trends was different in the presence of BLS compared to that of regular tissue culture plates. The results indicate that C4-2B and MC3T3 osteoblast cells were effectively targeted by pVTK bone-targeted nanoparticles. While, BP bone-targeted nanoparticles are capable of targeting PC-3 and RAW 264.7 macrophage cells. These results collectively indicate that pVTK- and BP-based bone targeting strategies can facilitate selective delivery of chemotherapeutic agents to metastatic prostate cancer in bone and the cross-talk between cancer cells and bone cells could be inhibited by using a specific targeting strategy (pVTK or BP), which opens doors to new personal bone metastasis therapies.

Chapter 1

Introduction

1.1 Objective

Prostate cancer is the second leading cause of cancer death in men in the US behind lung cancer. In the US, prostate cancer is diagnosed in approximately 1 of every 6 men, with 1 out of 39 men dying because of this disease [1]. The American Cancer Society estimates approximately 180,890 new cases of prostate cancer will be diagnosed in 2016 with 26,120 deaths occurring from the disease in the US [1]. Tremendous advances in the detection and treatment of prostate cancer especially, the widespread use of prostate-specific antigen (PSA) screening over the past four decades have led to a significant increase in the 5-year survival rate for local prostate cancer, which is almost 100% [1]. Although improving the treatment rate of prostate cancer localized to the prostate gland, almost four-fifth of patients whose prostate cancer have spread to a distant organ (metastasize) survive no more than five years [2].

The main treatment approaches for prostate cancer are **radical prostatectomy (RP)** which is an operation to remove the partial or whole prostate gland with surrounding tissues or **radiation therapy**. These treatment strategies are capable of increasing the survival rate of patients diagnosed with primary cancer. However, they are associated with significant complications and side effects such as incontinence and erectile dysfunction that greatly deteriorate the patient's quality of life [3, 4]. A recent review showed that the specimen in 49% of men undergoing RP show insignificant or indolent cancer (i.e. organ-confined cancer lesion < 0.5 mL) [5]. In

comparison, 73% of patients initially enrolled in active surveillance who underwent RP reveal significant cancer on RP specimens [6].

Another treatment strategy of prostate cancer is hormonal therapy as the male sex hormone testosterone is known to stimulate the growth of prostate cancer cells. In this treatment option, testosterone is inhibited or the production level is decreased by some hormonal medications (i.e. Flutamide, Bicalutamide, Nilutamide, Leuprolide, Goserelin, Triptorelin, Histrelin, etc) in order to prevent testosterone binding to the cancer cells resulting in the shrinking and slowing down the cancer cells growth [7]. However, after a period of time the cancer cells develop resistance to this therapy by not responding to the treatment anymore. Moreover, the side effects include hot flashes, decreased sexual desire, loss of bone density with an increased risk of fracture (osteoporosis), erectile dysfunction, fatigue, increased risk of diabetes and heart attacks/strokes, weight gain, decreased muscle mass, anemia, and memory loss have been observed [7, 8].

In the case of hormonal therapy resistance, **chemotherapy** is another option with/out hormone therapy for patients whose metastatic prostate cancer have grown despite hormone therapy [9-11]. Paclitaxel and docetaxel have been used against prostate cancer for a long time and **Cabazitaxel (CTX)** was recently approved by FDA for patients with mCRPC who were previously treated with a docetaxel-containing regimen [12]. It is similar to its taxen ancestors. Nevertheless, disparate of the new drug has poor affinity for P-glycoprotein-mediated efflux pumps that leads to taxane resistance in tumors in the case of P-glycoprotein overexpression [13]. The other issues on chemotherapeutics they are typically associated with adverse side effects including hypersensitivity reactions, peripheral edema, and pericardial effusions because of the Tween 80 used to solubilize the drug [14]. Further, non-specific distribution of taxanes throughout the body results in neural, cardiac, and musculoskeletal toxicities [15].

The current therapeutic modalities radiotherapy, hormone therapy, and chemotherapy are not aimed to specifically treat the disease at the bone metastasis stage, but they may contribute to treat them. Moreover, in the presence of multiple bone metastatic nodules, these modalities are greatly limited to treat and lead to systemic side effects due to the lack of desired drug concentration in bone. In addition, in the case of the advanced stage of the metastasis, various complications may be noticeable such as osteolysis, spinal cord compression, hypercalcemia, increased fracture incidence, and permanent pain due to the fact that the bone metabolism and microenvironment are disrupted and induce imbalance between bone formation and bone resorption [16, 17]. Moreover, around two-third of pain patients suffering from bone metastases complain about break-through pain, which described as a simultaneous appearance of strong pain despite taking of strong pain killers, or analgesics [18].

Bisphosphonates (BPs) have been preferred due to its dual functionality namely, for the treatment of bone metastasis as well as for the reduction the occurrence of pain because of broken bone or excess bone hydrolysis. BPs have potent inhibitor functions on osteoclast-mediated bone resorption via binding to the bone mineral following their uptake by osteoclasts through fluid-phase endocytosis from acidified bone surface during osteolytic resorption [19]. Inside the osteoclasts, it acts by inhibiting the prenylation of small GTPases that control cytoskeletal function, vesicular trafficking, and apoptosis [20, 21]. In addition to this osteoclast activity, they have been shown to have direct effects on non-resorbing cells in the presence of resorbing osteoclasts with transcytosis uptake mechanism [22]. Further having functions in bone environment BPs show that they are able to strongly reduce invasion and migration of PC-3 prostate cancer cells [23]. Alendronate (ALE), a BP, also inhibits PC-3 cell adhesion to extracellular matrix proteins *in vitro* [24] and secretion of MMPs by tumor cells [25]. Other

bisphosphonates (clodronate, pamidronate, ibandronate and zoledronate) have been shown to induce apoptosis of breast cancer cells *in vitro* [26, 27], inhibit angiogenesis, [28, 29] and at high concentrations inhibit cell proliferation [30]. Although BPs have all these extraordinary features their therapeutic activity in bone metastasis is insufficient due to ineffective therapeutic concentration.

To address the current treatment problems associated with primary and bone-metastasized prostate cancer, this dissertation has two main strategies: i) investigating nanodroplet-mediated histotripsy, a novel ultrasound-based focal ablation method, in a 3D prostate cancer spheroid model to overcome aforementioned issues of primary cancer treatments **(Chapter 2),** ii) engineering bone targeted "smart" polymeric micelles that are able to encapsulate a large dose of anti-cancer agents without any toxic effects and specifically carry the therapeutics to prostate metastasized bone lesion **(Chapter 3 and 4)**.

1.2 Ablation Techniques

Currently available ablation modalities are radiofrequency ablation (RFA), microwave ablation (MWA), laser ablation (LA), and high-intense focused ultrasound (HIFU) that are thermal based and minimally invasive coupled with imaging modalities such as ultrasound imaging, computed tomography (CT), and magnetic resonance imaging (MRI) to monitor tumor location, shrinkage, and temperature changes [31, 32]. The underlying principle of each technique relies on heating up the diseased tissue resulting in the denaturation of proteins, followed by cell death. Basically, RFA is an electrosurgical technique that uses high-frequency alternating current (AC) and inserts the electrode to heat tumor for thermal coagulation. During treatment, temperature is

increased between 60-100 °C to induce protein coagulation with damage to cytosolic and mitochondrial enzymes and DNA-histone complexes leading to coagulative necrosis [33]. A main drawback of RFA is the difficulty in targeting a tumor whereby the blood flow through adjacent vessels cool the temperature down leading to incomplete ablation, which is called the “heat-sink” effect [34].

The second ablation technique is MWA, which uses higher frequency between 900 MHz and 2.5 GHz comparing to RFA and the inserted probes function as an antenna to create electromagnetic field inside the tumor to generate heat based on rapid oscillation of water molecules. This causes molecular friction and a rapid rise in thermal energy throughout the field leading to kill the tumor cells [35].

Laser thermal ablation is another technique to induce thermally mediated coagulation necrosis employed for tumor destruction. The aim is similar to RFA and MWA techniques but in here the intense and highly focused laser beam delivers a high energy dose to the diseased area. However, water and hemoglobin absorb the light beam which limits the penetration depth. Therefore, this issue is overcome with near-infrared (NIR) laser light that is ideal for *in vivo* hyperthermia applications. NIR light demonstrates maximal penetration of tissue comparing to other light sources, thereby reaching deep inside the tissue. However, even NIR laser source can penetrate only a maximum of ~1 cm so it is used only for superficial tumors not deep tissue tumors [36].

Penetration problem is solved with ultrasound based ablation strategies that are able to target deeper tissue. One of the most widely used ultrasound ablation techniques is high-intensity focal ultrasound (HIFU) that focuses acoustic energy into a focal point that is aligned to the tumor tissue leading to heat generation, which induces protein coagulation and necrosis similar to RFA

and MWA [37-39]. While these minimally invasive techniques require an electrode or antenna to deliver electromagnetic waves, HIFU system is totally non-invasive. Therefore, it does not disturb the tumor lesion or overlay tissues with probe insertion. While all of these thermally-based ablation techniques have shown success, these techniques are limited due to the "heat-sink" effect [40]. Another limitation of thermal ablation techniques is non-homogenous temperature distribution through the tumor lesion lowers its efficacy results in not killing 100% of tumor cells, regrowth of residual tumor at the ablation margin, and inability to effectively treat large size tumors with a single treatment session so treatment takes a long time. Furthermore, the treatment is evaluated before and after with imaging systems such as CT or MRI due to lacking of real time imaging (except HIFU system) and MRI thermometry system is used to monitor simultaneously temperature changes during treatment and assure feedback in real-time with MRI/HIFU system [39, 41].

Most of these limitations can be addressed by **histotripsy**, which is a new US-based treatment strategy with certain advantages over the existing ablative techniques. Histotripsy therapy uses high-intensity, focused ultrasound pulses in a short time period (< 10 μs), which is different than high intensity focused ultrasound (HIFU) thermal ablation, to produce non-thermal tissue fractionation [42, 43]. In histotripsy, the delivery of high-pressure, focused ultrasound pulses leads to generating a cluster of microbubbles (bubble cloud) from pre-existing gas pockets in the tissue where the rapid expansion and collapse of the microbubbles disrupts cells and other tissue structures [44-49]. Moreover, **histotripsy** is not affected by the heat-sink effect, a safe ablation ability even proximity to vessels [50], and more importantly the cavitation cloud and the resulting tissue damage can be monitored in real-time with ultrasound imaging system [51]. All these

advantages suggest that histotripsy has the potential to overcome many of the limitations facing invasive surgery and thermal ablation procedures.

It is clear that tremendous efforts have been made in the last decades to improve the currently available ablation techniques. A major limitation of all techniques is that there is no selectivity and targetability mechanisms that are able to discriminate tumors from surrounding healthy tissues to minimize the many side effects and increase the ablation efficiency. In specific to histotripsy, for example, the treatment currently relies upon MRI or ultrasound imaging to successfully target the tumor volume, which can often be difficult for small or multi-focal tumor nodules. Developing a strategy to target histotripsy to specific cells of interest (i.e. tumor cells) will undoubtedly improve the success of histotripsy ablation and extend this ablation approach to a much broader patient population. To improve the effectiveness of histotripsy, our team has developed ultrasound active perfluorocarbon encapsulated nano-sized polymeric particles that have promising results addressing the current ablation techniques problem. In the next section, ultrasound active particle design is mentioned with a historical perspective and the following section will give more details on ultrasound active nanodroplet-based histotripsy from synthesis to US characterization.

1.2.1 Ultrasound Active Particles

Ultrasound (US) is one of the most frequently used diagnostic imaging methods. It is a non-invasive, high penetration signal, and comparatively inexpensive imaging method besides that owning safety, portability, and real-time images [52]. To improve image contrast, ultrasound contrast agents (UCA) are used to enhance the backscattered signal. The main point behind UCA is an impedance mismatch between the contrast agent and the adjacent tissue to enhance the received signal strength [53]. There is a great interest to capsulate gas, perfluorocarbons, or air

within protein, lipid, or polymer shell to form microbubbles (1-10 μm) to increase the acoustic impedance mismatch [54]. The history of ultrasound active materials started at the end of the 1960s, it was observed that agitated saline injection increased detectable US signal during the examination due to the fact that enrichment of gas pockets in the solution as a result of agitation process enabled to backscatter to the applied US signal [55]. However, the produced bubbles were unstable because of high surface tension. More than 20 years later of this observation, the first commercially available, FDA approved air-filled microbubbles with an albumin shell -Albunex®- was developed [56]. Other UCAs filled with air that had been clinically approved in Europe and Japan are Echovist® and Levovist® shelled by galactose. However, all these air filled microbubbles were withdrawn from the market because of stability issues and very short circulation time related to the high solubility of air in water [57, 58]. This issue is overcome by replacing the air with nonsoluble gasses, PFCs, with their low solubility in the aqua system and good biocompatibility features. PFCs entrapped in phospholipid or cross-linked serum albumin microparticles (Optison®, Sonazoid®, SonoVue®, Luminity®) have been on the market that are frequently used in cardiology and liver/kidney imaging [59, 60]. Other than these microbubbles, there have been many polymer based microbubbles that are currently in clinical trials but not FDA approved. For example, poly(D,L-lactide-co-glycolide) (PLGA) is the most common biocompatible, degradable polymer is preferred to form MB to adjust US scattering for the imaging of cardiovascular diseases [61] and as well as identification of lymph nodes near tumor lesion [62].

Besides the application of MBs in imaging, they have also been employed to enhance drug/gene delivery, especially tumor inhibition with the support of US to increase the permeability of the vascular/cell membrane using US sonoporation or cavitation effect [63]. Although MBs offer promising effect for both enhancing the imaging capabilities of US and being used for therapy

with combination of drug/gene delivery, they have significant limitations that restrict the further employment of US systems for the treatment of solid tumors. For instance, MBs are unable to pass through the vasculature and accumulate inside the solid tumor bed since the MBs are too large to take advantage of the tumor's leaky vasculature that forms less than 600-800 nm cutoff size gaps between the endothelial cells, and poor lymphatic drainage, which is called enhanced permeability and retention (EPR) effect [64]. Another restriction of MB applications is that they are not stable in blood circulation, macrophages can easily detect and phagocytize the microbubbles because of their micron sizes, and lacking of biocompatible shield. Therefore, the microbubbles are rapidly cleared from the circulation, which leads to high volume injection or continuous dosing during imaging or treatment to reach effective US signal [65]. Because of these limitations of MBs, many research groups have recently designed nanodroplets and nanoemulsions that can extravasate into a tumor's interstitial space for targeted imaging [66-69], drug delivery [70], and ablation [71, 72]. However, these previous studies were focused only thermal ultrasound ablation with HIFU not histotripsy. Therefore this technique enhances the concerns related to HIFU tissue ablation with requiring long treatment duration and superficial skin burns and does not allow for cell selective ablation due to thermal spread [73].

1.2.2 ND Mediated Histotripsy

One of the primary obstacles facing all ablation techniques is achieving tissue targetebility and cellular level selectivity that can discriminate tumor cells from the healthy cells. Although histotripsy has shown a significant improvement in precision and targeting capabilities compared to thermal ablation methods, histotripsy still requires the visualization of a tumor prior to treatment using non-invasive imaging modalities in order to apply the treatment to a tumor. In addition, histotripsy requires very high pressures (> 25 MPa) to ablate the tissue. To address these concerns,

our group has developed an approach that combines acoustically sensitive nanoparticles with histotripsy, termed nanodroplet-mediated histotripsy (NMH). In order to lower the pressure required for histotripsy and use the advantage of tumor microenvironment where systemically administered nanoparticles (< 600 nm) can passively accumulate because of the dense network of vessels with defective vascular architecture and lack of a smooth muscle layer resulting in large fenestrations [64], our research team has engineered fluorinated amphiphilic triblock copolymers that self-assemble in aqueous medium to form nano-sized droplets (< 300 nm) encapsulating liquid perfluorocarbons in the core [46]. These NDs can be functionalized with targeting agents such as peptides, antibodies, or small molecules in order to enhance the NDs accumulation near/inside the tumor cells and can kill the tumor selectively while protecting the surrounding healthy tissues under reduced histotripsy pressure.

Since perfluorocarbons are not miscible with most of the organic solvents and aqua based solutions [74], they have been preferred to be encapsulated inside emulsion with its lipid portion or they need some contents such as amphiphilic feature having hydrophobic blocks or fluorinated components to increase their solubility [75-78]. For this reason, we preferred the fluorinated monomer, HDFMA, to be able to increase perfluorocarbons solubility in the system. However, fluorinated polymer PHDFMA faces similar solubility problem of perfluorocarbons because of the high number of fluorine contents. Therefore, we added co-monomer MMA and co-polymerized with HDFMA to solubilize HDFMA containing polymer in organic solvents. The middle block plays an important role in the triblock copolymer design. Since this block reacts with two side blocks, it should have two functional end groups and form a thin shell layer in the middle of the formulated nanodroplets allowing phase transition. Therefore, it should contain another functionality to be further reacted to the cross-linker. With these design aspects, we set the ATRP

reaction with anthracene functional, Br-end group initiator with *t*-BA monomer to synthesize P*t*BA with a molecular weight around 1500 Da. P*t*BA, is used as a precursor of cross-linkable block that further can easily be hydrolyzed into acid groups to be able to be functionalized for shell cross-linked after self-assembly of block copolymer into nanodroplets. The third block of the block copolymer is PEG, which gains this triblock copolymer structure not only hydrophilic character to increase the copolymer's solubility in aqua environment but also hemocompatibility, which means no protein adsorption on the particles, no macrophage recognition and minimum interaction with blood cells during blood circulation so that PEG can enhance the particle circulation time. To couple the PEG block to the middle block Anth-P*t*BA-N_3, we introduced the alkyne functionality on the PEG block. To do that, commercially available monohydroxyl end functional PEG (2 kDa) was reacted with 4-pentynoic acid. After well-characterized individual blocks were synthesized, they were coupled to each other via one-pot "click" reactions between alkyne functional PEG and azide functional P*t*BA and retro DA reaction between furan protected maleimide functional P(HDFMA-*co*-MMA) and anthracene functional P*t*BA was occurred. The successful coupling was initially confirmed by ^{1}H NMR spectroscopy. Last but not least in copolymer synthesis, PEG-*b*-P*t*BA-*b*-P(HDFMA-*co*-MMA) copolymers were hydrolyzed using TFA in order to achieve COOH functionality that can react with a diamine functional crosslinker to form a cross-linked shell after self-assembly of block copolymer into nanodroplets. We demonstrated that perfluoropentane (PFP)-loaded nanodroplets allowed for a 2.5-fold decrease in the acoustic pressure required for histotripsy ablation. Further, PFP-loaded nanodroplets did not show particle size and concentration changes upon incubation with bovine serum albumin (BSA) for 24 h at 37 °C [46]. In another study, we demonstrated the feasibility of using the PFP-loaded nanodroplet-mediated histotripsy approach for targeted ablation in agarose tissue phantoms containing a layer of embedded red

blood cells [79]. Moreover, we investigated the effect of ultrasound frequency (345 kHz-3 MHz) on nanodroplet-mediated histotripsy (NMH), with results showing that lower frequency improved the effectiveness of NMH by increasing the size of the focal region, increasing bubble expansion, and decreasing the cavitation threshold [80] (The details of this study can be found in **Appendix 1**). Finally, a separate study was conducted by our team to compare two different perfluorocarbon types, perfluoropentane (PFP, boiling point~29°C, surface tension~9.5 mN/m) and perfluorohexane PFH, boiling point ~56°C, surface tension~1.2 mN/m), on the nanodroplet formulations. Both PFP-loaded and PFH-loaded nanodroplets significantly reduced NMH cavitation threshold compared to the histotripsy threshold. However, the investigation of sustainable cavitation nuclei over multiple pulses pointed out PFH-loaded nanodroplets cavitation activity were able to survive over 1000 pulses, whereas PFP-loaded nanodroplets were destroyed by the cavitation process in less than 50 pulses, likely due to the lower boiling point [81, 82]. **Appendix 2** discusses the ND composition effect on histotripsy with details. Lastly, to understand the physical mechanisms underlying the nanodroplet cavitation process, **Appendix 3** elucidates the role of positive and negative pressure on cavitation nucleation in NMH [83]. Last but not least, **Chapter 2** investigates the efficiency of these well characterized in both material and US sides NDs in 3D prostate cancer spheroid ablation.

1.3 Bone Metastasis

The reason of prostate cancer mortality is not from the primary cancer burden but metastasis spread of the primary cancer cells to distant organs, especially bone. Bone is the most frequent site of prostate cancer metastasis identified at autopsy in up to 90% of patients dying from prostate cancer bone metastasis [84, 85]. Although improving the treatment outcomes of prostate

cancer localized to the prostate gland, two-thirds of patients whose prostate cancer have spread to distant organ live no more than five years [2]. The main reason of high death rate of bone metastasis is a lack of effective targeting therapy options to minimize the cancer progression in bone. It is clear that urgently designing of an effective therapeutic system for the treatment of bone metastasis that requires understanding the molecular interactions between tumor cells and bone microenvironment. To target these interactions might open new treatment strategies of bone metastasis.

1.3.1 Mechanism of Metastases

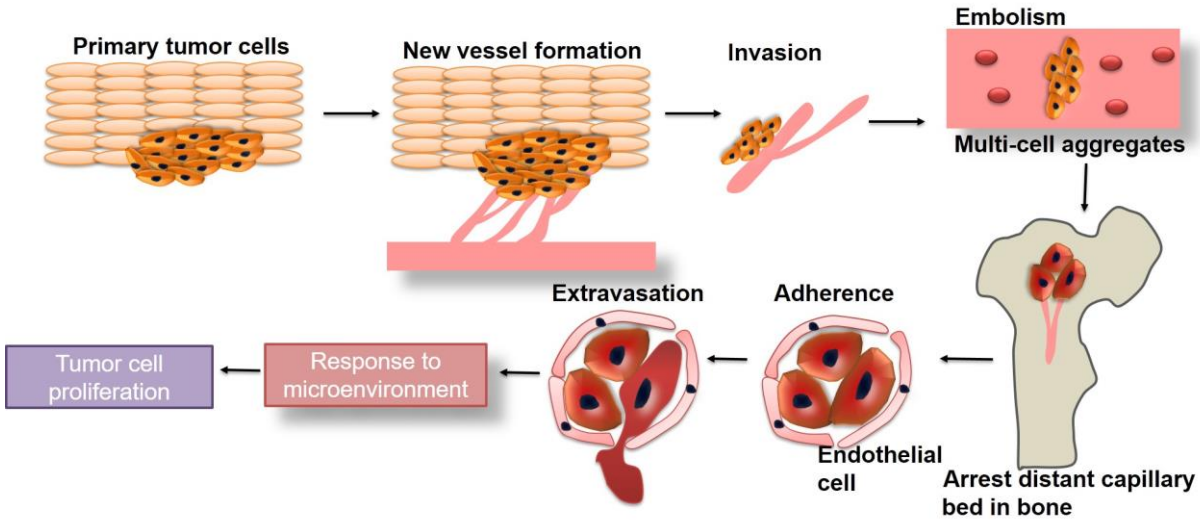

Figure 1.1 The cycle of metastasis from the primary tumor to a bone.

Metastasis is an extremely complex process whereby cancer cells circulate throughout the body, establishing new colonies in distal organs different than the tumor originated organ (primary organ). To colonize a secondary site, like bone, a cancer cell must successfully complete a cascade of linked sequential steps: 1) detach from the primary tumor site; 2) intravasate into the newly formed vasculature, and gain access to the circulation, lymphatics or peritoneal space and survive in these environments against immune response and physical forces; 3) adhere to distant target

organ; 4) proliferate in the metastatic site of bone, which requires blood supply to the tumor for further expansion [86, 87]. The cancer cells can survive as entering the wide channeled sinusoids of the bone-marrow cavity and are placed to develop bone metastases as seen in **Figure 1.1**. The metastasized tumor cells supposed to have certain properties like mesenchymal-epithelial transition (MET) to proliferate and spread out in bone and make the microenvironment a favored place for tumor cells, It is necessity that tumor cells have the ability to migrate across the sinusoidal wall, assault the marrow stroma, produce their own blood supply and travel to the endosteal bone surface [88]. At this location, they stimulate the activity of osteoclasts or osteoblasts, thereby determining whether the subsequent bone metastasis is osteolytic or osteoblastic, which will be discussed with details under the title of "*Bone Remodeling in Cancer Lesion"*. Each of these events involves significant molecular interactions between the tumor cells and the bone microenvironment cells resulting in disruption of normal bone processes [86, 88].

1.3.2 Bone Biology and Bone Remodeling

Bone is a rigid and dense connective tissue that consists of water, inorganic matter, and organic material. Hydroxyapatite (HA) ($Ca_{10}(PO_4)_6(OH)_2$) is the main inorganic matter which stores 99% of the body calcium. Organic matrix is comprised of

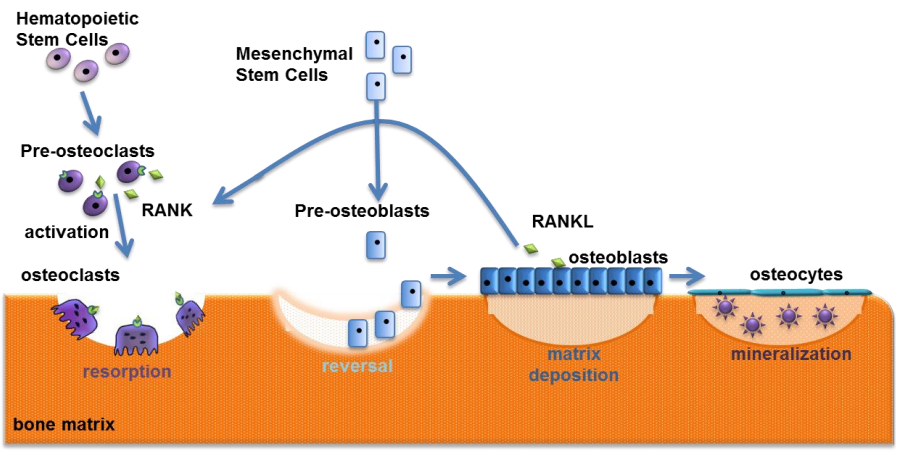

Figure 1.2 Bone microenvironment and regular bone remodeling cycle.

75% collagen and non-collagenous proteins. Deposition of inorganic mineral in the empty spaces of the collagen frame is responsible for strength, rigidness, and density of bone tissue [89].

Bone microenvironment houses a variety biological compartments such as marrow, nerves, blood vessels, endosteum, periosteum, cartilage, and cells. Further, several types of cells, such as mesenchymal stem cells, hematopoietic stem cells, preosteoblasts, and mature cells of the osseous tissue are in there with active duties not only related to bone functions but also immune cells and blood cells formations [90, 91]. Osteoblasts, osteoclasts, and osteocytes are three main types of mature osseous cells that remodel the dynamic nature of bone as depicted in **Figure 1.2**. The osteoblast is a mononucleate cell which has a key role on bone forming by depositing a protein matrix. On the other site, osteoclast that is a multinucleate bone resorbing cell is responsible for bone degradation and function by secreting acidic hydrogen ions and a variety of proteolytic enzymes. Osteoblasts migrate to the surface of bone where they can become entrapped through the deposition of bone matrix around them. In the formed lacunae, osteoblast can transform osteocytes. Osteoblasts and osteoclasts are vital cells in the bone remodeling cycle since they have a direct function in bone health by balancing bone formation and bone resorption through the bone remodeling cycle [89]. Bone remodeling can be altered by various parameters. Various factors, such as PTH, calcitonin, vitamin D, growth hormones, steroids, and cytokines, are also actively involved in bone remodeling. The imbalance between bone formation and bone resorption results in undesired effect such as bone loss, enlarged, or weak bones, and fractures [92, 93]. Disease states such as osteoporosis and tumor metastases affect remodeling. [89, 94].

1.3.3 Bone Remodeling in Cancer Lesion

Bone turnover is a regular process of the removal of old bone called bone resorption and forming of by new bone. Due to this regular bone resorption and formation make bone

microenvironment rich in metabolite ingredients providing a favorable place to progress and proliferate of the tumor cells. Thus prostate cancer cells frequently metastasize to the skeletal system. Because of bone microenvironment with its rich metabolite ingredients that provides a favorable place to progress and proliferate of the tumor cells. It is well-known that prostate cancer preferentially localizes to bone with highly active bone turnover because of aforementioned reasons [86, 95-97]. Although prostate cancer is radiographically characterized as osteoblastic, recent molecular studies have shown that many bone metastases contain either osteoblastic, osteolytic, or both characters [98].

For instance, prostate cells secrete a variety of factors such as endothelin-1 (ET-1) [99], bone morphogenetic proteins (BMP) [100], insulin-like growth factor (IGF) [101], platelet-derived

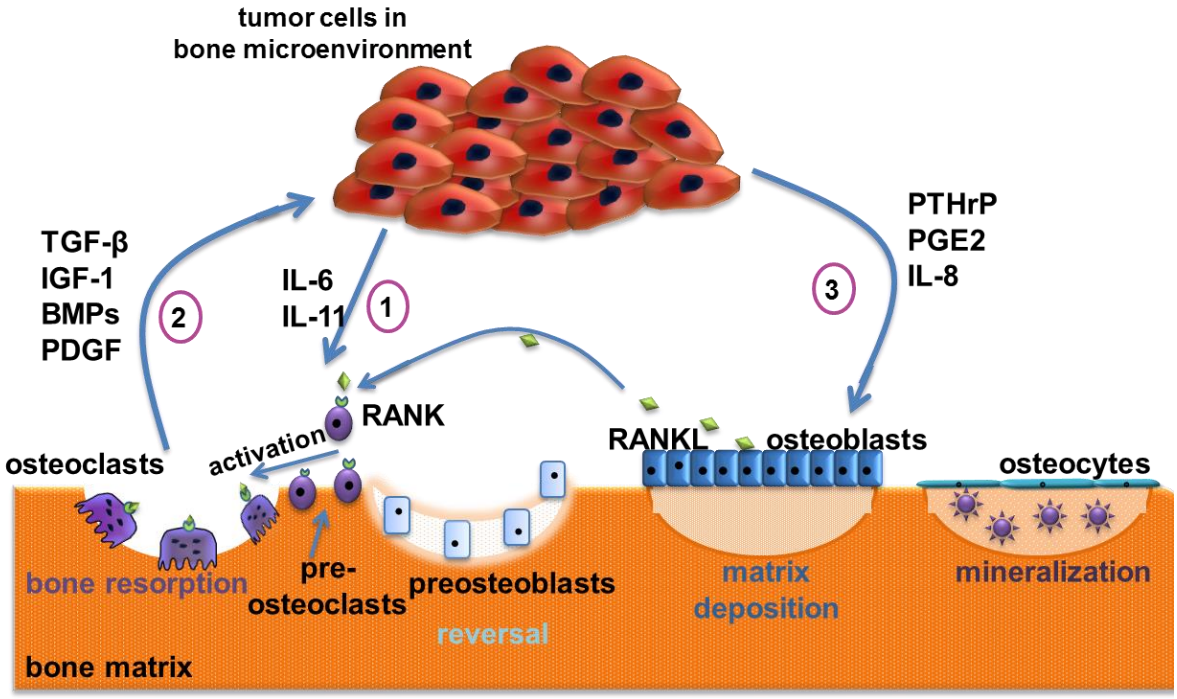

Figure 1.3 Bone vicious cycle.

The interaction between tumor cells and bone micro enviorement.

growth factor (PDGF) [102], parathyroid hormone-related protein (PTHrP) [103], transforming growth factor-β (TGF-β) [104] that direct or indirectly promotes bone mineralization. For instance, ET-1 is a significant mediator of osteoblastic bone metastases and is found in a high level in the plasma of advanced prostate cancer patients [105]. Moreover, it is secreted by prostate cancer cells and activates tumor cell proliferation. Bone microenvironment with IL-1β, TNF-α, and TGF-β also supports the expression of ET-1[106]. Bone morphogenetic proteins (BMPs) are a member of the TGF-β family. They have functions not only on new bone formation but also some roles on apoptosis, differentiation, proliferation, and morphogenesis [98]. Proteins such as TGF-β activated by PSA from prostate cancer cells and MMPs secreted by osteoblasts also contribute to augment of IGF-I leading to cancer cell growth in bone. In addition to these osteoblastic factors, metastases prostate cancer cells produce several other factors that enhance osteoclast activity. Prostate cancer cells have been shown to secrete the receptor activator of nuclear factor κ B ligand (RANKL), which causes differentiation of osteoclast precursor cells into active osteoclasts [107]. PTHrP, IL-11, and IL-6 factors trigger osteoblasts to express RANKL and decrease the level of OPG, which is a soluble decoy receptor that inhibits osteoclast differentiation through its binding to RANKL [108]. Other than RANKL/RANK/OPG bone resorption factors are IL-8, TNF-α, and vascular endothelial growth factor (VEGF) induce osteoclastogenesis [109-111]. As a result of these factors related to bone resorption, the growth factors, such as TGF-β and IGFs and Ca^{2+} are released from bone matrix that promotes more tumor cell growth and this tumor cells and bone cells interaction cycle is called ‘vicious cycle’ [112] as described in **Figure 1.3**.

1.3.4 Limitations Current Bone Metastases Therapy

The current prostate cancer therapeutic modalities -hormone therapy and chemotherapy- are not aimed to specifically treat the tumor in the bone lesion so these therapies have limitations

such as lacking of desired drug concentration in bone. In addition, in the case of advanced stage of the metastasis various complications may be noticeable such as osteolysis, spinal cord compression, hypercalcemia, increased fracture incidence and permanent pain due to the fact that the bone metabolism and microenvironment are disrupted and induce imbalance between bone formation (osteoblast activity) and bone resorption (osteoclast activity) [16, 113]. Moreover, around two-thirds of patients have suffered from bone metastases complain about break-through pain, which described as a simultaneous appearance of strong pain, which is one of the skeletal-related events (SRE), despite of taking of strong pain killers, or analgesics [114].

Bisphosphonates (BPs), which FDA approved in treating multiple myeloma, breast cancer metastasis and prostate cancer metastasis to bone, are addressed some of above limitations [115] as an adjuvant therapy to prevent SRE for managing of metastatic bone pain, and lowering the risk of broken bones. Further, BPs are co-administered with doxorubicin, docetaxel and paclitaxel to enhance anticancer therapeutic activity [116-119].

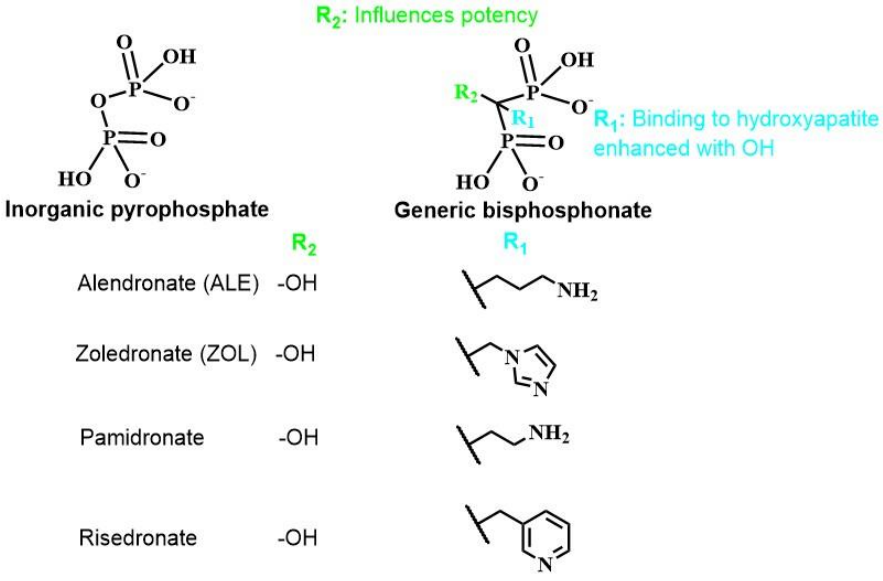

Figure 1.4 Basic structures of pyrophosphate and bisphosphonates.

Development of BPs in chronological perspective gives a brief information about BPs actions, target, and limitations. In the late of 1960s Fleisch et al. reported the first biological function of pyrophosphate on inhibition of the formation and dissolution of calcium phosphate crystals which has a key regulator of bone resorption and formation [120]. However, the major issue of pyrophosphate is the rapid hydrolysis in the circulation before reaching to bone. This unstable form of the formulation where the oxygen bind to two phosphates (P-O-P) is replaced by a carbon (P-C-P) called bisphosphonates which are a more chemically stable member of pyrophosphate analogues **(Figure 1.4)**. This elemental substitution overcomes a main issue of hydrolysis of the bonds, and enhances the stability of the structure with a capable of being delivered to bone [121].

BPs have a high affinity for hydroxyapatite constituting the major bone inorganic structure due to the fact that the oxygen atoms bound to phosphate chelate the Ca^{2+} ions in bone [122]. The major target cell population of BPs is osteoclasts as explained in bone biology and bone remodeling section because osteoclasts release the factors that make the environment rich in acidity and proteases results in degrading bone surface in which BPs bound [123, 124]. The released BPs from the bone surface is internalized by osteoclasts via fluid-phase endocytosis [125] exhibiting inhibition effect through either mitochondrial adenine nucleotide translocase (ANT) pathway with not containing nitrogen atoms in the BPs structure [126] or mevalonate pathway with containing a nitrogen atom [127]. The BPs that have a direct function in the second pathway are (10-100)-folds more potent than the BPs formulation acted in the ANT pathway. Basically, mevalonate pathway requires for prenylation of small GTPases like Rac, Ras, or Rab, which has a direct role in cholesterol synthesis, cytoskeletal organization, bone resorption, and cell morphology [128]. Inhibition of prenylation reduces the osteoclast activity and triggers apoptosis

[129]. In addition to BPs's antiresorptive role, BPs have direct functions such as antitumor [130], antiangiogenic [131], and antimigratory [132] effects.

Neither cancer chemotherapy nor BP based cancer therapies demonstrate desired level therapeutic activity like slowing down tumor progression or increasing the lifespan of bone metastasized patients [133]. Recently, nanomedicine/macromolecular based approaches have attracted tremendous attention as a drug delivery vehicle. These nanoparticles can accumulate in tumor tissue because of the EPR effect that described under the title of **ND mediated Histotripsy (NMH)**, which is called passive targeting, as well. By these nanomedicine approaches, the active drug concentration can be enhanced in tumor microenvironment while minimizing the systemic side effect of the drug. However, the drug dose at bone tumor microenvironment is usually low by the passive targeting, resulting in the poor efficacy for tumor inhibition. To further improve the specific targeting and delivery efficiency to bone metastasis, active targeting ability of the nanomedicine approach is essential. Furthermore, the excess of irregular bone formation or bone degradation due to the disease effects on bone face to exposure of HA to blood carries, which provide active targeting opportunities to bone metastasized tumor lesion in bone. BPs, acidic or phosphorylated peptides, and noncollagenous proteins have been preferred to target bone metastasis to carry higher chemotherapeutics or imaging markers to distinguished the disease level [134, 135].

1.3.5 Peptide vs. Bisphosphonate Targeting

Small peptides are one of the common motives for bone targeting drug delivery, which is inspired by bone tissue engineering concepts aiming to grow bone cells by manipulating the bone crystal structures. Basically, biological form crystals have been wide-range studied and shown that a subset of the matrix macromolecules are closely integrated with the mineral phase that regulates

crystal growth and also provide an anchoring point for cells and proteins connect to matrix proteins to the bone crystals [136, 137]. These macromolecules are basically in acidic character, which are noncollagenous proteins (phosphophoryn, bone Gla protein, osteonectin and bone small proteoglycan 11) that are found in bone exhibit binding affinity on hydroxyapatite with as low as 10^{-7} M of dissociation constant due to the repeating (being rich in) amino acids such as glutamic or aspartic acid. These amino acids display a negative charge because of carboxylate groups on the amino acid structures so they are able to chelate calcium ions on the surface of HA. Also, peptide sequences of repetitive glutamic acid and ascorbic acid units interacted exclusively with HA *in vitro* and *in vivo* [136-138]. Other than these acidic character amino acid units, phosphorylated amino acids also exhibit a specific adsorption on HA structures with a positive correlation of phosphorylated numbers [139]. For instance, Kohn's group has identified HA-specific peptide sequence through the use of phage display that containing more than 10^9 bacteriophage expressing sequences against interested HA material [140]. After selection of interested peptide sequences, these peptides were further characterized with computational modeling, and ELISA and shown that the apatite-specific 12-mer peptide VTKHLNQISQSY (VTK) [140, 141]. After the identification of the 12-mer peptide, VTK, it was phosphorylated through the serine residue on VTK (pVTK) and characterized in terms of biomimetic apatite. It was demonstrated that pVTK had a 10-fold increase in adsorption to the apatite surface comparing to VTK peptide. Furthermore, pVTK are able to inhibit the mineralization in pre-osteoblastic cells with a dose-dependent response [142].

Another strategy for bone targeting is BPs decorated nanoparticles or polymers due to the fact that BPs have a strongly binding affinity to bone HA mentioned in previous sections in detail. The use of BPs on nanomedicine tools has several significant advantages. For example, ALE,

which is a member of BPs, is decorated on the particles because of its primary NH_2 groups that allow its conjugation easily to the COOH unit of any nanomedicine tools. Further, BPs coupled particle are able to show synergistic effects with the carried therapeutics through the particles in addition to BPs that can be coupled to the particle surface with degradable linkages (pH sensitive or enzyme sensitive) so in the active environment where the linkage is broken and free BPs can be released for extra therapeutic activity [143].

In the literature some studies compared the binding kinetics of peptides and BPs to HA. For instance, 8 repeating units of Asp or Glu peptide demonstrated faster binding to HA compared with PAM, or ALE in first 1 h in vitro but then a similar high binding profile for within 24 h [144, 145]. In the HA binding comparison of PEG-D-$(Asp)_8$ with PEG-ALE is 80% and 66% for 1 h incubation, respectively [145]. Nonetheless, ALE functionalized gold NPs showed faster and 6 or 16-fold higher binding in HA compared with Glu, or phosphonic acid, respectively [146]. Wang et al. compared the in vivo bone binding location of acidic peptide and ALE. They showed that peptide could bind to resorption side while ALE-particles bound to both bone formation and resorption sites [145].

1.3.6 Bone Targeted Drug Delivery Strategies with Macromolecules or Nanoparticles

A few bone targeted drug delivery studies were conducted on different bone metastasis and bone diseases such as breast, prostate cancer bone metastasis and osteosarcoma bone cancer with different therapeutics and nanomedicine tools [143, 147]. For example, one of the greatest example of peptide ($(AspSerSer)_6$) based delivery systems is shown by Zhan et al. who used dioleoyl trimethylammonium propane (DOTAP)-based cationic liposomes to carry osteogenic siRNA targeting casein kinase-2 interacting protein-1. With this bone targeted gene delivery system, they exhibited that this approach significantly promoted bone formation, enhanced the bone micro-

architecture and increased the bone mass in both healthy and osteoporotic rats [148]. In another study, Thamake et al. designed ALE coated PLGA nanoparticles that co-encapsulated curcumin and bortezomib to further enhance the therapeutic efficiency and overall clinical outcome of the treatment of bone metastatic breast cancer. Even though these drugs are known as synergistic effect once used in combination, the researcher did not see any synergism in the anti-osteoclastogenic activity of these agents. In vivo imaging modalities exhibited that higher ALE-particles accumulated in tumor metastasized bone comparing to controls. Further, ALE-coated PLGA nanoparticles protected bone resorption and decreased the rate of tumor growth in an intraosseous model of bone metastasis [149]. Another research carried out by Miller et al. by conjugating paclitaxel (PTX) and ALE with PEG to increase water solubility of PTX and target to bone for the treatment of bone metastatic breast cancer. They showed that combined therapeutic effect with PTX (anti-cancer agent) and ALE (anti-angiogenic, and anti-cancer agent in high dose) as improving PTX's pharmacokinetics, biodistribution, and enhancing its efficacy while reducing its side-effects [150]. The same group also worked on dendritic PEG bearing ALE and PTX to increase number of targeting unit on the micellar particles and tested on PC-3 prostate cancer in vitro model showing a high cytotoxicity, comparable to that of free PTX and ALE combination. Further, they showed that prolonged half-life of the drugs with this conjugation strategy in mice [151]. Segar et al. also tested ALE and TNP-470, which is a potent anti-angiogenic agent, conjugated with N-(2-hydroxypropyl) methacrylamide (HPMA) copolymer through a Glycine-Glycine-Proline-Norleucine linker that can be cleavable by cathepsin K enzyme, which is cysteine protease over expressed at the bone resorption site. By using TNP-470 conjugated macromolecular delivery system, they reduced the too many side effects of free drug formulation in clinic such as neurological dysfunction, and low WBC counts, which prevented clinical applications. They

demonstrated that ALE and TNP-470 conjugated HPMA reduced VEGF-induced vascular hyperpermeability by 92% and remarkably inhibited osteosarcoma growth in mice by 96% with co-delivery of two synergistic drugs [152]. Uludag group developed thiol-BPs coupled to micellar and liposomal particles to create mineral binding nanocarriers. They tested 3 different drugs, carboxyfluorescein (CF), DOX, and lysozyme (LYZ) in the particle formulations. The drug entrapped in BP-liposome showed a slower release profile from treated collagen/HA scaffold model. Therefore, they concluded that this prolong release profile of collagen/HA composite scaffold and BP-liposomes are promising for bone tissue engineering and regenerative medicine applications [153, 154]. The most common bone targeting moiety is ALE because of its primary NH_2 functional group leading its conjugation to the polymers or nanoparticles easily. Chaudhari et al. first time showed that zoledronate (ZOL) conjugated PEG-polybutyl cyanoacrylate (PBCA) NPs used on BO2 and MCF-7 breast cancer cell lines. Basically they designed ZOL-conjugated DOX-loaded PEGylated PBCA NPs for bone metastasis treatment. They found that enhanced cytotoxic effect in both BO2 and MCF-7 cell lines due to higher uptake following ZOL-mediated endocytosis as compared to free drug conditions. Further, the in vivo study demonstrated that DOX-loaded ZOL-conjugated PEG-PBCA NPs were highly localized to the tumor infected bone. Based on the cell cycle and apoptosis analyses this treatment strategy showed synergetic effect in tumor cells [155].

All in all, **Chapter 3** of this thesis describes the engineering of high-dose anticancer agent (CTX) loaded *"smart"* micellar nanoparticles to control drug release profile and delivery of the agent efficiently to the diseased tissue with minimal toxic effect to healthy tissues. After the selection of optimum anticancer agent carrier particle formulation, **Chapter 4** investigates the bone targeting capability of BP or pVTK-labeled of the characterized particle formulation in

Chapter 3 and their bone and cancer cells uptake differences in bone like microenvironment. Finally, **Chapter 5** discusses the conclusion of this research work and proposes future work to advance the developed bone-targeted drug carrier systems to preclinical studies.

Chapter 2

Non-invasive Ablation of Prostate Cancer Spheroids Using Acoustically-Activated Nano-Droplets

The material in this chapter is submitted to the following journal: **O. Aydin,** E. Vlaisavljevich, Y. Y. Durmaz, Z. Xu, and M. ElSayed "Mechanical Ablation of Prostate Cancer Spheroids Using Acoustically-Activated Nano-Droplets", *Molecular Pharmaceutics.*

2.1 Introduction

The widespread use of prostate-specific antigen (PSA) screening and the increase in life expectancy have increased the number of men diagnosed with prostate cancer [156]. These patients are routinely managed with definitive therapy including radical prostatectomy (RP) or radiation therapy (RT), which are associated with significant complications and side effects such as incontinence and erectile dysfunction that greatly deteriorate patient's quality of life [3, 4]. Analysis of RP specimen reveals that 49% of men undergoing RP show insignificant or indolent cancer (i.e. organ-confined cancer lesion < 0.5 mL) [5] compared to 73% of the patients initially enrolled in active surveillance who undergo RP and reveal a significant cancer on RP specimens [6]. Analysis of RP specimens showed that 38% were unifocal [157] and 80% of the total tumor volume in multifocal disease arose from the index tumor with extracapsular extension present in only 28% of these patients [158]. These results clearly indicate that a large population of prostate cancer patients have a biologically unifocal disease, which suggests the potential for using focal therapy (i.e. targeted ablation of the cancer lesions) as an alternative treatment strategy to RP [159].

Success of focal therapy depends on the ability to detect and image tumor tissue, target the cancer lesions, monitor the therapeutic response, and assess the results [159].

Histotripsy is a noninvasive tissue ablation technique that controllably fractionates soft tissue using a dense cavitation bubble cloud generated by short duration ultrasound pulses under high acoustic pressure (~25-30 MPa) [43, 49, 160]. Earlier research shows that histotripsy treatments initiate and maintain a dense cavitation bubble cloud over multiple pulses (often >100) until the treated tissue is completely fractionated into a liquid homogenate with complete loss of the cellular structure [43, 49, 161]. The process by which histotripsy achieves tissue fractionation has been shown to be the rapid expansion and collapse of cavitation bubbles, which fractionates soft tissues into an acellular homogenate by inducing very large strains to the adjacent tissue structures [162]. Currently, non-invasive tissue removal using histotripsy is being clinically evaluated in benign prostatic hyperplasia [163], deep vein thrombosis [164], congenital heart disease [165, 166], and cancer [45, 167]. Despite the promise of histotripsy as an ablation therapy, the limitation of histotripsy is that 1) it is not targeted, and 2) it requires very high pressure. In some applications, very high pressure cannot be achieved due to the limited acoustic window or deep located target. Therefore, nanodroplet-mediated histotripsy (NMH) can be used to overcome the limitations by lowering the threshold.

To address the limitations of histotripsy, our group has developed acoustically-activated nanodroplets to achieve selective mechanical fractionation of diseased tissue at low acoustic pressure. Specifically, we designed and synthesized an amphiphilic triblock copolymer composed of a hydrophilic poly(ethylene glycol) (PEG) block, a central poly(acrylic acid) (PAA) block, and a hydrophobic poly(heptadecafluorodecyl methacrylate-*co*-methyl methacrylate) (P(HDFMA-*co*-MMA)) block, which proved to self-assemble and encapsulate 2% v/v perfluorocarbon (PFC)

forming acoustically-activated nanodroplets [168]. We used a chemical cross-linker to covalently "stitch" the central PAA blocks forming a flexible polymer shell that displays a brush of biocompatible PEG chains, which can be further functionalized to display different ligands (e.g. sugars, peptides, antibodies, or aptamers) to allow selective targeting to specific disease sites. Our earlier results show that the nanodroplets rapidly expand forming microbubbles (>500μm) before energetically collapsing at an acoustic pressure that is 2.5-fold lower than the acoustic pressure needed to generate the same bubble cloud using the histotripsy pulse alone [168]. Results also confirm the feasibility of imaging nanodroplets expansion into microbubbles and their subsequent cavitation using therapeutic ultrasound, which is the basis for their potential use in ultrasound-guided ablation therapy [45, 80, 83]. We investigated the effect of changing the PFC core from perfluoropentane (PFP, boiling point ~29 ºC, surface tension ~9.5 mN/m) to perfluorohexane (PFH, boiling point ~56 ºC, surface tension ~11.9 mN/m) on the acoustic and ablative properties of PFP-loaded and PFH-loaded nanodroplets [169]. Both PFP-loaded and PFH-loaded nanodroplets exhibited a significantly reduced cavitation threshold compared to the cavitation threshold of histotripsy alone. However, the PFH-loaded nanodroplets maintained the bubble cloud over 1000 pulses compared to PFP-loaded nanodroplets, which were destroyed by the cavitation process in less than 50 pulses likely due to the lower boiling point of the PFP core [80, 169]. Further, the PFH-loaded nanodroplets generated well-defined ablation lesions in the RBCs layers sandwiched in tissue-mimicking gel phantoms indicating a stronger ablative capacity compared to PFP-loaded nanodroplets [168].

In this study, we expand on our previous research studying NMH and investigate the feasibility of achieving ablation of PC-3 and C4-2B prostate cancer cells *in vitro* using PFP- and PFH-loaded nanodroplets at acoustic pressures significantly below the regular histotripsy. When

using a single ultrasound pulse of <2 cycles in duration, cavitation can be reliably generated with the peak negative pressure directly exceeds the intrinsic threshold of the medium without any externally injected agents. The histotripsy intrinsic threshold is ~26-30 MPa for water-based soft tissues such as tumors. Within nanodroplets, cavitation can be generated by a single ultrasound pulse of <2 cycles significantly lower pressures than the histotripsy intrinsic threshold [45, 80, 168, 169]. While prior work had demonstrated the initial feasibility of the NMH process, this study represents the first time NMH will be used for the treatment of cancer cells, which is a significant step in the development of this technology. Specifically, we examine the effect of histotripsy pulses on the viability of individual 3D spheroids of PC-3 and C4-2B cancer cells suspended in culture medium and encapsulated in tissue-mimicking gel phantoms in order to gain an understanding of the process in which NMH mechanically fractionates cancer cells in 3D cellular microenvironment into acellular homogenates. We evaluate the effect of incubating individual PC-3 and C4-2B prostate cancer cells and their 3D spheroids in solution and gel phantoms with PFP- and PFH-loaded nanodroplets on cell viability when treated with ultrasound at different frequencies. We quantitatively compared the ablative capacity of PFP- and PFH-loaded nanodroplets against PC-3 and C4-2B spheroids and evaluated the viability of cellular debris. Results clearly show the potential of these acoustically-activated nanodroplets in achieving image-guided ultrasound-mediated ablation of prostate cancer.

2.2 Experimental Section

2.2.1 Materials

2,2`- (ethylenedioxy)-bis(ethylamine) (Sigma-Aldrich, 98%, St. Luis, MO), 2-(*N*-morpholino)ethanesulfonic acid monohydrate (MES, Sigma-Aldrich, >99.9 % St. Luis, MO),

tetrahydrofuran anhydrous (THF, Sigma-Aldrich, >99.9 % St. Luis, MO), resazurin sodium salt (Sigma-Aldrich, St. Luis, MO), PEG Bioultra 35,000 (Sigma-Aldrich, St. Luis, MO), Dextran 500,000 (Spectrum, Gardena, Ca), Bovine Serum Albumin (BSA, Sigma-Aldrich, St. Luis, MO), Ultrapure Agarose (Invitrogen, Carlsbad, Ca) were used as delivered. RPMI medium 1640, fetal bovine serum (FBS), 0.25% trypsin/0.20% ethylene diamine teraacetic acid (EDTA), phosphate buffered saline (PBS), penicillin/streptomycin/ amphotericin, sodium pyruvate, nonessential amino acid solutions, the Live/Dead cytotoxicity Kit for mammalian cells (Calcein AM and Ethidium homodimer-1), and agarose were purchased from Invitrogen Corporation (Carlsbad, CA). Perfluoropentane (PFP, Alfa Aesar, 97% ca. 85% n-isomer) and perfluorohexane (PFH, SynQuest Lab, > 98%) were directly used without prufication. *N*-hydroxy succinimide (NHS, 97 %), and *N*-(3-Dimethylaminopropyl)-*N* ethylcarbodiimide hydrochloride (EDC, >98 %) were purchased from Fluka (St. Luis, MO). T-75 flasks, Costar 96-well plates, and cell culture supplies were purchased from Corning Inc. (Corning, NY).

2.2.2 Instruments

A 500 MHz Varian Mercury system (Palo Alto, CA) was used to record all the ^{1}H NMR and ^{13}C NMR spectra of polymer blocks at room temperature. Gel permeation chromatography (GPC) analysis was done using a Viscotek GPCmax Autosampler system consisting of a pump and Water 2414 refractive index (RI) detector. The molecular weight and molecular weight distribution of synthesized polymers were determined based on their elution volume on a Styragel HR 4E column compared to a series of poly(methyl methacrylate) standards (PolyAnalitik Inc, Canada) using THF as a mobile phase at a flow rate of 1 mL/min at 35 ^{o}C. The data was analyzed

using Viscotek OmniSEC Omni-01 software. Perkin-Elmer FT-IR Spectrum 4100 type A machine was used to confirm the azidation of different polymer blocks.

2.2.3 Formulation of PFP- and PFH-Loaded Nanodroplets

The amphiphilic, triblock PEG_{45}-*b*-PAA_{12}-*b*-P($HDFMA_8$-*co*-MMA_{20}) copolymer was used to prepare PFP- and PFH-loaded nanodroplets with equal PFC loading (2% v/v) following published protocols [168]. Briefly, the PEG_{45}-*b*-PAA_{12}-*b*-P($HDFMA_8$-*co*-MMA_{20}) polymer was synthesized using a combination of atom transfer radical polymerization (ATRP) and "click" coupling techniques followed by purification and confirmation of polymer composition using GPC, ^{1}H NMR, and MALDI techniques following established protocols [80, 168]. Formulation of different nanodroplets started by dissolving the copolymer in tetrahydrofuran (THF) (0.2% w/v) and cooling down the polymer solution to 0 $^{\circ}$C before adding the PFP (2% v/v) or PFH (2% v/v) while vigorously stirring the copolymer-perfluorocarbon mixture **(Figure 2.1)**. An equal volume of deionized water was added drop-wise to the polymer/PFC mixture to initiate micelle formation while keeping the solution in an ice bath for 1h before transferring the micelles solution to a dialysis bag (MWCO of 1 KDa) and dialyzing overnight against ice-cold 2-(*N*-morpholino)ethanesulfonic acid monohydrate solution (MES buffer, pH 5.5) to remove the THF and obtain a milky solution of uncross-linked PFP- and PFH-loaded nanodroplets. Each formulation was transferred to a round bottom flask and mixed with 2,2`-(ethylenedioxy)-bis(ethylamine) to cross-link the carboxylic acid groups in the central PAA block in the polymer backbone via NHS/EDC coupling chemistry forming the cross-linked nanodroplets with a flexible polymer shell. Shell cross-linked nanodroplets were dialyzed against ice-cold water for 12 hours to remove the unreacted cross-linker and reaction byproducts.

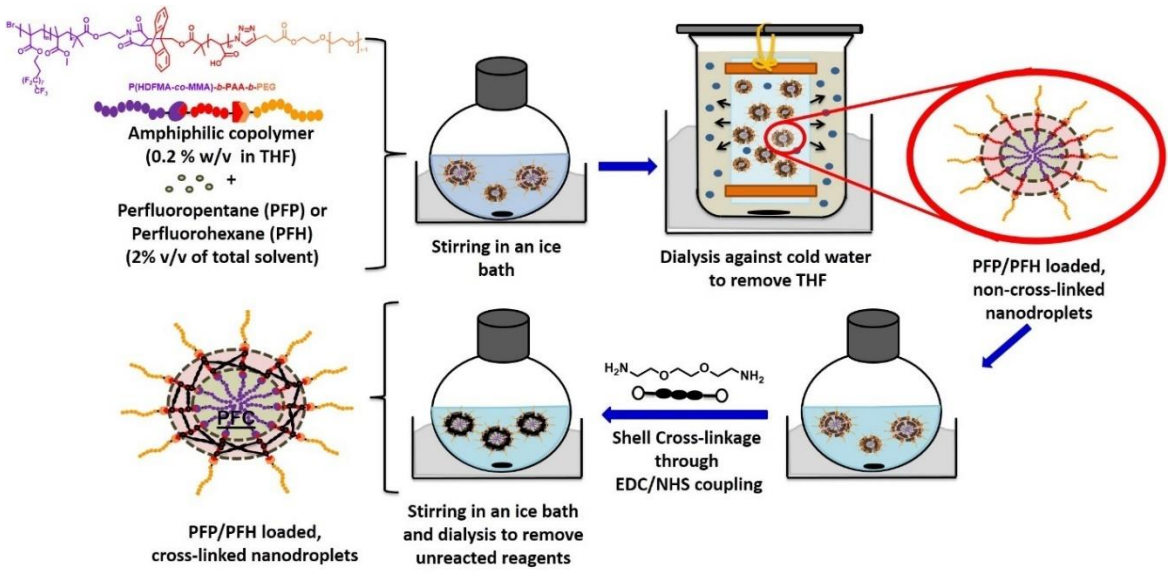

Figure 2.1 Schematic presentation showing the formulation of PFP- and PFH-loaded nanodroplets using amphiphilic PEG_{45}-*b*-$(PAA)_{12}$-*b*-P($HDFMA_8$-*co*-MMA_{20}) copolymers.

2.2.4 Nanodroplets Characterization

Size and concentration of PFP- and PFH-loaded nanodroplets were measured using the Nanoparticle Tracking Analysis (NTA) at 37°C. The NanoSight™ LM10 system (Malvern Instruments, Amesbury, UK) equipped with a temperature-controlled 405 nm laser module, a high sensitivity scientific Complementary Metal Oxide Semiconductor (sCMOS) camera (Hamamatsu, Orca, Hamamatsu City, Japan), and a syringe pump was used for the collection of NTA data. Briefly, nanodroplets solutions were diluted to the appropriate concentration using deionized water before imaging where 60s videos (5 videos per sample) were acquired and analyzed using the NTA software (Version 3.0, Build 0066) at 37 °C. We plotted nanodroplets concentration as a function of droplet size with the error bars representing the standard deviation of the repeat measurements for each sample. The mean size and standard deviation values obtained by the NTA software correspond to arithmetic values calculated with the sizes of all particles analyzed by the software.

The error bars displayed on the graphs were obtained by the standard deviation of a minimum of five different samples.

We investigated the stability of PFH-loaded nanodroplets NDs when incubated bovine serum albumin (BSA) as a model serum protein for 24 hours at 37 °C while stirring by monitoring the change in droplets size and concentration using NTA. This analysis was done by mixing 900 µL of PFH-nanodroplets with 100 µL of BSA (20 µg/mL) and imaging droplets solution following our previously published protocol [168]. All statistical evaluations were carried out with unpaired two tailed Student's *t* tests where $p < 0.05$ indicates statistically significant difference between groups.

2.2.5 Cell Culture

PC-3 and C4-2B prostate cancer cells were cultured following published protocols [170]. Briefly, both cell lines were cultured in RPMI-1640 supplemented with 10% FBS and 1% antibiotic/antimycotic solution. PC-3 and C4-2B cells were incubated at 37 °C and 5% CO_2 while changing the culture medium every other day and passaging the cells using 0.05% trypsin/EDTA solution after reaching 80% confluence. The passage number for PC-3 and C4-2B cells used in the cytotoxicity and ablation studies was in the range between 25 and 40.

We used the Aqueous Two-Phase System (ATPS) to prepare PC-3 and C4-2B spheroids following published protocols [171] with minor modifications. Briefly, 5.0% (w/w) of PEG (35,000 Da) and 12.8% (w/w) of dextran (500,000 Da) stock solutions were prepared in the culture medium and kept at 37°C. The surface of flat-bottom 24-well plates and cell holders were coated with 300 µL and 650 µL of a boiled agarose solution 2% (w/v) in double distilled water, respectively, to get a non-adherent surface. We allowed the agarose solution to cool down to room temperature and solidify in 10 min before washing twice with PBS and adding 500 µL of 5.0%

(w/w) PEG solution to each well. PC-3 and C4-2B cells were prepared at a concentration of 700,000 cells/µL in 12.8% (w/w) aqueous dextran before adding 0.8 µL of this cell solution to the PEG solution in each well. Given that PEG and dextran solutions are immiscible, we allowed the cells to aggregate and grow at the interface for 24-48 hours to get uniform spherical spheroids. We measured the horizontal and vertical diameters of each spheroid using an inverted microscope (Olympus IX51, Melville, NY) before adding more culture medium and incubating for longer periods of time to increase the size of the spheroids. The spheroids were ready for use in 2 days of culture under these conditions We confirmed the viability of the cultured spheroids by incubating them with a solution of 3 µM Calcein AM and ethidium homodimer-1 for 2 hours before washing excess dye using PBS and examining the spheroids under an Olympus IX51 fluorescent microscope (Melville, NY) coupled with 130 W U-HGLGPS fluorescence light source and a TL4 power supply unit. Fluorescent images were captured and analyzed using the Olympus image software analySIS® where green and red fluorescence indicated live and dead cells, respectively.

2.2.6 Nanodroplets Cytotoxicity

We evaluated the non-specific toxicity PFP- and PFH-loaded nanodroplets by incubating them with PC-3 and C4-2B cells. Briefly, PC-3 and C4-2B cells were seeded at a seeding density of 10 x 10^3 cells/well in 96-well plates and allowed to adhere for 24 h before adding the nanodroplets at concentrations between 0-100 µg/mL and incubating for 48 h. At the end of the incubation period, the culture medium was removed and the cells were incubated with 200 µL of the Resazurin dye at a dilution of 1/10 for 4 h before measuring solution fluorescence (λ_{ex}= 570 nm, λ_{em}= 590 nm) using the Fluoroskan Ascent FL plate reader (Thermo Fisher Scientific, Waltham, MA). Fluorescence values were normalized to that observed with PC-3 and C4-2B cells incubated in the regular culture medium (control group) to calculate the percentage of viable cells

in response to different treatments. The nanodroplets concentration that resulted in a statistically significant reduction in cell viability was considered cytotoxic.

2.2.7 Ablation of PC-3 and C4-2B Cells and Spheroids in Solution

A 345 kHz ultrasound transducer was designed to generate a histotripsy bubble cloud and image the cavitation of PC-3 and C4-2b cells and spheroids using a clinical ultrasound imaging system (Philips HDI 5000 Ultrasound system, Bothell WA, USA). The 345 kHz transducer was designed to generate short, high-pressure, 1-2 cycle histotripsy pulses and had a geometric focus of 150 mm, an aperture size of 272 mm, and an effective f-number of 0.55. Elements were driven in phase with a custom high-voltage pulser that was developed in-house. The pulser was connected to a field-programmable gate array (FPGA) board (Altera DE1 Terasic Technology, Dover, DE) specifically programmed for histotripsy pulsing. This setup allowed the transducers to output short pulses consisting of less than two cycles. A fiber optic probe hydrophone built in-house [172] was used to measure the acoustic output pressure of the transducers. At high negative pressure levels ($p-$ > 23 MPa), the acoustic output could not be directly measured due to cavitation at the fiber tip. Therefore, these pressures were estimated by a summation of the output focal $p-$ values from individual transducer elements with these approximations assuming minimal nonlinear distortion of the waveform occurring within the focal region. In a previous study [44], this estimated $p-$ was found to be accurate within 15% compared to direct focal pressure measurements in water and in a medium (1,3 butanediol) with a higher cavitation threshold. The transducer was placed inside a tank of degassed water at room temperature (22°C) with the elements completely submerged. A computer-positioning system was built to support the tube containing the treatment solution and to adjust the position of the tube with respect to the transducer focus. The desired concentration (2 x 10^8 particles/mL) of PFP- or PFH-NDs was added to the solution of 200,000 individual PC-3 or

C4-2B prostate cancer and, in a separate study to three PC-3 or C4-2B spheroids in 2 mL of PBS in the treated tube. Individual PC-3/C4-2B cells and spheroids were suspended in PBS before being added to the rubber tube, which was placed in the focal zone of the 345 kHz array transducer placed inside a degassed water tank at room temperature. The tube was positioned in the focal zone of the 345 kHz array transducer using a PC-controlled console and scanned from the bottom to the top and vice versa for 5 minutes to ensure the exposure of the while volume of the solution to the ultrasound treatment **(Figure 2.2)**. At the end of the 5 min ablation treatment, the solutions of PC-3 and C4-2B cells/spheroids were collected and mixed with the resazurin dye to quantify the fraction of viable cells following the same protocol described earlier and used to assess NDs toxicity. The number of viable PC-3 and C4-2B cells was normalized to that incubation in PBS without exposure to NDs or ultrasound treatments to calculate the effect of different treatments on the viability of individual cancer cells and 3D spheroids.

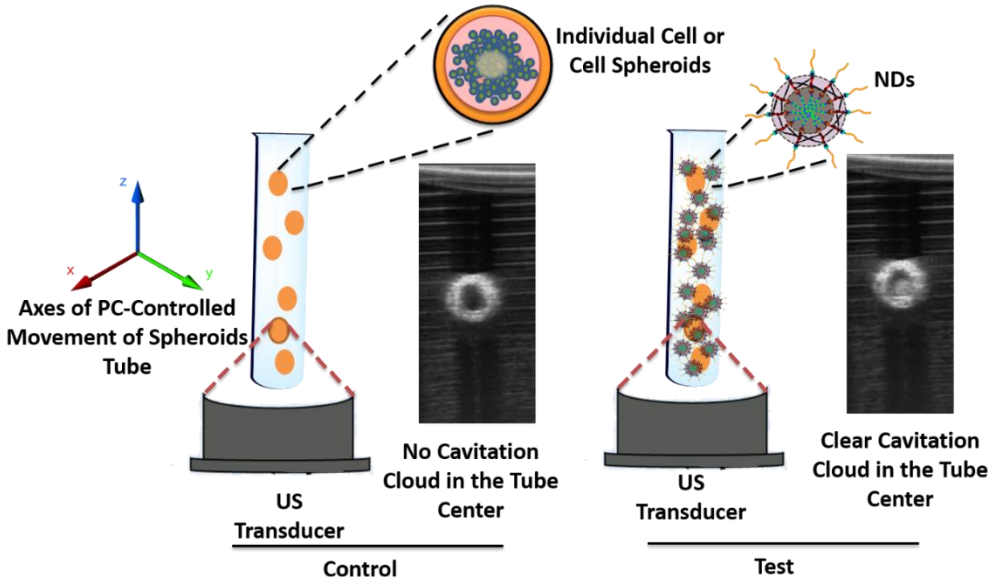

Figure 2.2 Schematic drawing of the experimental setup incorporating a 345 kHz transducer with the focus aligned to the center of test tubes containing either prostate cancer spheroids alone (control) or spheroids mixed with PFP or PFH-loaded nanodroplets (test).

2.2.8 Visualizing the Ablation of PC-3 and C4-2B Spheroids in a Tissue Mimicking Environment

We investigated the effect of PFP- and PFH-NDs on PC-3 and C4-2B spheroids in agarose phantoms as an accepted 3D model of cancer cell-tissue matrix interactions [173-175]. Tissue phantoms containing 2% (w/v) agarose were prepared by slowly mixing agarose powder into PBS heated to the boiling temperature and keeping the solution stirring on a hot plate until the gel turned completely transparent and allowed to boil for an additional 10 minutes. Agarose solutions were allowed to cool down before being degassed under a partial vacuum (~20 kPa, absolute) for 30 minutes. Agarose phantoms containing the nanodroplets were prepared by slowly adding the desired volume of the nanodroplets solution into the cold agarose solution while stirring before pouring into rectangular polycarbonate holders with acoustic windows and keeping this mixture at room temperature to allow the agarose solution to solidify forming tissue phantoms with embedded PFP- or PFH-loaded nanodroplets or without nanodroplets (control phantoms).

A 500 kHz ultrasound transducer was designed to generate a histotripsy bubble cloud and image the cavitation of PC-3 and C4-2B cells and spheroids. The 500 kHz transducer was designed to generate short, high-pressure, 1-2 cycle histotripsy pulses and had a geometric focus of 40 mm, an aperture size of 71 mm, and an effective f-number of 0.56. Elements were driven in phase with a custom high-voltage pulser that was developed in-house. The pulser was connected to a field-programmable gate array (FPGA) board (Altera DE1 Terasic Technology, Dover, DE) specifically programmed for histotripsy pulsing. This setup allowed the transducers to output short pulses consisting of less than two cycles. A fiber optic probe hydrophone built in-house [172] was used to measure the acoustic output pressure of the transducers.

A high-speed 1 megapixel CCD camera (Phantom V210, Vision Research) with a frame rate of 2000 frame per second (fps) was aligned above the microscope (Nikon Eclipse Ti, 10X

magnification) **(Figure 2.3)** to study the interactions between the generated bubble cloud and the cancer cells over multiple pulses. The camera was externally triggered from the FPGA signal board to synchronize recorded images with the histotripsy pulse at specific delay intervals. An exposure time of 20 µs was used for each recorded frame and the camera was triggered to record images 24 µs after the arrival of each pulse. The 3D spheroids were formulated following the ATPS method described earlier. These spheroids were cultured on agarose gels for 3 days at 37°C and 5% CO_2 before treating the cells with 100 histotripsy pulses applied at a pulse repetition frequency of 1 Hz. The camera recorded 20 images after each pulse using a 10X magnification lens. In approximately 3 of these images, the bubble cloud was still present while cell displacement and deformation was observed in the following images since these effects lasted significantly longer than the bubble cloud [162].

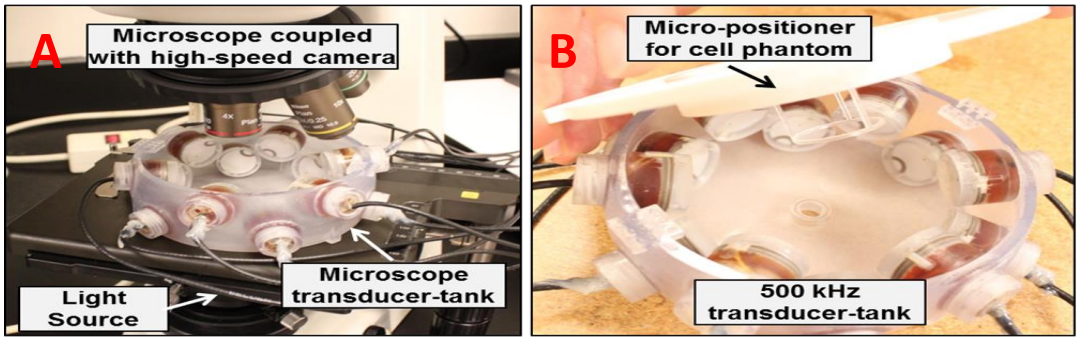

Figure 2.3 The 3D spheroids phantom histotripsy set-up.

(A) A custom built microscope transducer-tank with a three-axis positioning system was built to investigate the ability of nanodroplet-mediated histotripsy to fractionate tumor spheroids. (B) Prostate cancer spheroids were aligned at the transducer focus using a micro-positioner, and histotripsy pulses were applied to the spheroids which were embedded inside an agarose gel to mimic a three-dimension tissue structure.

To examine the ability of PC-3 cells to regrow after NDs-mediated ablation, the homogenate of PC-3 spheroids incubated with PFH-NDs and treated with histotripsy were collected after treatment and centrifuged at 1000 rpm for 5 min. The collected homogenate was mixed with 500 µL of fresh RPMI 1640 medium, seeded in a 24-well plate, and incubated for 48

hours under the regular culture conditions. Untreated (no PFH-NDs and no histotripsy pulses) PC-3 spheroids were processed following the same protocol and used as a control group. After 48 hours, the ability of the cultured homogenate to grow viable cells was evaluated using the resazurin viability assay coupled with microscopic examination using an inverted microscope (Olympus IX51, Melville, NY) with a 4X objective lens.

2.3 Results and Discussion

2.3.1 Formulation and Characterization of PFP- and PFH-Loaded Nanodroplets

Our previous reports show that PEG_{45}-*b*-$(PAA)_{12}$-*b*-$P(HDFMA_8$-*co*-$MMA_{20})$ triblock copolymer can efficiently encapsulate PFP and PFH forming nanodroplets (NDs) [74, 80, 83, 168, 169] and we followed the same formulation protocol to obtain PFP- and PFH-loaded NDs for these studies. Results of the NTA shows that PFP-and PFH-loaded NDs have a similar average size and size distribution profiles **(Figure 2.4A, Table 2.1).** Specifically, the average size of PFP-loaded NDs was between 100 nm and 450 nm with the size of major peak < 300 nm **(Figure 2.4A)** and an average diameter of 177 ± 1.9 nm **(Table 2.1)**. In comparison, PFH-loaded NDs exhibited a slightly larger size distribution between 100 nm and 600 nm with 3 peaks in the range of 200-300 nm, 300-450 nm, and 450-600 nm **(Figure 2.4A)** and an average diameter of 233.9 ± 3.9 nm **(Table 2.1)**. The larger size of the PFH-loaded NDs compared to PFP-loaded ones can be a result of the difference in miscibility between PFP and PFH in the THF/copolymer mixture. Briefly, our experimental observations indicate that PFP homogenously disperses in the THF/copolymer mixture during NDs formulation whereas, PFH tends to phase separate from the THF/copolymer mixture. We broke down PFH phase separation by drop-wise addition of water to the THF/polymer mixture and vigorous mixing, which triggered breakdown of the PFH phase and

mixing with the aqueous phase coupled with self-assembly of the polymer forming PFH-loaded NDs. The hydrophilic PEG corona stabilized both PFP- and PFH-loaded NDs and inhibited their aggregation or precipitation in solution at 4 °C and 25 °C. Given that >99% PFP- and PFH-loaded NDs have an average diameter < 400 nm, they are in the size range to preferentially extravasate across tumor's leaky vasculature and accumulate in tumor tissue with low risk of inducing pulmonary embolism [176, 177].

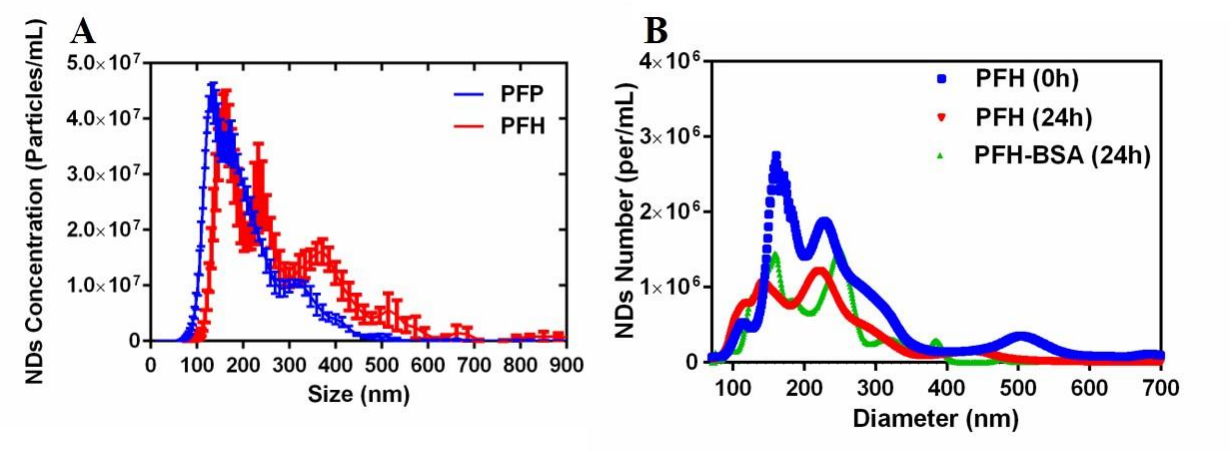

Figure 2.4 Size distribution of PFP and PFH-loaded NDs.

(A) The concentration and size distribution of PFP (blue line) and PFH (red line)-loaded nanodroplets (B) Stability test of PFH-NDs in the presence or absence of BSA for 24 h at 37 °C, PFH-NDs at 0h (blue line), PFH-NDs at 24h (red line), and PFH-NDs at 24h with presence of BSA (green line). All measurements were calculated using Nanoparticles Tracking Analysis (NTA) and NTA 3.0 build 66 software. Results are the average of five independent experiments ± standard error of the mean (error bars not shown for B to clearly seen the lines).

Table 2.1 Size distribution of PFP or PFH-loaded nanodroplets with 10%, 50%, 90% of particles size fraction and their average size.

Size (nm)	D10	D50	D90	Mean
PFP-NDs	**111.0±1.4**	**155.7±2.1**	**268.5±6.7**	**177.9±1.9**
PFH-NDs	**135.3±2.6**	**192.7±5.3**	**373.7±7.2**	**233.9±3.9**

Serum albumin is the major soluble blood protein, which adsorbs to the surface of particles in the systemic circulation and labels them for hepatic clearance [170, 178]. We investigated the stability of the PFH-NDs upon incubating with bovine serum albumin (BSA) at 37 °C for 24 h by monitoring the change in NDs size and concentration using NTA. Results show that the average diameter of PFH-NDs before incubating at 37 °C (0 h) is 251.9 ± 11.2 nm, which dropped to 221.5 ± 8.7 nm after incubating the NDs at 37 °C for 24 hours **(Figure 2.4B)**. This drop in average NDs size is a result of the loss of the fraction of NDs with an average size ~500 nm, which resulted in ~40% of NDs concentration probably due to loss of poorly encapsulated PFH in large NDs. Incubation of PFH-NDs with BSA at 37 ℃ for 24h similarly reduced average NDs size to 228.7 ± 10.3 nm and NDs concentration was similar in the presence and absence of BSA **(Figure 2.4B).** These results indicate that the PEG corona limits the interaction of PFH-NDs with BSA, which increased NDs against complete dissolution and aggregation in the presence of BSA as a model serum protein at 37 °C. It is worth noting that the size of PFP-NDs did not change under similar experimental conditions but the concentration decreased by 20% at 37 ℃ regardless of the presence or absence of BSA [168]. These results indicate that PFP-NDs and PFH-NDs will exhibit minimal interaction with serum proteins *in vivo*.

2.3.2 Cytotoxicity of PFP- and PFH-Loaded Nanodroplets

To investigate the toxicity of the nanodroplet particles, we performed *in vitro* cytotoxicity experiments using a resazurin viability assay, which is a very common dye to show cell viability, proliferation and cytotoxicity with a simple, rapid, sensitive, and reliable way. Basically, it relies on reduction of resazurin (blue, nonfluorescent form) to resorufin (pink, highly fluorescent) by viable cells. The metabolized form of the dye enters the cytosol and is converted to the fluorescent form by mitochondrial enzyme activity by accepting the electron from NADPH, FADH, NADH,

and cytochromes [179]. Both prostate cancer cell lines were treated with a variety of concentrations between 0 to 100 µg/mL of PFP or PFH-loaded nanodroplets calculated initial polymer weight that added to the formulation and the end volume of the dialysis step in ND formulation for 24 h under regular cell culture conditions compared to negative controls of non-treated cells and positive controls of Triton-x 100 treated cells. It is important to highlight the maximum concentration that we used is 100 times more than used in the tube cell ablation particle concentration. Further, results show that incubation of PFP- and PFH-loaded NDs with PC-3 and C4-2B cells did not affect their viability up to a concentration of 100 µg/mL except only PFH-NDs at the highest particle concentration **(Figure 2.5).** Overall, this result points to biocompatible character of the particles. As a result, particle concentration even at 50 µg/mL of NDs concentration (> 80-fold more particle concentration what we used for NMH) usage is not expected to be an issue *in vivo* because of the particles cytotoxicity profile.

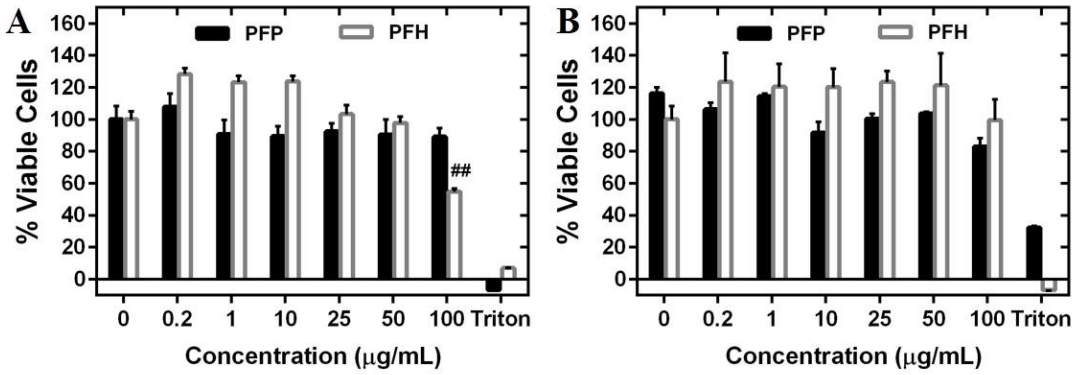

Figure 2.5 Evaluation of in vitro toxicity of PFP- and PFH-loaded nanodroplets towards

PC-3 (A) and C4-2B (B) prostate cancer cells as a function of concentration of the polymeric carrier (0-100 µg/mL) with Triton-X 100 positive control. Results are the average of two independent experiments with 5 replicates ± standard error of the mean. We compared cell viability under each condition to the viability of untreated cells (negative control) using one-way ANOVA with Tukey test where # for PFH denotes $p \leq 0.05$, and ## denotes $p \leq 0.01$.

2.3.3 Ablation of PC-3 and C4-2B Cells and Spheroids in Solution

We investigate the effect of combining individual prostate cancer cells and spheroids with PFP- and PFH-loaded NDs in a rubber tube and exposing this mixture to histotripsy pulses as shown in **Figure 2.2**. We hypothesized that applying histotripsy pulses with peak negative pressures of ~10.7–12.8 MPa would activate the PFP- and PFH-NDs resulting in generation of a bubble cloud that would energetically collapse and cause the mechanical ablation of individual cancer cells and 3D tumor spheroids. In comparison, PC-3/C4-2B cells/spheroids mixed with the NDs but were not treated with histotripsy pulses and PC-3/C4-2B cells/spheroids not mixed with the NDs but treated with histotripsy pulses will not experience ablative forces and will remain viable after the treatment. To test this hypothesis, we added an equal number (2×10^8 droplets/mL) of PFP- and PFH-loaded NDs to the designated tubes before applying histotripsy pulses to the center of the tube at a pulse repetition frequency of 10 Hz and peak negative pressure of 10.7 MPa. The tubes containing NDs showed a bubble cloud in the center of the tube **(Figure 2.2)** which was monitored in real time using a clinical ultrasound imaging system. In contrast to, no cavitation bubble clouds were observed in the tubes without NDs. Quantifying the changes in cell viability in response to different treatments using the resazurin dye show the ablative capacity associated with each treatment **(Figure 2.6)**. Results show that PC-3 and C4-2B cells **(Figure 2.6A)** and spheroids **(Figure 2.6B)** that were not incubated with NDs or treated with ultrasound exhibited 100% viability at the end of the treatment and were used a reference for normalization of other treatments. Similarly, incubating PC-3 and C4-2B cells **(Figure 2.5A)** and spheroids **(Figure 2.5B)** with PFP- and PFH-NDs without shining ultrasound did not affect cell viability. However, exposure to 1-2 cycle histotripsy pulses at low acoustic pressure (10.7 MPa) in absence of NDs caused less than ~20% reduction in the viability of both PC-3 and C4-2B cells **(Figure 2.6A)**. By

combining PFP- and PFH-NDs and exposure to 1-2 cycle histotripsy (10.7 MPa), significant ablation of PC-3 and C4-2B cells and spheroids was observed **(Figure 2.6)**.

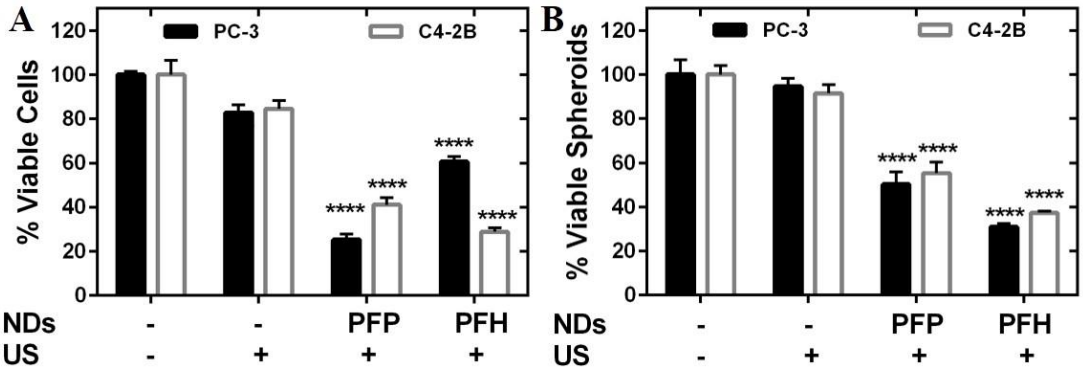

Figure 2.6 Effect of PFP and PFH-loaded nanodroplets on the viability of PC-3 and C4-2B cultured as individual cells (A) or 3D spheroids (B) upon exposure to 1-2 cycle histotripsy pulses (10.7 MPa) applied with a pulse repetition frequency of 345 kHz.

Cell viability was measured using Resazurin viability assay and results were normalized to untreated cells (negative control; – NDs and – US). Results are the average of four experiments ± standard error of the mean. We compared cell viability under each condition to the viability of untreated cells (negative control) using one-way ANOVA with Tukey test where * denotes $p \leq 0.05$, ** denotes $p \leq 0.01$, *** denotes $p \leq 0.001$, and **** denotes $p \leq 0.0005$.

Specifically, combining the NDs with ultrasound resulted in ablation of 40-70% and 60-70% of suspended PC-3 and C4-2B cells, respectively (**Figure 2.6A)**. Similarly, combining the NDs with ultrasound resulted in ablation of 40%-60% of PC-3 and C4-2B spheroids (**Figure 2.6B)**. Upon added nanodroplets to cell/spheroid samples with applied 10.7 MPa ultrasound, we got quite further ablation therapeutic effects. For example, PFP-nanodroplets with ultrasound resulted in the death of almost 80% and 60% of the individual PC-3 and C4-2B cells, respectively (**Figure 2.6A)**. PFH-nanodroplet results showed cell death rates of 40% and 75% for the PC-3 and C4-2B cells, respectively. On the other hand, more than 50% and 40% of the PC-3 and C4-2B spheroids were destroyed with PFP-nanodroplets, respectively. Moreover, the therapeutic activity of PFH-

nanodroplets on PC-3 and C4-2B spheroids reached to 70% and 60% cell ablation, respectively **(Figure 2.6B)**. The nanodroplets containing PFP or PFH resulted in higher cavitation so these offer higher therapeutic activity in response to the histotripsy treatment based on the viability assay results. These ablation rates of cells/spheroids are obtained just after single treatment in a certain time interval. These ablation rates can be improved by using targeted NDs and scanning the ultrasound therapy focus to cover the entire tumor volume, which will be expected to achieve complete ablation of the target tumor. It is worth noting that these ablation rates of cells/spheroids are obtained from treating in a certain time interval. The cell ablation rates are expected to be improved when using targeted NDs. In addition, by scanning the ultrasound therapy focus to cover the entire tumor volume, we expect to achieve complete ablation of the entire target tumor.

2.3.4 Visualizing the Ablation of PC-3 and C4-2B Spheroids in a Tissue Mimicking Environment

We investigated the ability of PFP- and PFH-loaded NDs to ablate PC-3 and C4-2B spheroids in an environment that mimics the mechanical properties that exist *in vivo*. We utilized the ATPS to grow millimeter-sized spheroids in 2 days, which were placed on an agarose gel and allowed to grow and establish cell-gel interactions. We applied ultrasound pulses at peak negative pressures of 12.8 MPa and 26.2 MPa to the spheroids layer. The formation of a bubble cloud and the associated cell fractionation was monitored using high speed optical imaging after each pulse. Results show that histotripsy pulses (26.2 MPa) and the bubble cloud generated by the NDs at low acoustic pressure (12.8 MPa) fractionated the spheroids in the targeted region, forming an acellular homogenate **(Figure 2.7A-C).** Using these images, we quantified the ablation area in response to different treatments **(Figure 2.7D).** Results show that applying US at acoustic pressure below the histotripsy intrinsic threshold (12.8 MPa) in tissue phantoms that were not loaded with either NDs did not cause significant ablation (<20%) of the embedded spheroids. In comparison, applying

histotripsy pulses at acoustic pressures near the intrinsic threshold (26.2 MPa) caused a statistically higher ablation of the embedded spheroids, reaching 80% of the spheroids area. Combining PFP-NDs with ultrasound at a peak negative pressure of 12.8 MPa caused an ablation of ~40% of the embedded spheroids. Whereas, combining PFH-NDs with ultrasound at a peak negative pressure of 12.8 MPa ablated ~80% of the embedded spheroids, similar to the ablation observed with the histotripsy pulses applied at high acoustic pressure (26.2 MPa). It is worth noting that, while only 80% of the total spheroid volume was ablated in these experiments, this volume represented the entire targeted region in which the histotripsy bubble cloud was generated. The observed difference in ablative capacity of PFP- and PFH-loaded NDs is likely due to the difference in the stability of the NDs over multiple pulses. Our earlier research showed that PFH-NDs generate a bubble cloud with a large number of sustainable cavitation nuclei remaining over multiple pulses compared to PFP-NDs, which can only generate a bubble cloud during the initial pulses [80]. Another important point that drawn attention in here is the ablation is carried out only in the region of bubble activities under the transducer focal point, which dictates the damage location. Since the purpose of this study was to demonstrate the ability of NMH to fractionate tumor cells and investigate the mechanism of the resulting damage, histotripsy was only applied to a single location to compare the efficiency of ND formulations in the same conditions. Therefore, the fractionation is localized in the ultrasound focal region treated with the bubble cloud, while the untreated spheroid region remained intact, demonstrating the precision of NMH ablation. This approach explains why the reported ablation percentages for all tested cases are below 100%, since the treatment focus was not scanned to cover the entire tumor spheroids. Previous studies have shown that histotripsy using high pressure pulses alone can completely homogenize the target tissue volume with no viable cells remaining by scanning the therapy focus to cover the entire volume,

which is validated by the results of this study that show NMH completely fractionated the portion of the tumor that was exposed to the bubble cloud. This finding suggests that NMH will be capable of completely fractioning 100% of the tumor volumes under the circumstance of mapping the histotripsy transducer focus to cover the whole spheroid volume.

Although the difference between nanodroplets and microbubbles for particle-assisted histotripsy is not specifically investigated in this study, we have discussed these features in some of our previous works [45, 79]. In general, we would expect to achieve similar cell fractionation using both nanodroplets and microbubbles for enhanced histotripsy in cases where cavitation bubbles are generated. The primary differences between these two approaches are more related to 1) particle size and 2) cavitation initiation properties rather than any differences between the fractionation process that occurs once the cavitation bubbles are formed, which appears to be similar for NMH, histotripsy, and microbubble-enhanced histotripsy based on previous observations. The advantage of using nanodroplets rather than microbubbles, as discussed in the previous studies, is that the nanodroplets can 1) be synthesized into the optimal size range to accumulate inside a tumor volume [168] while microbubbles are too large and 2) cavitation initiation from nanodroplets shows a distinct threshold behavior similar to the histotripsy intrinsic threshold, [79] which has many advantages for developing NMH for selective ablation. In contrast, microbubbles do not show the same distinct threshold behavior, since the initial threshold behavior is not dominated by bubble nucleation as is the case with nanodroplets.

Further, we investigated the residual viability of cancer spheroids after treatment with PFH-NDs by evaluating cell growth from the ablated spheroids. We compared cell growth using microscopic examination and fraction of viable cells as shown in **Figure 2.8**. Microscopic examination shows low density of viable cells emerging from the homogenate of PC-3 spheroids

treated with PFH-NDs compared to highly dense cells observed with untreated cells **(Figure 2.8A).** Results of the resazurin assay shows that the number of viable cells established from the culture of PC-3 homogenate was ~20% of the number of viable cells established from the untreated PC-3 (control group) **(Figure 2.8B).** These results show the low viability and the proliferation of residual cells after NDs treatment.

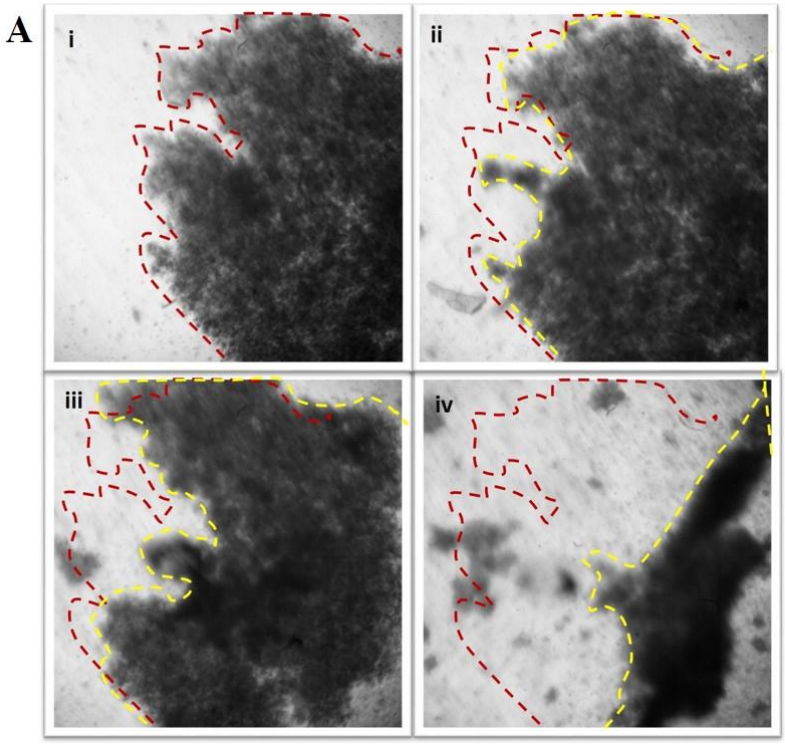

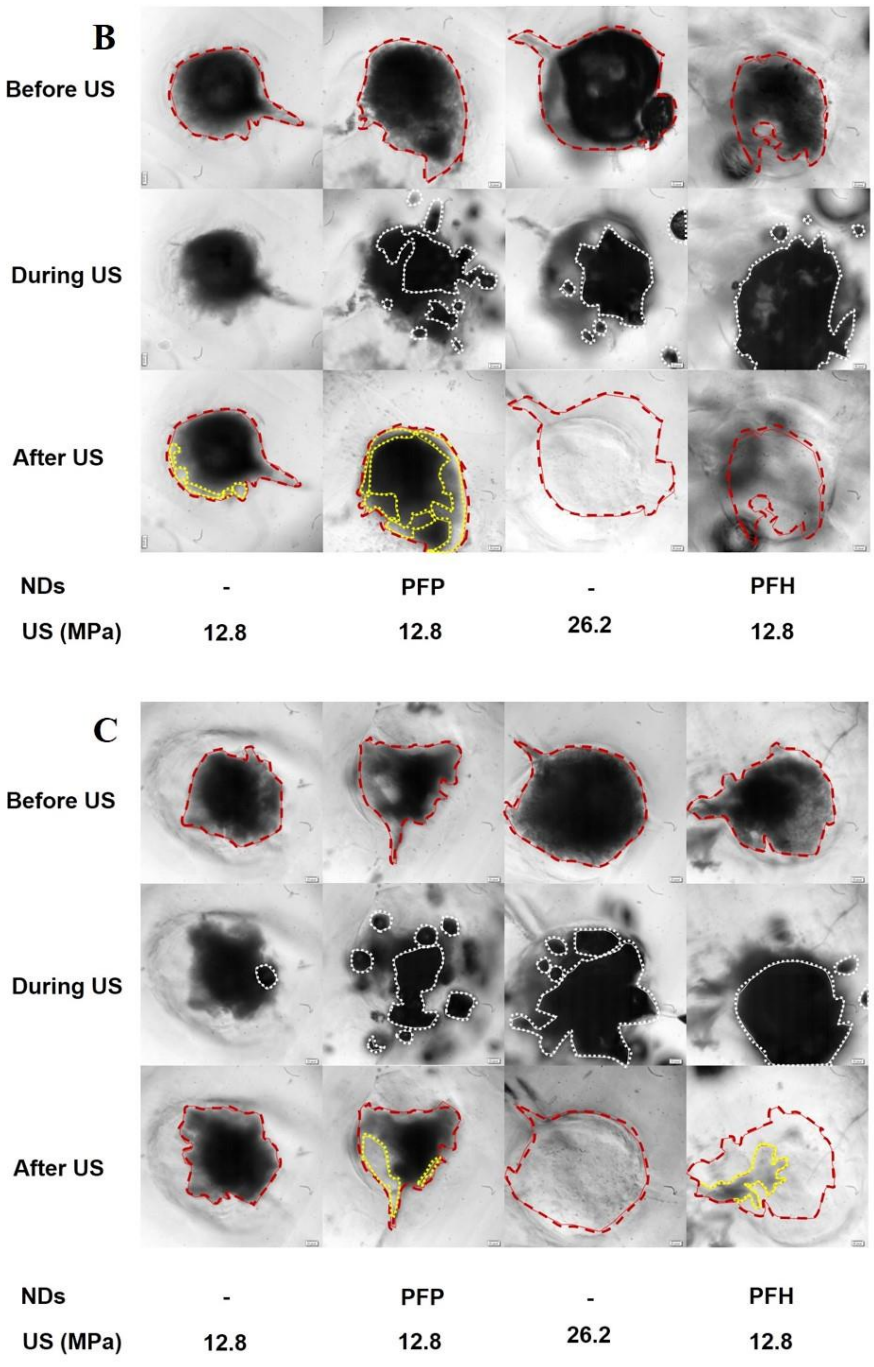
B
Before US
During US
After US
NDs
-
PFP
-
PFH
US (MPa)
12.8
12.8
26.2
12.8
C
Before US
During US
After US
NDs
-
PFP
-
PFH
US (MPa)
12.8
12.8
26.2
12.8

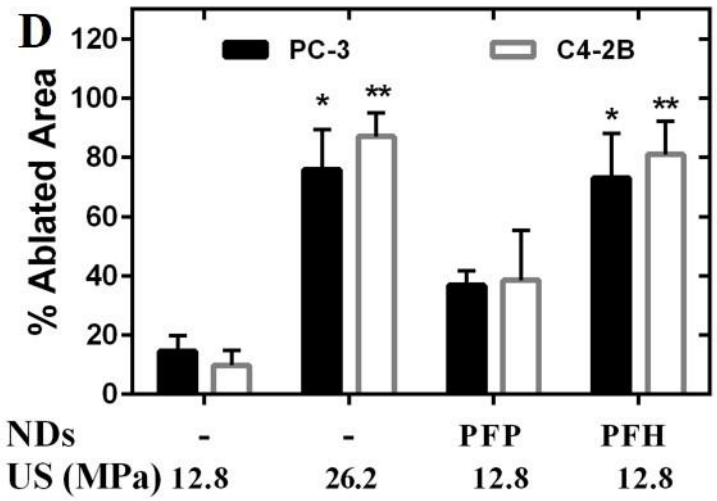

Figure 2.7 3D tumor model cell-bubble results demonstrate nanodroplet-mediated histotripsy can fractionate prostate cancer cells into accellular debris.

A PC-3 prostate cancer spheroid was cultured on an agarose tissue phantom to mimic cells inside a tissue extracellular matrix. 100 histotripsy pulses were applied to the call layer containing nanodroplets at a pressure significantly below the histotripsy threshold without nanodroplets. (A) Digitized video capture images of NMH during treatment, cavitation bubbles were observed at the transducer focus and cells were observed to be mechanically ruptured. After treatment, no/less cells remained intact in the region in which the histotripsy bubble cloud was observed. (B) PC-3 3D spheroid NMH, the first column is the treatment of no ND with 12.8 MPa of US pressure, the second column is the PFP NDs mediated histotripsy with 12.8 MPa of US pressure, the third column is no ND with 26.2 MPa of US pressure, and the forth column is the PFH NDs mediated histotripsy with 12.8 MPa of US pressure. Each row is separated with before, during, and after US treatments. The spheroid border, cavitation bubbles, and ablated spheroid section were encircled with red, white, and yellow colors, respectively to be easily distinguished the treatment efficiency. The cross bar is 200 μm. (C) C4-2B 3D spheroid NMH, the first column is the treatment of no ND with 12.8 MPa of US pressure, the second column is the PFP NDs mediated histotripsy with 12.8 MPa of US pressure, the third column is no ND with 26.2 MPa of US pressure, and the forth column is the PFH NDs mediated histotripsy with 12.8 MPa of US pressure. Each row is separated with before, during, and after US treatments. The spheroid border, cavitation bubbles, and ablated spheroid section were encircled with red, white, and yellow colors, respectively to be easily distinguished the treatment efficiency. The cross bar is 200 μm. (D) Calculation of the fractionated spheroid area after the ablation treatment with lower pressure (12.8 MPa), high pressure (26.2 MPa), PFP loaded NDs, or PFH loaded NDs. The areas are calculated from the ultrafast recording camera images equipped with a 4X microscope objective. Results are the average of three independent experiments ± standard error of the mean.

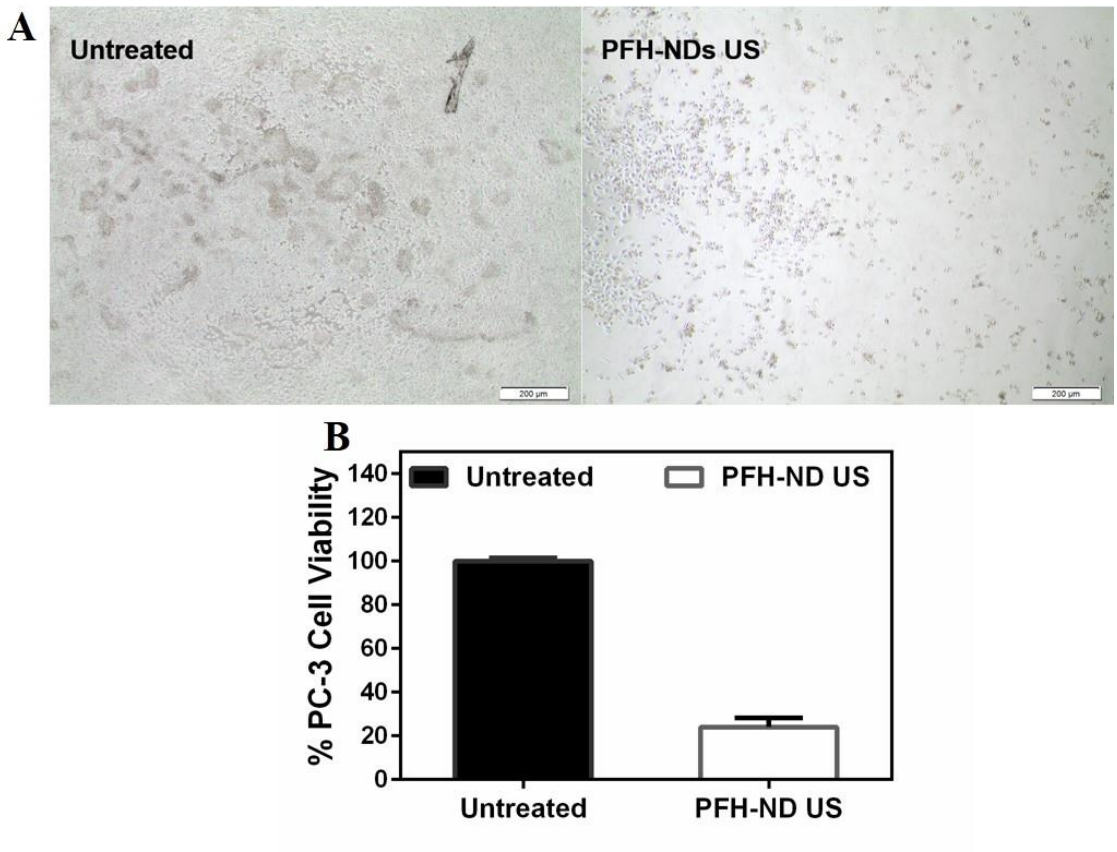

Figure 2.8 (A) Regrown of the ablated PC-3 cells with PFH-NDs under US for 2 days comparing to untreated spheroids under light microscopy (the cross-bar shows 200 µm) and (B) assayed with resazurin viability dye.

2.4 Conclusions

Results of this study show the ability of nanodroplets-mediated histotripsy to ablate prostate cancer cells and spheroids in solution and in tissue-mimicking phantoms. Further, the results indicate that PFP-NDs and PFH-NDs exhibit minimal interaction with the model blood protein, serum albumin in the model system as monitoring the particle sizes. The ability to ablate PC-3 and C4-2B spheroids using PFP- and PFH-NDs at acoustic pressures below the histotripsy intrinsic threshold. The PFH-NDs formulation with low pressure demonstrated that NMH can be used to fractionate cancer cells and tumor spheroids with similar efficient to conventional

histotripsy but at significantly reduced acoustic pressure. This finding suggests that NMH has the potential to achieve selective ablation of tumors while sparing the surrounding normal tissue.

2.5 Acknowledgement

We would like to thank S. Capracotta, PhD (Technical Specialist, Nano Sight, School of Public Health, University of Michigan) for her help on NTA size and concentration measurements. O. Aydin acknowledges the support of the Turkish Republic the Ministry of National Education PhD Fellowship Program (1416). This material is based upon work supported by a National Science Foundation Graduate Research Fellowship to E. Vlaisavljevich. This work was supported by a grant from the United States Department of Defense (W81XWH-11-PCRP-ID) to Dr. M ElSayed. Disclosure notice: Dr. Z. Xu and Dr. E. Vlaisavljevich have financial interests and/or other relationship with HistoSonics Inc.

Chapter 3

Formulation of acid-sensitive micelles for delivery of cabazitaxel into prostate cancer cells

The material in this chapter is published from the following article: **O. Aydin,** I. Youssef, Y. Y. Durmaz, G. Tiruchinapally, and M. E. H. ElSayed, "Formulation of Acid-Sensitive Micelles for Delivery of Cabazitaxel into Prostate Cancer Cells" *Molecular Pharmaceutics*, **2016**, *13* (4), 1413–1429 **(2016)**.

3.1 Introduction

Taxanes is a family of hydrophobic, small molecular weight, drug molecules that include paclitaxel, docetaxel, and cabazitaxel, which exhibit cytotoxic activity against rapidly proliferating cancer cells [180]. Taxanes exhibit their cytotoxicity by blocking cell cycle progression through stabilizing the microtubules, centrosomal impairment, induction of abnormal spindles, and suppression of spindle microtubule dynamics, which triggers apoptosis by aberrant mitosis or by subsequent multinucleated G1-like state related to mitotic slippage depending on cell type and drug schedule [181]. The FDA approved the use of paclitaxel (Taxol®, Bristol-Myers Squibb, Princeton, NJ) for treatment of ovarian cancer [182], recurrent and metastatic breast cancer [183], and as a second line therapy for patients with HIV-related Kaposi's sarcoma and non-small cell lung carcinoma [184, 185]. The FDA also approved the use of docetaxel (Taxotere®, Sanofi-Aventis LLC, Bridgewater, NJ) for treatment of advanced breast [186], lung [187], and ovarian

cancer [188]. However, clinical use of taxanes is associated with significant side effects including hypersensitivity reactions, neurotoxicity, bone marrow suppression, fluid retention (i.e. edema, ascites, pleural effusions), diarrhea, nausea, vomiting, numbness, and loss of hair due to the non-specific distribution to healthy tissues [189, 190]. Further, the use of surfactants such as cremophor and polysorbate 80 to increase the intrinsically poor aqueous solubility of taxanes (e.g. paclitaxel's and docetaxel's solubility = 0.7 μg/mL and 6-7 μg/mL, respectively) has been shown to enhance the toxicity of the parent drug by causing allergic reactions, peripheral edema, and pericardial effusions [14, 191, 192]. Alternative formulations such as drug-loaded liposomes, albumin-based nanoparticles, polymer-drug conjugates, and self-assembled micelles have been developed to eliminate the need for toxic solubilizing agents and to target the loaded chemotherapeutic cargo to cancer cells [193-196]. Many of these strategies proved successful in enhancing the therapeutic activity of the loaded anticancer drug and reducing the associated toxicity in clinical settings leading to the development and clinical use of Abraxane (paclitaxel-loaded albumin nanoparticles) for treatment of breast, lung, and pancreatic cancer [197, 198], and Opaxio (polyglutamic acid-paclitaxel conjugate), which is being evaluated in Phase III trials in patients with advanced ovarian cancer (NCT00108745) [199].

CTX is a chemotherapeutic agent that proved effective in killing resistant prostate cancer cells *in vitro* and in preclinical animal models [200]. These results led to FDA approval of cabazitaxel (Jevtana®, Sanofi-Aventis LLC, Bridgewater, NJ) as a new treatment option for patients with castrate-resistant prostate cancer (CRPC) whose disease progresses during or after docetaxel treatment [201-203]. Activity of CTX in CRPC is attributed to its poor affinity for the ATP-dependent P-glycoprotein (P-gp) efflux pump compared to docetaxel, which is a strong substrate for P-gp [204, 205]. Given that CTX is a lipophilic, practically insoluble in water, and

chemically unstable drug [206], it is formulated as lyophilized powder in single-use vials containing 60 mg anhydrous CTX and 1.56 gm of the polysorbate 80 surfactant to aid its dissolution when mixed with the appropriate diluent made of 13% (w/w) ethanol in water [207]. Preparation of CTX for infusion into CRPC patients requires two dilutions and the use of polysorbate 80 as a solubility enhancer increase the risk for development of side effects particularly hypersensitivity reactions including generalized erythema, hypotension, and bronchospasm [208]. We are interested in developing surfactant-free, water-soluble, and stable formulations of CTX that can be eventually targeted towards cancer cells in both the primary tumor (i.e. prostate gland) and distant metastases (e.g. cancer lesions in bone). To achieve this goal, we focused on the development of water-soluble nano-sized micelles that can encapsulate CTX in their core, shuttle the CTX cargo into the cytoplasm of aggressive prostate cancer cells, and trigger efficient cancer cell death.

We report the synthesis of a new amphiphilic triblock copolymer composed of a hydrophilic poly(ethylene glycol) (PEG) block, a central poly(acrylic acid) (PAA) block, and a hydrophobic poly(methyl methacrylate) (PMMA) block. We evaluated the ability of poly(ethylene glycol-*b*-acrylic acid-*b*-methyl methacrylate) (PEG-*b*-PAA-*b*-PMMA) copolymer to self-assemble into micelles that encapsulate NR (a hydrophobic fluorescent dye) and CTX in the hydrophobic core. We report the synthesis of the acid-labile 2,2'-(propane-2,2-diylbis(oxy)-diethanamine linker and its reaction with the carboxylic acid groups in the central PAA block to cross-link adjacent polymer chains forming shell cross-linked micelles (SCLM). We compared the release of the loaded cargo (i.e. NR and CTX) from uncross-linked micelles (NSCLM) and SCLM upon incubation in aqueous buffer solutions with physiologic (pH = 7.4) and endosomal (pH = 5.0) pH values. We investigated the uptake of CTX-loaded SCLM and NSCLM into PC-3 and C4-

2B prostate cancer cells and the associated anticancer activity compared to free CTX at different drug concentrations. We evaluated micelle's biocompatibility by measuring the hemolysis of red blood cells (RBCs) and platelets aggregation upon incubation with different micelle concentrations. We also measured the adsorption of bovine serum albumin (BSA) as a model serum protein to the surface of SCLM and NSCLM as a function of incubation time and subsequent uptake of opsonized micelles by THP-1 macrophages.

3.2 Experimental Section

3.2.1 Materials

Cabazitaxel (CTX) is a generous gift from Sanofi-Aventis US LLC (Bridgewater, New Jersey). Poly(ethylene glycol) monomethylether (PEG, M_n: 5000 g/mol, Sigma-Aldrich), Copper (I) bromide (CuBr, Sigma-Aldrich, 99.9 %), anhydrous tetrahydrofuran (THF, Sigma-Aldrich, >99.9 %), triethylamine (TEA, Sigma-Aldrich, ≥99%), *N*,*N*'- dicyclohexylcarbodiimide (DCC, Sigma-Aldrich, 99 %), *N*-(2-hydroxyethyl)-phthalimide (Sigma-Aldrich, 99%), 1,6-diphenyl-1,3,5-hexatriene (DPH, Sigma-Aldrich, 98%), resazurin sodium salt (Sigma-Aldrich), 2-methoxy propene (Sigma-Aldrich, 97%), phorbol myristate acetate (PMA, Sigma-Aldrich, ≥99%), benzene (anhydrous, Sigma-Aldrich, 99.8%), 2-propanol (anhydrous, Sigma-Aldrich, 99.5%), *p*-toluene sulfonic acid (Sigma-Aldrich, ≥98.5%), 4-pentynoic acid (Sigma-Aldrich, 99 %), α-bromoisobutyryl bromide (Sigma-Aldrich, 98%), adenosine 5'-diphosphate (ADP, Sigma-Aldrich, ≥95%), *N*-hydroxy succinimide (NHS, Fluka, 97 %), *N*-(3-dimethylaminopropyl)-*N*′-ethylcarbodiimide hydrochloride (EDC, Fluka, >98 %), dimethylaminopyridine (DMAP, Acros, 99 %), sodium azide (NaN_3, Acros, 99 %), trifluoroacetic acid (TFA, Acros, 99 %), Nile red (TCI AMERICA, Portland, OR), and Tween ®20 (EMD Chemicals, Billerica, MA) were used as

delivered without further purification. Methyl methacrylate (Sigma-Aldrich, MMA, 99 %), *tert*-butyl acrylate (Sigma-Aldrich, *t*BA, 98 %)**,** and N, N, N', N'', N''-pentamethyldiethylenetriamine (PMDETA, Sigma-Aldrich, 99 %) were first purified by passing through a basic alumina column to remove the added inhibitor before using.

3.2.2 Instruments

A 500 MHz Varian Mercury system (Palo Alto, CA) was used to record all the ^{1}H NMR and ^{13}C NMR spectra of polymer blocks, the acid-labile linker, and the micelles at room temperature. Gel permeation chromatography (GPC) analysis was done using a Viscotek GPCmax Autosampler system consisting of a pump and Water 2414 refractive index (RI) detector. The molecular weight and molecular weight distribution of synthesized polymers were determined based on their elution volume on a Styragel HR 4E column compared to a series of poly(methyl methacrylate) standards (PolyAnalitik Inc, Canada) using THF as a mobile phase at a flow rate of 1 mL/min at 35 °C. The data was analyzed using Viscotek OmniSEC Omni-01 software. Perkin-Elmer FT-IR Spectrum 4100 type A machine was used to confirm the azidation of different polymer blocks. The 90Plus particle size analyzer (Brookhaven Instruments Corporation, Holtsville, NY) was used to measure micelles' size and surface charge. The JEOL 3011 high resolution electron microscope (JEOL USA Inc., Peabody, MA) was used to image micelles morphology.

3.2.3 Synthesis of amphiphilic PMMA-*b*-PAA-*b*-PEG copolymer

Amphiphilic PMMA-*b*-PAA-*b*-PEG triblock copolymer was synthesized by a combination of atom transfer radical polymerization (ATRP) technique and "click" coupling reactions **(Figure 3.1)**. Briefly, the hydrophobic PMMA block was synthesized using the ATRP technique [209] and utilized as a macro initiator for copolymerization of *tert*-butyl acrylate (*t*BA) to obtain the PMMA-

b-P*t*BA-Br copolymer. The bromine (Br) end groups were converted to azide (N_3) to allow *"click"* coupling to the alkyne-functionalized PEG block forming the (PMMA-*b*-P*t*BA-*b*-PEG)

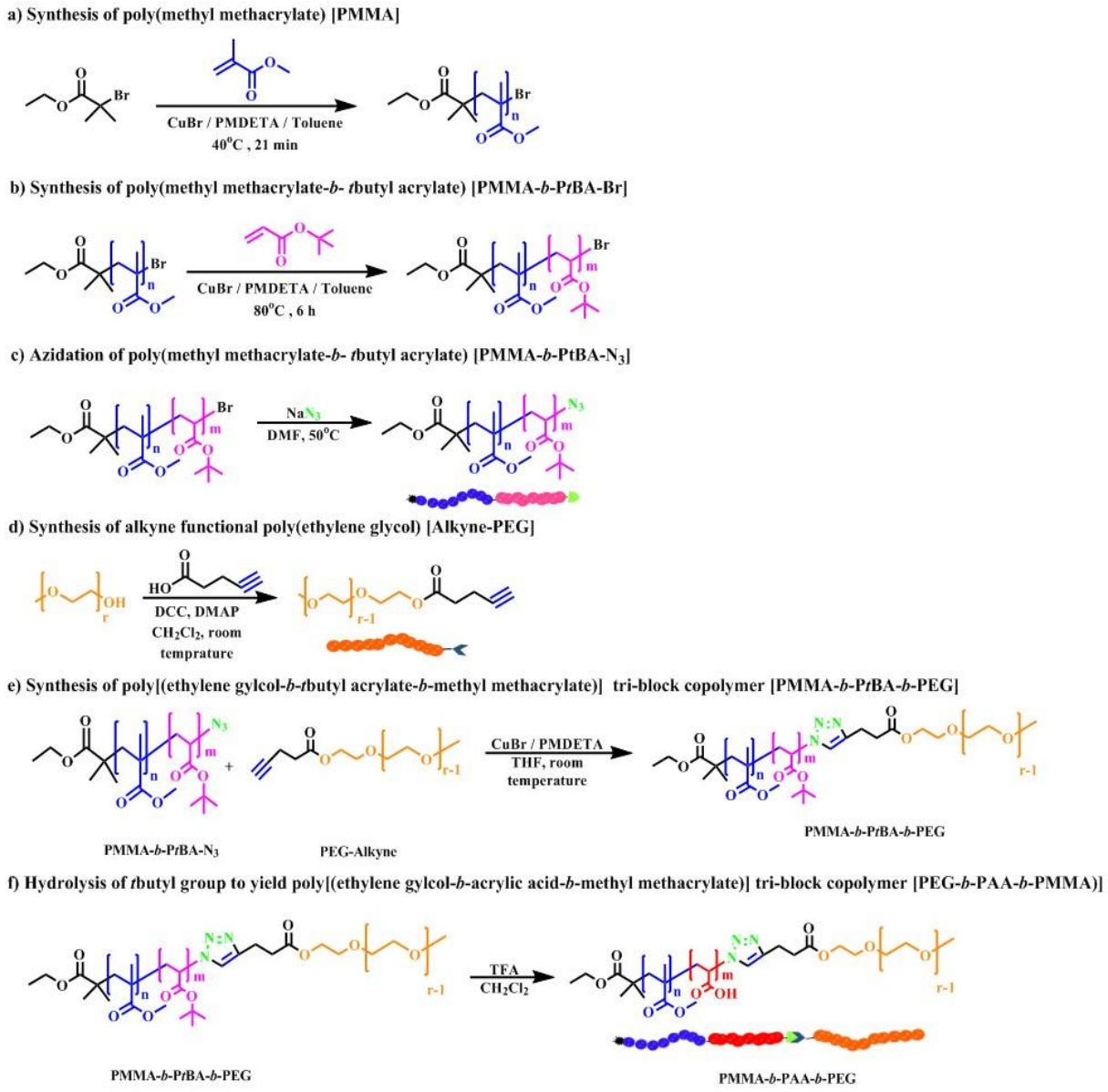

Figure 3.1 Scheme for the synthesis of PEG-*b*-PAA-*b*-PMMA copolymers.

copolymer. Acid hydrolysis was used to remove the *tert*-butyl groups in the central P*t*BA block and obtain the desired (PMMA-*b*-PAA-*b*-PEG) copolymer.

3.2.4 Synthesis of the hydrophobic PMMA block

The hydrophobic PMMA block was synthesized by ATRP following published protocols [210]. Briefly, the MMA monomer (30 mL, 282 mmol), CuBr catalyst (202 mg, 1.41 mmol), *N*,*N*,*N*′,*N*′,*N*″-pentamethyldiethylenetriamine (PMDETA) ligand (294 mg, 1.41 mmol), ethyl-2-bromoisobutyrate initiator (207 μL, 1.41 mmol), and 30 mL of toluene were introduced into a Schlenk tube and the reaction mixture was degassed by three freeze–pump–thaw cycles. The tube was then placed in a temperature-controlled oil bath at 40 °C for 21 min. The polymerization mixture was diluted with THF, passed through a neutral alumina column to remove the copper complex. THF was removed by rotary evaporation and the mixture was precipitated in hexane. Results show that 30% of MMA monomers were converted into PMMA block with $M_{n,theo}$ = 4855 g/mol, $M_{n,NMR}$ = 4400 g/mol, $M_{n,GPC}$ = 4855 g/mol, and M_w/M_n = 1.27. ^{1}H NMR of the PMMA block (500 MHz, $CDCl_3$, δ) shows: 4.21 (2H, CH_3-*CH_2*-O-CO-C(CH_3)$_2$), 3.57 (s, 3H, C*H_3*-O-CO), 1.95 (2H, C*H_2*-C*(CH$_3$)*-CO), 1.85 (6H, O-CO-C(C*H_3*)$_2$), 1.22 (3H, *CH_3*-CH_2-O-CO-C(CH_3)$_2$) **(Appendix D, Figure D.1)**.

3.2.5 Synthesis of azide-functionalized PMMA-*b*-PtBA-N_3 copolymer

The PMMA block was used as a macro initiator for block copolymerization with *tert*-butyl acrylate to obtain PMMA-b-P*t*BA block copolymer. Briefly, PMMA (2.22 g, 0.5 mmol), CuBr (72 mg, 0.5 mmol), PMDETA (104 μL, 0.5 mmol), *t*BA (7.32 mL, 50 mmol), and 18.3 mL toluene were introduced into a Schlenk tube and the reaction mixture was degassed by three freeze–pump–thaw cycles. The tube was then placed in a temperature-regulated oil bath at 80 °C for 6 h. The reaction mixture was diluted with THF before passing through a neutral alumina column to remove the copper complex, THF was removed by rotary evaporation and the mixture was precipitated in cold methanol/water (80/20 v/v). $M_{n,NMR}$: 8000 g/mol. $M_{n,GPC}$: 9596 g/mol, M_w/M_n: 1.23. ^{1}H NMR of the PMMA-*b*-P*t*BA-Br polymer (500 MHz, $CDCl_3$, δ) shows: 4.05 (2H, CH_3-C*H_2*-O-CO and

1H, CH_2-C*H*-Br), 3.56 (s, 3H, CO-O- CH_3), 2.24 (CH_2C*H*-CO), 1.86-0.82 (6H, O-CO-C(CH_3)$_2$, CO-O-C(CH_3)$_3$, *CH_2*-C*CH_3*,) **(Appendix D, Figure D.2)**.

The terminal Br groups in PMMA-*b*-PtBA-Br polymer were converted to azide by reacting with excess NaN_3 to allow *"click"* coupling to the alkyne-functionalized PEG block. Briefly, PMMA-*b*-P*t*BA-Br (1 g, 1.25 x 10^{-1} mmol) and 20 equivalents of NaN_3 (0.16 g, 2.5 mmol) were stirred together in DMF overnight at 50 °C. The polymer was dissolved in CH_2Cl_2, extracted with water followed by reverse extraction of the water phase with CH_2Cl_2, combining the organic layers, and drying over Na_2SO_4. Finally, the organic layer was evaporated to obtain the PMMA-*b*-PtBA-N_3 Polymer. $M_{n,GPC}$ = 10,073 g/mol, M_w/M_n = 1.18. ^{1}H NMR (500 MHz, $CDCl_3$, δ) shows: 4.05 (2H, CH_3-C*H_2*-O-CO), 3.77 (CH_2C*H*-N_3), 3.58 (s, CO-O-CH_3), 2.26 (CH_2-C*H*-CO), 1.93-0.83 (6H, O-CO-C(CH_3)$_2$, CO-O-C(CH_3)$_3$, *CH_2*-C*CH_3*,) **(Appendix D, Figure D.3)**.

3.2.6 Synthesis of alkyne-functionalized poly(ethylene glycol) (PEG-Alkyne)

PEG (M_n: 5000 g/mol) with mono-hydroxyl functional end group (5 g, 1.0 mmol), 4-pentynoic acid (147 mg, 1.5 mmol), *N*,*N'*-dicyclohexylcarbodiimide (DCC) (206 mg, 1.0 mmol), 4-dimethylaminopyridine (DMAP) (122 mg, 1.0 mmol), and 25 mL of dichloromethane (DCM) were introduced into a round bottom flask and allowed to stir overnight at room temperature. After filtration of the formed salts, the reaction mixture was concentrated by rotary evaporation and the PEG polymer was precipitated three times in diethyl ether followed by filtration. The yield was 3.80 gm (76%) with 94% functionalization efficiency. ^{1}H NMR (500 MHz, $CDCl_3$, δ): 4.26 (t, 2H, CO-O-C*H_2*), 3.71 (t, 2H CO-O-CH_2-C*H_2*-O), 3.65 (bs, 450H, O-C*H_2*-C*H_2*), 3.38 (s, 3H, CH_2-CH_2-O-C*H_3*), 2.58 (2H, CH_2-C*H_2*-CO-O), 2.51 (2H, CH_2-C*H_2*-CO-O), 1.99 (1H, alkyne proton) **(Appendix D, Figure D.4)**.

3.2.7 *"Click"* coupling of PMMA-*b*-P*t*BA-N_3 and PEG-Alkyne blocks

PEG-Alkyne (447 mg, 8.78 x 10^{-2} mmol, 1 equivalent), PMMA-*b*-P*t*BA-N_3 (710 mg, 9.66 x 10^{-2} mmol, 1.1 equivalent), CuBr (15.1 mg, 1.05 x 10^{-1} mmol, 1.2 equivalent), PMDETA (21.9 μL, 1.05 x 10^{-1} mmol, 1.2 equivalent), and 6 mL of DMF were introduced into a Schlenk tube and the reaction mixture was degassed by three freeze-pump-thaw cycles before placing the tube in an oil bath at room temperature for 48 h. The reaction mixture was diluted with THF, passed through a neutral alumina column to remove the copper complex, and the polymer was precipitated twice in diethyl ether and a third time in methanol before being collected by centrifugation. The polymer product was dissolved in DCM and precipitated several times in a DCM/hexane mixture to remove unreacted PEG following a published protocol [210]. The molecular weight and molecular weight distribution of the PMMA-*b*-P*t*BA-*b*-PEG polymer are $M_{n,GPC}$ = 20,281 g/mol and M_w/M_n = 1.08. ^{1}H NMR (500 MHz, $CDCl_3$, δ) shows: 7.46 (bs, 1H, triazole ring proton), 4.25 ($CH_2C\mathit{H}$-triazole and CO-O-C$\mathit{H_2}$), 4.05 (2H, CH_3-C$\mathit{H_2}$-O-CO), 3.64 (bs, O-C$\mathit{H_2}$-C$\mathit{H_2}$), 3.59 (s, CO-O-CH_3), 3.38 (s, 3H, CH_2-CH_2-O-C$\mathit{H_3}$), 3.05 (2H, triazole-C$\mathit{H_2}$-CH_2-CO-O), 2.76 (2H, triazole-CH_2-C$\mathit{H_2}$-CO-O), 2.26 (CH_2-CH-CO), 1.93-0.83 (6H, O-CO-C(CH_3)$_2$, CO-O-C(CH_3)$_3$, $\mathit{CH_2}$-C$\mathit{CH_3}$) **(Appendix D, Figure D.5)**.

The *tert*-butyl groups in the central block were hydrolyzed using trifluoroacetic acid (TFA) to obtain the corresponding carboxylic acid. Briefly, the PMMA-*b*-P*t*BA-*b*-PEG polymer was dissolved in DCM followed by adding 10-fold TFA (compared to the molar concentration of the *tert*-butyl groups) at 0°C under argon atmosphere. The reaction mixture was stirred for 30 min at 0°C and allowed to stand stirring for 24 h at room temperature. DCM and TFA were evaporated with an air stream and the PMMA-*b*-PAA-*b*-PEG polymer was precipitated in methanol. $M_{n,GPC}$ =

14,860 g/mol and M_w/M_n = 1.15 for the PMMA-*b*-PAA-*b*-PEG polymer. ^{1}H NMR (500 MHz, $CDCl_3$, δ) showed complete loss of the *tert*-butyl protons at 1.45 ppm **(Appendix D, Figure D.6)**.

3.2.8 Synthesis of acid-labile 2,2'-(Propane-2,2-diylbis(oxy))-diethanamine cross-linker

The acid-labile 2,2'-(Propane-2,2-diylbis(oxy))-diethanamine cross-linker was synthesized following published methods [211-215]. Briefly, *N*-(2-hydroxyethyl)-phthalimide (5.0 g, 26.15 mmol, 1 equivalent) was completely dissolved in 100 mL of dry benzene and cooled down to 0 °C in an ice bath. 2-methoxy propene (2.5 mL, 26.15 mmol, 1 equivalent) was carefully added to the solution along with *p*-toluene sulfonic acid (50 mg, 0.78 mmol). The reaction mixture was stirred for 1.5 h while keeping the temperature at 0 °C to avoid loss of the highly volatile 2-methoxy propene. The flask was then connected to a trap and the mixture was heated to 45 °C under high vacuum to remove the methanol formed during the reaction. Additional benzene was added and subsequently evaporated for 6 h before quenching the reaction by adding triethylamine (6.67 mL) and allowing the reaction mixture to warm up to room temperature. Acetic anhydride (1.33 mL) was added to convert unreacted alcohol groups into the corresponding acetate and the mixture was stirred overnight. The reaction mixture was then precipitated by drop wise addition to hexane. The precipitated powder was collected and recrystallized twice from ethyl acetate yielding a white solid. Reaction yield was 70%. ^{1}H NMR (500 MHz, $CDCl_3$, δ) shows: 1.3 (6H, s, CH_3-C), 3.6 (4H, t, CH_2-O), 3.80 (4H, t, CH_2-N), 7.4-7.8 (8H, dt, ArH) **(Appendix D, Figure D.7)**. Calculated $[M^+H]^+$ ($C_{23}H_{22}N_2O_6$) m/z = 422.15 and found $[M^+Na]^+$ = 445.1.

The formed 2,2'-(Propane-2,2-diylbis(oxy))bis(diethane-2,1diyl)bis(isoindoline-1,3-dione) (400 mg) was deprotected by refluxing overnight with 5 mL of 6 M NaOH to obtain 2,2'-(Propane-2,2-diylbis(oxy))-diethanamine. The final product was extracted three times by a mixture of $CHCl_3$/iPrOH (1/1 v/v) and dried over anhydrous sodium sulfate before evaporating the organic

layer to obtain an amber-colored oil. The reaction yield was 50%. ^{1}H NMR (500 MHz, $CDCl_3$, δ) shows: 1.36 (6H, s, CH_3-C), 1.44 (4H, bs, NH_2), 2.81 (4H, t, CH_2-NH_2), 3.45 (4H, t, CH_2-O). ^{13}C NMR (500 MHz, $CDCl_3$) δ (ppm for TMS): 24.98, 42.18, 62.88, and 99.79. Calculated $[M^+H]^+$ ($C_7H_{19}N_2O_2$) m/z = 162.14 and found $[M^+H]^+$ = 163.14 and $[M^+Na]^+$ = 185.1.

3.2.9 Formulation of PMMA-*b*-PAA-*b*-PEG polymers into micelles

Amphiphilic PMMA-*b*-PAA-*b*-PEG polymer (10 mg, $8.66x10^{-4}$ mmol) was dissolved in 1.5 mL of THF by stirring for 5 minutes before adding drop wise to 15 mL of water in a sonicating water bath. After 2 hours of stirring at room temperature, the solution mixture was transferred to a dialysis bag (MWCO 1KDa), which was placed in a large water bath for 24 hours. After 24 h of dialysis, the solution of uncross-linked micelles (NSLCM) was lyophilized to obtain the corresponding powder. Micelle cross-linkage using the acid-labile 2,2'-(Propane-2,2-diylbis(oxy))-diethanamine started by acidifying the NSCLM solution down to pH 4.0 by adding 1N HCl followed by 150 µL of *N*-(3-dimethylaminopropyl)-*N'*-ethylcarbodiimide hydrochloride (EDC) (8.28 mg, $4.32x10^{-2}$ mmol) and 150 µL of *N*-hydroxy succinimide (NHS) (2.49 mg, $2.16x10^{-2}$ mmol) in 100 mM 2-(N-morpholino)ethanesulfonic acid (MES) solution and stirring for 3 hours to form the NHS esters of the carboxylic acid groups in the central PAA block. The pH of the micelle solution was adjusted to 9.2 using a 1N NaOH solution before adding the 2,2'-(Propane-2,2-diylbis(oxy))-diethanamine cross-linker and stirring the reaction mixture for 9 h at room temperature. By adjusting the amount of the 2,2'-(Propane-2,2-diylbis(oxy))-diethanamine cross-linker added to the micelle solution, we cross-linked 50% or 100% of the NHS-activated carboxylic acid groups in the central PAA block to obtain shell cross-linked micelles (SCLM). Specifically, 0.44 mg, $0.27x10^{-2}$ mmol and 0.88 mg, $0.54x10^{-2}$ mmol of the 2,2'-(propane-2,2-diylbis(oxy))-diethanamine cross-linker were added to the NHS-activated NSCLM solution to

prepare SCLM-50 (50% PAA cross-linkage density) and SCLM-100 (100% PAA cross-linkage density), respectively. After 9 hours of stirring at room temperature, the reaction mixture was dialyzed against double distilled H_2O with pH 9.0 for 24 h before lyophilization **(Figure 3.2)**.

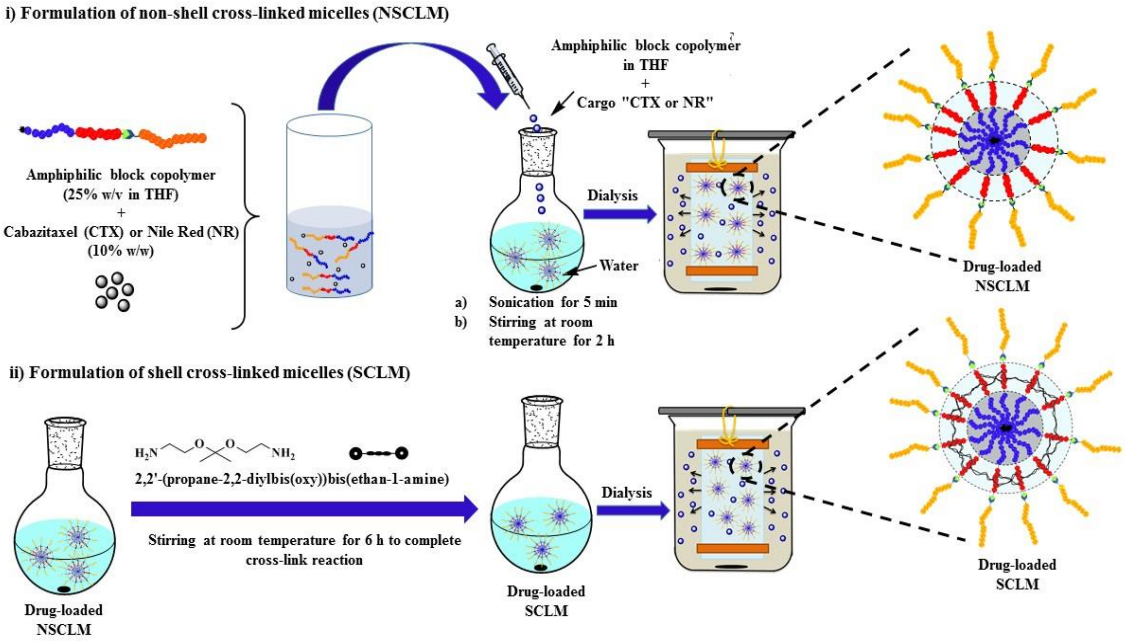

Figure 3.2 A schematic drawing showing the formulation of PEG-*b*-PAA-*b*-PMMA polymers into NR- and CTX-loaded NSCLM and SCLM micelles.

NR- and CTX-loaded micelles were formulated following the same protocol. Briefly, PMMA-b-PAA-b-PEG polymer (15 mg, 8.66 $x10^{-4}$ mmol) was dissolved in 2.25 mL of THF by stirring for 5 minutes before adding the 10% w/w solution of NR or CTX and stirring for an additional 30 min at room temperature. This solution mixture was added drop wise into 22.5 mL of double distilled water while sonicating to trigger micelle formation followed by stirring for 2 h at room temperature to obtain a homogenous solution of NR- or CTX-loaded NSCLM solution. A fraction of the NR- or CTX-loaded NSCLM solution was reacted with NHS/EDC to convert the

carboxylic acid groups of the PAA block into the activated NHS ester before adding the 2,2'-(Propane-2,2-diylbis(oxy))-diethanamine cross-linker following the same procedure described earlier to prepare SCLM. We controlled the amount of the cross-linker added to the reaction mixture to prepare NR- and CTX-loaded SCLM-50 and SCLM-100 micelles to investigate the effect of shell cross-linkage density on the loading and release of the NR and CTX cargo. NR- and CTX-loaded NSCLM were transferred to dialysis bags with a MWCO of 1 KDa and dialyzed against double distilled water containing tween 80 (0.5% w/v) for 2 hours to remove free NR and CTX from the micelles solution followed by dialysis against double distilled water for 24 hours before lyophilization to obtain NR- and CTX-loaded NSCLM as dry powder. NR- and CTX-loaded SCLM-50 and SCLM-100 micelles were dialyzed against double distilled water with pH 9.0 for 24 h before lyophilization.

After lyophilization, 1 mg of the dry powder was dissolved in 10 mL of THF followed by measuring UV absorbance at 550 nm and 230 nm to quantify the amount of NR and CTX present in solution using concentration versus absorbance calibration curves (NR concentration range was 0-50 µM and CTX concentration range was 0-300 µM). We calculated NR and CTX content in the dry micelles and their loading efficiency using the following equations.

$$\textbf{NR/CTX Content}\ (\%\textbf{Weight}) = \frac{\textit{Calculated amount of NR or CTX in dry powder}}{\textit{Total weight of the dry powder}}\ \boldsymbol{x}\ \mathbf{100}\ \% \quad \text{…Eq. 3.1}$$

$$\textbf{Loading efficiency}\ (\%) = \frac{\textit{Calculated amount of NR or CTX in dry powder}}{\textit{Amount of NR or CTX used in micelle formulation}}\ \boldsymbol{x}\ \mathbf{100}\ \% \quad \text{Eq. 3.2}$$

3.2.10 Micelles characterization

The transition of PMMA-*b*-PAA-*b*-PEG polymer from unimers to micelles in aqueous solutions was investigated by monitoring the change in NR fluorescence upon increasing polymer's concentration following a published protocol [216]. Specifically, self-assembly of the PMMA-*b*-PAA-*b*-PEG polymer into micelles and NR encapsulation in the hydrophobic core has

been shown to increase its fluorescence signal, which was used to measure the critical micelle concentration (CMC) of this amphiphilic polymer. Briefly, PMMA-*b*-PAA-*b*-PEG polymer was dissolved in DI water at different concentrations ranging from 0.0001 to 0.6 mg/mL. A 0.1 mM stock solution of NR in THF was prepared and 10 µL aliquots were transferred to glass vials and allowed to air dry for 2 hours at room temperature before adding 1 mL of different polymer solutions, mixing in a sonicating water bath for 1 hour, and allowing to stand at room temperature for 2 hours. The fluorescence intensity of NR in different polymer solutions was measured (λ_{ex}= 550 ± 2 nm, λ_{em}= 620 ± 2 nm) using a Fluoroskan Ascent FL plate reader (Thermo Fisher Scientific, Waltham, Ma), which was plotted against polymer concentration to determine the CMC. Further, the size and zeta potential of empty and NR/CTX-loaded NSCLM, SCLM-50, and SCLM-100 micelles were measured using a 90Plus particle size analyzer with ZetaPALS capability (Brookhaven Instruments Corporation, Holtsville, NY) at 25 °C following established protocols [217]. The morphology of NSCLM was visualized using the JEOL 3011 high resolution electron microscope. Briefly, 1 mg of NSCLM micelles was dissolved in 1 mL of distilled water by mixing and 10µl of the solution was placed on a 400 mesh grid (Ted Pella Inc., Redding, CA) before imaging at a magnification of 10,000X under an accelerating voltage of 300kV.

3.2.11 NR and CTX Release Studies

Release of NR and CTX from NSCLM, SCLM-50, and SCLM-100 was investigated as a function of solution pH and incubation time. Briefly, 1 mg of NR- and CTX-loaded NSCLM, SCLM-50, and SCLM-100 micelles were dissolved in 2 mL of PBS with pH 7.4 or 5.0 before transferring to dialysis cassettes (MWCO 3,500 Da), which were immersed in 150 mL of PBS (pH 7.4) or acetate buffer (pH 5.0) containing 0.5% w/v Tween20 and kept at 37°C while stirring at 150 rpm. Release of NR from NR-loaded micelles was quantified by drawing four 200 µL samples

from the release media after 0.5, 1, 1.5, 2, 2.5, 3, 3.5, 4, 4.5, 5, 5.5, 6, 6.5, 7, 7.5, 8, 10, 13, and 24 hours from immersing the dialysis cassettes in the release solution followed by measuring NR fluorescence in the collected samples (λ_{ex} = 550 nm, λ_{em} = 620 nm) using the Fluoroskan plate reader. Similarly, release of CTX from CTX-loaded micelles was quantified by drawing four 200 µL samples from the release media after 1, 2, 4, 6, 8, 12, 14, 16, and 24 hours from immersing the dialysis cassettes in the release solutions followed by measuring the amount of CTX in each sample using high pressure liquid chromatography (HPLC). Briefly, CTX solutions were analyzed using a C18 Ascentis Express column (Water Corp, Milford, MA; 2.7 µm, 15 cm x 3.0 mm) connected to a Waters HPLC system equipped with a UV dual absorbance detector. A mixture of solvent A (650 mL of H_2O and 350 mL of ACN) and solvent B (250 mL of H_2O and 750 mL of ACN) was used as a mobile phase to resolve the released CTX on the C18 column starting with a gradient of solvent A:solvent B of 100:0 for 7 min, 62:38 for 29 min, 22:78 for 0.1 min, and 100:0 for 9 min at a flow rate of 0.6 mL/min while keeping the column at 40 °C throughout the analytical run. Absorbance of the eluting CTX molecules was measured at 230 nm. The total amount of the released CTX was calculated based on UV absorbance versus concentration calibration curve using the Waters Breeze software.

3.2.12 Cell Culture

PC-3 and C4-2B prostate cancer cells were a generous gift from Dr. Evan Keller (University of Michigan) and were cultured following published protocols [218]. Briefly, PC-3 cells were cultured in RPMI-1640 while C4-2B cells were cultured in T-medium, which were both supplemented with 10% fetal bovine serum (FBS; Gibco, Carllsbad, CA) and 1% antibiotic-antimycotic solution (Gibco, Carllsbad, CA). PC-3 and C4-2B cells were incubated at 37 °C and 5% CO_2 while changing the culture medium every other day and passaging the cells using 0.05%

Trypsin-EDTA solution after reaching 80% confluence. The passage number for PC-3 and C4-2B cells used in the uptake and cytotoxicity studies was in the range between 25 and 40.

HEK 293 human embryonic kidney cells were a generous gift from Dr. Rhima Coleman (University of Michigan) and were cultured in DMEM medium supplemented with 10% fetal bovine serum. The cells were incubated at 37 °C and 5% CO2 while changing the culture medium every other day and passaging the cells using 0.5% Trypsin-EDTA solution after reaching 80% confluence.

Non-adherent THP-1 acute monocytic leukemia cells were a generous gift from Dr. Katsuo Kurabayashi and Dr. Jianping Fu (University of Michigan), which were cultured in RPMI-1640 medium supplemented with 10% FBS and 120 μM β-mercaptoethanol. THP-1 cells were activated into phagocytic and adherent ones by seeding in 24-well plates at a seeding density of 200,000 cells/well followed by incubating with regular culture medium supplemented with 200 nM phorbol myristate acetate (PMA) for 3 days. Differentiated and adherent THP-1 cells were cultured for 5 more days in PMA free culture medium before using in uptake studies. Both non-adherent and differentiated THP-1 cells were cultured in a humidified 5% CO_2 at 37 °C.

3.2.13 Cellular uptake studies

PC-3 and C4-2B human prostate cancer cells were seeded in 24-well plates at a seeding density of 2 x 10^5 cells/well and allowed to adhere for 24 h before incubating with free NR, or NR-loaded NSCLM, SCLM-50 and SCLM-100 micelles at equivalent NR concentrations (1, 2, 5, 10 and 100 nM) for 2 h. Treated PC-3 and C4-2B cells were washed three times with PBS before being trypsinized with 0.05% trypsin-EDTA solution, centrifuged at 1000 rpm for 5 min to form pellets, suspended in 1 mL PBS, and analyzed using CyAn™ ADP Flow Analyzer (Beckman

Coulter, Brea, CA) at characteristic NR excitation (λ_{ex} = 488 nm) and emission (λ_{em} = 617 nm) wave lengths.

We investigated the effect of NSCLM, SCLM-50, and SCLM-100 micelles on the fluidity of PC-3 and C4-2B cell membranes using the 1,6-diphenyl-1,3,5-hexatriene (DPH) probe following published protocols [219]. Briefly, suspensions of PC-3 and C4-2B were washed twice with PBS before incubating with 2 μM DPH staining solution for 1 h at 37 °C. Cells were pelleted down and washed twice with PBS to remove excess DPH before suspending them in PBS and mixing with different micelle solutions at a micelle concentration of 1 nM [220]. We measured the fluorescence intensity of DPH (λ_{ex} = 365 nm and λ_{em} = 400–500 nm) directly before adding the micelle solution and at different incubation time points up to 1 hour using a QM4 fluorescence spectrophotometer (Perkin-Elmer, Waltham, MA). Using DPH fluorescence at different time points, we calculated the change in membrane microviscosity using the following equation.

$$r_o / r = 1 + C(r)\, T\, \tau / \eta \quad \text{Eq} \quad \text{..... Eq. 3.3}$$

Where r_o is the limiting fluorescence anisotropy for DPH, which equals 0.362 and r is the measured fluorescence anisotropy at different time points. T is the absolute temperature, τ is the exited state lifetime that equals 10 ns, and C(r) is a molecular shape parameter, which equals 8.6 x 10^5 poise.deg^{-1}.s^{-1} [219]. Membrane microviscosity was normalized to its intrinsic (base line) viscosity observed before incubating with different micelles to show the change in membrane fluidity in response to different micelles as a function of incubation time.

3.2.14 Anticancer activity of CTX-loaded micelles

PC-3 and C4-2B cells were seeded at a seeding density of 10 x 10^3 cells/well in 96-well plates and allowed to adhere for 24 h before incubating with free CTX, CTX-loaded NSCLM,

SCLM-50 and SCLM-100 micelles at equivalent concentrations (500, 200, 100, 75, 50, 25, 10, 7.5, 5, 2.5, 1, 0.5 and 0.1 nM) of CTX for 48 h. PC-3 and C4-2B cells were also incubated with empty NSCLM, SCLM-50 and SCLM-100 micelles at the same amounts used to deliver different doses of CTX to assess the intrinsic toxicity of the micelles. At the end of the incubation period, the culture medium was aspirated and cells were incubated with 200 µL of the Resazurin dye at a dilution of 1/10 for 3 h before measuring solution fluorescence (λ_{ex}= 570 nm, λ_{em}= 590 nm) using the Fluoroskan Ascent FL plate reader. Fluorescence values were normalized to that observed with PC-3 and C4-2B cells incubated in the regular culture medium (control group) to calculate the percentage of viable cells in response to different treatments.

3.2.15 Intrinsic micelles toxicity

We evaluated the micelles toxicity on normal healthy cells by incubating HEK 293 cells with empty NSCLM and SCLM-50 micelles. Briefly, HEK 293 cells were seeded at a seeding density of 10,000 cells/well in 96-well plates and allowed to adhere overnight before incubating with empty (no CTX loading) NSCLM and SCLM-50 micelles for 48 hours. We measured the change in the proliferation of HEK 293 cells incubated with increasing concentrations of NSCLM and SCLM-50 micelles reaching 50-100 folds the IC_{50} of CTX when delivered using the same carriers compared to untreated HEK 293 cells (control). Change in cell proliferation was quantified by aspirating the particles solution and incubating the cells with 200 µL of the Resazurin dye at a dilution of 1/10 for 4 hours before measuring solution fluorescence (λ_{ex}= 570 nm, λ_{em}= 590 nm) using the Fluoroskan Ascent FL plate reader. Fluorescence values were normalized to that of untreated HEK 293 cells (control group) to calculate the percentage of viable cells in response to different concentrations of NSCLM and SCLM-50 micelles.

3.2.16 Hemocompatibility assays

We evaluated the hemocompatibility of NSCLM, SCLM-50, and SCLM-100 micelles by investigating the adsorption of bovine serum albumin (BSA) as a model serum protein to micelles surface as function of time and micelles interaction with red blood cells (RBCs) and platelets *in vitro*. Briefly, blood samples were freshly collected from human volunteers following IRB-approved protocols into 10 mL EDTA-coated vacutainer tubes before centrifuging at 3,000 rpm for 5 min to separate the RBCs from the plasma supernatant. The RBCs layer was washed three times with 0.15 M sodium chloride solution before diluting to a total volume of 10 mL using PBS (pH 7.4) by gently inverting the tube following published protocols [221]. Approximately 2.5 x 10^7 RBCs were mixed with 550 µL of PBS (pH 7.4) and 250 µL of 1 µM NSCLM, SCLM-50 or SCLM-100 solutions in Eppendorf tubes that were incubated in a shaking water bath at 37 °C for 1 h. All tubes were centrifuged at 14,000g for 5 min to pellet down the RBCs and 200 µL of the supernatant solutions were transferred into a flat-bottom 96-well plate to measure the UV absorbance of the leaked hemoglobin at 541 nm using the Multiskan microplate reader (Thermo Fisher Scientific Inc., Waltham, MA). Absorbance of each supernatant solution was normalized to the UV absorbance of the supernatant solution of RBCs incubated with Triton X-100 (positive control) to calculate % RBCs hemolysis triggered by incubation with different micelle formulations.

To investigate platelets interaction with different micelles, we collected fresh blood from euthanized C57BL/6 mice using 20 gauge needles flushed with 3.2% sodium citrate, which was mixed with 1 volume HEPES tyrode buffer before centrifuging twice at 50Xg for 10 min to collect the platelet rich plasma (PRP) layer. The blood was centrifuged one more time with 1 volume of HEPES tyrode buffer at 1200Xg to collect the platelet poor plasma (PPP) layer. We mixed 10µL

of 1 μM NSCLM, SCLM-50, and SCLM-100 solutions with 500μL of PRP solution pre-warmed to 37 °C followed by monitoring platelets aggregation over a period of 10 minutes using the Aggro-Link data reduction system (Chrono-log Corporation, Havertown, PA) following published protocols [222-224]. Similarly, we monitored platelet aggregation upon mixing 500 μL of PRP solution with 10μL of 10μM ADP and collagen (5μM) (1:1 v/v) mixture and PBS as positive and negative controls, respectively.

Finally, we investigated binding of bovine serum albumin (BSA) as a model serum protein to SCLM-50 micelles (test) and G5-$(NH_2)_{128}$ dendrimers (positive control) to assess micelles opsonization as a function of incubation time. Briefly, SCLM-50 micelles and G5-$(NH_2)_{128}$ particles were dissolved in PBS (pH 7.4) at a 250 nM particle concentration, mixed with BSA solution (0.5 mg/mL) in a quartz cuvette, and incubated at 37 °C for 60 min. We measured the fluorescence of BSA tryptophan residues (λ_{ex} = 280 nm, λ_{em} = 300–400 nm) at time zero (I°) and at different incubation time points (I) using the QM4 fluorescence spectrophotometer (Perkin-Elmer, Waltham, MA). We quantified the quenching of BSA fluorescence as a function of incubation time by dividing initial BSA fluorescence (I°) by that observed at different time points (I). We compared the calculated I°/I ratio for BSA incubated with different particle solutions to that of BSA alone at different time points using student's *t* test to determine the statistical significance in the observed change in BSA fluorescence at different time points.

3.2.17 Macrophages uptake of opsonized micelles

We investigated the phagocytosis of NSCLM, SCLM-50, and SCLM-100 micelles by differentiated THP-1 (dTHP-1) cells to determine their ability to resist opsonization and clearance by activated macrophages. Briefly, NR-loaded NSCLM, SCLM-50, and SCLM-100 were dissolved in PBS at a NR concentration of 10nM before mixing with 4 mL fetal bovine serum

(FBS) and incubating for 1 hour at 37°C to allow micelles opsonization by serum proteins. The opsonized particles were then incubated in regular culture medium with dTHP-1 cells for 2 hours at 37 °C followed by aspirating the culture medium, washing the cells with PBS, and treatment with accutase to detach the THP-1 cells forming a cell suspension. THP-1 cell suspensions were centrifuged at 1,000 rpm for 5 min and suspended in PBS before being analyzed by flow cytometry using CyAn™ ADP Analyzer to determine the number of NR- labeled cells. Uptake of FITC-IgG (Phagocytosis Assay Kit, Cayman Chemical, Ann Arbor, MI) by dTHP-1 cells was quantified following manufacturer's protocol. Uptake of different particles into dTHP-1 cells was normalized to that of FITC-IgG (positive control) to determine the ability of different particle to resist opsonization by serum proteins and phagocytosis by activated macrophages.

3.3 Results and Discussion

3.3.1 Synthesis of amphiphilic PMMA-*b*-PAA-*b*-PEG polymer

It is critical to achieve control over the size/molecular weight of the hydrophilic and hydrophobic blocks to trigger the assembly of narrowly dispersed micelles. Therefore, we utilized a combination of ATRP technique and alkyne-azide cycloaddition *"click"* reaction to synthesize the amphiphilic PMMA-*b*-PAA-*b*-PEG polymer with a well-defined composition and molecular weight. The literature provides multiple examples of the ability to inhibit non-specific adsorption of serum proteins to particles surface and the associated clearance by phagocytic macrophages using a "brush" of PEG chains with an average molecular weight of 5kDa [225]. Therefore, we decided to use a 5kDA PEG block in the synthesis of the PMMA-*b*-PAA-*b*-PEG polymer. Given FDA approval of using PMMA, P*t*BA, and PAA polymers as excipients in controlled-release pharmaceutical formulations,[226-228] we similarly used MMA and *t*BA monomers to synthesize

the hydrophobic PMMA block and central PAA block, respectively. To achieve hydrophilic/hydrophobic balance in polymer composition, the target molecular weight of the hydrophobic block was 5kDa. By adjusting the molar feed ratio of the MMA monomer, the ethyl-2-bromoisobutyrate initiator, and PMDETA ligand to 200/1/1 and allowing the polymerization reaction to go for 21 min at 40 °C, we were able to synthesize the PMMA block with the desired molecular weight. Calculating the ratio between the methyl protons of the MMA monomers appearing at 3.57 ppm to the initiator protons at 4.21 ppm shows the polymerization of 44 MMA units forming the PMMA block with a M_{nNMR} of 4,603 g/mol **(Appendix D, Figure D.1)**. GPC analysis of the PMMA block shows a symmetric unimodal peak indicating a M_{nGPC} of 4,855 g/mol and a polydispersity index (PDI, M_w/M_n) of 1.27 **(Appendix D, Figure D.9)**. Both ^{1}H NMR and GPC analysis confirms successful synthesis of the PMMA block with the desired molecular weight.

We used PMMA-Br as a macro-initiator to start the polymerization of *t*BA monomers with the goal of extending the PMMA block with 25 units of *t*BA monomers. By adjusting the ratio of *t*BA monomers, PMMA-Br as a macroinitiator, and PMDETA ligand to 100/1/1, 27 *t*BA monomers were polymerized into the P*t*BA block with M_{nNMR} of 8,063 g/mole as shown in the ^{1}H NMR spectrum **(Appendix D, Figure D.2)**. GPC analysis of the PMMA-*b*-P*t*BA-Br copolymer shows a symmetric peak with an earlier elution volume indicating a M_{nGPC} of 9,596 g/mol and a PDI (M_w/M_n) of 1.23. The terminal Br groups transformed to azide were monitored by ^{1}H NMR **(Appendix D, Figure D.3)** and FT-IR. Similarly, our results show that commercial PEG was reacted with 4-pentynoic acid and results show that ≥ 95% of the terminal OH groups were converted to alkynes **(Appendix D, Figure D.4)**. PEG-alkyne and PMMA-*b*-P*t*BA-N_3 were "clicked" with a 95% efficiency to form the PMMA-*b*-P*t*BA-*b*-PEG polymer, which is confirmed

by the characteristic proton of the triazole ring at 7.46 ppm **(Appendix D, Figure D.5)** and loss of the azide and alkyne peaks on the FTIR spectrum. The ^{1}H NMR spectrum of PMMA-*b*-P*t*BA-*b*-PEG polymer shows a M_{nNMR} of 11,547 g/mol while GPC analysis shows a M_{nGPC} of 14,860 g/mol and a PDI (M_w/M_n) of 1.15. We decided to polymerize *t*BA monomers instead of AA monomers to avoid the reported reaction of the carboxylic acid groups with the metal complexes, which interferes with ATRP [229]. We removed the *tert*-butyl groups by acid-mediated hydrolysis using TFA, which is confirmed by the disappearance of the methyl protons of the *tert*-butyl groups at 1.43 ppm **(Appendix D, Figure D.6)**.

3.3.2 Micelles formulation and characterization

Similar to other amphiphilic polymers,[230, 231] we expected PMMA-*b*-PAA-*b*-PEG polymer to self-assemble into micelles with the PMMA block forming the hydrophobic core, the PAA block forming a hydrophilic shell, and the PEG block forming an extended brush when added to aqueous solutions. To determine the critical micelle concentration (CMC) of PMMA-*b*-PAA-*b*-PEG polymer, we monitored the change in the intensity of NR fluorescence upon increasing polymer concentration in water. Specifically, we relied on monitoring the increase in NR fluorescence upon transitioning from the bulk aqueous solution to the hydrophobic environment within the micelle's core to determine whether the polymer exists in a unimer or micelle conformation similar to previous reports [232, 233]. Results show baseline NR fluorescence in presence of low concentrations (0.1-10 µg/mL) of PMMA-*b*-PAA-*b*-PEG polymer, which gradually increased with the increase in polymer concentration above 11 µg/mL **(Figure 3.3)**. This change in NR fluorescence as a function of polymer concentration shows that the PMMA-*b*-PAA-*b*-PEG polymer switches from a unimer to a self-assembled micelle at a critical micelle concentration (CMC) of 11 µg/mL **(Figure 3.3)**. Given that the literature shows CMC values

ranging between 0.3 and 70 µg/mL for different polymer compositions,[234-239] the observed low CMC for PMMA-*b*-PAA-*b*-PEG polymer indicates the stability of the formed micelles and their potential as drug delivery vehicles.

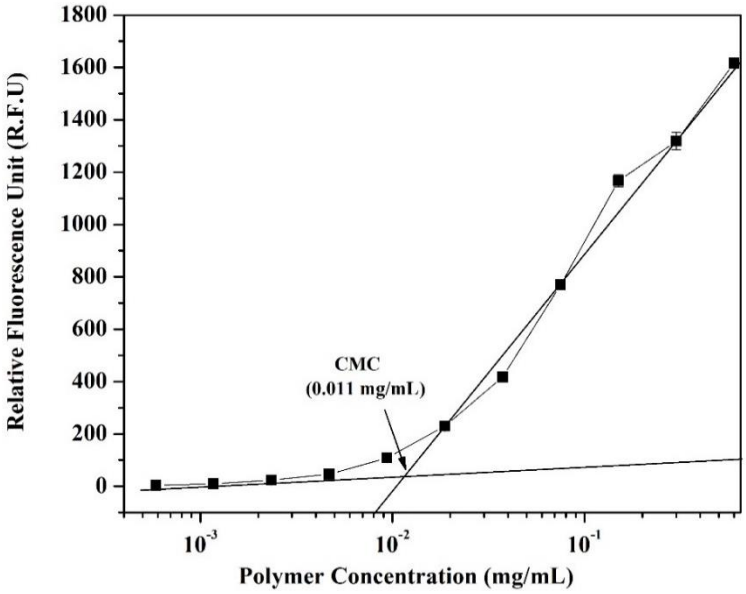

Figure 3.3 The relationship between the concentration of PEG-*b*-PAA-*b*-PMMA polymer and NR fluorescence, which is used to calculate the critical micelle concentration (CMC).

One of the key challenges with self-assembled carriers including micelles is their dilution when injected into the systemic circulation, which brings polymer concentration below the CMC causing rapid release of the loaded cargo before reaching the targeted tissue [240]. For micelles loaded with chemotherapeutic agents, the "burst" release of the loaded cargo results in significant systemic toxicity,[241] which dramatically reduces their clinical value. To address this issue, we designed an acid-labile linker with two terminal amine (NH_2) groups, which can react with the carboxylic acid groups (COOH) in the central PAA block to cross-link or "stitch" adjacent polymer chains forming an acid-sensitive shell. We hypothesized that SCLM will retain the loaded drug

better than NSCLM and will selectively release their cargo when internalized via endocytosis into cancer cells in response to the acidic pH of the endosomes.

Both ^{1}H NMR and ^{13}C NMR analysis were used to confirm shell cross-linkage in SCLM compared to NSCLM **(Figure 3.4)**. **Figure 3.4A** shows the ^{1}H NMR spectrum of the diamine cross-linker and the four characteristic H_a-H_d proton peaks. Specifically, the protons (H_a) of the two germinal methyl groups are observed as a singlet at δ 1.36 ppm, the two CH_2 protons (H_b) next to the oxygen atoms are observed as a triplet at δ 3.45 ppm, the two CH_2 protons (H_c) next to the amines are observed as a multiplet at δ 2.81 ppm, and the amine protons (H_d) are observed as a broad singlet at δ 1.44 ppm. By comparing the ^{1}H NMR spectra of SCLM and NSCLM **(Figure 3.4B)**, one can identify the characteristic proton peaks of the linker in SCLM spectrum, which confirms successful cross-linkage of the polymer shell. Briefly, the protons (H_a) of the two germinal methyl groups are observed as a triplet at δ 0.96 ppm with a coupling constant <1.0 Hz, which indicates that H_a protons are tightly packed close to the H_b protons. Similarly, H_b and H_c protons are observed as multiplets at δ 3.33 ppm and δ 3.05 ppm while the amine proton (H_d) is observed at δ 7.66 ppm indicating the formation of amide bonds confirming shell cross-linkage. The ^{13}C NMR spectra of the diamine cross-linker, SCLM, and NSCLM provide additional evidence of successful shell cross-linkage in SCLM. Specifically, the ^{13}C NMR spectrum of the diamine linker in $CDCl_3$ shows the two germinal $\underline{C}H_3$ (C_a) at δ 24.98 ppm, the peaks of C_b and C_c carbons at δ 62.88 ppm and δ 42.18 ppm, respectively, while the quaternary carbon (C_d) peak is observed at δ 99.79 ppm **(Figure 3.4C)**. Similarly, the ^{13}C NMR of SCLM shows C_a, C_b and C_c peaks at δ 23.54, δ 62.15 and δ 51.05 ppm **(Figure 3.4D)**, which corresponds to their characteristic shifts observed in the cross-linker spectrum. It is important to note that the characteristic cross-

linker peaks are missing in the ^{1}H NMR and ^{13}C NMR spectra of NSCLM confirming successful cross-linkage of the polymer shell in SCLM only.

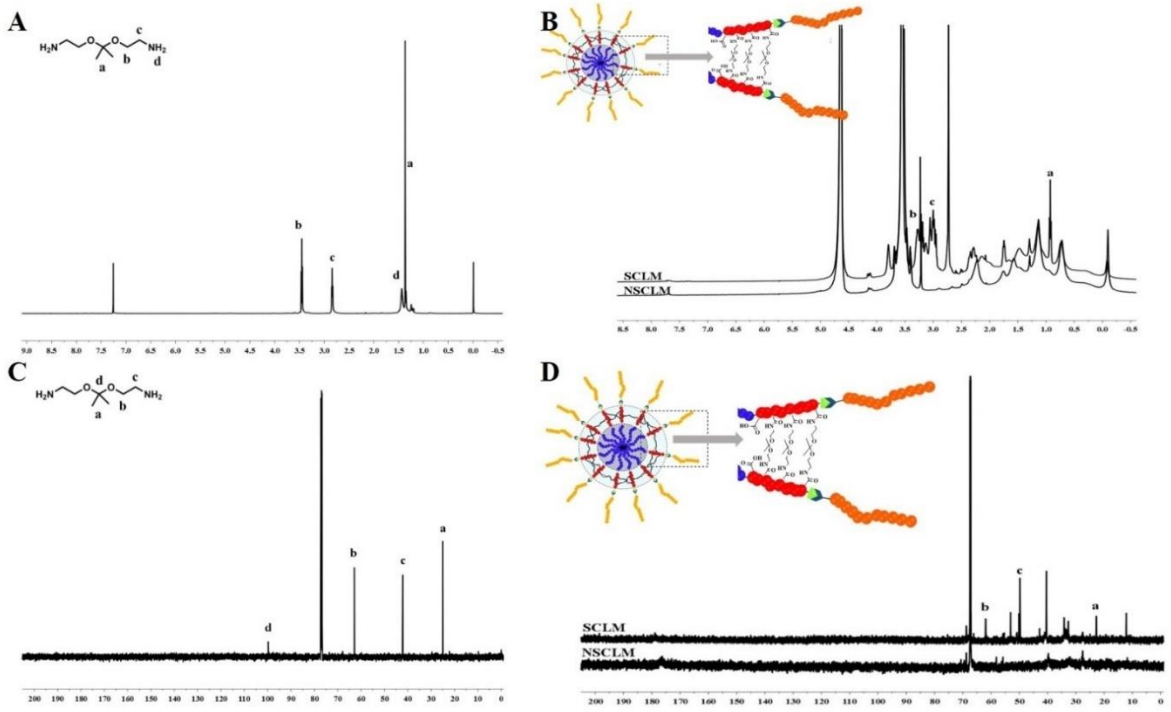

Figure 3.4 NMR Spectra of the pH-labile cross-linker.
(A) ^{1}H NMR and (C) ^{13}C NMR of the acid-labile 2,2'-(propane-2,2-diylbis(oxy))-diethanamine cross-linker recorded in $CDCl_3$. (B) ^{1}H NMR and (D) ^{13}C NMR of the NSCLM and SCLM micelles recorded in D_2O, which confirms successful cross-linkage of central PAA blocks.

We characterized the size and surface charge of empty (no cargo) and NR- and CTX-loaded micelles in NSCLM and SCLM using dynamic light scattering and zeta potential measurements, respectively. Results show that empty NSCLM and those loaded with NR and CTX have similar average sizes of 48.41 ± 3.92 nm, 42.88 ± 4.81 nm, and 46.68 ± 7.65 nm, respectively **(Figure 3.5)**. Similarly, empty and NR- and CTX-loaded SCLM had average diameters of 46.44 ± 11.80 nm, 47.64 ± 15.48 nm, and 54.06 ± 9.14 nm, respectively. There was no statistical difference between empty and loaded micelles regardless of the type of cargo or whether the micelles shell

was cross-linked or not, which indicates the stability of the formed micelles and their suitability to encapsulate a range of therapeutic molecules. Given that the gaps in the endothelial lining of tumor vasculature are 200-600 nm in size,[242] both NSCLM and SCLM can easily penetrate across leaky tumor vasculature and accumulate in tumor tissue *in vivo*. The recorded zeta potential of NSCLM and SCLM is -38.1 ± 3.16 mV and -24.5 ± 6.71 mV, respectively. The observed negative surface charge of the micelles is probably due to the free COOH groups in the central PAA block, which in combination with the PEG brush will minimize non-specific interaction with serum proteins and the subsequent clearance by phagocytic macrophage cells (e.g. Kupffer cells in the liver) [225].

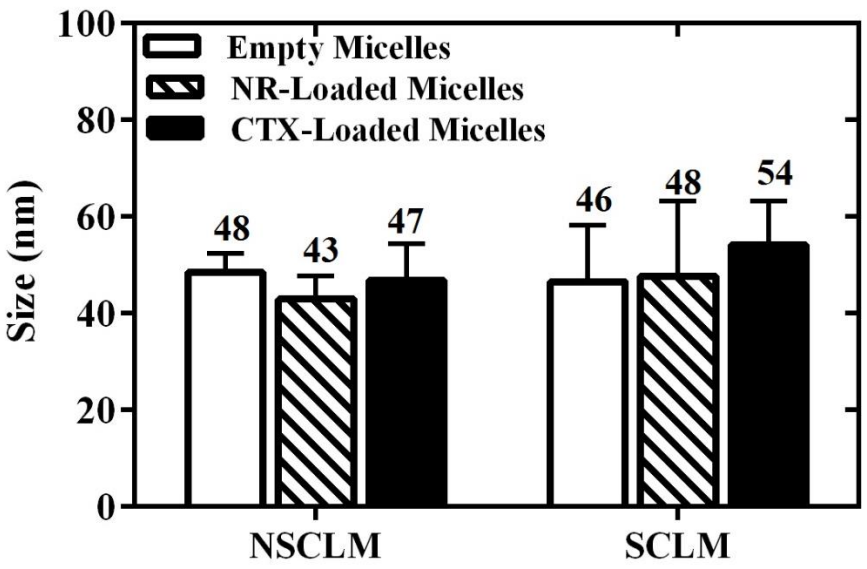

Figure 3.5 The size of empty, NR-, and CTX-loaded micelles. Results show the average + standard error of the mean (SEM) of three independent solutions for each micelle formulation.

3.3.3 Nile Red and Cabazitaxel release from NSCLM and SCLM

Release of drug molecules from the micelles' hydrophobic core is expected to change as a function of solution pH and incubation time. To test this hypothesis, we evaluated the release of NR as a model hydrophobic drug encapsulated in NSCLM, SCLM-50, and SCLM-100 in PBS (pH 7.4) and citrate buffer (pH 5.0) to predict NR release in the systemic circulation and the acidic endosomes, respectively. Results show that encapsulation efficiency of NR in NSCLM, SCLM-50, and SCLM-100 micelles was 82.29 ± 7.53%, 71.64 ± 6.61%, and 81.15 ± 7.32%, respectively.

We aimed to achieve 10% w/w loading of NR in different micelles and results show 7.60±0.64%, 6.69±0.38%, and 7.51±0.59% w/w loading in NSCLM, SCLM-50, and SCLM-100 micelles, respectively. Using micelle solutions containing 0.5 mg/mL polymer (i.e. ~50-folds the CMC) and encapsulating NR loaded in dialysis bags with MWCO 3,500 Da, we investigated NR release in different buffer solutions by measuring NR fluorescence (λ_{ex}=550 nm and λ_{em}=620 nm) at different time points up to 30 h.

Results show that 0.52 ± 0.14% of the loaded NR was released from NSCLM after 3h in PBS (pH 7.4) and gradually increased with the increase in incubation time reaching 43.59 ± 1.38% of the loaded NR after 30h **(Figure 3.6A)**. In comparison, 0.26 ± 0.11% of the loaded NR was released after 3h of dialyzing SCLM-100 micelles against PBS (pH 7.4), which gradually increased reaching 28.35 ± 0.88% of the loaded NR after 30h. The observed decline in cumulative NR release from SCLM-100 compared to NSCLM clearly indicates that cross-linkage of the carboxylic acid groups in the central PAA block significantly reduces "burst" release of the loaded cargo at physiologic pH. Reducing the number of cross-linked carboxylic acid groups by 50% in SCLM-50 resulted in release of 0.3 ± 0.08% of the loaded NR over 3h, which gradually increased reaching 45.20 ± 0.93% of the loaded NR after 30h. Comparing NR release profiles from SCLM-50 and SCLM-100 shows that controlling the degree of cross-linkage of carboxylic acid groups in the central PAA block controls the release of the encapsulated cargo in physiologic pH.

By changing the dialysis solution to citrate buffer, we investigated the release of the encapsulated NR in acidic environment (pH 5.0) similar to that of the endosomes. Results show that 0.06 ± 0.03% of the loaded NR in NSCLM was released over 1.5h and gradually increased reaching 90.93 ± 1.36% of the loaded cargo over 30h **(Figure 3.6A)**. In comparison, 0.68 ± 0.22% of the loaded NR in SCLM-100 micelles was released over 3h and increased reaching 46.52 ±

1.49% over 30h, which is significantly higher ($p \leq 0.001$) than NR released observed in neutral PBS (pH 7.4). Similarly, 1.18 ± 0.16% of the loaded NR in SCLM-50 micelles was released over 3h and increased reaching 80.89 ± 3.69 % over 30h, which is significantly higher ($p \leq 0.001$) than NR released observed in neutral PBS (pH 7.4). Difference in NR release profiles from SCLM-50 and SCLM-100 in neutral (pH 7.4) and acidic (pH 5.0) buffers clearly confirms the sensitivity of the cross-linked polymer shell to the acidic stimuli as a release mechanism that still discriminates between different micelles based on their shell cross-linkage density.

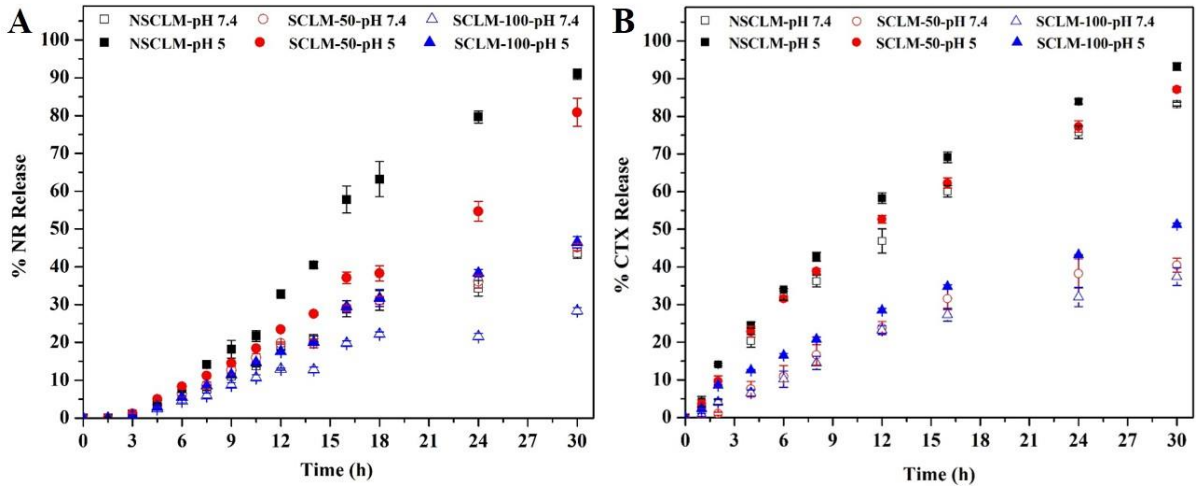

Figure 3.6 NR and CTX release profile from the micelle formulations.
Release of NR (A) and CTX (B) from NSCLM, SCLM-50 and SCLM-100 micelles in PBS (pH 7.4) and acetate buffer (pH 5.0) solutions as a function of time.

Similarly, we prepared CTX-loaded NSCLM, SCLM-50, and SCLM-100 aiming to achieve 10% w/w loading of CTX and results show w/w loading of 5.18 ± 0.53%, 3.77 ± 0.36%, and 4.72 ± 0.04%, respectively. Results also show that encapsulation efficiency of CTX in NSCLM, SCLM-50, and SCLM-100 micelles was 54.63 ± 5.94%, 39.13 ± 3.89%, and 49.58 ± 0.41%, respectively. Size of CTX-loaded NSCLM and SCLM-100 particles was 46.68 ± 7.65 nm and 54.06 ± 9.14 nm, which is similar to the size of empty and NR-loaded micelles **(Figure 3.5)**.

We quantified CTX release from CTX-loaded NSCLM, SCLM-50, and SCLM-100 micelle solutions loaded in dialysis bags with MWCO 3,500 Da and placed in PBS (pH 7.4) and citrate buffer (pH 5.0) at different time points up to 30 h. As expected, CTX was quickly released from NSCLM in PBS buffer (pH 7.4) starting with 4.12 ± 0.63% within 2 h and gradually increasing to reach 83.21 ± 0.52% of the loaded cargo after 30 hours **(Figure 3.6B)**. CTX release from NSCLM into citrate buffer (pH 5.0) started with 14.11 ± 0.34% of the cargo within 1h and gradually increased reaching 93.16 ± 1.01% over 30 hours **(Figure 3.6B)**. In comparison, CTX release from SCLM-100 micelles in PBS buffer (pH 7.4) started with 4.1 ± 0.83% over 2h and gradually increased to 37.43 ± 2.35% over 30h **(Figure 3.6B)**, which is a lower cumulative release than that observed with NSCLM due to cross-linkage of 100% of the central acrylic acid groups. In citrate buffer (pH 5.0), CTX release started at 8.56 ± 0.22% over 2 hours and increased to 51.26 ± 0.39% over 30h due to hydrolysis of the acid-labile linker and release of the encapsulated cargo **(Figure 3.6B)**. SCLM-50 micelles released 1.09 ± 0.41% of the loaded CTX over 2h in PBS buffer (pH 7.4) which increased to 40.45 ± 1.83% over 30h, which is a similar release profile to that observed with SCLM-100 micelles in neutral pH. However, 9.68 ± 1.40% of the loaded CTX was released over 2h in citrate buffer (pH 5.0) and increased to 87.13 ± 0.71% over 30h **(Figure 3.6B)**. This higher CTX release in acidic citrate buffer is a result of cross-linkage of only 50% of the central acrylic acid groups. These results collectively indicate successful formulation of acid-sensitive SCLM that efficiently encapsulated CTX and retained the bulk of the loaded cargo at physiologic pH but quickly released it in response to acidic stimuli similar to those established in the endosome.

3.3.4 Cell uptake of NR-loaded micelles

We investigated the uptake of NR-loaded NSCLM, SCLM-50, and SCLM-100 micelles compared to free NR into PC-3 and C42B cells after incubating for 2h at 37°C by measuring the

percentage of NR-labeled cells and the intensity of NR fluorescence per cell as a function of NR concentration (1, 5, 10, 100 nM) using flow cytometry. Results show that NR-loading into NSCLM, SCLM-50, and SCLM-100 micelles labeled 95.74 ± 0.27%, 45.23 ± 1.61%, and 44.11 ± 2.64% of PC-3 cells, which is significantly higher than the 24.35 ± 0.56 % cells labeled by free NR at NR concentration of 1nM **(Figure 3.7A)**. At higher NR concentrations, 100% of PC-3 cells were labeled upon incubation with free NR and NR-loaded micelles. However, by analyzing the intensity of intracellular fluorescence at each concentration of NR, results show that NR loading into NSCLM, SCLM-50, and SCLM-100 micelles significantly increased the amount of NR delivered into the cytoplasm of each cell compared to free NR at 5, 10, and 100nM **(Figure 3.7C)**.

Incubating C42B cells with 1nM on NR loaded into NSCLM, SCLM-50, and SCLM-100 micelles results in labeling 43.84 ± 7.97%, 17.37 ± 1.91%, and 18.32 ± 1.31% of the cells compared to labeling 21.81 ± 8.43% of the cells by the free NR **(Figure 3.7B)**. At higher NR concentrations (5, 10, and 100nM), 100% of PC-3 cells were labeled upon incubation with free NR and NR-loaded micelles. However, analysis of the intensity of intracellular fluorescence at each concentration shows that NSCLM exhibit higher intracellular fluorescence at a low concentration of 5nM compared to free NR **(Figure 3.7D)**. Whereas, SCLM-50 and SCLM-100 micelles exhibited higher intracellular fluorescence compared to free NR only at the concentration of 100nM **(Figure 3.7D)**.

The observed increase in intracellular fluorescence of PC-3 and C42B cancer cells upon incubation with NR-loaded NSCLM compared to free NR and NR-loaded SCLM-50 and SCLM-100 micelles **(Figure 3.7C and 3.7D)** is an interesting observation that prompted further investigation.

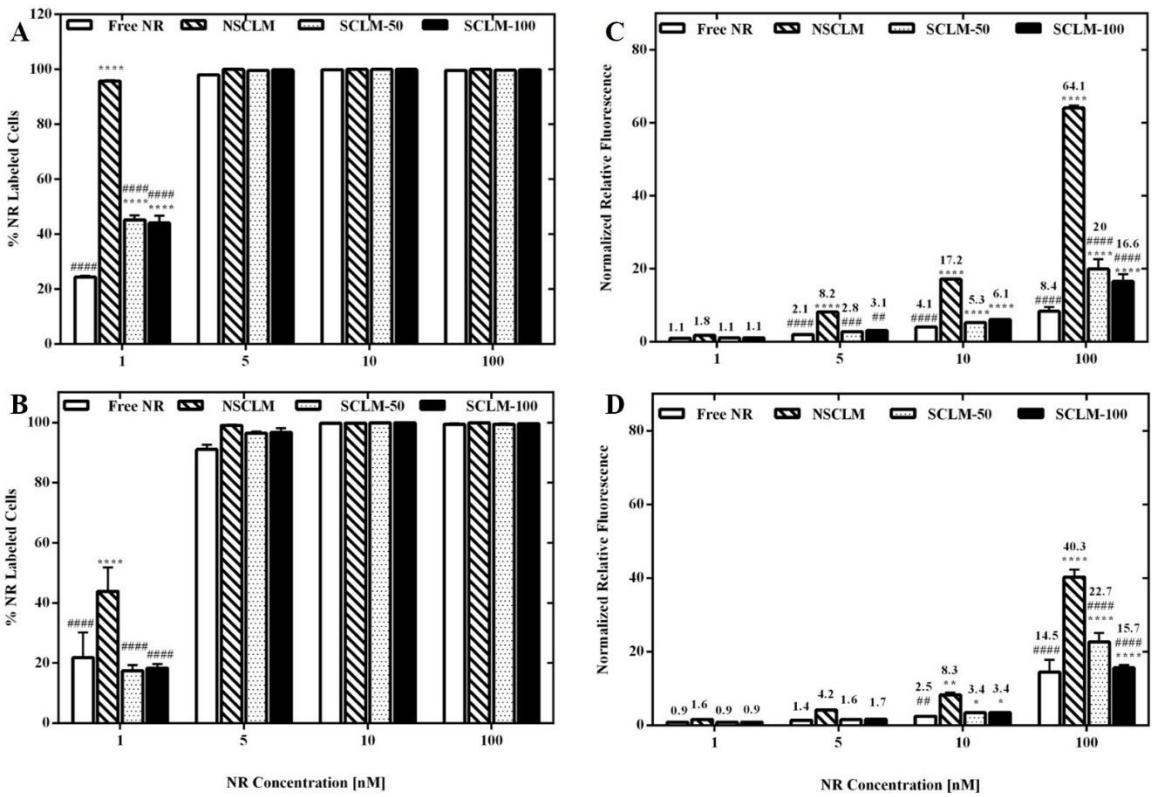

Figure 3.7 Uptake of free NR, NR-loaded NSCLM, SCLM-50, and SCLM-100 micelles into PC-3 (A and C) and C4-2B (B and D) prostate cancer cells.
Results are the average of four samples + standard error of the mean. Statistical difference between the uptake of SCLM-50 and SCLM-100 micelles and the uptake of free NR (*) and NSCLM (#) was evaluated using two-way ANOVA with Tukey's multiple comparisons test where * and # denote $P \leq 0.05$, ** and ## denote $P \leq 0.01$, *** and ### denote $P \leq 0.001$, and **** and #### denote $P \leq 0.0005$.

We hypothesized that dilution of the NSCLM solution in the culture medium led to release of PEG-*b*-PAA-*b*-PMMA unimers that insert the hydrophobic PMMA block into the cell membrane causing an increase in membrane fluidity, which enhances the diffusion of NR into the cells. To test this hypothesis, we investigated the interaction between NSCLM and SCLM-100 micelles with PC-3 and C42B cells based on the change in the fluorescence polarization spectrum of DPH compared to untreated (control) cells following published methods [220, 243, 244]. Results show that PC-3 and C42B cells treated with NSCLM at the concentration needed to deliver 1nM of NR show a rapid drop in membrane microviscosity within 15 minutes, which remained

constant for 60 minutes **(Figure 3.8A and B)**. In comparison, cells treated with SCLM-100 micelles did not exhibit any change in membrane microviscosity, which was similar to that observed with control cells (i.e. treated with DPH only) **(Figure 3.8A and B)**. These results are supported by previous reports showing that P85 block copolymer increases the fluidity of the cell membrane when used at concentrations lower than the critical micelle concentration (CMC) due to interaction of the hydrophobic poly(propylene oxide) block with the lipid bilayer [245].

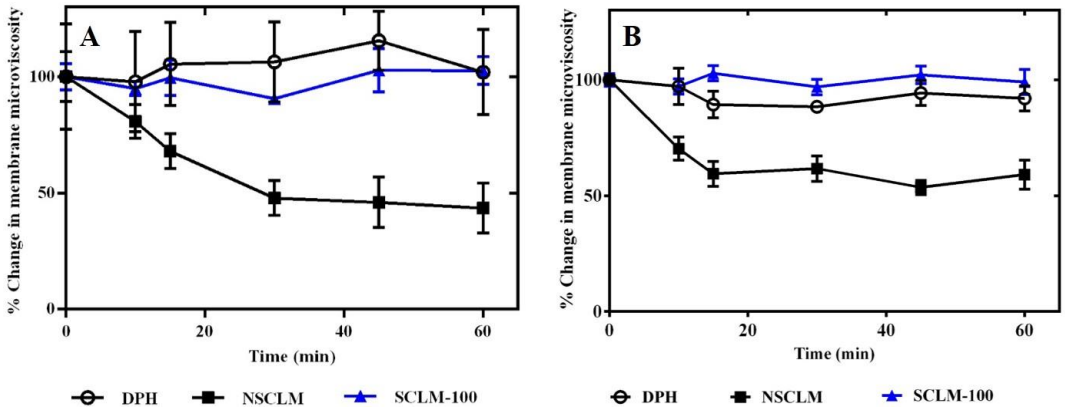

Figure 3.8 The change in microviscosity of the membranes of PC-3 (A) and C4-2B (B) prostate cancer cells.
That indicated by the drop in DPH fluorescence as a function of incubation time with NSCLM and SCLM-100 micelles. Results show the average of the calculated microviscosity at different time points normalized to its initial value (time = 0 min, 1.40 ± 0.22 poise for PC-3 cells and 24.43 ± 0.52 poise for C4-2B cells) ± standard error of the mean.

3.3.5 Cytotoxicity of CTX-loaded micelles

We compared the effect of free CTX and CTX-loaded NSCLM, SCLM-50, SCLM-100 micelles on the viability of PC-3 and C4-2B prostate cancer cells as a function of CTX concentration (0.1-500 nM). Results also show that NSCLM and SCLM-50 micelles exhibit higher toxicity towards PC-3 **(Figure 3.9A)** and C4-2B cells **(Figure 3.9B)** compared to equal concentrations of free CTX. The difference in cytotoxicity of different micelles compared to free CTX is indicated by the difference in their IC_{50} values **(Figure 3.9 and Table 3.1)**. Results show

IC_{50} for CTX-loaded NSCLM and SCLM-50 micelles of 0.60 ± 0.17 and 0.76 ± 0.18 nM, respectively, which is significantly lower than the IC_{50} of free CTX (0.96 ± 0.20 nM) in PC-3 cells. Similarly, the IC_{50} of CTX-loaded NSCLM and SCLM-50 micelles (2.66 ± 0.81 and 1.72 ± 0.52 nM) in C4-2B cells is significantly lower than that of the free drug (3.33 ± 0.63 nM). The observed higher activity of CTX-loaded NSCLM and SCLM-50 micelles can be attributed to higher uptake and efficient release of the cytotoxic cargo into cancer cells compared to the free drug.

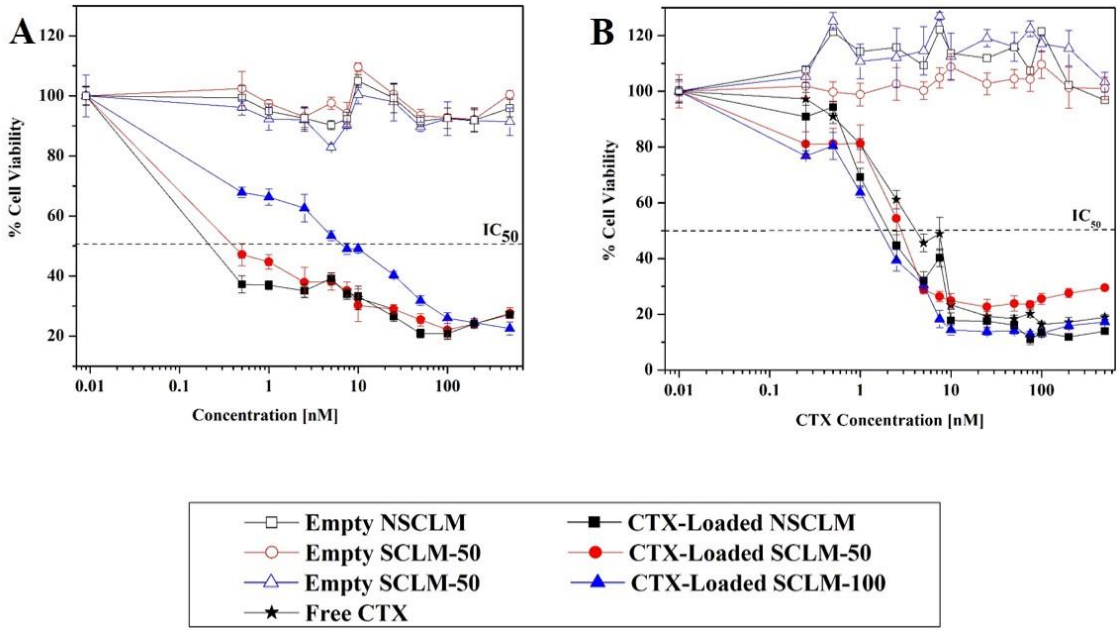

Figure 3.9 Effect of free CTX, CTX-loaded micelles, and empty micelles on PC-3 (A) and C4-2B (B) prostate cancer cells as a function of equivalent CTX concentration (0.01 - 500 nM).
Each experiment was carried out in triplicate. Results represent the average ± standard error of the mean. Curves were fitted to a log concentration versus % surviving fraction (% SF) model using Graphpad Prism Software. The IC_{50} value for each treatment (dotted horizontal line) was calculated using Graphpad Prism Software.

It is interesting to note that SCLM-100 micelles are less toxic to cancer cells compared to NSCLM and SCLM-50 micelles despite of their similar uptake, which is probably a result of the higher cross-linkage density of the central acrylic acid block resulting in slower or incomplete release of the encapsulated CTX cargo **(Figure 3.8 and Table 3.1)**. Similarly, the observed higher

toxicity of NSCLM and SCLM-50 micelles towards PC-3 cells compared to C4-2B can be attributed to a combination of factors including difference in intrinsic sensitivity towards CTX indicated by the lower IC_{50} of free CTX with PC-3 cells compared to C4-2B cells **(Table 3.1)**.

Table 3.1 The IC_{50} of free CTX and CTX-loaded micelles in PC-3 and C4-2B cells

Treatment	IC_{50} in PC-3 Cells (nM)	IC_{50} in C4-2B Cells (nM)
Free CTX	0.96 ± 0.20	3.33 ± 0.63
CTX-loaded NSCLM	0.60 ± 0.17	2.66 ± 0.81
CTX-loaded SCLM-50	0.76 ± 0.18	1.72 ± 0.52
CTX-loaded SCLM-100	5.08 ± 0.74	2.66 ± 0.56

Further, the difference in the kinetics and net micelles uptake by both cells lines indicated by higher intracellular fluorescence observed with NR-loaded NSCLM and SCLM-50 micelles in PC-3 cells **(Figure 3.7C)** compared to C4-2B **(Figure 3.7D)** leading to a higher intracellular concentration of the toxic cargo in the cytoplasm of PC-3 compared to C4-2B resulting in higher cell death. The difference in micelles uptake between both cell lines has been reported and correlated with difference in the composition of the lipid membrane of both cell lines,[243, 246] which further supports these results.

We also examined the effect of empty micelles (i.e. no CTX loading) on PC-3 and C42B cells viability using the same micelles concentrations used to deliver a specific concentration of the toxic CTX cargo. Results show that empty NSCLM, SCLM-50, and SCLM-100 micelles did not negatively affect the viability of PC-3 and C42B cells **(Figure 3.9)**. Furthermore, results also show no reduction in proliferation or viability of HEK 293 cells (a model of healthy organs) when incubated with NSCLM and SCLM-50 micelles at concentrations that are 50-100 folds higher than

the IC_{50} of CTX delivered by these carriers **(Figure 3.10)**. These results collectively indicate the biocompatibility of the polymeric carrier and the acid-labile linker used in micelles formulation.

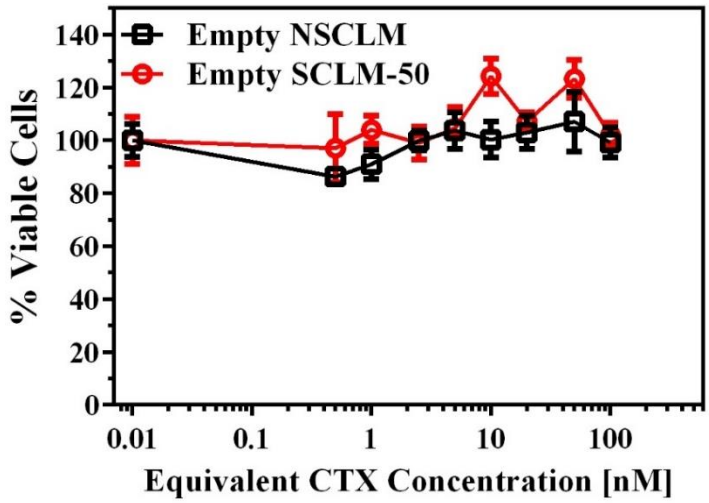

Figure 3.10 Effect of empty NSCLM and SCLM-50 micelles on HEK 293 cells as a function of micelles concentration used to deliver a given concentration of CTX (0.01 - 100 nM). Each experiment was carried out in triplicate. Results represent the average ± standard error of the mean.

3.3.6 Micelles Hemo-Compatibility

In vivo activity of our micelles will depend on a delicate balance between their selective cytotoxicity towards prostate cancer cells while remaining inert towards healthy tissues and cells. The interaction between the micelles and serum proteins, red blood cells (RBCs), and macrophages in the blood influences micelles residence in the systemic circulation, clearance by the reticular endothelial system (RES), and their distribution profile [247, 248]. Therefore, we investigated RBCs hemolysis and platelet activation upon incubating with NSCLM, SCLM-50, and SCLM-100 micelles to determine their hemo-compatibility. Results show that incubating NSCLM, SCLM-50, and SCLM-100 micelles needed to deliver 100 and 1000 nM of CTX with RBCs caused hemolysis of only 3-4% of the cells, which is similar to the baseline hemolysis observed upon incubating RBCs with PBS (control) **(Figure 3.11A)**. The lack of hemolytic capacity of our

micelles at 50-500 folds the IC_{50} of CTX-loaded micelles is a result of high surface PEGylation, which has been shown to reduce the hemolytic activity of particulate carriers [249].

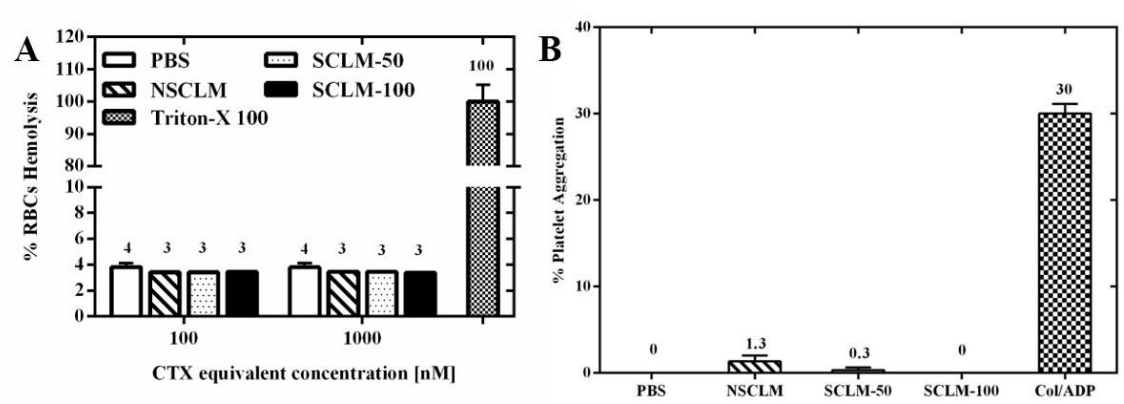

Figure 3.11 Micelles hemo-compatibility tests.

(A) The % of RBCs hemolysis upon incubating with NSCLM, SCLM-50, SCLM-100, normalized to that observed upon incubating the RBCs with Triton X-100 (positive control) for 60 min. RBCs were incubated with PBS (negative control) to determine baseline hemolysis due to cell handling. (B) The % of aggregated platelets observed upon incubation with PBS (negative control), NSCLM, SCLM-50, SCLM-100, and Col/ADP (positive control). Results show the average + standard error of the mean. The observed RBCs hemolysis and platelets aggregation upon incubation with different micelle compositions was compared to that observed upon incubation with PBS two-way ANOVA with Tukey's multiple comparisons test.

Similarly, we investigated platelets activation when incubated with NSCLM, SCLM-50, and SCLM-100 micelles compared to collagen/ADP mixture (positive control) using light transmission aggregometry following published protocols [224]. Results show that SCLM-50 and SCLM-100 micelles caused insignificant platelet aggregation that was similar to that observed with PBS (negative control) **(Figure 3.11B)**. However, NSCLM caused a slight increase in platelet aggregation compared to PBS, which can be attributed to the release of polymer unimers and exposure of the hydrophobic PMMA block that bind to and activate platelets in solution. These results collectively indicate that SCLM-50 micelles are most suited for *in vivo* testing.

3.3.7 Micelles opsonization & macrophage uptake

Adsorption of serum proteins to particulate carriers including micelles has been shown to be a key mediator of their recognition and clearance by the tissue-fixed macrophages including Kupffer cells in the liver plus splenic and lung macrophages [248]. Given that albumin is a major plasma protein,[250] we investigated its adsorption to micelles surface to determine the liability of different formulations to opsonization by serum proteins *in vivo*. We measured the change in the intrinsic fluorescence of the two tryptophan residues (λ_{ex} is 280 nm and λ_{em} is 300-400 nm) located in albumin's hydrophobic binding site to quantify albumin's adsorption to SCLM-50 micelles compared to G5-NH_2 (positive control) as a function of time following published protocols [64, 77]. Results show that the fluorescence intensity of BSA mixed with SCLM-50 remained constant throughout the experiment with $I^o/I \sim 1.1$, which is similar to the intrinsic fluorescence of free BSA **(Figure 3.12A)**. In comparison, cationic G5-NH_2 particles strongly quenched BSA intrinsic fluorescence indicated by the difference in fluorescence intensity at the beginning of the study (I^o) and at different time points (I) with more than 2-folds difference after 60 minutes. Results clearly show that the PEG corona of SCLM-50 coupled with micelles neutral surface suppressed the albumin adsorption to particle's surface, which will dramatically reduce micelles clearance by the reticular endothelial system.

In order to investigate the effect of exposing different micelles to serum proteins on their recognition and internalization by tissue-resident macrophages, we evaluate the uptake of NR-loaded NSCLM, SCLM-50, and SCLM-100 micelles by differentiated THP-1 cells using flow cytometry. Specifically, we incubated 10 nM of NR-loaded NSCLM, SCLM-50, and SCLM-100 micelles with fetal bovine serum (FBS) for 1 hour at 37°C to allow adsorption of a protein corona to particle's surface before incubating with differentiated and activated dTHP-1 cells. Uptake of

fluorescently-labeled FITC-IgG was used to assess the phagocytic activity of dTHP-1 cells (i.e. positive control). Results show that FITC-IgG particles were internalized by 90% of dTHP-1 cells indicating strong activity of the phagocytosis machinery in these cells **(Figure 3.12B)**.

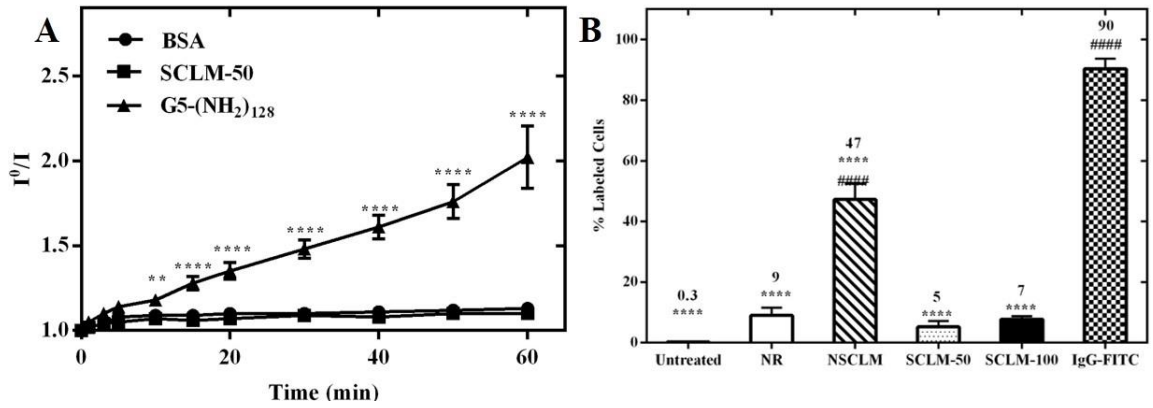

Figure 3.12 Micelles opsonization and macrophage uptake tests.

(A) The change in fluorescence intensity of BSA (I^o/I) upon incubation of 0.2 mg/mL BSA with 250 nM of cationic G5-$(NH_2)_{128}$ (positive control) and SCLM-50 particles (test) at 37 ºC for 60 minutes. Results are the average of three samples ± standard error of the mean. Statistical difference between the fluorescence intensity of BSA (I^o/I) upon incubation with different particles compared to that observed with free BSA at the same incubation time point is denoted by ** or ****, which indicates $p \leq 0.01$ or $p \leq 0.0005$, respectively. (B) Uptake of free NR, NR-loaded SCLM-50 and SCLM-100 micelles, and FITC-IgG (positive control) into differentiated THP-1 (dTHP-1) cells after incubating for 2 hours at equivalent NR concentration of 10 nM. Results are the average of three samples + standard error of the mean. Uptake of NSCLM, SCLM-50, and SCLM-100 was compared to that of free NR (#) and FITC-IgG (*) using two-way ANOVA with Tukey's multiple comparisons test where * and # denote $P \leq 0.05$, ** and ## denote $P \leq 0.01$, *** and ### denote $P \leq 0.001$, and **** and #### denote $P \leq 0.0005$.

In comparison, SCLM-50 and SCLM-100 micelles were internalized by only 5% and 7% of dTHP-1 cells, which is similar to the uptake of free NR. This indicates the poor recognition of cross-linked micelles by activated macrophages even after exposure to serum proteins. In comparison, NSCLM labeled 50% of dTHP-1 cells indicating efficient delivery of the NR dye into the cells, which is not surprising given the similar effect observed with PC-3 and C4-2B cells **(Figure 3.7)** and the effect of polymer unimers on membrane fluidity **(Figure 3.8)**. The observed higher uptake of 10 nM NR-loaded SCLM-50 and SCLM-100 by prostate cancer cells coupled

with their significantly lower recognition and uptake by activated macrophages clearly indicate their ability to achieve selective delivery of their cargo to cancer cells while evading clearance by tissue-resident macrophages. Further, the optimized hydrolysis kinetics of the shell cross-linker in SCLM-50 coupled with efficient release of the loaded cargo make this micelle composition particularly suited to be a platform for targeted delivery of anticancer drug into prostate cancer cells.

3.4 Conclusions

Results show the successful synthesis of an amphiphilic triblock copolymer (PMMA-*b*-PAA-*b*-PEG), which proved to self-assemble in aqueous media forming nano-sized micelles that efficiently encapsulate hydrophobic small molecules like Nile Red and cabazitaxel. Cross-linkage of the polymer shell using an acid-labile linker allows controlled and tunable release of the cytotoxic cargo. SCLM-50 micelles exhibited the highest cytotoxic activity towards PC-3 and C4-2B cancer cells *in vitro* with IC_{50} values that are significantly lower than free CTX. Further, SCLM-50 micelles did not cause hemolysis of RBCs, trigger platelet activation, acquire an albumin corona, or get phagocytosed by activated macrophages, which make this micelle platform an ideal carrier for selective delivery of CTX into prostate cancer cells.

3.5 Acknowledgements

Mr. Omer Aydin likes to recognize the financial support of the National Ministry of Education of the Republic of Turkey. Mr. Ibrahim Youssef recognizes the financial support of the Ministry of Higher Education of the Arab Republic of Egypt through the Joint Supervision Fellowship Program. Mr. Ibrahim Youssef also recognizes the support of Dr. Ahmed Fadda, Dr.

ElSayed Afsah, and Dr. Ibrahim El-Sherbiny for serving as the dissertation committee at Mansoura University, Mansoura, Egypt. The authors thank Dr. Daniel Eitzman and Dr. Jinsang Kim at the University of Michigan for granting access to the Aggro-Link Data Reduction System (Chrono-log Corporation, Havertown, PA) and the QM4 Fluorescence Spectrophotometer (Perkin-Elmer, Waltham, MA) used to measure platelets aggregation and changes in albumin fluorescence, respectively.

3.6 Supporting Information

Additional ^{1}H-NMR spectra of PMMA, PMMA-*b*-PtBA, PEG-alkyne, and PEG-*b*-PAA-*b*-PMMA polymers and their elution profiles on a size exclusion chromatography column are supplied in the Appendix 4.

Chapter 4

Differential Targeting of Prostate Cancer Cells, Osteoblasts, and Osteoclasts using pVTK Peptide- and Bisphosphonate-Functionalized Micelles

The material in this chapter is submitted to the following journal: **O. Aydin,** G. Tiruchinapally, I. Youssef, H. Ramaraju, Y. Y. Durmaz, K. Kozloff, D. H. Kohn, and M. ElSayed "Differential Targeting of Prostate Cancer Cells, Osteoblasts, and Osteoclasts using pVTK Peptide- and Bisphosphonate-Functionalized Micelles", *Advanced Healthcare Materials.*

4.1 Introduction

In the US, prostate cancer is diagnosed in nearly 1 of every 7 men, with 1 out of 39 men dying because of this disease [1]. Tremendous advances in the detection and treatment of primary prostate cancer, especially widespread use of prostate-specific antigen (PSA) screening over the past four decades, have led to a significant increase in the 5-year survival rate for local prostate cancer, which is now almost 100% [1]. Bone is the most frequent site of prostate cancer metastasis identified at autopsy in up to 90% of patients dying from prostate cancer bone metastasis [84, 85]. Although improving the treatment rate of prostate cancer localized to the prostate gland, 27 % of patients whose prostate cancer metastasized to distant organs live more than five years [2].

It is clear that the reason of prostate cancer mortality is not from the primary cancer burden but metastatic spread of the primary cancer cells to distant organs. The bone is the most frequent

site of prostate cancer metastasis due to the fact that the bone microenvironment supports fertile ground with high turnover rate and protection to the cancer cells described with the *"Seed & Soil"* theory [251, 252]. After occupying sites of highly active bone turnover, cancer cells start to manipulate and take control of the bone metabolism to make the environment more favorable place for tumor cells [253]. Prostate cancer cells have been shown to secrete the receptor activator of nuclear factor κ B ligand (RANKL), which causes differentiation of osteoclast precursor cells into active osteoclasts (i.e. bone degrading cells) [107]. Metastatic prostate cancer cells also secrete IL-8, TNF-α, and vascular endothelial growth factor (VEGF), which induce osteoclastogenesis (i.e. formation of osteoclasts) [109-111]. Activated osteoclasts cause localized degradation of the bone matrix in the cancer lesion, which causes a sharp drop in the environment pH down to as low as 4.5 [254]. Degradation of the bone matrix causes an increase in local Ca^{2+} concentration and the release of multiple growth factors such as transforming growth factor-β (TGF-β) and insulin-like growth factor (IGF) that support the growth and proliferation of prostate cancer cells [112]. Interestingly, prostate cancer cells have been shown to secrete multiple factors such as endothelin-1 (ET-1), bone morphogogenetic proteins (BMP), platelet-derived growth factor (PDGF), and parathyroid hormone-related protein (PTHrP) that directly and indirectly activate osteoblasts (bone-forming cells) to deposit new bone matrix at the resorption sites to form crystallized woven bone [98, 255]. This irregular bone formation or bone degradation forms defects on the bone structure leading to increase hydroxyapatite surface area [256]. Further, excess amount of bone formation harbors positively charges Ca^{2+} ions on apatite surface [257]. The enhancement of surface area and Ca^{2+} provide targeting possibilities to metastasized bone hydroxyapatite. All these activation processes of osteoblasts and osteoclasts by metastatic prostate cancer cells and

enhancement of cancer cell proliferation by the established osteolytic activity in the cancer lesion constitute a “vicious cycle” increases the proliferation of cancer cells [258].

According to the type of stimulating factors, either osteoclasts or osteoblasts can be active and determine whether the subsequent bone metastasis is osteolytic, osteoblastic, or in mix form. Each of these events involves significant molecular interactions between the tumor cells and the bone microenvironment cells cross-talks resulting in the disruption of normal bone processes [86, 88]. Prostate cancer is even radiographically characterized as osteoblastic. Recent molecular studies have showed that many bone metastases are mixed and contain both osteoblastic and osteolytic characteristics [98].

Current bone metastasis therapeutic options consist of systemic treatments such as hormone therapy and chemotherapy. In details, hormone therapy is also called androgen deprivation therapy (ADT) that relies on reducing level of male hormones that stimulate prostate cancer cells so the goal of ADT is to shrink the prostate cancer. Nevertheless, ADT is not completely cure prostate cancer and in a while the cells gain resistance against ADT. Whereas, the most effective chemotherapy is taxenes, which approved by FDA for the treatment of primary prostate cancer and hormone resistance prostate cancer. The principle action mechanism of taxenes is suppression of microtubule functions as stabilizing the microtubules so triggering of apoptosis by aberrant mitosis [259]. However, neither are more than palliative care to improve the quality of bone metastasized the patients’ life [260]. In addition, in the case of advanced metastatic disease various complications may be noticeable, such as osteolysis, spinal cord compression, hypercalcemia, increased fracture incidence, and permanent pain due to the fact that bone metabolism and microenvironment are disrupted and there is an imbalance between osteoblast and osteoclast activity [16, 113]. Moreover, around two-thirds of patients have suffered from bone

metastases complain about break-through pain, which is described as a simultaneous appearance of strong pain, despite of taking of strong pain killers and/or analgesics [114]. Therefore, pain is included in one of the skeletal-related events (SRE) of bone metastasis.

One of the clinically preferred therapeutics for bone metastatic cancer is bisphosphonates (BPs). Pamidronate, Risedronate, Alendronate, and Zolendronate are common BPs in the market containing nitrogen in their structures shown in **Figure 1.4**. This nitrogen content where located in a specific orientation of the backbone of the BPs makes these BPs are extremely potent and constitute a 'pharmacophore' [261]. Zolendronate is shown the most potent BP between all BPs because of contribution of nitrogen content and as well as hydrophobic binding pocket of imidiazole [262, 263]. In molecular level, BPs knock-down of prenylation of small GTPases like Rac, Ras, or Rab, which have a role on cholesterol synthesis, cytoskeletal organization, bone resorption, and cell morphology [128]. Inhibition of prenylation reduces the osteoclast activity and triggers apoptosis [129]. Because of these pharmacological effects, BPs reduce the resorptive capability of osteoclasts. In addition to BPs's antiresorptive role, BPs have direct functions such as antitumor [130], antiangiogenic [131], and antimigratory [132] effects. Further BPs are co-administered with doxorubicin, docetaxel and paclitaxel [116-119] as cocktail therapies for the treatment of bone metastasis. BPs are FDA-approved against osteoporosis, Paget's disease, pediatric bone diseases [264], multiple myeloma, breast cancer metastasis, or prostate cancer to bone [115] as an adjuvant therapy to prevent SRE for managing of metastatic bone pain, and lowering the risk of broken bones since BPs have potent inhibitor functions on osteoclast-mediated bone resorption via binding to the bone mineral and then is taken up by osteoclasts through fluid-phase endocytosis from acidified bone surface during osteolytic resorption [19].

Neither cancer chemotherapy nor BP-based cancer therapies demonstrate the desired level of therapeutic activity in terms of regressing tumor progression or increasing lifespan of bone metastasized patients [133]. These therapies have limitations such as environment mediated drug resistance in bone metastasis in the presence of plenty cytokines and growth factors [265] and not being able to achieve the desired drug concentration in bone because of lacking of bone targetebility. Due to drug resistance and inefficient chemotherapy concentration in metastasized bone, higher concentration of chemotherapy is employed which leading to non-specific systemic side effects [266]. These limitations may be addressed by targeted delivery to cancer lesions and specific cells in these lesions [149, 267] .

Recently, nano- and macromolecular-based approaches have attracted tremendous attention as drug delivery vehicles. These vehicles can accumulate into tumor tissue because of the enhanced permeation and retention (EPR) effect [242] and enhance the concentration of active drug in the tumor microenvironment while minimizing the systemic side effect of the drug. However, the drug dose that reaches the bone tumor microenvironment is usually low when only relying on passive targeting, resulting in the poor efficacy for tumor inhibition seen clinically. To further improve the specific targeting and delivery efficiency to bone metastasis, active targeting of nanomedicine approaches is essential. Furthermore, the excess of irregular bone formation or bone degradation due to the tumor cells effects on bone anatomy provides active targeting opportunities to metastasized tumor lesion in bone. BPs, acidic or phosphorylated peptides, as well as noncollagenous proteins have been used to carry higher amount of chemotherapeutics or imaging markers to identify metastatic lesions in bone [134, 135].

Segvich et. al identified specific peptide sequences (APWHLSSQYSRT, VTKHLNQISQSY and STLPIPHEFSRE) using the phage display that contains more than 10^9

bacteriophages expressing sequences against target bone-like mineral and hydroxyapatite disk [140]. These identified peptides are specifically designed for dual functions like adhering the apatite layer, whereas promoting cell adhesion with the cell recognition perspective so that these dual-functional peptides can improve bone tissue regeneration. After selection of interested peptide sequences, these peptides were further characterized with computational modeling and ELISA to identify the apatite-specific 12-mer peptide VTKHLNQISQSY (VTK) [140, 141]. After the identification of the 12-mer peptide, VTK, it was phosphorylated through the serine residue on VTK (pVTK) and characterized in terms of bio-mimetic apatite. pVTK had a 10-fold increase in adsorption to the apatite surface compared to VTK peptide. Furthermore, pVTK are able to inhibit the mineralization in pre-osteoblastic cells with a dose dependent response [142]. As conclusion, the logic of using pVTK as a bone targeted ligand, therapeutics encapsulated in pVTK-targeted particles might be delivered to metastasized lesion in bone efficiently. In addition, the direct effect in osteoblasts may also contribute to inhibition of the cross-talk between the tumor cells and osteoblasts.

Due to high affinity of BPs the bone apatite as mentioned previous, they are well-known and well-studied bone targeting small molecules other to carry therapeutics to bone in a carrier than their pharmacological activity in osteoclasts and cancer cells [135, 143, 150]. BPs are electrostatically adsorbed on bone apatite and chelate to the Ca^{2+} ions in the bone [268]. Once carriers are conjugated with BPs, they gain osteotropicity [150]. Therefore, particles conjugated with BPs not only carry therapeutics to metastasized bone to kill the cancer cells but also synergistic combination of decorated BPs on the particle to osteoclasts leading to slow-down osteoclasts resorption.

The main idea of bone targeted particles regardless of targeting ligand type is to deliver drugs to the targeted organ. However, there have been no investigation about specificity of these targeting ligands in terms of cellular internalization difference between the cells (cancer cells, osteoblasts, and osteoclasts) on a bone-like surface. As indicated before, different cancer cells interact with bone microenvironment in unique ways leading to variation in whether the tumor cells/bone become osteolytic, osteoblastic, or mixed form. For example, PC-3 prostate cancer is a known osteolytic character [269, 270], whereas C4-2B prostate cancer is in a mixed form of osteolytic and osteoblastic [271, 272]. Despite these differences, the internalization of bone-targeted particle into various tumor and bone cells through BLS has not been investigated, yet. We hypothesize that the internalization rate of bone targeted particles (peptide or BP) could be different on BLS compared to regular tissue culture plate surfaces, perhaps due to the cells manipulating BLS.

To the best of our knowledge there is no comparison between peptide (pVTK)- and BP-targeted particles despite their individual importance on bone targeting in different cell lines on BLS. To test the cellular level targetibility differences of pVTK vs BP, we report the synthesis of two different novel bone-targeted particles with pVTK- or BP-based, pH sensitive "smart" particles **(Figure 4.1)**. In our previous study we developed shell-cross-linked, pH-sensitive polymeric micellar particles containing a triblock copolymer composed of a hydrophilic poly(ethylene glycol) (PEG) block, a central poly(acrylic acid) (PAA) block, and a hydrophobic poly(methyl methacrylate) (PMMA) block [273]. We loaded the non-targeted "smart" particles with a model drug and showed amenable drug release kinetics and high biocompatibility. In the present work, we functionalized these particles with a PEG block targeted by either pVTK or BP, which has a unique function like directing and accumulating the *"smart"* particles in metastasized

bone. We evaluated the physicochemical characterization of varying percentages (5, 10, and 20%) ligands on either pVTK or BP-targeted particles. We compared the binding capability of FITC-labeled pVTK and BP particles upon incubation in aqueous buffer with bone powder at pH 7.4 as a function of targeting ligand density. To test our hypothesis, we investigated the uptake of FITC-labeled, pVTK and BP-decorated particles into PC-3/C4-2B prostate cancer cells, MC3T3 pre-osteoblasts, RAW 264.7 macrophages, and activated RAW 264.7 osteoclast cells versus non-targeted control particles. We measured the uptake of these particles into cells cultured on regular culture plates versus BLS. We also encapsulated an anti-cancer agent, Cabazitaxel (CTX), into the core of non-targeted, pVTK-, or BP-decorated particles. Finally, we explored the therapeutic effect of CTX-loaded non-targeted, pVTK, or BP-targeted particles on the following four cell lines on BLS: PC-3, C4-2B, MC3T3, RAW 264.7, and RANKL activated RAW 264.7 cells.

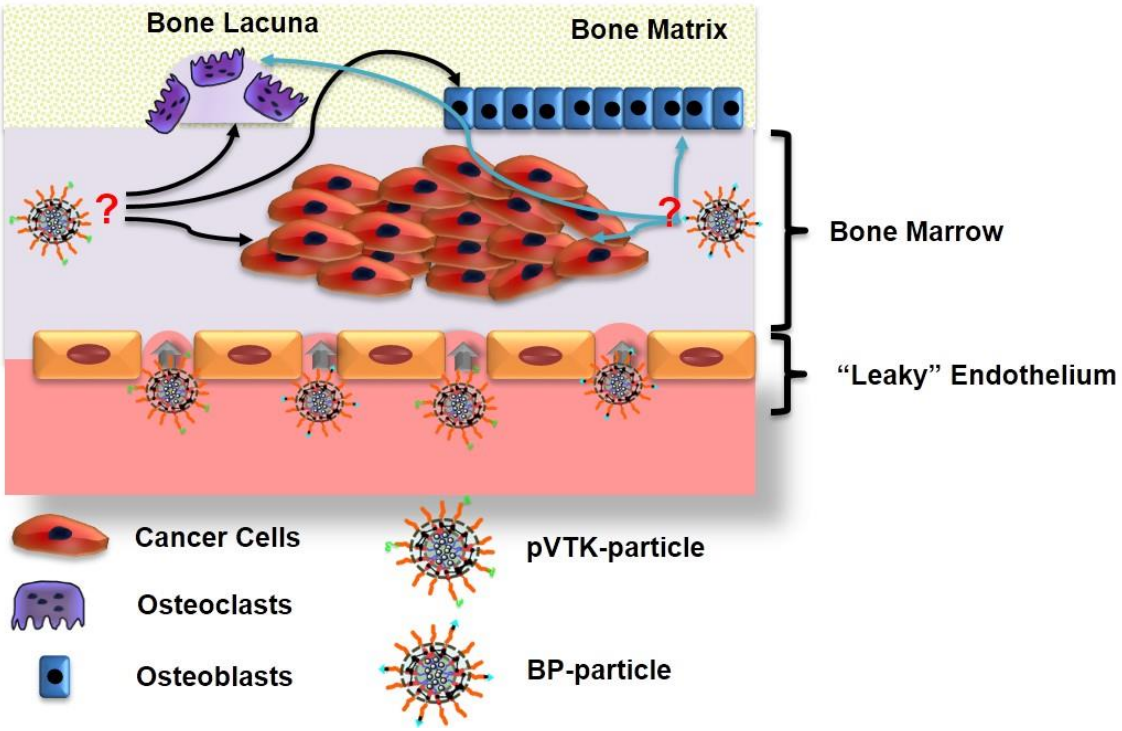

Figure 4.1 The hypothesized M-pVTK and M-BP nanomedicine-based therapies to modulate cancer cells in bone microenvironment.

4.2 Experimental Section

4.2.1 Materials

Cabazitaxel (CTX) was purchased from Selleckchem (Houston, US). Imidazole 4-carboxylic acid (Ark Pharma Inc, USA), tert-butyl-3-bromopropionate (Sigma-Aldrich), potassium hydroxide (KOH, Sigma-Aldrich), phosphorus pentachloride (PCl_5, Sigma-Aldrich), *N*,*N*-diisopropylethylamine (DIPEA, Alfa Aesar), 4-pentynoic acid (Aldrich, 98%), *N*,*N*′-dicyclohexylcarbodiimide (DCC, TCI chemicals), N-(3-dimethylaminopropyl)-N′-ethylcarbodiimide hydrochloride (EDC, Sigma-Aldrich), 2-(N-morpholino)ethanesulfonic acid (MES, Sigma-Aldrich) N-hydroxy succinimide (NHS, Fluka), 4-dimethylaminopyridine (DMAP, Sigma-Aldrich, 99%), trifluoroacetic acid (TFA, Acros chemicals, 99 %), phosphonic acid

(H_3PO_3, Sigma-Aldrich), phosphonic oxychloride ($POCl_2$, Alfa Aesar), chlorobenzene (Alfa Aesar), anhydrous tetrahydrofuran (THF, Sigma-Aldrich, >99.9 %), methyl methacrylate (Sigma-Aldrich, MMA, 99 %), *tert*-butyl acrylate (*t*BA, Sigma-Aldrich, *t*BA, 98 %), and N, N, N', N'', N''-pentamethyldiethylenetriamine (PMDETA, Sigma-Aldrich, 99 %) were first purified by passing through a basic alumina column to remove the added inhibitor before using. 1,4-Dioxane (Anhydrous, Sigma-Aldrich), triethylamine (TEA, Sigma-Aldrich, ≥99%), 98%), 4-pentynoic acid (Sigma-Aldrich, 99 %), sodium hydride (NaH, Sigma-Aldrich, 60% dispersion in mineral oil, washed with hexane before use). Poly(ethylene glycol) monomethylether (PEG, M_n: 5000 g/mol, Sigma-Aldrich), α-NHS-ω-Alkyne PEG (M_n: 5000 from Rapp Polymere, Germany). Copper (I) bromide (CuBr, Sigma-Aldrich, 99.9%), sodium azide (NaN_3, Acros Chemicals), 1-ethyl-3-(3-dimethylaminopropyl)carbodiimide HCl (EDC.HCl, Aldrich), hydroxybenzotriazole (HOBt, Sigma-Aldrich), triethylamine (TEA, Sigma-Aldrich), tetrahydrofuran anhydrous (THF, Sigma-Aldrich, >99.9 %), dichloromethane anhydrous (DCM, Sigma-Aldrich, >99.9 %), N-N-dimethylformamide anhydrous (DMF, Sigma-Aldrich, >99.9 %), resazurin sodium salt (Sigma-Aldrich), hydroxyapatite (HA, Sigma-Aldrich, reagent grade powder), Trizma® Pre-set crystals (pH: 7.5, Sigma-Aldrich), *p*VTK-NH_2 (targeting ligand made with 12 amino acids, phosphorilated VTKHLNQISQSY, GeneScript, NJ, US) were used as received.

4.2.2 Instruments

All the polymer blocks, the acid-labile linker and the micelles were characterized by nuclear magnetic resonance spectroscopy (NMR) at room temperature. ^{1}H NMR and ^{13}C NMR spectra of 5–10 % (w/w) solutions in $CDCl_3$, DMSO-d6 or D_2O were recorded on 400, 500 and 700 MHz Varian Mercury systems (Palo Alto, CA) at room temperature, respectively. NMR

spectra were referenced using Me_4Si (0 ppm), residual $CHCl_3$ (δ ^{1}H-NMR 7.26 ppm, ^{13}C-NMR 77.0 ppm, CD_3SOCD_3 (δ ^{1}H-NMR 2.49 ppm, ^{13}C-NMR 39.5 ppm and D_2O (δ ^{1}H-NMR 4.56 ppm).

Gel permeation chromatography measurements were obtained from a Viscotek GPCmax Autosampler system consisting of a pump and Water 2414 refractive index (RI) detector. The molecular weight and molecular weight distribution of final polymers were determined based on their elution volume on an Styragel HR 4E column compared to a series of poly(methyl methacrylate) standards (PolyAnalitik Inc, Canada) using THF as a mobile phase at a flow rate of 1 ml/min at 35 ^{o}C. Data were analyzed using Viscotek OmniSEC Omni-01 software.

Perkin-Elmer FT-IR Spectrum 4100 type A was used in determination of the formation of the azide function group.

Dynamic Light Scattering (DLS) 90Plus particle size analyzer (Brookhaven Instruments Corporation, Holtsville, NY) was used to measure micelles size and surface charge of the micelles.

4.2.3 Synthesis of non-targeted, pVTK targeting, and BP-targeting amphiphilic copolymers

4.2.3.1 Synthesis of PMMA-Br (1)

The hydrophobic PMMA block was synthesized by ATRP reaction by following our published protocol [273]. Briefly, the MMA monomer (30 mL, 282 mmol), CuBr catalyst (202 mg, 1.41 mmol), PMDETA (294 mg, 1.41 mmol), ethyl-2-bromoisobutyrate as initiator (207 µL, 1.41 mmol), and 30 mL of toluene were introduced into a Schlenk tube and the reaction mixture was degassed by three freeze–pump–thaw cycles. The reaction mixture was then placed in a temperature-controlled oil bath at 40 °C for 21 min **(Figure 4.2)**. After the given time, the polymerization mixture was diluted with THF, passed through a neutral alumina column to remove

the copper complex. THF was removed by rotary evaporation and the mixture was precipitated in hexane. PMMA-Br **(1)** *Conversion*: 30%, $M_{n,NMR}$ = 5201 g/mol.

^{1}H NMR of the PMMA block (700 MHz, $CDCl_3$): δ 1.12 (3H, CH_3-CH_2-O-CO-C(CH_3)$_2$, H_a), 1.60 (6H, O-CO-C(CH_3)$_2$, H_c), 1.80 (s, 3H, CH_2-C-CH_3, H_e), 1.80-2.00 (2H, CH_2-C(CH_3)-CO, H_d), 3.57 (s, 3H, CH_3-O-CO, H_f), 4.08 (2H, CH_3-CH_2-O-CO-C(CH_3)$_2$, H_b); ^{13}C NMR (175 MHz, $CDCl_3$): δ 14.10 (C_a), 16.44, 18.74, 22.64 (C_d), 25.25, 29.04, 31.57 (C_h), 34.64, 40.82 (C_e), 44.53, 44.88 (C_f), 51.80 (C_j), 54.37 (C_g), 60.04 (C_b), 68.0 ($C_{g\text{-}Br}$), 176.97 (C_c), 177.78 (C_i), 178.09 (C_i).

4.2.3.2 Synthesis of PMMA-b-PtBA-Br copolymer (2)

The PMMA block was used as a macro initiator for block copolymerization with *tert*-butyl acrylate to obtain PMMA-*b*-P*t*BA block copolymer. Briefly, PMMA-Br (**1**, 2.22 g, 0.5 mmol), CuBr (72 mg, 0.5 mmol), PMDETA (104 µL, 0.5 mmol), *t*BA (7.32 mL, 50 mmol), and 18.3 mL toluene were introduced into a Schlenk tube and the reaction mixture was degassed by three freeze–pump–thaw cycles. The reaction mixture was then placed in a temperature-regulated oil bath at 80 °C for 6 h. The reaction mixture cooled down to room temperature and diluted with THF before passing through a neutral alumina column to remove the copper complex, THF was removed by rotary evaporation and the mixture was precipitated in cold methanol/water (80/20 v/v) to obtain PMMA-*b*-P*t*BA-Br **(2)**. In the ^{1}H NMR we found 21 <u>CH</u> protons of P*t*BA polymer indicating that we were able to attach 21 *t*BA units. $M_{n,NMR}$: 7892g/mol.

^{1}H NMR of the PMMA-*b*-PtBA-Br block copolymer (700 MHz, $CDCl_3$): δ 1.22 (3H, CH_3-CH_2-O-CO-C(CH_3)$_2$, H_a), 1.52 (6H, O-CO-C(CH_3)$_2$, H_c), 1.42 (s, 9H, -C-(CH_3)$_3$, H_i), 1.80 (s, 3H, CH_2-C-CH_3, H_e), 1.80-1.94 (2H, CH_2-C(CH_3)-CO, H_d), 1.96 (CH_2<u>C*H*</u>-CO, H_h), 2.24 (<u>CH_2</u>CH-CO, H_g), 3.57 (s, 3H, CH_3-O-CO, H_f), 4.08 (3H, CH_3-CH_2-O-CO-C(CH_3)$_2$, H_b & H_h-Br); ^{13}C NMR

(175 MHz, $CDCl_3$): δ 16.29 (C_a), 18.60, 27.57 (C_h), 27.89 (C_n),27.96 (C_d), (29.56, 29.90, 30.206 C_g), 37.25 (C_e), (41.28, 41.76, 42.21, (C_l), 44.41, 44.53 (C_k), 44.75, 45.40 (C_f), 51.70, 52.42, 52.58 (C_j), 53.30, 54.10, 54.27, 54.32, 60.38 (C_b), 80.21 (C_o), (173.82, 174.07 (C_c), (176.85, 177.01, 177.68 (C_m), (177.95, 177.98, 178.27 (C_i).

4.2.3.3 Synthesis of azide functionalized PMMA-b-PtBA-N_3 copolymer (3)

The terminal Br groups in PMMA-*b*-P*t*BA-Br polymer were converted to azide by reacting with excess NaN_3 to allow *"click"* coupling to the alkyne-functionalized PEG block. Accordingly, PMMA-*b*-P*t*BA-Br (**2**, 1 g, 1.25 x 10^{-1} mmol) and 20 equivalents of NaN_3 (0.16 g, 2.5 mmol) were stirred together in DMF at 50 °C for 24 h. The polymer was dissolved in DCM, extracted with water followed by reverse extraction of the water phase with DCM, combined the organic layers, washed with brine solution and dried over Na_2SO_4. Finally, the organic layer was evaporated to obtain the PMMA-*b*-P*t*BA-N_3 **(3)**. $M_{n,GPC}$ = 10,073 g/mol, M_w/M_n = 1.18.

^{1}H NMR of the PMMA-*b*-P*t*BA-N_3 block co-polymer (700 MHz, $CDCl_3$): δ 1.12 (3H, CH_3-CH_2-O-CO-C(CH_3)$_2$, H_a), 1.24 (6H, O-CO-C(CH_3)$_2$, H_c), 1.42 (s, 9H, -C-(CH_3)$_3$, H_i), 1.80 (s, 3H, CH_2-C-CH_3, H_e), 1.80-1.94 (2H, CH_2-C(CH_3)-CO, H_d), 1.96 (CH_2CH-CO, H_h), 2.24 (CH_2CH-CO, H_g), 3.57 (s, 3H, CH_3-O-CO, H_f), 4.08 (3H, CH_3-CH_2-O-CO-C(CH_3)$_2$, H_b); ^{13}C NMR (175 MHz, $CDCl_3$): δ 16.42 (C_a), 18.60, 27.92 (C_h), 27.97 (C_n), 28.06 (C_d), 38.21 (C_e), (41.37, 41.82, 42.28 C_g), (44.52, 44.62 (C_k), (44.84, 44.87 (C_f), 51.77 (C_j), 52.47, 53.38 (C_l), 54.17, 54.36, 60.46 (C_b), 80.30 (C_o), (174.11 (C_c), (176.94, 177.10 (C_m), (177.76, 178.02, 178.06 (C_i).

4.2.3.4 Synthesis of Alkyne-PEG (3a)

Commercially available 5 kDa PEG-OH (5.0 g, 1 mmol) and 4-pentynoic acid (147 mg, 1.5 mmol) were dissolved in DCM (25 mL) and added DMAP (122 mg, 1 mmol), DCC (310 mg, 1.5 mmol) in DCM (25 mL) at room temperature and stirred for overnight. The salts were filtered;

the filtrate was concentrated and precipitated in diethyl ether (3 x 500 mL) to obtain compound **(3a)** in 3.6 g with 71% yield and 92 % functionalization efficiency.

^{1}H NMR (500 MHz, $CDCl_3$): δ 1.93 (s, 1H, alkyne proton), 2.38-2.60 (m, 10H, $CH_2C\mathit{H_2}$-CO-O), 3.17 (s, 2H), 3.30 (s, 3H, O-C$\mathit{H_3}$), 3.40-3.80 (bs, 450H, O$C\mathit{H_2}C\mathit{H_2}$), 4.18 (s, 2H CO-O-$CH_2$-C$\mathit{H_2}$-O); ^{13}C NMR (125 MHz, $CDCl_3$): δ 14.07, 33.00, 58.78, 63.58, 68.43, 68.81, 69.43, 69.82, 70.32, 71.26, 71.68, 72.21, 82.19, 106.38, 138.94, 157.07, 171.46. MALDI $[M]^+$ *Alkyne-poly(ethylene glycol)* obsd 5008.

4.2.3.5 Synthesis of PMMA-b-PtBA-PEG (4)

PEG-Alkyne (**3a**, 476 mg, 9.52 x 10^{-2} mmol, 1.1 equivalent), PMMA-*b*-P*t*BA-N_3 (**3**, 710 mg, 8.65 x 10^{-2} mmol, 1 equivalent), CuBr (15.1 mg, 1.05 x 10^{-1} mmol, 1.2 equivalent), PMDETA (21.9 μL, 1.05 x 10^{-1} mmol, 1.2 equivalent), and 6 mL of DMF were introduced into a Schlenk tube and the reaction mixture was degassed by three freeze-pump-thaw cycles and stirred at room temperature for 48 h. The reaction mixture was diluted with THF, passed through a neutral alumina column to remove the copper complex, and the polymer was transferred into dialysis cassette (MWCO 7 kDa) and dialyzed for 1 day against DI water and lyophilized to obtain crude polymer. The polymer product was dissolved in DCM and precipitated several times in a hexane to remove unreacted PEG material. The molecular weight of the PMMA-*b*-P*t*BA-*b*-PEG polymer **(4)** was calculated as 12,900 g/mol using ^{1}H NMR data.

^{1}H NMR (500 MHz, $CDCl_3$) δ 6.96 (bs, 1H, triazole ring proton), 4.25 ($CH_2C\mathit{H}$-triazole and CO-O-C$\mathit{H_2}$), 4.05 (2H, CH_3-C$\mathit{H_2}$-O-CO), 3.64 (bs, O-C$\mathit{H_2}$-C$\mathit{H_2}$), 3.59 (s, CO-O-CH_3), 3.38 (s, 3H, CH_2-CH_2-O-C$\mathit{H_3}$), 3.05 (2H, triazole-C$\mathit{H_2}$-CH_2-CO-O), 2.76 (2H, triazole-CH_2-C$\mathit{H_2}$-CO-O), 2.26 (CH_2-CH-CO), 1.93-0.83 (6H, O-CO-C($C\mathit{H_3}$)$_2$, CO-O-C($C\mathit{H_3}$)$_3$, $\mathit{CH_2}$-C$\mathit{CH_3}$).

4.2.3.6 Boc deprotection from PMMA-b-PtBA-b-PEG (5)

PMMA-*b*-P*t*BA-*b*-PEG (**4**, 20 mg, 0.0014 mmol), was dissolved in DCM (2 mL) and added TFA (1.5 mL) at 0 °C and stirred at room temperature for overnight. The solvents were evaporated on rotavapor (40 °C) and the residue was transferred into dialysis bag (MWCO 1 kDa) and dialyzed for 1 day against DI water and lyophilized to obtain PMMA-*b*-PAA-*b*-PEG copolymer **(5)**, in 18 mg, 94% yield.

^{1}H NMR (700 MHz, $CDCl_3$): δ 6.92 (bs, 1H, triazole ring proton), 4.25 ($CH_2C\mathit{H}$-triazole and CO-O-C$\mathit{H_2}$), 4.05 (2H, CH_3-C$\mathit{H_2}$-O-CO), 3.64 (bs, O-C$\mathit{H_2}$-C$\mathit{H_2}$), 3.59 (s, CO-O-CH_3), 3.38 (s, 3H, CH_2-CH_2-O-C$\mathit{H_3}$), 3.05 (2H, triazole-C$\mathit{H_2}$-CH_2-CO-O), 2.76 (2H, triazole-CH_2-C$\mathit{H_2}$-CO-O), 2.26 (CH_2-CH-CO), 1.93-0.83 (6H, O-CO-C($C\mathit{H_3}$)$_2$, $\mathit{CH_2}$-C$\mathit{CH_3}$). The molecular weight of the PMMA-*b*-PAA-*b*-PEG copolymer **(5)** are $M_{n,NMR}$ = 11,722 g/mol.

4.2.3.7 Synthesis of PMMA-b-PtBA-b-PEG-NHS copolymer (6)

Compound PMMA-*b*-P*t*BA-N_3 polymer (**3**, 60 mg, 5.12 x 10^{-2} mmol per azide unit), CuBr (11 mg, 7.68 x 10^{-2} mol), PMDETA (16 µL, 1.45 x 10^{-7} mmol) and commercially available Alkyne-PEG-NHS (40 mg, 8.04 x 10^{-3} mmol) in DMF (3 mL) was added into a schlenck tube (25 mL) under argon atmosphere. The mixture was degassed by three freeze–pump–thaw cycles and stirred at room temperature for 2 days. After the given time, the reaction mixture was diluted with THF and passed through a neutral alumina column to remove the copper complex and evaporated the solvent by rotary evaporator. The mixture was precipitated in cold diethyl ether. After decantation of ether, material was dried under air, then dissolved in DCM and hexane was added into it until it gets cloudy (precipitated), obtained PMMA-*b*-P*t*BA-*b*-PEG-NHS **(6)** in 70 mg, 70% yield.

^{1}H NMR (500 MHz, $CDCl_3$, δ): 0.80 (s, 50H, H_c), 0.88 (s, 3H), 0.98 (s, 26H, H_e), 1.08 (s, 3H), 1.14-1.24 (t, 6H, including H_a), 1.29 (s, 8H), 1.39 (bs, 199H, Hi), 1.77 (bs, 35H, H_d), 1.82-

2.04 (m, 27H), 2.18 (bs, 20H, H_g), 2.28 (bs, 15H, Hg), 2.36 (t, 6H, *J* = 7.0 Hz), 2.48 (t, 2H, *J* = 2.0 Hz), 2.54 (t, 2H, *J* = 2.0 Hz), 2.90 (s, 3H), 2.99 (s, 4H), 3.34-3.50 (m, 14H), 3.55 (s, 96H, H_f), 3.60 (s, 450H, PEG protons, H_l), 3.74 (t, 8H, *J* = 5.0 Hz, H_k), 4.04 (t, 2H, *J* = 6.0 Hz, H_b), 4.19 (t, 1H, *J* = 5.0 Hz, H_h), 7.46 (bs, 1H, H_j); ^{13}C NMR (125 MHz, $CDCl_3$): δ 14.73 (C_a), 16,35, 18.64, 24.99 (C_c), 27.85, 27.94, 28.01 (all 3 belongs to Boc carbons, C_i), 29.59 (C_e), 35.05, 35.27 (C_g), 35.59, 37.11, 39.10, 3917, 41.29, 41.76, 42.22, 44.44, 44.79, 51.69 (C_f), 52.56, 54.11, 54.31 (C_d), 60.38 (C_b), 68.44 (C_k), 69.71, 69.78, 69.87, 70.00, 70.10 (C_l), 70.33, 70.45, 72.46 (Ch), 80.23 (Boc quaternary carbon), 173.85 (C_3), 174.07, 176.85 (C_1), 177.68 (C_2), 177.97 (C_4).

4.2.3.8 Synthesis of PMMA-b-PtBA-b-PEG-pVTK polymer (7)

PMMA-*b*-P*t*BA-*b*-PEG-NHS (**6**, 27 mg, 2.16 x 10^{-3} mmol) was dissolved in DMF (1.5 mL) and added EDC (1.24 mg, 6.48 x 10^{-3} mmol), HOBt (0.87 mg, 6.48 x 10^{-3} mmol), and DIPEA (2.25 µL 1.29 x 10^{-2} mmol) and stirred for 15 min. *p*VTK (5.45 mg, 2.59 x 10^{-3} mmol) was dissolved in DMSO (1 mL) and added slowly, drop wisely and stirred at room temperature for 2 h then heated to 35 °C for 2 days. After the given time, the mixture was cooled down to room temperature diluted with DI water (2 mL) and transferred into dialysis cassette (MWCO 7 kDa) and dialyzed against deionized water for 24 h followed by lyophilization to obtain PMMA-*b*-P*t*BA-*b*-PEG-pVTK copolymer **(7)** in 28 mg, 90% yield.

^{1}H NMR (700 MHz, CD_3SOCD_3): δ 0.73 (s, 50H, H_c), 0.84 (s, 12H, valine CH_3), 0.93 (s, 26H, H_e), 1.06 (s, 3H), 1.22 (s, 16H, including H_a), 1.29 (s, 8H), 1.38 (bs, 200H, Hi), 1.60-2.04 (m, 75H, including H_d), 2.04-2.20 (m, 20H), 2.22-2.30 (m, 20H, H_g), 2.30-2.34 (m, 12H), 2.34-2.44 (m, 6H), 2.58 (bs, 2H), 2.72 (m, 2H), 2.79 (s, 3H), 2.93 (s, 4H), 3.14-3.24 (m, 14H), 3.35-3.45 (m, 100H, H_f), 3.45-3.75 (s, 450H, PEG protons, H_l), 3.78-3.84 (m, 8H, H_k), 4.02 (t, 2H, *J* = 5.0 Hz, H_b), 4.19 (t, 1H, H_h), 4.74 (s, 1H), 5.03 (s, 1H), 5.31 (s, 1H), 5.54 (s, 2H), 5.63 (s, 4H),

6.46-8.50 (m, 14H, including H_j); ^{13}C NMR (175 MHz, CD_3SOCD_3): δ 13.92, 14.17 (C_a), 16.06, 16.24, 18.43, 22.07, 24.43, 24.86 (C_c), 25.08, 26.58, 27.46, 28.44, 28.55, 28.68, 28.83 (all 6 belongs to Boc carbons, C_i), 29.01, 29.46 (C_e), 31.27, 33.46, 33.57, 34.06, 35.08 (C_g), 36.60, 38.56, 40.81, 41.47, 43.87, 44.25, 51.70 (C_f), 53.76 (C_d), 60.08 (C_b), 62.62, 63.06, 64.12, 65.46, 66.94, 69.10 (C_k), 69.27, 69.42, 69.59, 69.65, 69.77, 70.46, 71.20 (PEG carbons, C_l), 72.47 (Ch), 79.92 (Boc quaternary carbon), 83.72, 109.90, 118.90, 124.06, 126.32, 127.66, 129.61, 142.84, 169.99, 170.28, 171.01, 171.58(C_3), 172.93, 173.21, 173.77, 176.13 (C_1), 177.09 (C_2), 177.33 (C_4); ^{31}P NMR (283 MHz, CD_3SOCD_3): δ 2.04.

4.2.3.9 Synthesis of PMMA-b-PAA-b-PEG-pVTK polymer (8)

PMMA-*b*-P*t*BA-*b*-PEG-pVTK copolymer (**7**, 22 mg, 1.51 x 10^{-3} mmol) was dissolved in DCM:TFA (1.5:1, 3 mL) and stirred at 0 °C for 2 h, later stirred at room temperature for another 2 h. The solvents were evaporated by rotary evaporation (temperature 30 °C) and added DCM (2 mL) several times and evaporated until there is no TFA left. Finally, the compound was dissolved in double distilled water/THF mixture and transferred into dialysis cassette (MWCO 7 kDa) and dialyzed against deionized water for 24 h followed by lyophilization to obtain PMMA-*b*-PAA-*b*-PEG-pVTK copolymer **(8)** in 18 mg, 90% yield.

^1H NMR (700 MHz, $CDCl_3$): δ 0.75-0.90 (bs, 69H, H_c, Valine CH_3), 1.00 (bs, 26H, H_e), 1.11 (s, 4H), 1.24 (s, 110H, including H_a), 1.36-145 (m, 16H), 1.61 (bs, 15H), 1.74-2.06 (m, 50H, including H_d), 2.22-2.60 (m, 16H, H_g), 2.96 (s, 3H), 3.04 (s, 4H), 3.42-3.54 (m, 100H, H_f), 3.54-3.75 (s, 450H, PEG protons, H_l), 3.86-3.94 (m, 8H, H_k), 3.98-4.24 (m, 16H, including H_b), 4.32-4.64 (m, 7H, including H_h), 4.88 (bs, 1H), 5.02 (s, 1H), 5.28 (s, 1H), 5.33 (s, 2H), 6.03 (s, 2H), 6.54-7.12 (m, 6H), 7.30-8.50 (m, 20H, including H_j, COOH peaks); ^{13}C NMR (175 MHz, $CDCl_3$): δ 13.99, 14.88 (C_a), 16.45, 18.73, 22.63, 24.85 (C_c), 25.15, 27.16, 27.86, 29.07, 29.19, 29.30,

29.40, 29.69 (C_e), 31.86, 32.68, 33.53, 33.96, 34.09, 34.99, 35.71, 35.84 (C_g), 37.32, 37.60. 39.50, 41.37, 44.51, 44.85, 45.48, 51.77 (C_f), 52.50, 53.38 (C_d), 54.13, 54.37, 60.48 (C_b), 63.29, 64.50, 64.73, 65.08, 65.56, 66.00, 67.41, 67.99, 68.33, 68.53, 69.57 (C_k), 69.93, 70.15, 70.42 (PEG carbons, C_l), 71.36, 72.30, 73.24, 75.99, 82.64, 114.38, 114.71, 116.03, 127.73, 129.61, 129.81, 129.87, 130.00, 159.21, 172.05, 173.88, 174.19, 174.26, 176.14, 176.96, 177.12, 177.77, 178.07, 178.36; ^{31}P NMR (283 MHz, $CDCl_3$): δ -20.22. The approximate molecular weight of PMMA-*b*-PAA-*b*-PEG-pVTK is 13190.

4.2.3.10 Synthesis of 1-(3-(tert-butoxy)-3-oxopropyl)-1H-imidazole-4-carboxylic acid (9)

N-alkylation of Imidazole 4-carboxilic acid was carried out according to known method with some modifications [274]. Commercially available imidazole 4-carboxilic acid (0.25 g, 2.23 mmol) was dissolved in DI water (3 mL) and added KOH (0.375 g, 6.69 mmol) at room temperature and stirred for 3 h. After the given time, water was evaporated by rotary evaporation and dried over high vacuum. The residue was dissolved in DMSO:1,4 Dioxane (4:1, 5 mL) and added DIPEA (1.16 mL, 6.69 mmol) followed by *ter*t-butylbromo-propionate (0.74 mL, 4.46 mmol) at room temperature and stirred at 50 °C for 24 h. After the given time, the reaction mixture was cooled down to 0 °C, and neutralized with 1 N HCl and extracted twice with chloroform:*iso*-propanol mixture (8:2, 100 mL). The combined organic layer was washed with brine (25 mL) and dried over Na_2SO_4. The solvents were evaporated; residue was purified by precipitation method (THF: Hexane, 1:10) afforded undesired compound **(9a)**, in 0.3 g, 73% yield.

^{1}H NMR (400 MHz, DMSO-d6): δ 2.07 (t, 2H, *J* = 10.5 Hz, 1CH_2, H_d), 2.53 (t, 2H, *J* = 10.5 Hz, 1CH_2, H_c), 7.30 (bs, 1H, H_a), 7.55 (bs, 1H, H_b). ESI-MS $[M-H]^-$ $C_7H_7N_2O_4$ calcd 183.04, obsd 183.03.

We also tried other neutralization methods like using citric acid, Amberilite 120 H+ resin, could not serve the purpose. Later, we adopted a simple method; evaporating organic solvents on rotary evaporator and air dry to obtain solid 1-(3-(tert-butoxy)-3-oxopropyl)-1H-imidazole-4-carboxylic acid (**9**). This dry material was used for further reaction without purification. A portion of the crude material (20 mg) was purified for analytical confirmation purpose. The material was dissolved in chloroform:*iso*-propanol (7:3) and purified by preparative column chromatography using chloroform:*iso*-propanol (7:3) afforded compound **(9)**, in 12 mg, 70% yield. The yield is based on recovered pure material after column chromatography.

^{1}H NMR (700 MHz, DMSO-d6): δ 1.36 (s, 9H, C-($\underline{CH_3}$)$_3$, H_e), 2.71 (bs, 2H, CH_2, H_d), 4.12 (bs, 2H, CH_2, H_c), 7.30 (bs, 1H, Ar-C$\underline{H}$, H_a), 7.45 (bs, 1H, Ar-C$\underline{H}$, H_b); ^{13}C NMR (175 MHz, DMSO-d6): δ 27.67 (C_e), 36.26 (C_d), 42.16 (C_c), 80.43 (C_f), 121.08 (C_a), 136.24 (C_b), 141.49 (C_i), 166.07 (C_h), 169.93 (C_g). HR-MS $[M+H]^+$ $C_{11}H_{17}N_2O_4$ calcd 241.1188, obsd 241.1186.

4.2.3.11 Synthesis of tert-butyl 3-(4-(chlorocarbonyl)-1H-imidazol-1-yl)propanoate (10)

Compound **(9)** (20 mg, 0.083 mmol) was dissolved in DMSO (1.5 mL) and added PCl_5 (86 mg, 0.416 mmol) at room temperature and stirred for 4 h. After the given time, the material was used for further coupling reaction. A portion of the material (8 mg) was purified for analytical confirmation purpose. The material was dissolved in chloroform:*iso*-propanol (7:3) and purified by preparative column chromatography using chloroform:*iso*-propanol (7:3) afforded compound **(10)**, in 5 mg, 70% yield. The yield is based on recovered pure material after column chromatography.

^{1}H NMR (700 MHz, DMSO-d6): δ 1.28 (s, 9H, C-(CH_3)$_3$, H_e), 2.92 (bs, 2H, CH_2, H_d), 4.22 (bs, 2H, CH_2, H_c), 8.45 (bs, 1H, Ar-C$\underline{H}$, H_a), 9.45 (m, 1H, Ar-C$\underline{H}$, H_b). ESI-MS $[M+K]^+$ $C_{11}H_{15}ClKN_2O_3$ calcd 297.0408, obsd 295.2877.

4.2.3.12 Synthesis of Alk-PEG-NHBoc (11)

Commercially available 5 kDa BocHN-PEG-NH_2 (500 mg, 0.1 mmol) and 4-pentynoic acid (49mg, 0.5 mmol) were dissolved in DMF (7 mL) and added DIPEA (87 µL, 0.5 mmol) followed by EDC (38 mg, 0.2 mmol) at room temperature and stirred for overnight. The reaction mixture was precipitated in DCM/diethyl ether, then in THF/Hexane to obtain compound **(11)** in 430 mg, 86% yield; functionalization efficiency: 92 %.

^{1}H NMR (700 MHz, $CDCl_3$): δ 1.32 (a, 9H, C-($\underline{CH_3}$)$_3$, H_f), 1.92 (t, 1H, alkyne proton, *j* = 2.1 Hz, H_a), 2.29 (t, 2H, $\underline{CH_2}$, *j* = 7.0 Hz, H_b), 2.39 (t, 2H, $\underline{CH_2}$, *j* = 7.0 Hz, H_c), 2.62 (bs, 2H), 3.19 (d, 2H, HN-$\underline{CH_2}$, *j* = 4.2 Hz, H_d), 3.32-3.36 (m, 2H, $CH_2C\mathit{H_2}$-CO-O), 3.40-3.65 (m, 450H, $OC\mathit{H_2}C\mathit{H_2}$, H_e), 5.02 (bs, 1H), 6.41 (bs, 1H, N$\underline{H}$); ^{13}C NMR (175 MHz, $CDCl_3$): δ 14.45 (C_c), 28.08 (C_i), 34.74 (C_d), 38.90 (C_f), 39.97 (C_k), 68.97 (C_j), 69.43 (C_a), 69.811, 69.86, 70.19 (C_g), 70.91, 82.76 (C_b), 155.8 (C_h), 170.62 (C_e). MALDI $[M]^+$ Alk-PEG-NHBoc, obsd 5009.19. Note: Boc group might not survive during the analysis.

4.2.3.13 Synthesis of Alk-PEG-NH_2 (12)

Compound **(11)** (300 mg, 0.0059 mmol) was dissolved in DCM (12 mL) and added TFA (6 mL) at 0 °C and stirred at room temperature for overnight. The solvents were evaporated by rotary evaporation (40 °C) and the residue was transferred into dialysis bag (MWCO 1 kDa) and dialyzed for 1 day against DI water and lyophilized to obtain compound **(12)**, in 260 mg, 94% yield.

^{1}H NMR (700 MHz, $CDCl_3$): δ 1.96 (t, 1H, alkyne proton, *j* = 2.1 Hz, H_a), 2.34 (t, 2H, $\underline{CH_2}$, *j* = 7.0 Hz, H_b), 2.44 (dt, 2H, $\underline{CH_2}$, *j* = 7.0, 2.1 Hz, H_c), 3.11 (bs, 2H, HN-$\underline{CH_2}$, H_d), 3.36-3.40 (m, 2H, $CH_2C\mathit{H_2}$-CO-O), 3.42-3.72 (m, 450H, $OC\mathit{H_2}C\mathit{H_2}$, H_e), 5.26 (bs, 1H), 6.43 (bs, 1H, N$\underline{H}$), 7.55 (bs, 2H, N$\underline{H_2}$); ^{13}C NMR (175 MHz, $CDCl_3$): δ 14.59 (C_c), 29.42, 34.90 (C_d), 39.05 (C_f), 39.82,

66.78, 69.08 (C_a), 69.56, 69.63, 69.66, 69.74, 69.80, 69.86, 70.19 (C_g), 70.91, 82.86 (C_b), 170.83 (C_e). MALDI $[M]^+$ Alk-PEG-NH_2 obsd 5006.33.

4.2.3.14 Synthesis of Alk-PEG-Imidazole-ester (13)

The solubilized *tert*-butyl 3-(4-(chlorocarbonyl)-1H-imidazol-1-yl)propanoate (**10**, 26 mg, 0.101 mmol) in DMSO (1.5 mL), added DIPEA (17.5 µL 0.101 mmol) and stirred for 15 min. Alk-PEG-NH_2 (**12**, 0.1g, 0.0202 mmol) was dissolved in DMF (2 mL) and added slowly (drop wisely), stirred at room temperature for 4 h, later the temperature raised to 40 °C and stirred for 2 days. After the given time, the mixture was cooled down to room temperature, diluted with 2 mL of water and transferred into dialysis cassette (MWCO 3.5 kDa) and dialyzed against deionized water for 24 h followed by lyophilization**.** The dried polymer was dissolved in DCM and precipitated in hexane to obtain *(Alk-PEG-NH-Imidazole ester)* **(13)** in 86 mg, 83% yield.

^{1}H NMR (700 MHz, $CDCl_3$): δ 1.36 (s, 9H, C($\underline{CH_3}$)$_3$, H_j), 1.96 (bs, 1H, alkyne proton, H_a), 2.18 (bs, 2H, $\underline{CH_2}$, H_b), 2.38 (t, 2H, $\underline{CH_2}$, *j* = 7.0 Hz, H_c), 2.78 (bs, 2H, $\underline{CH_2}$, H_i), 3.09 (bs, 2H, HN-$\underline{CH_2}$, H_d), 3.36-3.40 (m, 2H, $CH_2C\mathit{H_2}$-CO-O), 3.40-3.80 (m, 450H, O$C\mathit{H_2}C\mathit{H_2}$, H_e), 4.18 (bs, 2H, $\underline{CH_2}$, H_h), 4.45-4.55 (m, 2H), 5.76 (bs, 2H), 6.43 (bs, 1H, N$\underline{H}$), 6.64 (bs, 1H, H_f), 6.84 (bs, 1H, H_g), 7.36 (bs, 1H, N$\underline{H}$); ^{13}C NMR (175 MHz, $CDCl_3$): δ 14.75 (C_c), 20.77, 29.01, 29.59, 29.84 (C_n), 31.88 (C_d), 34.29, 35.07 (C_l), 39.18 (C_f), 39.74, 42.09, 43.19 (C_k), 50.44, 55.95, 61.98, 69.14 (C_a), 69.78, 70.13, 70.46 (C_g), 71.40, 73.28, 76.10, 77.95, 83.04 (C_b), 119.04, 126.13 (C_i), 126.90, 127.63, 128.65 (C_j), 129.52, 136.45, 149.93 (C_m), 155.15 (C_h), 170.90 (C_e). MALDI $[M]^+$ *Alk-PEG-Imidazole-ester* obsd 5194.68.

4.2.3.15 Synthesis of Alk-PEG-Imidazole-acid (14)

Alk-PEG-NH-Imidazole ester (**13**, 80 mg, 0.154 mmol) in DI H_2O (3 mL) and added 1 N HCl solution at 0 °C to adjust the pH to 3.0 and stirred for 1 h. After the given time, the temperature

raised to room temperature and transferred into dialysis bag (MWCO 1 kDa) and dialyzed against DI water for 24 h followed by lyophilization**.** The dried polymer was dissolved in DCM and precipitated in hexane to obtain *(Alk-PEG-Imidazole acid)* **(14)** in 70 mg, 90% yield.

^{1}H NMR (700 MHz, $CDCl_3$): δ 1.96 (bs, 1H, alkyne proton, H_a), 2.20 (bs, 2H, $\underline{CH_2}$, H_b), 2.38 (bs, 2H, $\underline{CH_2}$, H_c), 2.68 (bs, 2H, $\underline{CH_2}$, H_i), 3.40-3.80 (m, 450H, OC*H*$_2$C*H*$_2$, H_e), 4.45-4.55 (m, 2H), 5.21 (bs, 2H), 5.56 (bs, 1H), 6.82 (bs, 1H, H_f), 7.14 (bs, 1H, H_g), 7.36 (bs, 1H, N$\underline{H}$). MALDI $[M]^+$ *Alk-PEG-Imidazole-acid* obsd 5076.77.

4.2.3.16 Synthesis of Alk-PEG-NH-Imidazole diphosphate (15)

Diphosphorilation of imidazole derivative was carried out according to known procedure with little modifications [275]. Accordingly, Alk-PEG-NH-Imidazole acid (**14**, 65 mg, 0.0127 mmol) was dissolved in chlorobenzene (3 mL) and added H_3PO_3 (2.8 mg, 0.0344 mmol) at room temperature. The temperature of the reaction mixture was increased to 80 °C, and added $POCl_3$ (4.7 mg, 0.0306 mmol) and stirred for 2.5 h. The reaction mixture was cooled down to 60 °C and added water (4 mL). Two layers were separated and water layer was refluxed for 18 h. It was then cooled to room temperature and diluted with methanol (3 mL) and stirred for 3 h. After the given time, the mixture was transferred into dialysis bag (MWCO 1 kDa) and dialyzed against deionized water for 24 h followed by lyophilization**.** The dried polymer was dissolved in DCM and precipitated in hexane to obtain *(Alk-PEG-Imidazole diphosphate,* **15**) in 38 mg, 58% yield.

^{1}H NMR (700 MHz, $CDCl_3$): δ 2.00 (t, 1H, alkyne proton, *j* = 7.0 Hz, H_a), 2.39 (t, 2H, $\underline{CH_2}$, *j* = 7.5 Hz H_b), 2.50 (dt, 2H, $\underline{CH_2}$, *j* = 6.5, 2.0 Hz, H_c), 2.76 (t, 2H, $\underline{CH_2}$, *j* = 5.5 Hz, H_i), 3.20 (bs, 2H, HN-$\underline{CH_2}$, H_d), 3.40-3.50 (m, 4H, CH_2C*H*$_2$-CO-O), 3.52-3.84 (m, 430H, OC*H*$_2$C*H*$_2$, H_e), 4.16-4.26 (m, 2H, $\underline{CH_2}$, H_h), 6.52 (bs, 1H, N$\underline{H}$), 7.58 (bs, 1H, H_f), 7.68 (bs, 1H, N$\underline{H}$), 7.80 (bs, 1H, H_g);

^{31}P NMR (283 MHz, $CDCl_3$): δ -19.98. MALDI $[M]^+$ *Alk-PEG-Imidazole-diphosphate* obsd 5238.31.

4.2.3.17 "Click" coupling to obtain PMMA-b-PtBA-b-PEG-Imidazole-diphosphate (16)

Alk-PEG-NH-Imidazole diphosphate (**15**, 7.3 mg, 0.00139 mmol, 1.1 equivalent), PMMA-*b*-P*t*BA-N_3 (**3**, 10 mg, 0.00127 mmol, 1 equivalent), CuBr (0.3 mg, 0.00278 mmol, 2 equivalent), PMDETA (0.5 μL, 0.00278 mmol, 2 equivalent), and 2 mL of DMF were introduced into a Schlenk tube and the reaction mixture was degassed by three freeze-pump-thaw cycles before stirring for 48 h at room temperature. After the given time, the reaction mixture was transferred into dialysis cassette (MWCO 7 kDa) and dialyzed against DI water for 48 h followed by lyophilization**.** The dried polymer was dissolved in DCM and precipitated in hexane to obtain *PMMA-b-PtBA-b-PEG-Imidazole-diphosphate* **(16)** in 15 mg, 94% yield.

^{1}H NMR (700 MHz, $CDCl_3$): δ 7.72 (bs, 1H, H_j), 7.52 (bs, 1H, H_i), 7.42 (bs, 2H, NH), 6.98 (bs, 1H, triazole ring proton, H_g), 5.34 (bs, 2H), 5.00 (s, 2H, O=P-OH), 4.15 (CH_2CH-triazole, H_k and CO-O-CH_2, H_b), 4.05 (2H, CH_3-CH_2-O-CO), 3.64 (bs, O-CH_2-CH_2, H_h), 3.59 (s, CO-O-CH_3, H_d), 2.42 (2H, CH_2, H_e), 2.12 (2H, CH_2, H_c), 1.36 (9H, CO-O-C(CH_3)$_3$, H_f), 1.22 (s, 3H, -CH_2-CH_3, H_a); ^{31}P NMR (283 MHz, $CDCl_3$): δ -13.50

4.2.3.18 Boc deprotection to obtain PMMA-b-PAA-b-PEG-BP (17)

PMMA-*b*-P*t*BA-*b*-PEG-NH-Imidazole diphosphate (**16**, 20 mg, 0.00139 mmol), was dissolved in DCM (2 mL) and added TFA (1.5 mL) at 0 °C and stirred at room temperature for overnight. The solvents were evaporated by rotary evaporation (40 °C) and the residue was transferred into dialysis bag (MWCO 1 kDa) and dialyzed for 1 day against DI water and lyophilized to obtain copolymer **(17)**, in 18 mg, 94% yield.

^{1}H NMR (700 MHz, $CDCl_3$): δ 7.43 (bs, 1H, H_j), 7.40 (bs, 1H, H_i), 6.97 (bs, 1H, NH), 6.97 (bs, 1H, triazole ring proton, H_g), 5.36 (bs, 2H), 5.00 (s, 2H, O=P-OH), 4.15 (CH_2C*H*-triazole, H_k and CO-O-C*H*$_2$, H_b), 4.05 (2H, CH_3-C*H*$_2$-O-CO), 3.63 (bs, O-C*H*$_2$-C*H*$_2$, H_h), 3.57 (s, CO-O-CH_3, H_d), 2.42 (2H, C*H*$_2$, H_e), 2.12 (2H, C*H*$_2$, H_c), 1.22 (s, 3H, -CH_2-*CH*$_3$, H_a).

4.2.3.19 Synthesis of Alkyne-PEG-NH-FITC (18)

Commercially available 5 kDa Alkyne-PEG-NH_2 (20 mg, 4 x 10^{-3} mmol) was dissolved in DI water (2 mL), and added FITC (1.9 mg, 4.8 x 10^{-3} mmol) in acetone (0.5 mL) and stirred at room temperature for 24 h. After the given time, water (3 mL) was added to the reaction mixture and transferred into dialysis bag (MWCO 1 kDa) and dialyzed against DI water for 24 h, followed by lyophilization to obtain compound **(18)** in 20 mg, 90% yield.

^{1}H NMR (700 MHz, $CDCl_3$): δ 1.55 (p, 2H, *J* = 4.5 & 11.00 Hz, CH_2), 1.74 (p, 2H, *J* = 4.5 & 11.00 Hz, CH_2), 1.95 (t, 1H, *J* = 1.5 Hz, alkyne proton), 2.19 (t, 4H, *J* = 5.0Hz, CH_2), 3.44 (q, 4H, *J* = 7.0 Hz, CH_2), 3.48-3.55 (m, 8H, CH_2C*H*$_2$-CO-O), 3.55-3.72 (bs, 430H, O*CH*$_2$*CH*$_2$), 4.74 (t, 4H CO-O-CH_2-C*H*$_2$-O), 6.12-8.40 (m, 10H, FITC aromatic protons); ^{13}C NMR (175 MHz, $CDCl_3$): δ 18.15, 24.72, 27.93, 29.29, 29.62, 64.97, 68.63, 69.61, 69.85, 70.17, 70.51, 71.45, 72.39, 84.09, 95.22, 97.07, 103.02, 108.87, 172.64, 231.37. MALDI $[M]^+$ *Alkyne-PEG-FITC* obsd 5376.

4.2.3.20 Synthesis of PMMA-b-PtBA-b-PEG-FITC (19)

Alk-PEG-NH-FITC (**18**, 216 mg, 4.02 x 10^{-2} mmol, 1.1 equivalent), PMMA-*b*-P*t*BA-N_3 (**3**, 300 mg, 3.65 x 10^{-2} mmol, 1 equivalent), CuBr (6.2 mg, 4.39 x 10^{-2} mmol, 1.2 equivalent), PMDETA (9.1 μL, 4.39 x 10^{-2} mmol, 1.2 equivalent), and 5 mL of DMF were introduced into a Schlenk tube and the reaction mixture was degassed by three freeze-pump-thaw cycles and stirred at room for 48 h. The reaction mixture was diluted with THF, and dialyzed against DI water for 2

days and lyophilized. The polymer was dissolved in DCM and precipitated several times in hexane mixture to remove unreacted PEG material.

^{1}H NMR (500 MHz, $CDCl_3$): δ 7.46 (bs, 1H, triazole ring proton), 4.25 ($CH_2C\mathit{H}$-triazole and CO-O-C$\mathit{H_2}$), 4.05 (2H, CH_3-C$\mathit{H_2}$-O-CO), 3.64 (bs, O-C$\mathit{H_2}$-C$\mathit{H_2}$), 3.59 (s, CO-O-CH_3), 3.38 (s, 3H, CH_2-CH_2-O-C$\mathit{H_3}$), 3.05 (2H, triazole-C$\mathit{H_2}$-CH_2-CO-O), 2.76 (2H, triazole-CH_2-C$\mathit{H_2}$-CO-O), 2.26 (CH_2-CH-CO), 1.93-0.83 (6H, O-CO-C(C$\mathit{H_3}$)$_2$, CO-O-C(C$\mathit{H_3}$)$_3$, $\mathit{CH_2}$-C$\mathit{CH_3}$).

4.2.3.21 Boc deprotection to obtain PMMA-b-PAA-b-PEG-FITC polymer (20)

PMMA-*b*-P*t*BA-*b*-PEG-FITC (**19**, 20 mg, 0.00139 mmol), was dissolved in DCM (2 mL) and added TFA (1.5 mL) at 0 °C and stirred at room temperature for overnight. The solvents were evaporated by air circulation and the residue was transferred into dialysis bag (MWCO 1 kDa) and dialyzed for 2 days against DI water and lyophilized to obtain compound **(20)**, in 18 mg, 94% yield.

^{1}H NMR showed complete loss of the *tert*-butyl protons at 1.36 ppm.; ^{1}H NMR (700 MHz, $CDCl_3$): δ 7.72 (bs, 1H, H_j), 7.52 (bs, 1H, H_i), 7.42 (bs, 2H, NH), 6.98 (bs, 1H, triazole ring proton, H_g), 5.34 (bs, 2H), 5.00 (s, 2H, O=P-OH), 4.15 ($CH_2C\mathit{H}$-triazole, H_k and CO-O-C$\mathit{H_2}$, H_b), 4.05 (2H, CH_3-C$\mathit{H_2}$-O-CO), 3.64 (bs, O-C$\mathit{H_2}$-C$\mathit{H_2}$, H_h), 3.59 (s, CO-O-CH_3, H_d), 2.42 (2H, C$\mathit{H_2}$, H_e), 2.12 (2H, C$\mathit{H_2}$, H_c), 1.22 (s, 3H, -CH_2-$\mathit{CH_3}$, H_a).

i) Synthesis of PMMA-*b*-P*t*BA-N_3

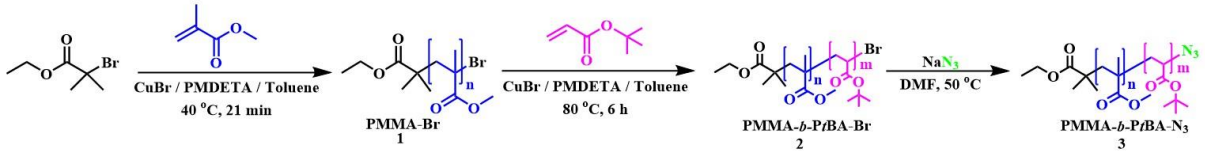

ii) Synthesis of triblock copolymer PMMA-*b*-PAA-*b*-PEG

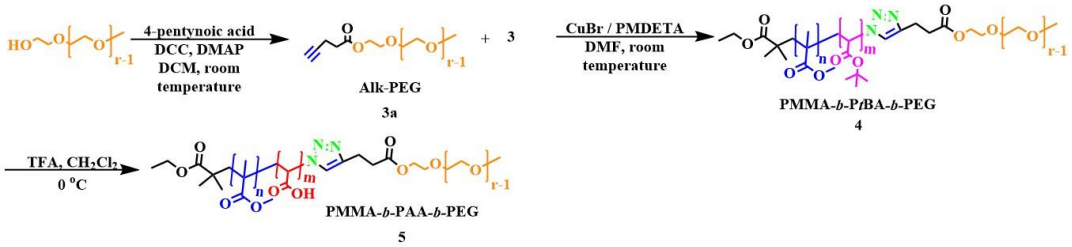

iii) Synthesis of triblock copolymer PMMA-*b*-PAA-*b*-PEG-pVTK

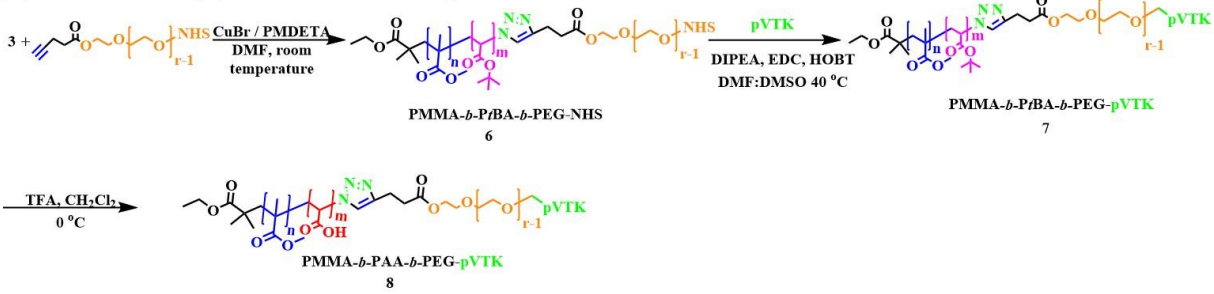

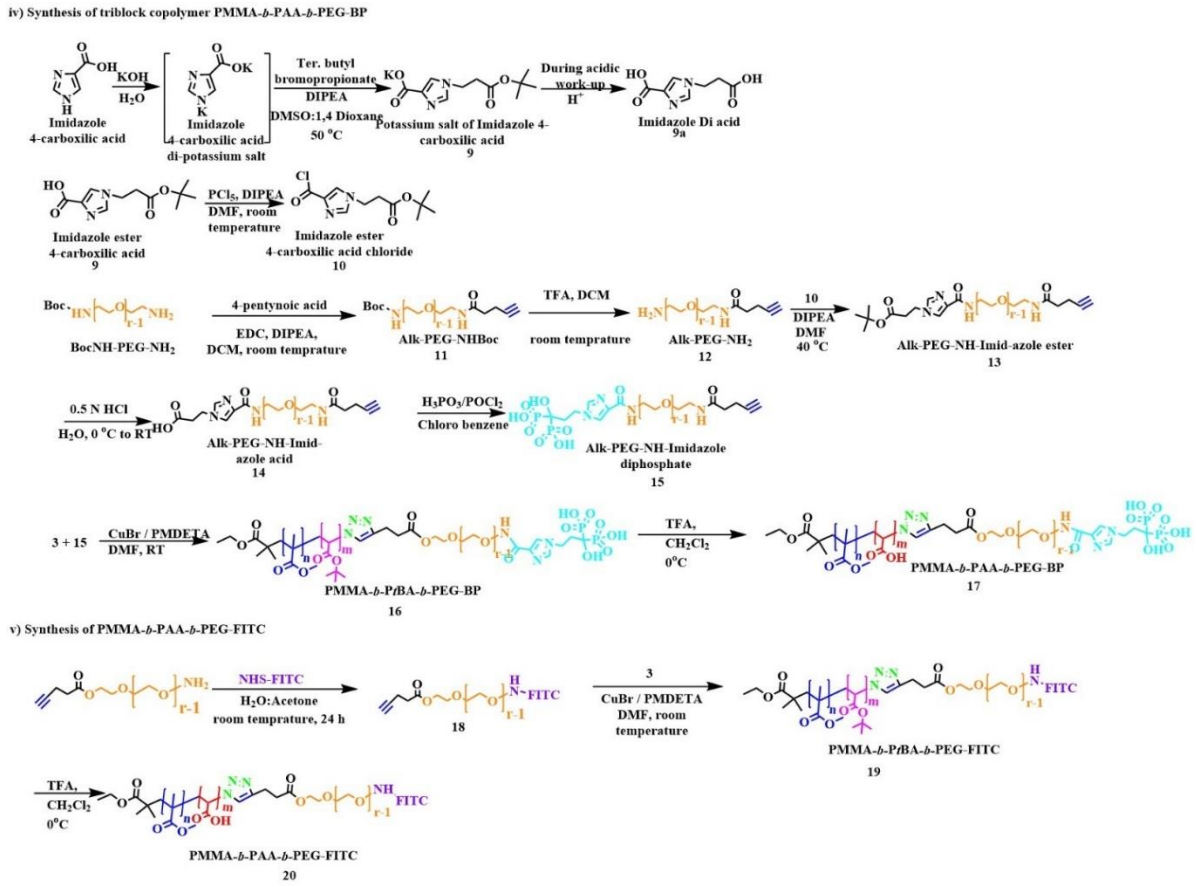

Figure 4.2 A schematic drawing showing i) scheme for synthesis of PMMA-*b*-P*t*BA-N_3 copolymers, ii) PMMA-*b*-PAA-*b*-PEG, iii) PMMA-*b*-PAA-*b*-PEG-pVTK, iv) PMMA-*b*-PAA-*b*-PEG-BP, and v) PMMA-*b*-PAA-*b*-PEG-FITC.

4.2.4 Formulation of PMMA-*b*-PAA-*b*-PEG copolymers into micelles

We formulated the non-targeted and a variety bone binding contents of micelles with two different targeting ligands (pVTK or BP). To prepare non-targeted or targeted particles we used our previous published protocol [273]. For example, to formulate non-targeted particles, amphiphilic PEG-*b*-PAA-*b*-PMMA copolymer (10 mg, 9.38×10^{-4} mmol) was dissolved in 1.5 mL of THF and stirred for 5 minutes before being added dropwise into 7.5 mL of water in a sonicating water bath. To formulate 5% pVTK micelles (M-pVTK$_{5\%}$), 9.5 mg of PEG-*b*-PAA-*b*-PMMA copolymer (8.91×10^{-4} mmol) and PMMA-*b*-PAA-*b*-PEG-pVTK copolymer (0.6 mg, 4.46×10^{-5}

mmol) were dissolved in 1.5 mL of THF and stirred for 5 minutes before being added dropwise into 7.5 mL of water in a sonicating water bath. To prepare 10% pVTK micelles (M-pVTK$_{10\%}$) and 20% pVTK micelles (M-pVTK$_{20\%}$), the same procedure was followed by keeping the total mole of the polymers constant but changing the mole:mole ratio of the targeting polymer block:non-targeted polymer block. With the same strategy, we prepared BP-micelles with different mole to mole ratio such as 5% BP (M-BP$_{5\%}$), 10% BP (M-BP$_{10\%}$), and 20% BP (M-BP$_{20\%}$) micelles. For instance, to prepare M-BP$_{5\%}$, 9.5 mg of PEG-*b*-PAA-*b*-PMMA copolymer (8.91×10^{-4} mmol) and PMMA-*b*-PAA-*b*-PEG-BP copolymer (0.5 mg, 4.46×10^{-5} mmol) were dissolved together in 1.5 mL of THF and stirred for 5 minutes before being added dropwise into 7.5 mL of water in a sonicating water bath. By changing the amount of non-targeted copolymer block and BP-copolymer block we prepared 10 and 20% BP targeting micelles with the same procedure.

After sonication, all particle formulations were stirred at room temperature for 1 h. To cross-link the particles, N-(3-dimethylaminopropyl)-N′-ethylcarbodiimide hydrochloride (EDC, 8.28 mg, 4.32×10^{-2} mmol) in 150 µL of 100 mM 2-(N-morpholino)ethanesulfonic acid (MES) solution and N-hydroxy succinimide (NHS, 2.49 mg, 2.16×10^{-2} mmol) in 150 µL of 100 mM MES solution were added and stirred for 3 h to obtain the NHS esters of the carboxylic acid groups in the central PAA block of the copolymers. Before adding to the pH sensitive cross-linker, the pH of the micelle solution was adjusted to 9.2 using 1N NaOH solution. Once the 2,2'-(Propane-2,2-diylbis(oxy))-diethanamine cross-linker added, the particle solutions were stirred for 6 h at room temperature. The particle solution mixture was transferred into a dialysis bag (MWCO 1kDa), which was placed in a large water bath for 24 hours before lyophilization.

4.2.5 Micelle Characterization

The size and zeta potential of empty non-targeted M, M-pVTK, (5, 10, and 20% pVTK mole/mole targeting density), and M-BP (5, 10, and 20% BP mole/mole targeting density) micelles were measured using a 90Plus particle size analyzer with ZetaPALS capability (Brookhaven Instruments Corporation, Holtsville, NY) at 25 °C following established protocols [217]. Results are presented as the mean of three replicates ± standard error of the mean (SEM).

4.2.6 Binding of M-pVTK and M-BP Particles to Bone Powder

The binding capability of the different particle formulations were tested on the granulated rat bone powder Rat bone powder was synthesized as previously described [276]. Briefly, rat forelimbs and hindlimbs were dissected free from soft tissue, bone marrow was flushed, bones were defatted ($CHCl_3$-MeOH for 4h, and 100% EtOH for 1h), dried overnight at 37 °C, homogenized using a cryomill at -150 °C, and sieved from 42 to 295 μm in diameter. The binding calculation relied on the fluorescence of either FITC-labeled pVTK peptide or FITC-labeled PMMA-*b*-PAA-*b*-PEG particles. The 4% (mole:mole) FITC-labeled M-pVTK$_{5\%}$, M-pVTK$_{10\%}$, M-pVTK$_{20\%}$, M-BP$_{5\%}$, M-BP$_{10\%}$, and M-BP$_{20\%}$ were prepared as described above. FITC-labeled particles (1 mg/mL) were dissolved in Trizma buffer (50 mM). Various particle solutions at different weights of volumes were incubated (100 μL) with 50 μL of bone powder (10 mg/mL) for 3 h. The background FITC-fluorescence (λ_{ex}: 490 nm λ_{em}: 520 nm) of each particle formulation was measured before particle incubation with bone powder. After 3 h incubation, the particles incubated with bone powder were centrifuged with 0.65 μm hydrophilic, low protein binding 96-well filter plate (MultiScreen®, Millipore) at 3000 rpm for 10 min. The filtered solutions were measured with Fluoroskan again to get post-fluorescence value for the calculation of particle binding. The volume-adjusted fluorescence difference between pre and post-fluorescence values

were normalized to the percent fluorescence of the particles in the absence of HA to obtain binding rates. The binding kinetics of pVTK peptide, M-pVTK, and M-BP were calculated from the bone powder or HA powder binding experiments. Results are presented as the mean of three replicates ± standard error of the mean (SEM).

4.2.7 Cell Culture

PC-3 and C4-2B cells were cultured following published protocols [218]. Briefly, PC-3 and C4-2B cells were cultured in RPMI-1640. Culture media for both cell lines was supplemented with 10% fetal bovine serum (FBS; Gibco, Carllsbad, CA) and 1% antibiotic-antimycotic solution (Gibco, Carllsbad, CA). MC3T3 and RAW 264.7 cell lines were cultured with the guidance of a published protocol [139]. To differentiate RAW 264.7 cells to osteoclast, mouse recombinant RANKL (Sigma R0525, St. Louis) at the final concentration of 50 ng/mL was used in the medium during the cell culture for 4-5 days [277]. All cell lines were incubated at 37 °C and 5% CO_2 while changing the culture medium every other day and passaging the cells using 0.05% Trypsin-EDTA solution after reaching 80% confluence except RAW 264.7 cells, which required a cell stripper to detach the cells from the plate surface.

4.2.7.1 Cellular uptake studies

PC-3, C4-2B, MC3T3, and RAW 264.7 cells were seeded in 24-well plates (regular cell culture plate) at a seeding density of 2 x 10^5 cells/well and allowed to adhere for 24 h before incubating with FITC-labeled non-targeted micelles, M-pVTK$_{10\%}$, and M-BP (0%, 5%, 10%, and 20% BP mole/mole) micelles at 40 µg/mL for 3 h. The treated cells were washed with PBS before being trypsinized with 0.05% trypsin-EDTA solution except for RAW 264.7 cells, which we used cotton swab to remove the cells from the surface, then centrifuged all cells at 1000 rpm for 5 min

to form pellets, suspended in 1 mL PBS, and analyzed using flow cytometry CyAn™ ADP Analyzer (Beckman Coulter, Brea, CA) with a characteristic FITC excitation laser at λ_{ex} = 488 nm.

The second particle uptake experiment designed as four cells lines were seeded first on the BLS at a seeding density of 2 x 10^5 cells/well and allowed to adhere for 24 h. RAW 264.7 cells were treated with RANKL for 4 days by changing the medium/RANKL every 2 days before the experiment set. During the experiment they were also treated with RANKL (50 ng/mL of final concentration). After 24 h cell attachment, 40 µg/mL of FITC label non-targeted micelles, M-pVTK$_{10\%}$, and M-BP$_{20\%}$ in OPTI-MEM medium were added to each well and incubated for 3 h. Results are presented as the mean of three replicates ± standard error of the mean (SEM).

4.2.8 Calculation of CTX loading content of the particles

CTX-loaded micelles were formulated following the same micelle preparation protocol [273]. In designed experiments we used CTX-loaded non-targeted micelles, M-pVTK$_{10\%}$, and M-BP$_{20\%}$. Briefly, the interested polymer mixture (dissolved in 0.75 mL of THF) was mixed with 1 mg of CTX in 0.75 mL of THF and stirred for 30 minutes. This solution was added dropwise into 7.5 mL of double distilled water while sonicating to trigger micelle formation followed by stirring for 3 h at room temperature. To cross-link the CTX-loaded particles, we followed the same procedure described earlier to prepare bone targeting particles. The particles were transferred to dialysis bags with MWCO of 1 KDa and dialyzed against double distilled water for 36 hours to remove free CTX and any impurity from the micelles solution. At the end, each particle solution was lyophilized to obtain CTX-loaded non-targeted M, M-pVTK, and M-BP as dry powder **(Figure 4.3)**.

We measured the amount of CTX in dry powder after obtained from lyophilization. 1 mg of dry powder was dissolved in THF (10 mL) and following our previous published protocol

briefly mentioned below [273]. We calculated the loading content and efficiency based on a concentration versus absorbance calibration curve (CTX 0-300 μM) by the following equations (1).

$$\text{Loading efficiency (\%)} = \text{(Amount of the drug in the particles)/}$$

$$\text{(Total amount of drug used in the preperation of particles)} \times 100\ \% \quad \text{Eq. 4.1}$$

Briefly, CTX solutions were analyzed using a C18 Ascentis Express column (Water Corp, Milford, MA; 2.7 μm, 15 cm x 3.0 mm) connected to a Waters HPLC system equipped with a UV dual absorbance detector. A mixture of solvent A (650 mL of H_2O and 350 mL of ACN) and solvent B (250 mL of H_2O and 750 mL of ACN) was used as a mobile phase to separate free CTX on the C18 column using an A:B gradient of 100:0 for 7 min, 62:38 for 29 min, 22:78 for 0.1 min, and 100:0 for 9 min at a flow rate of 0.6 mL/min while keeping the column at 40 °C throughout the run. Absorbance of eluting CTX molecules was measured at 230 nm. We determined the total amount of released CTX present in solution by integrating CTX absorbance versus elution volume using Waters Breeze software and comparing the observed values against a CTX calibration curve. Results are presented as the mean of three replicates ± standard error of the mean (SEM).

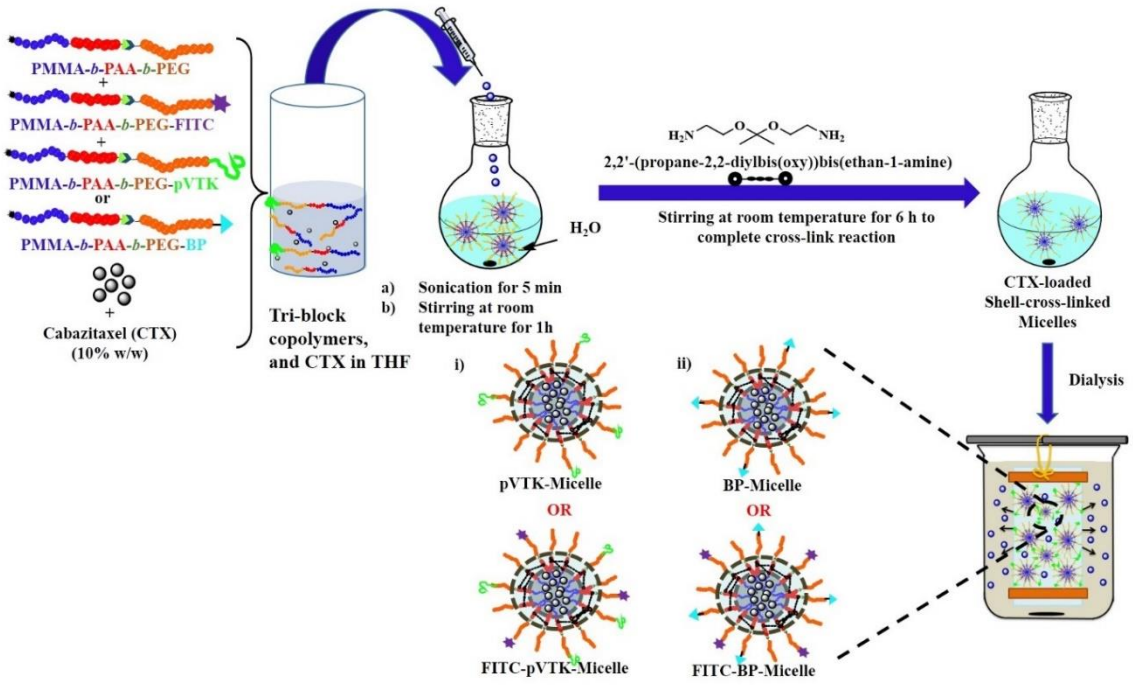

Figure 4.3 A schematic drawing of the formulation of PMMA-*b*-PAA-*b*-PEG tri-block copolymer into "smart" micelles i) M-pVTK or FITC tagged FITC-pVTK-Micelle and ii) M-BP or FITC-BP-Micelle.

4.2.9 Therapeutic activity of CTX-loaded micelles through bone like surface

The cells (PC-3, C4-2B, MC3T3, RAW 264.7, and activated RAW 264.7) were seeded at a seeding density of 60 x 10^3 cells/well in 24-well plates with a BLS and incubated for 24 h. CTX-loaded particles (non-targeted micelles, M-pVTK$_{10\%}$, and M-BP$_{20\%}$) at the concentration of 0.1, 1, and 10 nM CTX-loaded particle concentrations in 400 µL of the medium, and free CTX at equivalent concentration were added to the cells on the BLS and incubated for 48 h. At the end of the incubation period, the culture medium was aspirated and cells were washed with PBS to remove particles, then incubated with 1000 µL of Resazurin Dye at a dilution of 1/10 in the OPTI-MEM medium for 3-4 h before measuring solution fluorescence (λ_{ex}= 570 nm, λ_{em}= 590 nm) using the Fluoroskan Ascent FL plate reader. Fluorescence values were normalized to that observed with

four cell lines incubated in the regular culture medium (control group) to calculate the percentage of viable cells in response to different particle groups. Results are presented as the mean of three replicates ± standard error of the mean (SEM).

4.2.10 Statistical analysis

Results are representative of at least three independent trials of each experiment, and data is represented as the mean of those replicates + SEM. Analysis of the data were done using a two-tailed Student's t-test where the population means were statistically significant at $P \leq 0.05$.

4.3 Results and Discussion

4.3.1 Synthesis of Amphiphilic PMMA-*b*-PAA-*b*-PEG Copolymer

We synthesized PMMA-*b*-PAA-*b*-PEG polymer as described in our previous paper [273]. We merged an ATRP technique and alkyne-azide *"click"* coupling to synthesize amphiphilic polymer with a well-defined composition and molecular weight. This is essential to accomplish the control over the size/molecular weight of the hydrophilic and hydrophobic blocks to trigger the assembly of narrowly dispersed micelles. In the literature, we find that the 5kDa PEG "brush" is necessary to inhibit the non-specific adsorption of serum proteins to the particle surface and to prevent subsequent clearance by phagocytic macrophages. We used MMA and *t*BA monomers to synthesize the hydrophobic PMMA block and central PAA block, respectively. PMMA, P*t*BA, and PAA polymers, which are approved by the FDA to be used as excipients in controlled-release pharmaceutical formulations. To achieve a hydrophilic/hydrophobic balance in polymer composition, the target molecular weight of the hydrophobic block was approximately 5kDa. By adjusting the molar feed ratio of the MMA monomer, the ethyl-2-bromoisobutyrate initiator, and

PMDETA ligand to 200/1/1 and allowing the polymerization reaction for 21 min at 40 °C, we were able to synthesize the PMMA block with the desired molecular weight. Calculating the ratio between the methyl protons of the MMA monomers appearing at 3.57 ppm to the initiator protons at 4.21 ppm shows the polymerization of 50 MMA units forming the PMMA block **(1)** with a M_{nNMR} of 5,201 g/mol (**Appendix E**, **Figure E.1**). ^{1}H NMR confirms successful synthesis of the PMMA block with the desired molecular weight.

PMMA-Br was preferred as a macro-initiator to start the polymerization of *t*BA monomers with the goal of extending the PMMA block with 25 units of *t*BA monomers. By adjusting the ratio of *t*BA monomer, PMMA-Br as a macroinitiator, and PMDETA ligand to 100/1/1, 21 *t*BA monomers were polymerized into the P*t*BA block to form PMMA-*b*-P*t*BA-Br (**2**) with M_{nNMR} of 7,892 g/mole as shown in the ^{1}H NMR spectrum (**Appendix E**, **Figure E.3**). The terminal Br groups were transformed into azide groups with NaN_3 in DMF at 50 °C to obtain PMMA-*b*-P*t*BA-N_3 **(3)**. The ^{1}H NMR and FT-IR confirms the transformation was successful (**Appendix E**, **Figure E.5**). To synthesize the PEG-alkyne, commercially available PEG was reacted with 4-pentynoic acid, EDC, HOBt, and DIPEA in DCM to obtain PEG-alkyne **(3a)**, with functionalization efficiency of 92% (**Appendix E**, **Figure E.7**). We then *"click"* coupled PMMA-*b*-P*t*BA-N_3 **(3)** with PEG-alkyne **(3a)** to obtain PMMA-*b*-P*t*BA-*b*-PEG copolymer **(4)**, which was confirmed by ^{1}H NMR. The characteristic proton of the triazole ring was observed at 7.16 ppm (**Appendix E**, **Figure E.10**) and loss of the azide and alkyne peaks on the FTIR spectrum. The ^{1}H NMR spectrum of PMMA-*b*-P*t*BA-*b*-PEG polymer shows that the molecular weight of the polymer is $M_{n,NMR}$=12,900 g/mol. Afterwards the *tert*-butyl groups were deprotected by acid-mediated hydrolysis using TFA, which was confirmed by the disappearance of the methyl protons of the

tert-butyl groups at 1.42 ppm (**Appendix E**, **Figure E.11**). The molecular weight of the PMMA-*b*-PAA-*b*-PEG copolymer **(5)** is $M_{n,NMR}$ = 11,722 g/mol.

4.3.2 Synthesis of PMMA-*b*-PAA-*b*-PEG-pVTK conjugate polymer

We synthesized triblock amphiphilic copolymers having pVTK peptide, which acts as a targeting ligand to the surface of bone. Compound *PMMA-b-PtBA-N_3* polymer **(3)** and commercially available alkyne-PEG-NHS (5kDa) was "*click*" coupled in the presence of CuBr, PMDETA to obtain PMMA-*b*-P*t*BA-*b*-PEG-NHS polymer **(6)**, which was confirmed by ^{1}H-NMR. The characteristic proton of the triazole ring was observed at 6.62 ppm and PMMA methyl ester peak/PEG ethylene dioxide peaks at 3.50-3.60 ppm (**Appendix E**, **Figure E.12**). *PMMA-b-PtBA-b-PEG-NHS* (**6**) peptide was coupled with pVTK targeting ligand to obtain PMMA-*b*-P*t*BA-*b*-PEG-pVTK copolymers (**7**), which was confirmed by ^{1}H-NMR. The characteristic aromatic protons of histidine and tyrosine was observed at 7.00-8.00 ppm along with PMMA's methyl ester peak and PEG's ethylene dioxide peaks at 3.50-3.60 ppm (**Appendix E**, **Figure E.14**). Finally, the *tert*-butyl groups of P*t*BA was deprotected by acid-hydrolysis using TFA, which was confirmed by the disappearance of the methyl protons of the *tert*-butyl groups at 1.42 ppm (**Appendix E**, **Figure E.17**). The ^{31}P NMR also confirms the PEG-pVTK attachment to PMMA-*b*-PtBA and the phosphate peaks were observed at -20.22 ppm (in $CDCl_3$, **Appendix E**, **Figure E.19**). The molecular weight of the PMMA-*b*-PAA-*b*-PEG-pVTK copolymer **(8)** is $M_{n,NMR}$ = 13,190 g/mol.

4.3.3 Synthesis of PMMA-*b*-PAA-*b*-PEG-BP conjugate polymer

We synthesized triblock amphiphilic copolymers having BP as a targeting ligand, which is a zoledronic acid derivative. We synthesized the zoledronic acid derivative BP following a known method with some modifications [274]. N-alkylation of imidazole 4-carboxilic acid was reacted with KOH in DI water to obtain its potassium salt. After evaporating the water and subsequently

drying the sample, the residue was dissolved in DMSO:1,4 Dioxane (4:1, 5 mL) and added DIPEA followed by *ter*t. butylbromo-propionate to obtain 1-(3-(tert-butoxy)-3-oxopropyl)-1H-imidazole-4-carboxylic acid (**9**), which was confirmed by ^{1}H NMR and mass spectrum. The aromatic peaks were observed at 7.30 and 7.45 ppm, whereas tertiary butyl group observed at 1.36 ppm. (**Appendix E**, **Figure E.23**). The compound **9**'s carboxylic acid group was converted into acid chloride with PCl_5 to obtain acid chloride compound **10**. ^{1}H NMR shows that the aromatic peaks were shifted to 8.45 and 9.45 ppm (**Appendix E**, **Figure E.26**). The aromatic proton shifted to down field attributed to acid chloride formation.

To synthesize alkyne-PEG-NH_2 **(11)**, commercially available 5 kDa BocHN-PEG-NH_2 was coupled to 4-pentynoic in the presence of DIPEA, EDC with the functionalization efficiency of 92%. The ^{1}H-NMR confirmed the coupling and its characteristic peak for alkyne proton was observed at 1.92 ppm (**Appendix E**, **Figure E.28**). The Boc group was deprotected with TFA to obtain alkyne-PEG-NH_2 **(12)**. ^{1}H NMR confirmed the Boc deprotection as its characteristic peak at 1.36 ppm was disappeared (**Appendix E**, **Figure E.31**). Compound **(12)** was coupled to acid chloride **(10)** in the presence of DIPEA in DMF:DMSO to obtain Alk-PEG-NH-Imidazole ester (**13**). ^{1}H NMR confirmed the coupling and its characteristic peak for alkyne proton was observed at 1.96 ppm and Boc group at 1.36 ppm (**Appendix E**, **Figure E.34**). Alk-PEG-NH-imidazole ester, undergo ester hydrolysis in the presence of 1 N HCl solution (adjusted pH 3.0) at 0 °C to obtain Alk-PEG-Imidazole acid **(14)**. ^{1}H NMR confirmed the Boc deprotection as its characteristic peak at 1.36 ppm disappeared and all other peaks remained intact (**Appendix E**, **Figure E.37**). Diphosphorylation of the imidazole derivative was carried out according to a known procedure with little modifications [275]. Alk-PEG-NH-Imidazole acid **(14)** on reaction with H_3PO_3, $POCl_3$ in chlorobenzene gave Alk-PEG-Imidazole diphosphate **(15)** in 58% yield. From the ^{1}H NMR the

aromatic peaks were observed at 7.80 and 7.58 ppm, and the alkyne peak was observed at 2.00 ppm (**Appendix E**, **Figure E.39**). The ^{31}P NMR confirmed the phosphorylation and its phosphate peak was observed at -19.98 ppm (**Appendix E**, **Figure E.40**). The click coupling between Alk-PEG-NH-Imidazole diphosphate **(15)** and PMMA-*b*-P*t*BA-N_3 **(3)** was carried out in the presence of CuBr, PMDETA to obtain in PMMA-*b*-P*t*BA-*b*-PEG-Imidazole-diphosphate **(16)**. ^{1}H NMR confirms the coupling, the characteristic peak from both addendums observed in the NMR. The aromatic peaks were observed at 7.72 and 7.52 ppm, whereas triazole ring proton observed at 6.98 ppm and PMMA and PEG protons observed at 3.50-3.60 ppm (**Appendix E**, **Figure E.41**). The ^{31}P NMR showed that the phosphate group was shifted to -13.50 ppm (**Appendix E**, **Figure E.42**). All these NMR confirmations indicate that the coupling carried out successfully. The molecular weight of the PMMA-*b*-P*t*BA-*b*-PEG-BP polymer **(16)** is $M_{n,NMR}$ = 13130 g/mol.

Finally, we removed the *tert*-butyl groups of P*t*BA middle block polymer by acid-hydrolysis using TFA, which was confirmed by the disappearance of the methyl protons of the *tert*-butyl groups at 1.42 ppm (**Appendix E**, **Figure E.43**). The molecular weight of the PMMA-*b*-PAA-*b*-PEG-ZA copolymer **(17)** is $M_{n,NMR}$ = 11953 g/mol.

4.3.4 Synthesis of PMMA-*b*-PAA-*b*-PEG-FITC conjugate polymer

We synthesized triblock amphiphilic copolymer having FITC labeling for the particle HA affinity and cellular uptake studies. Commercially available 5 kDa Alkyne-PEG-NH_2 was treated with FITC in water:acetone (3:1) to obtain Alkyne-PEG-NH-FITC **(18)**. ^{1}H NMR shows that the FITC aromatic peaks were observed at 6.12-8.40 ppm, and the alkyne peak observed at 1.95 ppm (**Appendix E**, **Figure E.44**). We then *"click"* coupled PMMA-*b*-P*t*BA-N_3 (**3**) with FITC-PEG-alkyne (**18**) to obtain PMMA-*b*-P*t*BA-*b*-PEG-FITC polymer **(19)**, which is confirmed by ^{1}H-NMR, the characteristic proton of the triazole ring was observed at 7.46 ppm, along with PMMA

and PEG protons between 3.35-3.55 ppm (**Appendix E**, **Figure E.46 and Figure E.47**). From the ^{1}H NMR spectrum, the molecular weight of the PMMA-*b*-P*t*BA-*b*-PEG-FITC is M_{nNMR} of 13,282 g/mol. Finally, we deprotected the *tert*-butyl groups by acid-mediated hydrolysis using TFA, which is confirmed by the disappearance of the methyl protons of the *tert*-butyl groups at 1.42 ppm (**Appendix E**, **Figure E.48**). From the ^{1}H NMR spectrum, the molecular weight of the PMMA-*b*-PAA-*b*-PEG-FITC copolymer **(20)** is $M_{n,NMR}$ = 12,105 g/mol.

4.3.5 Bone Targeted Micelles formulation and characterization

In our previous study we showed that non-targeted triblock amphiphilic copolymers are able to self-assemble in aqueous solution [273]. Following the same protocol two different bone-targeted cross-linked particles, pVTK or BP decorated particles, with different targeting densities (0, 5, 10, 20% mole/mole) were formulated as seen in **Figure 4.3**. These particles were measured by dynamic light scattering (DLS) and measurements show that the particle size of each particle formulation spanned between 60-90 nm with no statistical difference in **Figure 4.4**. The size of bone targeted particles allows particle penetration not only from the permeable vasculature with average endothelial gaps typically between 200-600 nm (called the enhanced permeation and retention (EPR) effect [242]), but also from the sinusoidal gap in bone that has a cut-off pore size less than 80 nm [143]. Therefore, the size of these bone-targeted particles is ideal to efficiently penetrate tumor tissue in the metastasized bone. In addition, we incorporated a PEG brush (to form a corona) and a negative zeta potential to impart hemocompatibility on the "smart" particle during blood circulation with resistance against adsorption of serum proteins, lack of interaction with blood cells (i.e. platelets and RBCs) and minimize the non-specific particle uptake by these and healthy cells [247, 278, 279].

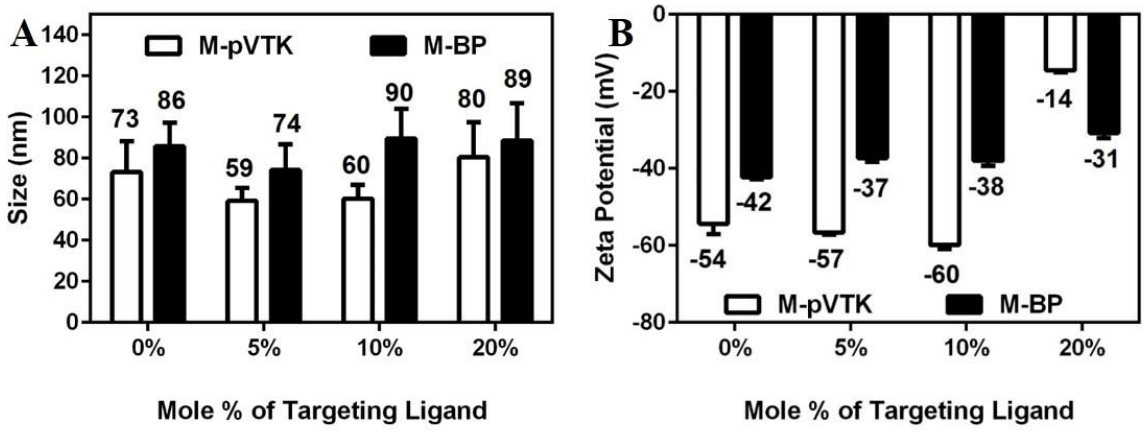

Figure 4.4 Bone-targeted particles characterizations.

(A) Size and (B) zeta-potential characterization of 0, 5, 10, 20% targeting ligand M-pVTK and M-BP particles. Results show the average + standard error of the mean (SEM) of three independent solutions for each micelle formulation.

4.3.6 Bone Powder Binding Kinetics of the M-pVTK and M-BP Particles

The main constituent of bone is HA, which is altered in the presence of diseased conditions. It is well-documented that phosphorylated or acidic peptides and BPs show a strong affinity to HA due to phosphonate, carboxyl groups, and negative charge of the moieties [139, 280]. To test the binding capability of pVTK conjugated polymers, pVTK-particles, and BP-particles we used HA powder, bone powder, and bone chips in seperate experiments. It is well understood that the pVTK peptide is capable of binding to HA surfaces [139-141]. We confirmed this by assessing whether pVTK-polymers have binding capability to HA powder, and we compared binding rates of pVTK-polymers to pVTK peptide alone. To do this we used FITC-labeled pVTK peptide and FITC-pVTK decorated PEG-*b*-PAA-*b*-PMMA to quantitatively determine the binding affinity to HA powder. After incubation for 3 h at 37 °C, 64% of pVTK peptide and 63% of pVTK-conjugated triblock copolymer bound to HA **(Figure 4.5A)**. Furthermore, the binding isotherm of pVTK and pVTK-conjugated copolymer was calculated to be 27.16 and 26.40 µM, respectively. These results

indicate that pVTK decorated triblock amphiphilic copolymers are able to bind HA as efficiently as free pVTK with similar kinetics without statistical difference.

Along with this result, we formulated FITC-labeled pVTK and BP micelles containing different targeting block densities such as 0, 5, 10, 20% (mole:mole) to estimate the binding affinity of bone-targeted particles to bone powder derived from rat bones. The bone powder was suspended in 100 mM Trizma buffer (pH 7.4) at the concentration of 10 mg/mL. Particles targeted either by pVTK or BP ligands prepared at varying concentration were dissolved in the same Trizma buffer then added to the bone powder suspensions and the mixtures were shaken for 3 h at 37 °C. Each particle solution was also treated without bone powder following the same protocol as control. After centrifugation the FITC fluorescence intensities of the filtered solutions were measured. The reduction in the FITC fluorescence intensity corresponding to the initial fluorescence intensity and untreated bone powder revealed the amount bound to bone powder. With this strategy we demonstrated the binding isotherms of bone targeted particles. 5, 10, and 20% bone targeting ligand containing pVTK micelles did not show statistically different binding kinetics compared to each other **(Figure 4.5B)**. On the other hand, 10 and 20% BP targeting ligand-containing micelles had higher binding kinetics compared to 5% BP micelles as seen in **Figure 4.5C**. Both pVTK and BP bone-targeted particles with each formulation followed the Langmuir isotherm model [281]. Furthermore, we tested pVTK particles (5, 10, 20%) on HA disks to see whether or not any affinity changing due to decreasing the surface area of binding site of the HA disk compared to HA powder. The HA disk binding results of M-pVTK$_{5\%}$, M-pVTK$_{10\%}$, and M-pVTK$_{20\%}$ exhibited 58%, 60% and 61% as measured by the fluorescent intensity of the particles, respectively **(Figure 4.5D)**. However, 20% pVTK bone targeting particles were affected by quenching of the FITC signal so the fluorescence image of post-treated HA chip has less

fluorescence intensity compared to M-pVTK$_{5\%}$ and M-pVTK$_{10\%}$. Among M-pVTK$_{5\%}$ and M-pVTK$_{10\%}$ particles, we quantified the highest fluorescence of the pVTK particle-bound HA chip from M-pVTK$_{10\%}$ particle **(Figure 4.5D)**. Therefore, M-pVTK$_{10\%}$ particles were preferred in future cellular experiments.

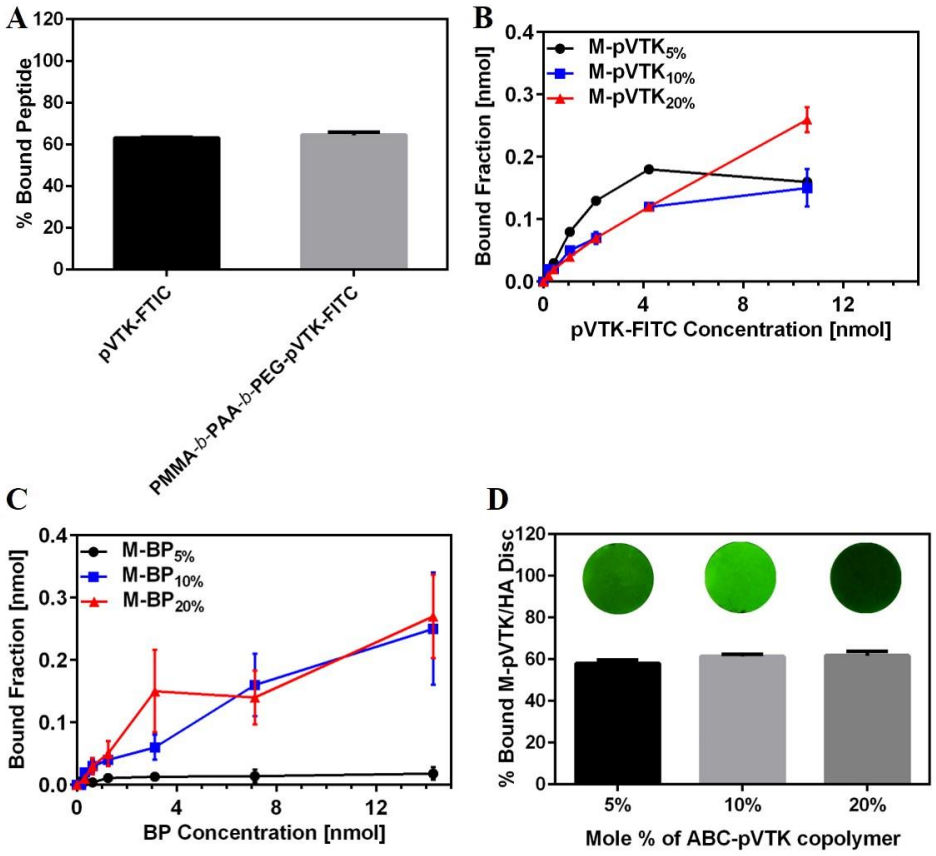

Figure 4.5 Binding of the particles to bone powder.

(A) The percentage bound of pVTK-FITC peptide and pVTK-FITC coupled PMMA-*b*-PAA-*b*-PEG triblock copolymer on HA powder (B) M-pVTK binding kinetics, (C) M-BP binding kinetics, and (D) 5, 10, 20% mole of pVTK targeting particle binding to HA disk and the fluorescence images of these disks after pVTK targeting particle binding. Results show the average + SEM of three independent solutions for each bone targeted particle formulation.

4.3.7 Cancer cell uptake of FITC-labeled particles

The cellular uptake of pVTK-conjugated bone-targeted particles (M-pVTK$_{10\%}$) was investigated in regular cell culture plates and BLS with comparison to non-targeted particles. Briefly, FITC labeled micelles at the concentration of 40 µg/mL were added to the seeded cancer cells - PC-3 and C4-2B - or bone cells - preosteoblast MC3T3 and preosteoclast RAW 264.7, or RANKL activated RAW 264.7 - in the presence of OPTI-MEM cell culture medium. All cells were treated with the particles for 3h at 37 °C. The internalized FITC-labeled micelles were quantified by measuring the percentage of labeled cells and fluorescence signal per cell using flow cytometry. First, we quantified M-pVTK$_{10\%}$ bone-targeted particles and micelles alone. 68%, and 78% of PC-3 cells; 38%, and 50% of C4-2B cells; 86%, and 95% of MC3T3; and 88% and 98% of RAW 264.7 cells on the regular surface were labeled by the FITC-tagged non-targeted micelles and M-pVTK$_{10\%}$ particles, respectively as seen in **Figure 4.6A**. The overall trend of cell labeling for non-targeted and pVTK-decorated particles was that the bone cells were significantly stained more than cancer cells. Further, the percentage of FITC-labeled MC3T3 and RAW 264.7 cells that were treated with pVTK-decorated particles were statistically higher ($p<0.05$) than non-targeted particles. Furthermore, we normalized the fluorescence intensity of FITC-labeled cells against non-treated cells to explore the difference in intracellular concentration of particle formulations (**Figure 4.6B**). The results demonstrate that the relative FITC fluorescence intensities augmented 15- and 15- in PC-3; 10- and 9- in C4-2B; 18- and 28- in MC3T3, and 14- and 20-fold in RAW 264.7 cells for FITC-tagged non-targeted, and M-pVTK$_{10\%}$ particles, respectively. The comparison of non-targeted and pVTK bone-targeted relative fluorescence intensity shows that there is no statistically difference between the particles in all cell lines. However, it is clear that the highest relative fluorescence fold is obtained by MC3T3 cells treated with pVTK particles. On the other hand, we conducted the same experiment settings in the presence of BLS to explore the changes

of bone-targeted particle internalization within BLS. The percentages of FITC-labeled PC-3 cells were 94, and 95 after incubating with non-targeted and M-pVTK$_{10\%}$ particles, respectively. A similar trend was also observed for C4-2B cells. Specifically, 97%, and 100% of these cells were labeled with non-targeted, and M-pVTK$_{10\%}$ particles, respectively. Moreover, 86%, and 96% ($p<0.01$) of MC3T3, and 43%, and 85% ($p<0.001$) of aRAW 264.7 cells were labeled by the FITC-tagged non-targeted, and M-pVTK$_{10\%}$ particles, respectively (**Figure 4.6A**).

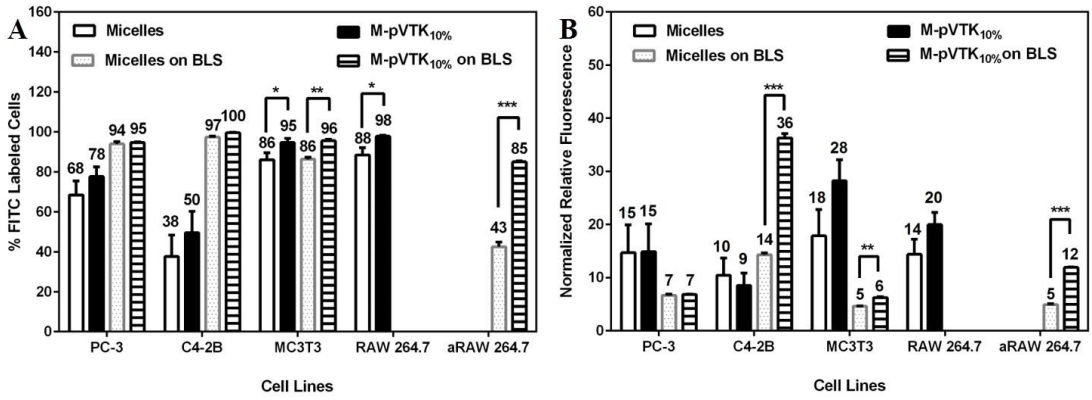

Figure 4.6 Prostate and bone cells uptake of the particles from regular cell culture plates and BLS.

The cells first seeded on the plate. After 24 h the particles are added to the top of the cells and incubated for 3 h. (A) M-pVTK$_{10\%}$ percent cell label, (B) Normalized mean fluorescence of FITC labelled cells. Results are the average of at least nine samples of triplicate experiments + SEM. Percentage of labeled the cells and normalized mean fluorescence increase by M-pVTK$_{10\%}$ were compared to FITC label non-targeted micelles using a two-tailed Student's t-test where * denotes $P < 0.05$, and *** denotes $P < 0.001$.

Furthermore, the relative fluorescence intensity of FITC labeled cells results show that 7, and 7-fold increased fluorescence intensity in PC-3 cells; 14, and 36-fold ($p<0.001$) increased fluorescence intensity in C4-2B cells; 5, and 6-fold ($p<0.01$) increased fluorescence intensity in MC3T3; and 5, and 12-fold ($p<0.001$) increased fluorescence intensity in aRAW 264.7 cells were treated by the FITC tagged micelles, and M-pVTK$_{10\%}$ particles, respectively (**Figure 4.6B**). As indicated in the FITC-labeled cell percentage, C4-2B and MC3T3 cells incubated with pVTK particles exhibited a statistically higher uptake rate compared to non-targeted particles. Thus,

pVTK targeting peptide might be an effective strategy to deliver therapeutics to C4-2B prostate cancer and osteoblasts in bone microenvironment.

In the second part of bone-targeted particle uptake of prostate cancer cells and bone cells, we evaluated the effect of BP targeting ligand on the internalization of FITC-labeled BP particles as a function of BP density (5, 10, and 20% BP particles) both in regular cell culture plate and BLS. We then compared there to non-targeted particles following the same procedure of pVTK particles. The results show that 91%, 88%, 89%, and 88% of PC-3 cells; 75%, 71%, 75%, and 73% of C4-2B cells; 96%, 89%, 94%, and 90% of MC3T3; and 97%, 98%, 99%, and 99% of RAW 264.7 cells were labeled by the FITC tagged non-targeted, M-$BP_{5\%}$, M-$BP_{10\%}$, and M-$BP_{20\%}$ particles, respectively (**Figure 4.7A**). Moreover, the normalized relative FITC fluorescence values of all particle values for PC-3, C4-2B, and MC3T3 were around 6, 5, and 9-fold, respectively. There was no statistical difference between non-targeted particles and the BP targeting particles in these cell lines. However, increasing the BP density 5%, 10%, and 20% of bone targeted particles in RAW 264.7 macrophage cells increased the normalized relative FITC fluorescence values 17- ($p<0.05$), 23- ($p<0.001$), and 57-fold ($p<0.001$) compared to 14-fold increase of non-targeted particles, respectively as seen in **Figure 4.7B**. This higher relative internalization by macrophage trend is supported by earlier reports showed that negatively charged particles and BPs or BP-decorated particles could target scavenger receptors on the cell membrane of macrophages cells [282, 283]. This result indicates BP-decorated bone-targeted particles are able to target macrophages. Since the highest relative fluorescence was measured with the 20% BP particle formulation, after this point we preferred to use this particle in further cellular experiments.

Finally, we designed a second BLS experiment set-up to explore the M-$BP_{20\%}$ particles uptake by seeding prostate cancer cells (PC-3 or C4-2B cells), or bone cells (MC3T3 or RANKL

activated RAW 264.7 cells), on BLS and maintained for 24 h in the incubator. Afterwards, the cells were treated with FITC-tagged particle that were either non-targeted, or M-BP$_{20\%}$ at a concentration of 40 µg/mL in OPTIMEM medium for 3 h at 37 °C. We followed the cellular uptake protocol that we described in previous cell uptake studies. The percentage FITC-labeled cells and the normalized intensity of intracellular fluorescence of the particles were quantified using flow cytometry. The percentages of FITC-labeled PC-3 cells were 94%, and 91% after incubating with non-targeted, and M-BP$_{20\%}$ particles, respectively. A similar trend was also observed for C4-2B cells. Specifically, 97%, and 94% of these cells were labeled with non-targeted, and M-BP$_{20\%}$ particles, respectively. Moreover, 86%, and 86% of MC3T3, and 43%, and 30% ($p<0.01$) of aRAW 264.7 cells were labeled by the non-targeted, and M-BP$_{20\%}$ particles, respectively (**Figure 4.7C**). Furthermore, the relative fluorescence intensity of FITC-labeled cells results show that 7, and 6-fold increased fluorescence intensity in PC-3 cells; 14, and 12-fold increased fluorescence intensity in C4-2B cells; 5, and 5-fold increased fluorescence intensity in MC3T3; and 5, and 4-fold increased fluorescence intensity in aRAW 264.7 cells were treated by the FITC-tagged non-targeted, and M-BP$_{20\%}$ particles, respectively (**Figure 4.7D**).

All in all, when **Figure 4.6, and 4.7** are compared in general cellular labeling or fluorescence intensity fold increase, it is clear that bone-targeted particle internalization through cancer and bone cells act differently because of the presence of BLS. For instance, PC-3 cells can be labeled about 90% when the cells are attached to the surface without the presence of a BLS. Another prostate cancer cell line, C4-2B, which is a mixed form (osteoblastic and osteolytic character) of bone metastasis cells can internalize comparatively less particles with PC-3 on regular tissue culture plate. These particle internalization rates are similar to our previous published study [273]. However, under the same experimental setup but with BLS **(Figure 4.6)**

the particle internalization rates increase to more than 90% range and pVTK bone-targeted particles are able to label 100% with a maximum of 36-folds relative fluorescence intensity increase. This pVTK-targeted particle uptake fold-enhancement in C4-2B is the highest rate comparing to MC3T3 and activated RAW 264.7 cells with $p<0.001$ and $p<0.01$, respectively. The reason of higher pVTK bone-targeted particle uptake profile of C4-2B cell line could be its osteoblast-like phenotype nature that are capable of mineralization with the production of bone surface alkaline phosphatase, osteocalcin, osteonectin, bone sialoprotein, and osteoprotegerin [284, 285]. Most importantly, the C4-2B cells produced hydroxyapatite mineral *in vitro*. This *in vitro* hydroxyapatite mineral production could raise up the pVTK-bone targeted particle affinity [286].

The MC3T3 cell line is a mouse preosteoblast cell. We also tested the pVTK and BP bone-targeted particles in MC3T3 cells using methodology similar to the tumor cells. The initial tests with particles in medium incubated in tissue culture plates show that both bone targeted particles have high cellular internalization rate (~90%). However, pVTK-particles achieve the highest statistically different cellular labeling with 95% and 28-folds relative intracellular fluorescence increase, as seen in **Figure 4.6**. However, in the case of cells on BLS and particles added afterwards in medium, we observe higher rates of internalization for all particle formulations. pVTK bone-targeted particles, in particular, have the highest MC3T3 cellular labeling with 96% and an increase in intracellular normalized fluorescence intensity by 6-folds **(Figure 4.6)**. These results clearly show that pVTK particles can be internalized by osteoblasts. Even pVTK-targeted particles show statistically higher cellular uptake in MC3T3, once compared in different cell lines (C4-2B and activated RAW 264.7), this particle shows the lowest normalized fluorescence fold with $p<0.001$ and $p<0.05$, respectively. Further, pVTK is a well-characterized peptide formulation

that is able to adsorb to the apatite surface and inhibits the mineralization in pre-osteoblastic cells with a dose dependent response [142]. Because of the direct interaction of pVTK with mineralized surface or cells, pVTK particles are preferentially internalized by MC3T3 and C4-2B cells.

Lastly, we investigated the bone-targeted particles uptake interactions with RAW 264.7 macrophage cells on regular tissue culture plate and RANKL-activated RAW 264.7 cells to osteoclasts on the BLS. Macrophage cells are capable of phagocytosis which means they

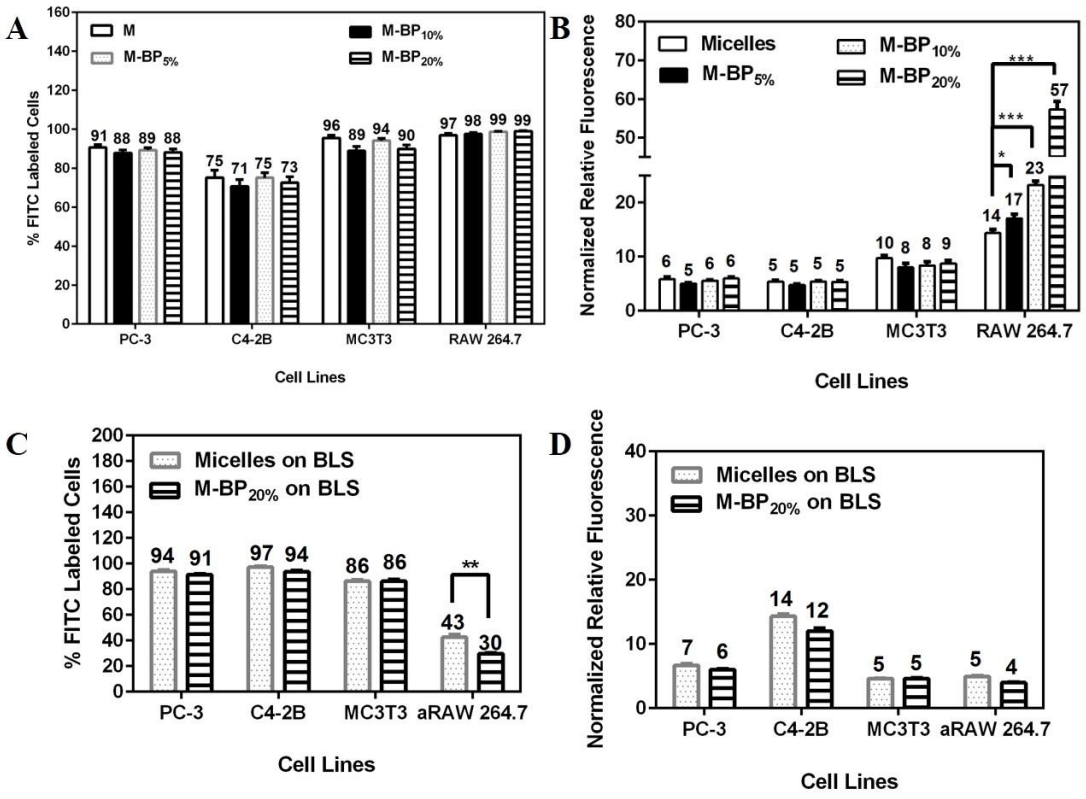

Figure 4.7 Prostate and bone cells uptake of the particles from regular cell culture plates and BLS.

The cells first seeded on the plate. After 24 h the particles are added to the top of the cells and incubated for 3 h. (A) FITC-label non-targeted Micelles, M-$BP_{5\%}$, M-$BP_{10\%}$, and M-$BP_{20\%}$, percent cell label on regular cell culture plates, (B) Normalized mean fluorescence of cells treated with FITC-label non-targeted Micelles, MI-$pBP_{5\%}$, MI-$pBP_{10\%}$, and MI-$pBP_{20\%}$ on regular cell culture plates. (C) FITC-label non-targeted micelles, and MI-$BP_{20\%}$ percent cell label on BLS, (D) Normalized mean fluorescence of cells treated with FITC-label non-targeted Micelles, and M-$BP_{20\%}$ on BLS. Results are the average of at least nine samples of triplicate experiments + SEM. Percentage of labeled the cells and normalized mean

fluorescence increase by M-BP particles were compared to non-targeted FITC-M micelles using a two-tailed Student's t-test where * denotes $P < 0.05$.

inherently internalize more particles compared to other cell lines. In the literature, negatively-charged particles and BP-targeted particles are known to be recognized by macrophages and also tumor activated macrophages (TAMs), which form approximately half of the tumor mass [287]. Many studies denote that TAMs contribute to drug resistance [288] and elevated number of TAMs are correlated with therapy failure and poor diagnosis [289, 290]. Therefore, direct effects on these cells in the tumor microenvironment could contribute to the treatment of bone metastasis [291]. Our results confirm the high affinity between macrophages and these types of particles, as both bone-targeted particles are able to label RAW 264.7 cells almost 100% **(Figure 4.7A)**. Increasing the number of BP targeting ligands displayed on the particles, the relative fluorescence intensity increases up to 57-folds **(Figure 4.7B)**. Therefore, by increasing the number of BP on the particle, these particle formulations can be used to deliver specific agents to macrophages or TAMs. Interestingly, when RAW 264.7 cells are differentiated with RANKL on the BLS we do not see higher internalization of BP-targeted particles compared to other particle formulations. Also, it is important that ruffled bordered macrophages indicative of osteoclasts activation and subsequent bone resorption with acidic enzymes. The lack of forming ruffled borders might affect the BP-particle uptake profile. This might be a mandatory effect in **Figure 4.7** that the cells are first seeded and followed by particle incubation with the cells. Because of inability to form ruffled border in osteoclasts treated with BP targeting particles, the labeled cells are the lowest with 30% between all particles. Furthermore, inhibition of ruffled border formations by BP-targeting particles as well as loading with an anti-cancer agent might have a synergistic effect in the treatment of bone

metastasis. Whereas, as seen in **Figure 4.6**, pVTK-targeted particles have the highest osteoclast uptake with the percentage of 85% and 12-fold normalized relative fluorescence increase.

Taken these cellular uptake results together, we can conclude that if bone metastasized cells are in osteolytic form (like PC-3 cells), BP-based targeting ligands are the ideal strategy to target cancer cells and TAMs. On the other hand, if the metastasized bone tumor is in a mixed format of both osteoblastic and osteolytic characteristics (like C4-2B cells), pVTK-targeting ligands are the preferred strategy for drug delivery.

4.3.8 Cytotoxicity of CTX-loaded micelles

To test the therapeutic effect of the bone targeted particles, we loaded CTX as a model anticancer agent in the core of the particles using our established drug encapsulation protocol [273]. The CTX loading content was measured in non-targeted, M-pVTK$_{10\%}$, and M-BP$_{20\%}$ particles by HPLC. The loading efficiency was calculated based on a concentration versus CTX absorbance calibration curve. Results show that encapsulation efficiencies of CTX in non-targeted particles, M-pVTK$_{10\%}$, and M-BP$_{20\%}$ particles were 30.03 ± 1.31%, 32.33 ± 4.87%, and 32.23 ± 4.75%, respectively. In our reference study, we determined the CTX IC$_{50}$ values of free and CTX-loaded particles in PC-3 and C4-2B cells between 0.6-5.0 nM. Based on the established previous study and bone targeted-particles cellular uptake experiments we examined the therapeutic activity of these CTX-loaded particles at 0.1, 1.0, and 10 nM CTX concentrations in comparison to equal concentrations of free CTX for 48 h using the established resazurin cytotoxicity assay. We expected that CTX-loaded bone-targeted particles would exhibit higher therapeutic effect since they are able to bind to the bone surface and higher particle internalization by cancer cells based on the type of targeting ligands. Results show the % of surviving all cell types decrease with the increase of the concentration of CTX incubated with all cell lines **(Figure 4.8)**. CTX-loaded non-

targeted particles exhibited the highest survival percentage between all concentrations and all cell lines on BLS comparing to free CTX and as well as pVTK- and BP- targeted particles. The reason of this higher survival rate is that free CTX can be internalized by all cell lines via diffusion mechanism, bone-targeted particles are able to be adsorbed on BLS leading to likely increase particles contact to the cells, and more particle internalization with bone targeting ligands. Once each cell line is evaluated with the highest treated CTX concentration with details, PC-3 cells are survival 60%, 83% ($p<0.001$), 78% ($p<0.001$), and 66% ($p<0.05$) with the treatment of free CTX, CTX-M, CTX-M-pVTK$_{10\%}$, and CTX-M-BP$_{20\%}$, respectively **(Figure 4.8A)**. BP bone-targeted particles display the lowest survival rate comparing to CTX-loaded particle formulations. The reasons of higher therapeutic effect could be BP-targeted particles having higher PC-3 cell uptake and as well as BP has anticancer effect. C4-2B cell viability percentages treated with free CTX, CTX-M, CTX-M-pVTK$_{10\%}$, and CTX-M-BP$_{20\%}$, are 41, 70 ($p<0.001$), 42, and 54 ($p<0.001$), respectively **(Figure 4.8B)**. CTX-loaded M-pVTK$_{10\%}$ shows overall similar cytotoxicity percentage like free CTX. This enhanced therapeutic effect could be contributed by the pVTK targeting motive, which gains specific internalization of M-pVTK particles by C4-2B. The survival rates of MC3T3 cells after treating with free CTX, CTX-M, CTX-M-pVTK$_{10\%}$, and CTX-M-BP$_{20\%}$, are 80%, 90 % ($p<0.001$), 79, and 85 ($p<0.05$), respectively **(Figure 4.8C)**. MC3T3 has higher survival rates with all CTX concentrations comparing to all other cell lines due to the fact that the model drug, CTX, is capable of targeting to epithelial cell lines such as prostate cancer cells not direct effect in osteoblasts. Because of the affinity of pVTK-targeted particles towards MC3T3 cells, the lowest viability rate is obtained by CTX-M-pVTK$_{10\%}$. The treatment of RAW 264.7 macrophage cells with free CTX, CTX-M, CTX-M-pVTK$_{10\%}$, and CTX-M-BP$_{20\%}$, exhibit 52%, 93 % ($p<0.001$), 66 ($p<0.001$), and 56, respectively **(Figure 4.8D)**. We found that M-BP$_{20\%}$

particles have the highest total fluorescence in RAW 264.7 cells indicating higher BP bone-targeted particle uptake profile comparing to other particle formulations. Because of higher particle internalization, CTX-loaded M-BP$_{20\%}$ show higher therapeutic effect in comparison to other formulations. Lastly, RANKL activated RAW 264.7 cells were treated with the same therapeutics -free CTX, CTX-M, CTX-M-pVTK$_{10\%}$, and CTX-M-BP$_{20\%}$- showing 72%, 82%, 73%, and 67% cell viability without statistically difference comparing to free CTX **(Figure 4.8E)**. However, the lowest viability is acquired with the treatment of CTX-loaded M-BP$_{20\%}$ particles, which is statistically different in comparison to CTX-loaded non-targeted particles ($p< 0.01$).

Once these *in vitro* results are interpolated to *in vivo*, it is noteworthy that free CTX, which is the highest viability knock-down for almost all cell lines, is lack of targeting of metastasized bone. Therefore, we do not expect to see efficient therapeutic effect because of not significant amount of free CTX accumulated in bone. Whereas, CTX-loaded non-targeted particles does not exhibit a higher cell viability inhibition effect in tumor cells as *in vitro*. However, some portion of non-targeted particles might accumulate in the bone metastasized tumor lesion due to EPR effect. Nevertheless, CTX-loaded pVTK-targeted particles exhibit similar therapeutic effect like free CTX in C4-2B cells whereas CTX-loaded BP-targeted particles show that a better therapeutic efficiency than other particles formulations *in vitro* conditions. Similarly, it is expected to observe higher *in vivo* therapeutic efficacy with both bone-targeted particles against prostate cancer metastasized in bone as comparing as comparing to free CTX and CTX-loaded non-targeted particles. Even the targeted-particles act efficiently, non-specific cytotoxicity or bone-targeted particle-associated osteonecrosis of the jaw could be possible limitations of this targeted therapy [292]. However, the number of bone-targeted particles accumulation in jaw could be minimized by changing the number of targeting number density on the particle formulation.

In here we showed that we could efficiently delivery of CTX-loaded bone-targeted particles to bone. CTX is only a model anti-cancer drug we have used. However, therapeutics could be chosen from a variety of options such as, anti-body, cytokines, proteins, or other anticancer agents with the proper bone-targeted strategy to inhibit a specific cell line and at the same time the cross-talk between bone and cancer cells. By doing this strategy, it is possible get more efficient and higher therapeutic effect.

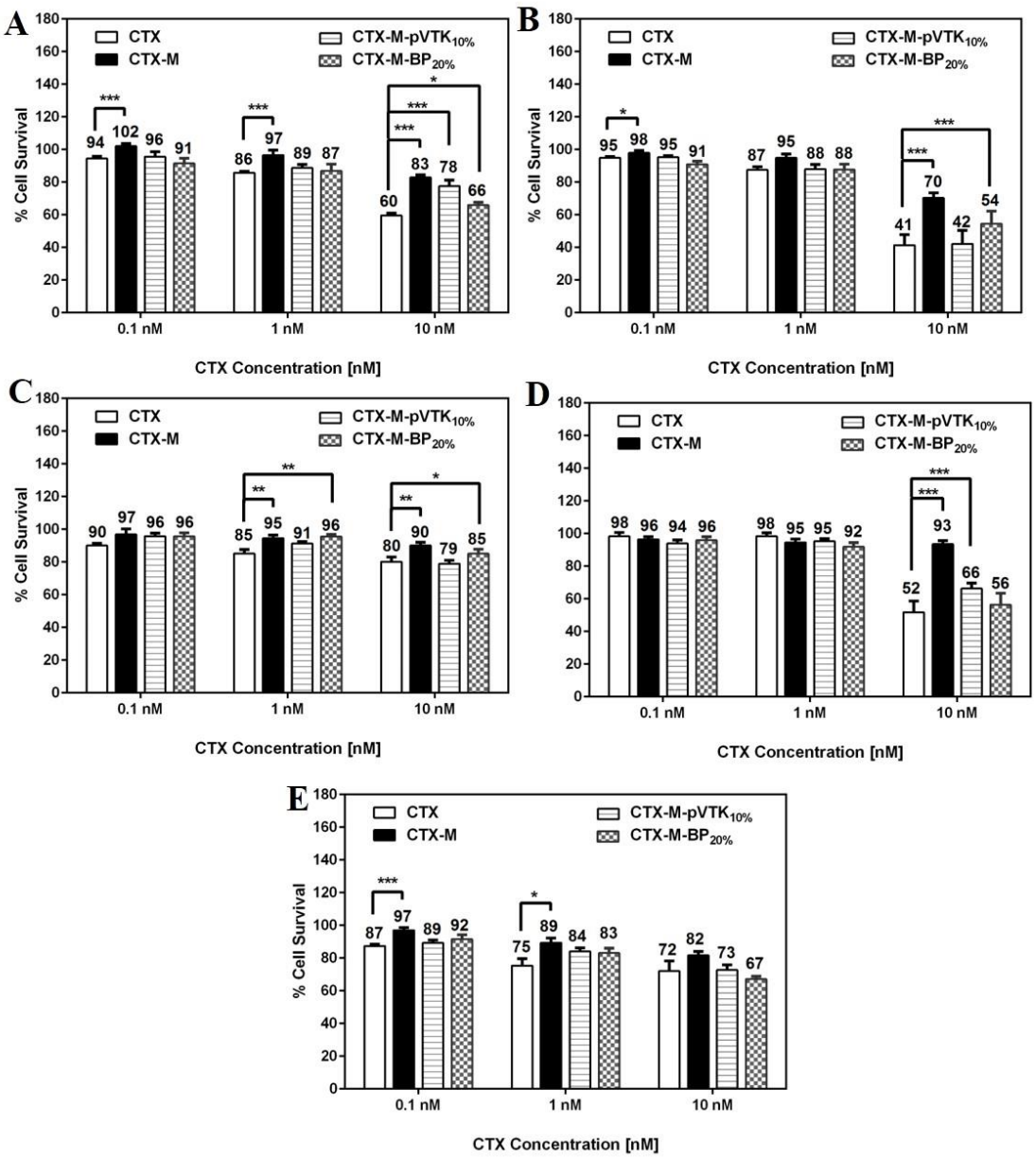

Figure 4.8 Therapeutic activity of CTX, and CTX-loaded particles in prostate and bone cells on BLS.

(A) PC-3, (B) C4-2B, (C) MC3T3, (D) RAW 264.7, and (E) RANKL activated RAW 264.7. The resazurin viability assay results of treated cells that normalized with untreated cells. Results are the average of triplicate experiments + SEM. Percentage of cell viability was compared to untreated cells using a two-tailed Student's t-test where * denotes $P < 0.05$, ** denotes $P < 0.01$, and *** denotes $P < 0.001$.

4.4 Conclusions

In summary, we have successfully synthesized two different bone-targeted pVTK-peptide and BP-decorated triblock amphiphilic copolymers via ATRP and *"click"* reactions. These copolymers self-assemble in an aqueous environment and form 60-90 nm size micelles with pH-sensitive cross-linking shells as a function of bone-targeted block densities. The results show that pVTK and BP decorated "smart" particles were able to bind to bone HA surface. pVTK bone-targeted particles exhibited preferential uptake into C4-2B prostate cancer cells and osteoblasts on the BLS. Whereas, BP bone-targeted "smart" particles were internalized preferentially by RAW 264.7 macrophage cells in regular tissue culture plates, and PC-3 cells internalized these particles higher than other cell lines on BLS. This cellular uptake difference on BLS reveals insights into personal medicine for the treatment of bone metastasis based on the metastasis type, either osteoblastic, osteolytic, or mix form. Further, these bone targeted particles were able to encapsulate Cabazitaxel, an anti-cancer agent, in the core with more than 30% drug-loading, enhancing the solubility and efficiency of a water insoluble drug. Moreover, CTX-loaded bone targeted particles showed higher therapeutic effect in prostate cancer cells on the BLS compared to free CTX and CTX-loaded non-targeted particle formulations. These results collectively show that pVTK and BP bone-targeting "smart" particles are an ideal drug carrier for selective delivery of anticancer agents into metastasized prostate cancer lesion in bone. We will investigate these particles *in vivo* to assess the efficacy of targeting ligands to metastatic prostate cancer in bone.

4.5 Acknowledgements

Omer Aydin recognizes the Fellowship from the National Ministry of Education of Republic of Turkey (#1416).

Chapter 5

Conclusion and Future Direction

5.1 Conclusion

Throughout this dissertation, we reported the design and synthesis of tri-block copolymer based nanoparticle systems that served as a platform technology for the treatment of primary as well as bone metastasized prostate cancer. Specifically, this research study successfully validated the use of the tri-block polymer platform in several applications ranging from (i) targeted nanodroplet-mediated histotripsy experiments that resulted in primary prostate cancer cell ablation at the 2-D cellular as well as 3-D spheroidal levels, ii) the efficacious delivery of anti-cancer drugs into primary prostate cancer cells via pH-sensitive "smart" micellar nanoparticles compared to the free drug. Furthermore, we demonstrated specific prostate cancer cell selectivity and functional delivery of anti-cancer drugs into bone metastasized prostate lesion using "smart" micellar nanoparticle formulations decorated with two different bone targeting agents (peptide vs bisphosphonate).

In the first part of this dissertation, we explored the effects of pre-defined ultrasound parameters on a library of well-characterized nanodroplet formulations (investigated in Appendix 1, 2, and 3). We previously showed that perfluoropentane, a widely used PFC, was successfully encapsulated in the core of tri-block amphiphilic copolymers that "self-assembled" into nanodroplet micelles (less than 200 nm in size) in aqueous systems. These acoustically active nanodroplets significantly reduced histotripsy cavitation threshold pressure in the phantom model

from 25-30 MPa to 8-13 MPa, thereby exhibiting the potential clinical application of NMH for targeted tissue ablation [46, 79]. Moreover, our studies also showed that lower frequencies (335 kHz and 500 kHz) improved the effectiveness of NMH by increasing the size of the focal region which, in turn, increased bubble expansion, and decreased cavitation threshold [80]. In another study, we evaluated the physico-chemical properties of nanodroplet formulations comprising two different perfluorocarbons namely, perfluoropentane (PFP) and perfluorohexane (PFH). While both nanodroplet formulations significantly reduced NMH cavitation thresholds compared to regular histotripsy interventions, we observed starkly different sustainable nuclei cavitation profiles in PFH-nanodroplet formulation over multiple pulses. The PFH-loaded nanodroplets showed a 20-fold higher cavitation activity over that of PFP-loaded nanodroplets because of the higher boiling point and surface tension of PFH [81, 82]. Finally, to explore the underlying physical mechanism of the nanodroplet cavitation process, we elucidated the role of positive and negative pressure on cavitation nucleation in NMH. The results showed that the cavitation nucleation phenomenon of NMH is closely related to the peak negative pressure of the incident wave [83].

In Chapter 2, we investigated the feasibility of achieving selective ablation of PC-3 and C4-2B prostate cancer cells in 3-D spheroid tissue mimic models using PFP-loaded and PFH-loaded nanodroplets at low acoustic pressure. Results showed that PFH- nanodroplets could be efficiently used for the ablation of tumor spheroids in the relevant 3-D microenvironment comparing to PFP-nanodroplets because of sustainable nuclei cavitation profiles in PFH-nanodroplet formulation over multiple pulses. Further, this result is a significant advancement upon previous NMH work and suggest that NMH can be used for targeted tumor ablation. Moreover, the significantly reduced pressure threshold values achieved through the use of PFH-

loaded nanodroplets compared to that of the current histotripsy methods using the tissues intrinsic gas pockets allows for the selective ablation of 3-D tumor models and as well as *in vivo*. Thereby, preserving the surrounding normal tissue, devoid of ND's, that require higher threshold pressure values to facilitate histotripsy-induced fractionation. Furthermore, the resulting PFP or PFH gas bubbles can function as ultrasound contrast agents, that can help identify tumor sites upon ultrasound imaging to facilitate guided and real-time tumor imaging during histotripsy treatment.

In Chapter 3, we reported the synthesis of new amphiphilic tri-block copolymers composed of a hydrophilic poly(ethylene glycol) (PEG) block, a central poly(acrylic acid) (PAA) block, and a hydrophobic poly(methyl methacrylate) (PMMA) block. Using standard characterization techniques, we showed the successful synthesis of amphiphilic tri-block copolymers, (PMMA-b-PAA-b-PEG), which proved to self-assemble in aqueous solutions forming nano-sized micelles that efficiently encapsulate hydrophobic small molecules such as Nile Red (NR, a hydrophobic fluorescent dye) and Cabazitaxel (CTX, model anticancer drug) into the hydrophobic core. Upon loading the desired concentration of hydrophobic small molecules into the core, we established acid-labile cross linkages between adjacent polymer chains forming shell cross-linked micelles (SCLM), specifically, through the reaction of 2, 2-(propane-2, 2-diylbis(oxy) diethanamine) with the carboxylic acid groups of the PAA block. We then evaluated the release profile of the loaded cargo (i.e., NR and CTX) from non-cross-linked micelles (NSCLM) and SCLM upon incubation in aqueous buffer solutions at both physiologic (pH = 7.4) and endosomal (pH = 5.0) pH values. The acid-labile cross linkages allow for a controlled and tunable release of the desired encapsulated cargo. Results illustrated that the SCLM-50 (half of the PAA units in the formulation are reacted with the pH-labile cross-linker) family exhibited the highest cytotoxic activity towards PC-3 and C4-2B cancer cells *in vitro* with IC_{50} values that were significantly lower than free CTX.

Moreover, SCLM-50 micelles did not cause hemolysis of red blood cells (RBCs), trigger platelet activation, acquire an albumin corona, or get phagocytosed by activated macrophages, which makes this micelle platform an ideal carrier for *in vivo* delivery of CTX into prostate tumors.

In chapter 4, we report the synthesis of two novel bone targeting nanoparticle strategies that comprised of coupling either a peptide, namely pVTK or bisphosphonate (BP) ligand to the PEG block of the tri-block copolymer to form two targeted, pH sensitive "smart" nanoparticle formulations. The objective of decorating the free end of the PEG block with either pVTK or BP ligands was to help facilitate selective binding and accumulation of the "smart" nanoparticles reported in Chapter 3 to metastasized bone. We evaluated the physicochemical properties of different molar ratios of targeting ligands (0, 5, 10, 20%) in both pVTK or BP nanoparticle formulations. We compared the binding capability of FITC-labeled pVTK and BP-coupled nanoparticles upon incubation in aqueous buffer solution with bone powder at pH 7.4 as a function of the targeting ligand density. The results showed that both pVTK and BP decorated "smart" particles were able to bind to bone HA surface. Further, we investigated the uptake profiles of FITC-labeled non-targeted, pVTK-labeled, and BP-labeled nanoparticles into PC-3 and C4-2B prostate cancer cells, MC3T3 pre-osteoblasts, and activated RAW 264.7 osteoclasts cultured on regular tissue culture plates and bone like surface plates. Finally, the anti-cancer agent, CTX, was loaded into the core of non-targeted, pVTK and BP-decorated nanoparticles with more than 30% loading efficiency. pVTK-targeted nanoparticles exhibited a preferential uptake into C4-2B prostate cancer cells and osteoblasts grown on the bone mimic surface. While, BP-targeted nanoparticles showed significantly higher internalization into RAW 264.7 macrophage cells cultured on regular tissue culture plates. Further, PC-3 cells cultured on bone like surfaces demonstrated higher uptake of BP-labeled nanoparticles compared to C4-2B prostate cancer cells.

Finally, we explored the therapeutic effect of non-targeted, pVTK, or BP-targeted particles that were either empty or CTX-loaded on the following four cell lines on pretreated BLS: PC-3, C4-2B, MC3T3, and RANKL activated RAW 264.7 cells. The results demonstrated that CTX-loaded bone targeted nanoparticles showed higher therapeutic effect in prostate cancer cells on the bone like surface compared to free CTX and CTX-loaded non-targeted particle formulations. All these results collectively show that pVTK and BP bone targeting "smart" nanoparticles are an ideal drug carrier for selective delivery of anticancer agents into prostate cancer lesion in bone.

5.2 Future Directions

Our immediate strategy is to perform pre-clinical validation studies with the ultimate goal of establishing two potentially promising and robust clinically-viable, nanotherapy platforms for the treatment of primary prostate cancer using targeted nanodroplet-mediated histotripsy systems as well as the treatment of bone metastasizing prostate cancer using either pVTK-peptide or BP-decorated nanoparticles encapsulating the desired anti-cancer drug. The pre-clinical phase will encompass the *in vivo* biodistribution of these nanoparticles in primary cancer and metastatic bone prostate cancer animal-tumor models, respectively. This initial study will assist us in the identification of the most efficient targeting strategy from a pharmacokinetics perspective that will result in the greatest preferential accumulation of the targeted particles in prostate cancer tissue or prostate cancer lesion in bone metastasis, respectively.

5.2.1 Development of Tumor Targeted Nanodroplets

To design prostate cancer targeted nanodroplets, we propose the use of J591, a monoclonal antibody [293], A-10 RNA [294] or peptide (sequence of WQPDTAHHWATL) [295, 296] that

will specifically bind to the extracellular domain of PSMA overexpressed on the surface of prostate cancer cells [297], as previously reported in the literature. We will conjugate these targeting ligands to the carboxylic group of COOH-PEG-Alkyne via the standard EDC/NHS coupling reaction following published protocols [298] to prepare the respective targeted-PEG-alkyne conjugates, which we will then react with PAA and P(MMA-*co*-HDFMA) blocks following methods described earlier in Chapter 2, Appendix 1, 2, and 3. We will design a library of targeted copolymers by varying the molar ratio of targeted-polymer conjugates (10%, 25%, and 50%) mixed with non-targeted tri-block copolymer to vary the number of the targeting ligands displayed on nanodroplets surface to determine the optimum targeted tri-block copolymer density on the nanodroplet formulations with conducting of cellular uptake experiments using flow cytometry. We will further investigate the physicochemical properties, echogenicity, and stability of targeted nanodroplets using the methods described in Appendix 1, 2, 3, and Chapter 2.

5.2.2 *In vivo* Nanodroplet Mediated Ultrasound Imaging

After defining well-characterized NMH US parameters and development of prostate cancer targeted nanodroplets, we will investigate the feasibility of using targeted nanodroplets for US imaging of prostate cancer micro-foci *in vivo*.

5.2.3 *In vivo* imaging of prostate cancer cells using targeted nano-bubbles

We will establish orthotopic tumors using approved IACUC animal protocols by injecting ~$1x10^6$ C4-2B-Lux and PC-3-Lux prostate cancer cells (expressing the luciferase enzyme) into the dorsolateral lobe of the prostate gland of male mice and monitor their growth by bioluminescence imaging (BLI) using IVIS imaging system (Caliper Life Sciences) [299, 300]. We will use this orthotopic mouse model (C42B-Lux) to investigate if targeted nanodroplets can selectively "home" into the implanted cancer cells and enhance their contrast with US imaging. We will

separate the tumor-bearing mice into two groups (n = 5 mice/group) where we will administer targeted nanodroplets (test group) and an equal volume of saline (control group) via tail vein injections. We will monitor the change in tumor volume using luminescence imaging every 3 days for a total of 6 weeks following established BLI protocols [300, 301]. Using the Verasonics system and 10 MHz imaging probe, we will image the prostate in both mice groups on the same day of the BLI following established US imaging protocols [302, 303]. Briefly, we will start image acquisition 10s before administering the assigned nanodroplets or saline solutions at pre-defined time points for 2 hours after injection. The fold enhancement in echogenic signal as a function of time will be calculated by subtracting the baseline value from each time point for each mouse. We will compare the calculated fold enhancement in echogenic signal in mice treated with targeted nanodropleted to the calculated echogenic signal in mice treated with saline at the same time points to determine: *i*) if targeted nanodroplets "home" into tumor lesions, and *ii*) the smallest tumor volume that can be imaged using these targeted nanodroplets. We will compare the hyper echogenic zone on US images to the zone of highest luminescence on BLI in all studies to confirm that enhanced scattering is localized to prostate cancer cells.

5.2.4 *In vivo* toxicity of targeted nanodroplets

We will investigate the toxicity profiles of our targeted nanodroplets by evaluating their hematologic (RBC & WBC and hematocrit value), liver (serum levels of ALT and AST enzymes), kidney (serum creatinine level), and heart (serum ROS level) toxicity compared to saline-treated mice 24-hours after each injection. The UM histology core will carry a blinded examination of the heart, lungs, liver, kidneys, and spleen isolated from both mice groups at the end of the imaging experiments to identify pathological signs of nano-droplet toxicity.

5.2.5 *In vivo* Nanodroplet Mediated Tumor Ablation

We will investigate the feasibility of ablating prostate cancer cells *in vivo* using targeted nano-bubbles combined with histotripsy.

5.2.5.1 Selective in vivo ablation of prostate cancer cells using targeted nano-bubbles

C42B-Lux cancer cells will be injected into the prostate of twenty mice and will be monitored for 5 weeks to determine changes in tumor volume using BLI before dividing the mice into four groups (n = 5 mice/group) where each group will receive a different treatment with the guidance of our approved protocol [300, 301]. We will administer 100 μL of targeted nanodroplets solution to the mice in group 1 (test) via tail vein injections. We will apply the histotripsy parameters that were most effective in ablating prostate spheroids *in vitro* to group 1 and evaluate the resulting therapeutic activity by measuring the reduction in the intensity of the luminescence signal after the treatment compared to its baseline value before the treatment using BLI. We will also use US imaging to monitor the drop in echogenic signal (hypoechogenic) of the cancer lesion after the histotripsy treatment. We will investigate the independent effect of targeted nanodroplets alone (group 2) and histotripsy alone (group 3) on ablation of prostate cancer cells using the same nanodroplets dose and histotripsy parameters applied to group 1, respectively. Saline will be injected to group 4 as a control. We will harvest the prostates from all mice and through a microscopic analysis by the histology core determine the size of the ablated tumor region and the extent of damage of the neighboring healthy tissue in response to each treatment. This ***pilot study*** will establish the therapeutic potential of targeted nanodroplet contrast agents in combination with histotripsy in ablating prostate cancer cells.

5.2.6 *In vivo* Validation of Bone Targeted Particles

After *in vitro* characterization of both bone targeted particles, we will focus on investigating the evaluation of bone targeting micelle particles activity *in vivo*.

5.2.6.1 Synthesis of Radio-Labeled and NIR Dye Labeled Copolymers

To do that, first we will synthesize radio-labeled particles using N-akylation reaction of NH_2 under reaction of iodoacetamide under basic conditions (pH 10) [304, 305]. Alkyne-PEG-NH_2 will be functionalized with I-[^{14}C] and then followed by alkyne-azide click chemistry strategy coupled to the copolymer block that we have used in targeting ligand and NIR 680RD dye functionalization of triblock copolymer. These radio and NIR 680RD labeled bone targeted particles will be used to quantify particles biodistribution and tracing in bone microenvironment.

5.2.6.2 Evaluation of Bone Targeted Particles Biodistribution

Two different bone metastatic prostate cancer mice models, which exhibit osteolytic (PC-3) [306], and osteoblastic/osteolytic mixed (C4-2B) [307] characters will be established by injecting a cell suspension comprising of either PC-3 or C4-2B cells ($2x10^5$ cells) into the proximal tibia. After tumors are established, the following experiments might be conducted. Each group of tumor-bearing mice model (n = 4) will be given a single bolus dose of [^{14}C]-pVTK and [^{14}C]-BP targeted particles (0.67 mg) via intravenous (I.V.) administration through tail-vein injections. The distribution of the particles as a function of time after injection (0.5, 2, 4, 8, 24, 36, 48, and 72 hours) will be quantified. The amount of radioactive nuclide present in the systemic circulation, tumor, bone, brain, heart, lungs, liver, kidney, spleen, and excretions will be quantified per microgram of each tissue through liquid scintillation counting. The amount of [^{14}C]-labeled particles distributed to each tissue will be normalized to the corresponding extraction efficiency for that tissue and results for each treatment group will be presented as the average % of the injected dose per tissue ± SEM [308]. The biodistribution results will also be used to evaluate the

blood to bone particle distribution ratio, blood to tumor distribution ratio, plasma retention time, and tumor retention ability of the particles per gram of organ. From the tumor retention time calculation, the dosing regimen, which is related to repeating injection interval based on the time point that the concentration of micelles in tumor starts to decrease, will be determined.

5.2.6.3 Tracing of bone targeted, NIR 680RD dye labeled particles

In previous *in vitro* bone mimic surface uptake studies, we showed that different targeting ligands exhibited varying binding propensities for different prostate cancer cell lines. For instance, pVTK is good at for targeting C4-2B and osteoblast cells, whereas BPs is a good candidate for targeting to PC-3 and macrophages. To evaluate if a similar trend extends to *in vivo* model, we will validate the targeting capabilities of our nanoparticles by tracing the NIR 680RD labeled bone targeted nanoparticles [309-311]. Briefly, we will inject NIR 680RD labeled both pVTK-targeted and BP-targeted nanoparticles into either the above mentioned bone metastatic mice models and healthy mice as a control via tail vein injections. Post particle injection, the proximal tibia's will be shaved and depilated, and the proximal tibial fluorescence will be monitored by *in vivo* non-invasive serial imaging at 2, 6, and 24 h (Maestro, CRi). After 24 h, the mice will be euthanized, following the dissection of the tibia and femur, and ex vivo imaging for to determine the spatial localization of the nanoparticles. Following fluorescent imaging, tibia and femurs will be imaged by micro–computed tomography (mCT) and the images reconstructed at 18-mm voxel size to correlate bone fluorescence with bone surface area in the distal femur/tibia following established protocols [309-311].

5.2.6.4 In vivo Anticancer Activity and Toxicity of CTX-Loaded Bone-Targeted Particles

The anticancer activity of the CTX-loaded bone targeted nanoparticles (~1.42 mg, calculated based on the maximum non-lethal dose for mice (25 mg/kg)) will be explored [312] by

injecting them into tumor-bearing mice models as a function of dosing regimen period as well as measuring tumor toxicity, in terms, of tumor volume compared to control treatments of free CTX (0.75 mg) and saline, and CTX-loaded non-targeted particles. The anticancer activity will be monitored by measured tumor volume up to 12 weeks for PC-3 and C4-2B tumor models, as well as by monitoring mouse survival rate. Further, at the end of *in vivo* anticancer activity study, the biocompability tests involving hematology evaluation of red blood cell count, neutrophil count, reticulocyte count, hemoglobin, hematocrit, white blood cell count, white blood cell percentage, platelet count will be conducted and organ/tissue pathology samples of the bone, brain, liver, kidney, spleen, heart, etc. will be collected and evaluated for organ toxicity by pathological evaluation performed with help of the UM histology and pathology facility. Free CTX will be used as a control in all cases.

Appendices

Appendix A

The Effects of Ultrasound Frequency on Nanodroplet-Mediated Histotripsy

The material in this chapter is published from the following article: E. Vlaisavljevich, **O. Aydin,** Y. Y. Durmaz, K-W Lin, B. Fowlkes, M. ElSayed, and Z. Xu "The Effects of Ultrasound Frequency on Nanodroplet-Mediated Histotripsy" *Ultrasound in Medicine and Biology*, 41(8), 2135, **2015**.

Introduction

Histotripsy is a noninvasive, image-guided tissue ablation method that controllably fractionates soft tissue through cavitation generated by high pressure, short duration ultrasound pulses [43, 49, 313]. Histotripsy depends on the initiation and maintenance of a dense cavitation bubble cloud to produce mechanical tissue fractionation [314, 315]. Previous work has shown that, using a 1-2 cycle pulse with a single dominant negative pressure phase, histotripsy bubbles can be reproducibly generated in tissue when the peak negative pressure is raised above the histotripsy intrinsic threshold of ~25-30 MPa [44, 316]. In order to effectively fractionate tissue into acellular

debris, histotripsy requires bubbles to rapidly expand into large cavitation bubbles, often greater than ~50μm in diameter [79, 313, 317, 318]. Using a pressure high enough to initiate a bubble cloud, histotripsy has been shown capable of completely fractionating soft tissue into a liquid-appearing homogenate with no cellular structures remaining [43, 49, 161]. Histotripsy is currently being studied for many clinical applications in which non-invasive tissue removal is desired including benign prostatic hyperplasia [319], deep vein thrombosis [164], congenital heart disease [165, 166], and cancer ablation [45, 167].

Although histotripsy has shown promise for many clinical applications including tumor ablation, this approach is limited to applications in which the target tissue can be identified and imaged prior to treatment, which is often not feasible in cancer patients with many small tumor nodules and micro-metastases. As a result, our team has developed a new targeted ablation approach combining perfluoropentane (PFP) encapsulated nanodroplets with histotripsy [46, 79]. This nanodroplet-mediated histotripsy (NMH) approach takes advantage of the significantly reduced cavitation threshold of the nanodroplets, allowing for cavitation to be selectively generated only in regions containing the nanodroplets [79]. Preparing nanodroplets in the size range of ~100-400 nm allows them to diffuse across the leaky tumor vasculature and preferentially accumulate in the tumor, which allows NMH to potentially achieve selective ablation of tumors [46, 79]. In a previous study [79], the initial feasibility of this approach was demonstrated, with results supporting our hypothesis that nanodroplets significantly decrease the histotripsy threshold to form a cavitation bubble cloud while maintaining the effectiveness of histotripsy tissue ablation. NMH was shown capable of creating microbubble expansion and collapse as well as well-defined ablation similar to histotripsy but at significantly lower pressure [79]. Furthermore, the potential to use this approach for simultaneous multi-focal ablation was demonstrated [79].

To build upon our initial study, this work aims to investigate the effects of ultrasound frequency on NMH. We hypothesize that lower frequency will offer multiple advantages for NMH therapy. First, as the transducer focal zone scales with the wavelength, a low frequency transducer will yield a large focal zone, allowing histotripsy to be applied simultaneously to cover large and/or multi-nodule tumors seeded with our nanodroplets, thus increasing the treatment efficiency for such tumors. Lower frequency is also more resistant to acoustic aberration and attenuation from bone obstruction and long overlying tissue, resulting in deeper penetration depth. The use of nanodroplets targeted for tumor uptake will allow selective ablation of such tumors without need to otherwise identify the treatment location, keeping the selectivity of targeting the tumor despite the larger focal zones. Additionally, we hypothesize that lower frequency will decrease the cavitation threshold using nanodroplets while facilitating greater bubble expansion compared to higher frequency. In this study, we tested this hypothesis by exposing tissue phantoms with and without nanodroplets to histotripsy pulses produced by 345 kHz, 500 kHz, 1.5 MHz, and 3 MHz histotripsy transducers. First, the probability of generating inertial cavitation from a single 1-2 cycle histotripsy pulse was measured for each frequency, with the cavitation threshold defined as the peak negative pressure at which the probability of generating cavitation, p_{cav}, from a single histotripsy pulse was 0.5 (i.e. $p_{cav} = 0.5$). Next, the effect of frequency on the size of NMH bubbles was compared using high speed optical imaging. Finally, the ability of PFP-encapsulated nanodroplets to act as sustainable cavitation nuclei over multiple pulses was investigated, as multiple pulses (often>100) are needed to completely destroy all the tumor cells within the treatment volume. Overall, these results will improve our understanding of the NMH process and help guide parameter optimization for multi-focal tumor ablation using NMH.

Methods

Formulation and Characterization of Nanodroplets

The ideal polymer composition and PFP content of the nanodroplets used in this study were identified in our previous study [46]. A poly(ethylene glycol)-*b*- poly(acrylic acid)-*b*-poly(heptadecafluorodecyl methacrylate-*co*-methyl methacrylate) triblock copolymer was synthesized using a combination of atom transfer radical polymerization (ATRP) and "click" coupling techniques to prepare PFP-loaded nanodroplets [46]. Briefly, the copolymers were dissolved in tetrahydrofuran anhydrous (THF, >99.9 %, Sigma-Aldrich, St. Louis, MO, USA) (0.2% w/v) and cooled down to 0 ^{o}C before the addition of perfluoropentane (PFP, 97% ca. 85% n-isomer, Alfa Aesar, Ward Hill, Massachusetts, USA) (2% v/v) while vigorously stirring the reaction mixture. An equal amount of water was slowly added to this solution mixture to trigger micelle formation and the mixture was stirred for 1h in an ice bath. The micelles solution was transferred into a dialysis bag (MWCO of 1 KDa, Spectrum, Rancho Dominguez, CA, US) and dialyzed against ice-cold 2-(*N*-morpholino) ethanesulfonic acid monohydrate solution (MES, 99 %, Acros Organics, Geel, Belgium) of pH 5.5 for 12 hours to remove the THF and get a milky solution of non- cross-linked PFP-loaded nanodroplets. This milky solution was transferred to a round bottom flask and mixed with the 2,2`-(ethylenedioxy)-bis(ethylamine) cross-linker (98% 2,2`-(ethylenedioxy)-bis(ethylamine), Sigma-Aldrich, St. Louis, MO, USA) which reacts with the central PAA block in the polymer backbone via NHS/EDC coupling chemistry (97% N-hydroxy succinimide; 98% N-(3-Dimethylaminopropyl)-N′-ethylcarbodiimide hydrochloride, Sigma-Aldrich, St. Louis, MO, USA) forming cross-linked nanodroplets with a flexible polymer shell. Shell cross-linked nanodroplets were dialyzed against ice-cold water for 12 hours to remove the byproducts of the cross-linkage reaction.

Concentration and size distribution of the nanodroplets were measured using Nanoparticle Tracking Analysis (NTA). Briefly, the NanoSight™ LM10 (Malvern Instruments, Amesbury, UK), equipped with a temperature-controlled 405 nm laser module, high sensitivity Scientific Complementary Metal–Oxide–Semiconductor (sCMOS) camera (Hamamatsu, Orca, Hamamatsu City, Japan), and a syringe pump was used for the collection of NTA data. Upon diluting the nanodroplet solution to the appropriate particle concentration with deionized (DI) water (Thermo Scientific, GenPure, Waltham, MA, US), image capture and analysis was carried out using the NTA software (Version 3.0, Build 0066, Malvern Instruments, Amesbury, UK) at 37°C. The samples were measured by capturing 60s videos (5 videos per each sample). **Figure A.1** is a representative plot showing the size distribution for a single sample of nanodroplets. The error bars represent the standard deviation of the repeat measurements of each sample. The mean size and standard deviation values obtained by the NTA software correspond to arithmetic values calculated with the sizes of all particles analyzed for each sample (n=5). Results from all samples demonstrated that the average size of the nanodroplets (NDs) was 177.9±1.9 nm with 10% of NDs have a diameter ≤ 111±1.4 nm, 50% of the NDs have a diameter ≤ 155.7±2.1 nm, 90% of the NDs have a diameter ≤ 268.5±6.7 nm, and >99% of the NDs smaller than 400 nm and <0.01% larger than 600 nm. These results clearly show that the average size of the NDs is much smaller than the size cutoff (~500 nm) of the tumor vasculature [320, 321].

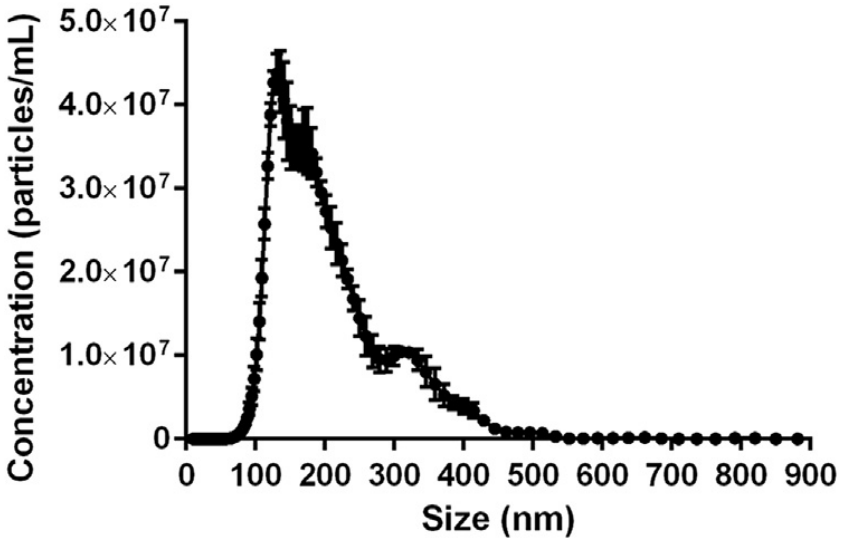

Figure A.1 Nanodroplet size distribution results show an average nanodroplet size of 177.9±1.9 nm.

Preparation of Tissue Phantoms

Agarose phantoms were used to provide a well-controlled viscoelastic medium for this study, as histotripsy bubble behavior is highly dependent on the tissue mechanical properties [322-324]. The Young's modulus of the agarose tissue phantom was 38kPa, which is within the range of the Young's modulus of hepatocellular carcinoma tumors (20.4–75 kPa), metastatic liver tumors (23.6–75 kPa), and prostate tumors (24 kPa) [325-327]. Tissue phantoms containing 1% agarose w/v were prepared by slowly mixing agarose powder (Agarose Type VII; Sigma-Aldrich, St. Louis, MO, USA) into saline solution (0.9% sodium chloride; Hospira, Lake Forest, Illinois, USA) heated to boiling temperature. The solution was stirred on a hot plate until the gel turned completely transparent and then allowed to boil for ten minutes. After boiling, solutions were allowed to cool and were degassed under a partial vacuum (~20 kPa, absolute) for 30 minutes. After degassing, phantoms containing nanodroplets were prepared by slowly adding the nanodroplets ($2.0x10^8$ particles/mL) into the agarose solution while stirring. The agarose mixtures

were poured into rectangular polycarbonate holders with acoustic windows and placed in a refrigerator at 4°C to allow the solution to solidify, forming tissue phantoms with embedded nanodroplets (test) or without nanodroplets (control). A nanodroplet concentration of $2.0x10^8$ particles/mL was used for all samples, as preliminary experiments demonstrated that lower concentrations (i.e. ~10^6-10^7 particles/mL) did not significantly reduce the cavitation threshold in comparison to control conditions.

Histotripsy Pulse Generation

Histotripsy pulses were generated at four ultrasound frequencies (345 kHz, 500 kHz, 1.5 MHz, and 3 MHz) using three custom-built histotripsy transducers. The 345 kHz pulses were generated by a twenty-element array transducer with a geometric focus of 150 mm, an aperture size of 272 mm, and an effective f-number of 0.55. The 1.5 MHz pulses were generated by a six-element array transducer with a geometric focus of 55 mm, an aperture of 79 mm in the elevational direction and 69 mm in the lateral direction, and effective f-numbers of 0.7 and 0.8 in the elevational and lateral directions, respectively. The 500 kHz and 3 MHz pulses were generated by a dual frequency array transducer that consisted of twelve 500-kHz elements and seven 3-MHz elements. For the 500 kHz elements, the geometric focus was 40 mm, the aperture size was 71 mm, and the effective f-number was 0.56. For the 3 MHz elements, the geometric focus was 40 mm, the aperture size was 80 mm, and the effective f-number was 0.5. The design of this dual frequency transducer has been described in detail in a previous study [328].

To compare the NMH cavitation threshold with the histotripsy intrinsic threshold, short pulses with a single dominant negative pressure half-cycle were applied to the tissue phantoms with and without nanodroplets. To generate a short therapy pulse, a custom high-voltage pulser developed in-house was used to drive the transducers. The pulser was connected to a field-

programmable gate array (FPGA) board (Altera DE1 Terasic Technology, Dover, DE, USA) specifically programmed for histotripsy therapy pulsing. This setup allowed the transducers to output short pulses of less than two cycles. A fiber-optic probe hydrophone built in-house [172] was used to measure the acoustic output pressure of the transducers. At higher pressure levels (p- > 23 MPa), the acoustic output could not be directly measured due to cavitation at the fiber tip. These pressures were estimated by a summation of the output focal peak negative pressure (p-) values from individual transducer elements. This approximation assumes minimal nonlinear distortion of the waveform occurs within the focal region. In a previous study [44], this estimated p- was found to be accurate within 15% compared to direct focal pressure measurements in water and in a medium (1,3 butanediol) with a higher cavitation threshold. Sample acoustic waveforms produced by the four frequency transducers are shown in **Figure A.2**.

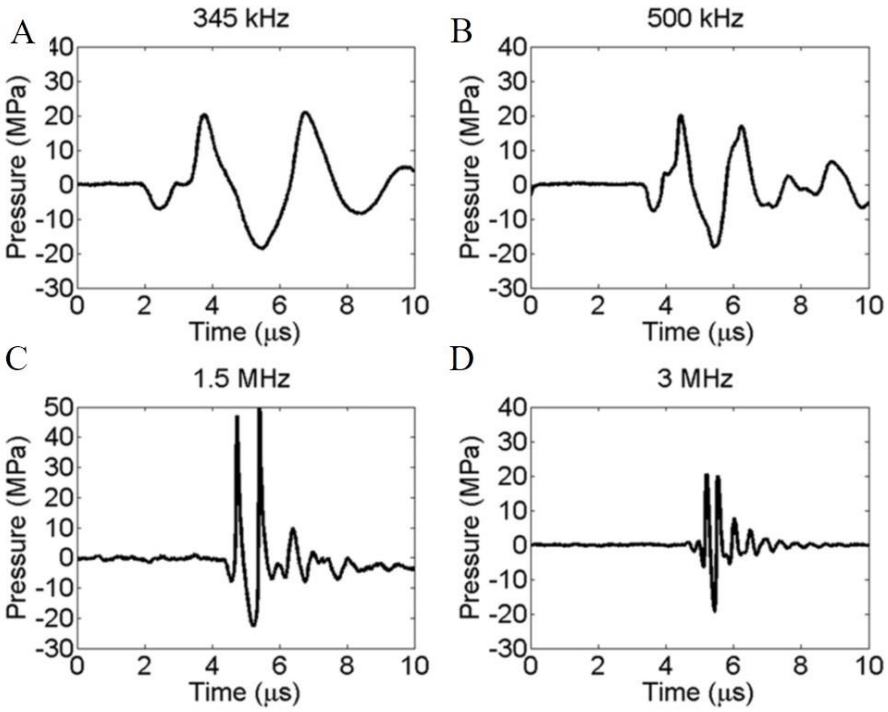

Figure A.2 Acoustic waveforms. Example of a 2-cycle histotripsy pulses generated by the 345 kHz, 500 kHz, 1.5 MHz, and 3 MHz histotripsy transducers.

Optical Imaging and Image Processing

High speed optical imaging was used to capture images of the focal zone after the propagation of each pulse through the focus for water and agarose tissue phantoms using two high speed cameras (**Figure A.3**). The optics were varied for the different transducers to provide the highest resolution based on the geometric constraints of the transducers and the available optical windows. For experiments with the 345 kHz and 1.5 MHz transducers, a high-speed, 1 megapixel CCD camera (Phantom V210, Vision Research, Wayne, NJ, USA) was aligned with the transducer and backlit by a continuous white-light source. The camera was focused using a macro-bellows lens (Tominon 1:4.5, F=105 mm; Kyocera, Kyoto, Japan), giving the captured images a resolution of approximately 5.9 µm per pixel and 3.4 µm per pixel for 345 kHz and 1.5 MHz, respectively.

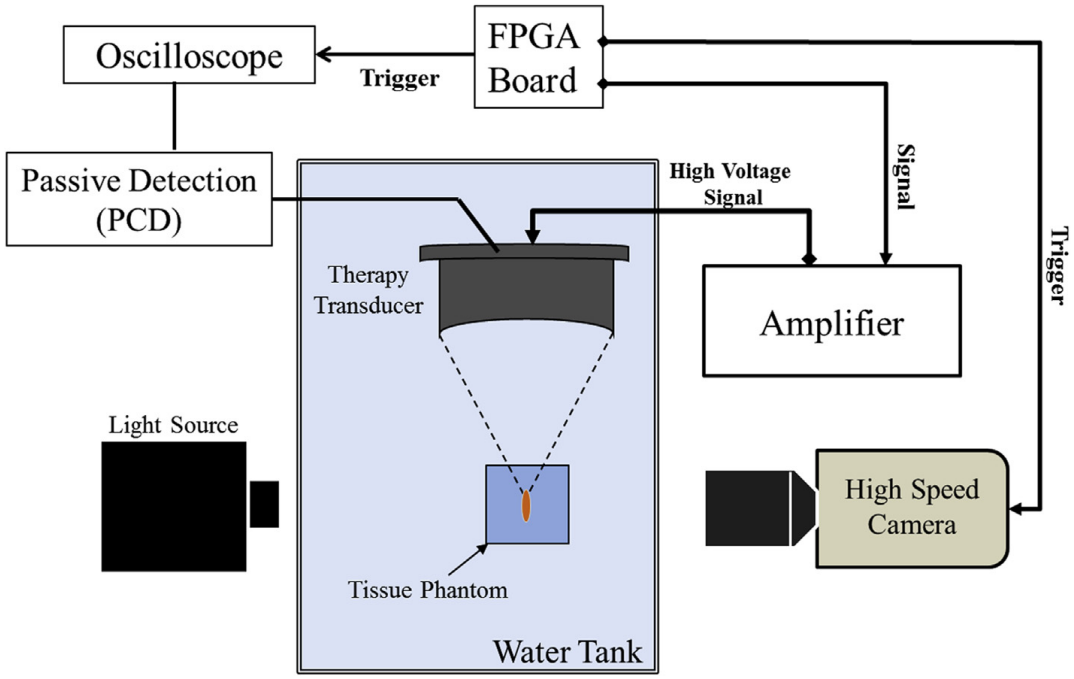

Figure A.3 Experimental set-up. The focus of the histotripsy transducer was aligned inside tissue phantoms with and without nanodroplets.

Cavitation was monitored using high speed optical imaging and passive cavitation detection using one of the therapy elements.

For experiments with the 500 kHz and 3 MHz dual frequency transducer, a digital, 1.3-megapixel CCD camera (PN: FL3-U3-13Y3M-C, Flea® 3, PointGrey, Richmond, BC, Canada) was positioned perpendicularly to the dual-frequency array transducer facing one of the transducer's optical windows. A Nikon 4X objective was attached to the camera with extension tubes to magnify the image plane, giving the captured images a resolution of approximately 2.5 μm per pixel. A pulsed white-light LED was placed on the diametrically-opposed optical window of the dual-frequency array transducer, which provided back-lit illumination. The cameras were triggered to record one image for each applied pulse. After acquisition, shadowgraph images were converted from grayscale to binary by an intensity threshold determined by the background intensity using image processing software (MATLAB, The Mathworks, Natick, MA, USA), as described in a previous study [44]. Bubbles were indicated as any black regions greater than 5 pixels in diameter. By this criterion, the minimum resolvable bubble radius was 14.75 μm, 6.25 μm, 8.5 μm, and 6.25 μm for the 345 kHz, 500 kHz, 1.5 MHz, and 3 MHz transducers, respectively.

Passive Cavitation Detection (PCD)

In addition to high speed imaging, an acoustic method was used to identify cavitation in the focal zone for cavitation threshold experiments. For each experiment, one of the transducer's therapy elements was also used for passive cavitation detection (PCD) to detect the presence of cavitation in the focal region (**Figure A.3**). The PCD signal was connected to an oscilloscope (LT372; Lecroy, Chestnut Ridge, NY, USA) with the time window selected to record the backscattering of the therapy pulse from cavitation bubbles [44, 316, 323]. To determine whether cavitation occurred during a pulse, the signal generated by backscattering of the incident pulse from the focus was analyzed following the method used in previous studies [44, 316]. A significant fraction of the incident wave energy is scattered when a cavitation bubble expands, greatly

increasing the backscattered pressure amplitude received by the PCD. This signal appeared on the PCD at the time point corresponding to two times the time of flight for the focal length of the respective transducers. The integrated frequency power spectrum (S_{PCD}) of the backscatter signal was used as a measure of whether cavitation occurred according to the method previously described by Maxwell *et al* [44].

NMH Cavitation Threshold

For cavitation threshold experiments, 100 pulses were applied inside each sample at each pressure level at a pulse repetition frequency (PRF) of 0.5 Hz. The PRF was kept low to minimize the possibility that cavitation from one pulse would change the probability of cavitation on a subsequent pulse. In a previous study, it was demonstrated that cavitation during a pulse increased the likelihood of cavitation on a following pulse for PRFs > 1 Hz, but this effect was not observed for PRFs below 1 Hz [44]. In addition to this low PRF, the focus was translated for each pulse by 1 mm transverse to the acoustic propagation direction in a 10 × 10 grid in order to minimize the effects of cavitation damage to the nanodroplets or tissue phantom sample from altering the probability of cavitation. For each pulse, cavitation was monitored using both high speed imaging and PCD, and the fraction of total pulses (out of 100) for which cavitation was detected was determined as the cavitation probability.

The probability of observing cavitation followed a sigmoid function, given by

$$P(p_-) = \frac{1}{2} + erf\left(\frac{p_- - p_t}{\sqrt{2\sigma^2}}\right) \quad \text{Eq. 6.1}$$

where *erf* is the error function, p_t is the negative pressure at which the probability p_{cav}=0.5, σ is a variable related to the width of the transition between p_{cav}=0 and p_{cav}=1, with ± σ giving the difference in pressure from about p_{cav}=0.15 to p_{cav}=0.85 for the fit [44]. The cavitation threshold

for each sample, p_t, is defined as the p- corresponding to p_{cav}=0.5 as calculated by the curve fit. Curve fitting for all data sets was performed using an OriginLab curve fitting program (OriginPro 9.1; OriginLab Corporation, Northampton, MA, USA). The fit curves for all samples were analyzed statistically to determine whether the differences in the values of p_t were significantly different from each other. The standard errors for p_t were estimated by a covariance matrix using the delta method [329]. The curves were compared using a two-sample t-test with statistic $t\left(p_{int1}-p_{int2},\sqrt{SE_1^2+SE_2^2}\right)$ at a 95% confidence interval. Results were considered statistically significant for $p<0.05$. Note that the standard error does not include the uncertainty in absolute pressure from the hydrophone measurement, only the uncertainty in the fit, because the values p_t are relative. A sample size of 3 tissue phantoms was used for each experimental condition.

NMH Bubble Size

To determine if nanodroplet-mediated cavitation bubbles were expanded similarly to histotripsy bubbles at higher pressure, optical images of the growth and collapse of bubbles were recorded by the high-speed camera. Nanodroplet-mediated cavitation bubbles were generated by the 345 kHz, 500 kHz, 1.5 MHz, and 3 MHz transducers at peak negative pressures slightly above the nanodroplet cavitation threshold at each frequency. More specifically, the peak negative pressure was 10.8 MPa (345 kHz), 10.3 MPa (500 kHz), 12.9 MPa (1.5 MHz), and 14.7 MPa (3 MHz). For comparison, bubbles were produced in tissue phantoms without nanodroplets at estimated peak negative pressures of 26.4 MPa (345 kHz), 26.3 MPa (500 kHz), 26.8 MPa (1.5 MHz), and 28.8 MPa (3 MHz), which is slightly above the intrinsic threshold without nanodroplets. The maximum radius of bubbles was compared by reconstructing the average expansion and collapse behavior using a series of time-delayed images of the bubbles produced by identical histotripsy pulses. The specific delay times were varied based on the frequency and

sample in order to reconstruct a sequence of bubble images and determine the time point corresponding to the maximum bubble radius, R_{max}. The R_{max} was compared between samples by analyzing results from 20 identical histotripsy pulses recorded at the time of maximum expansion, with each pulse applied to a different point in the sample (2 mm spacing) to prevent the effects of cavitation damage from altering the tissue phantom and nanodroplet properties. The size of single bubbles was measured for all twenty pulses to determine the bubble radius, and the mean and standard deviation in bubble radius were calculated. A sample size of 6 tissue phantoms was used for each experimental condition.

NMH Multi-pulse Sustainability

To determine if nanodroplets are sustainable cavitation nuclei over multiple pulses, 1000 ultrasound pulses were applied to a single focal region in tissue phantoms containing nanodroplets at a PRF of 1 Hz and peak negative pressures of 10.8 MPa (345 kHz), 10.3 MPa (500 kHz), 12.9 MPa (1.5 MHz), and 14.7 MPa (3 MHz). In a previous study, nanodroplet-mediated histotripsy created consistent, well-defined fractionation in tissue phantoms at 10 Hz PRF by maintaining cavitation at over multiple pulses [79]. However, it is unclear whether the nanodroplets themselves or the residual nuclei from previous pulses are responsible for seeding cavitation after the first few pulses. As a result, the PRF in this study was kept low (1 Hz) to minimize the contributions of residual nuclei from a previous pulse from effecting cavitation generation on a subsequent pulse in order to determine if nanodroplets continue to function as viable cavitation nuclei after the first few pulses or if the nanodroplets are destroyed in the cavitation process. Cavitation was monitored using high speed optical imaging, and the number of bubbles produced by each pulse was compared for 1000 histotripsy pulses in each sample. In order to quantify the ability of nanodroplets to sustain a cavitation bubble cloud over multiple pulses, the number of pulses before

cloud extinction, P_{Ext}, was plotted as a function of frequency. A sample size of 6 tissue phantoms was used for each experimental condition.

Results

NMH Cavitation Threshold

To investigate the effects of ultrasound frequency on the NMH threshold, histotripsy pulses were applied to tissue-mimicking agarose phantoms with and without nanodroplets using the 345 kHz, 500 kHz, 1.5 MHz, and 3 MHz histotripsy transducers. For all frequencies, cavitation bubbles

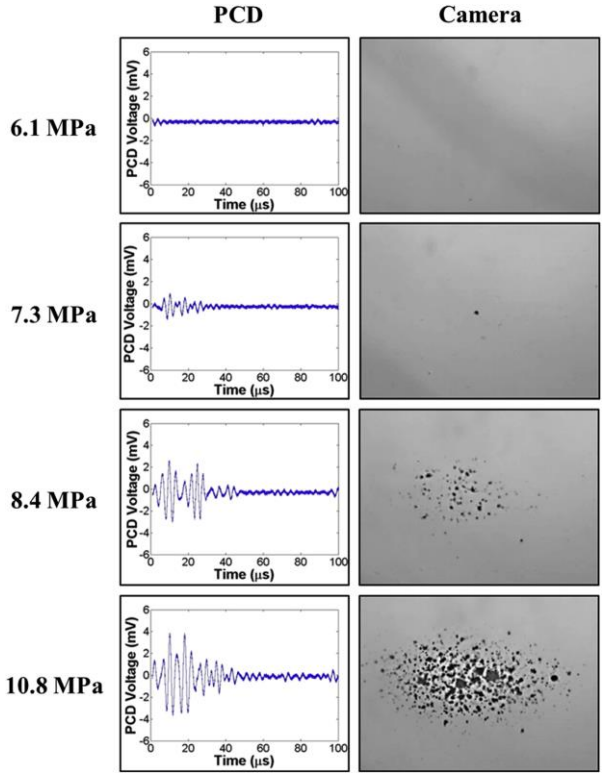

Figure A.4 Cavitation detection. Sample passive cavitation detection (PCD) signals (top) and high speed optical images (bottom) used for cavitation detection.

Results showed good agreement between the two methods. Representative images shown above are from 345 kHz histotripsy pulses applied to tissue phantoms containing nanodroplets.

were observed on the high-speed camera when a certain negative pressure was exceeded, with close agreement between optical imaging and PCD detection methods (**Figure A.4**), as seen in

previous studies [44, 316]. Results from phantoms without nanodroplets show that the histotripsy intrinsic threshold, p_{t_int}, was p_{t_int} =24.8±1.1 MPa, with σ_{mean} = 2.0 MPa for 345 kHz; p_{t_int} = 25.5±1.7 MPa, with σ_{mean} = 1.8 MPa for 500 kHz; p_{t_int} = 26.7±0.4 MPa, with σ_{mean} = 1.0 MPa for 1.5 MHz; and p_{t_int} = 26.8±0.5 MPa, with σ_{mean} = 0.9 MPa for 3 MHz (**Figure A.5**). Note that at lower amplitudes, cavitation was occasionally observed that deviated from the curve function, especially at lower frequency. These cavitation events were probably caused by contamination of the sample by heterogeneities in the liquid that could not be entirely avoided throughout the experiment. The effects of nanodroplets on the cavitation threshold demonstrated a significant decrease in the cavitation threshold compared to the histotripsy intrinsic threshold (**Figure A.5**). The NMH threshold for phantoms containing PFP nanodroplets, p_{t_PFP}, was p_{t_PFP} =7.4±0.1 MPa, with σ_{mean} = 1.4 MPa for 345 kHz; p_{t_PFP} = 9.2±0.9 MPa, with σ_{mean} = 0.8 MPa for 500 kHz; p_{t_PFP} = 10.5±0.2 MPa, with σ_{mean} = 0.4 MPa for 1.5 MHz; and p_{t_PFP} = 13.2±0.4 MPa, with σ_{mean} = 0.6 MPa for 3 MHz (**Figure 6.5**). The results of the cavitation threshold for all frequencies are plotted in **Figure 6.6**. Comparing the results for the NMH threshold and histotripsy intrinsic threshold demonstrated a significant decrease in the cavitation threshold and a significant increase in the steepness of the S-curve (σ) for samples containing nanodroplets at all frequencies. Additionally, it was observed that the NMH threshold was significantly decreased at lower frequency (**Figure A.6**).

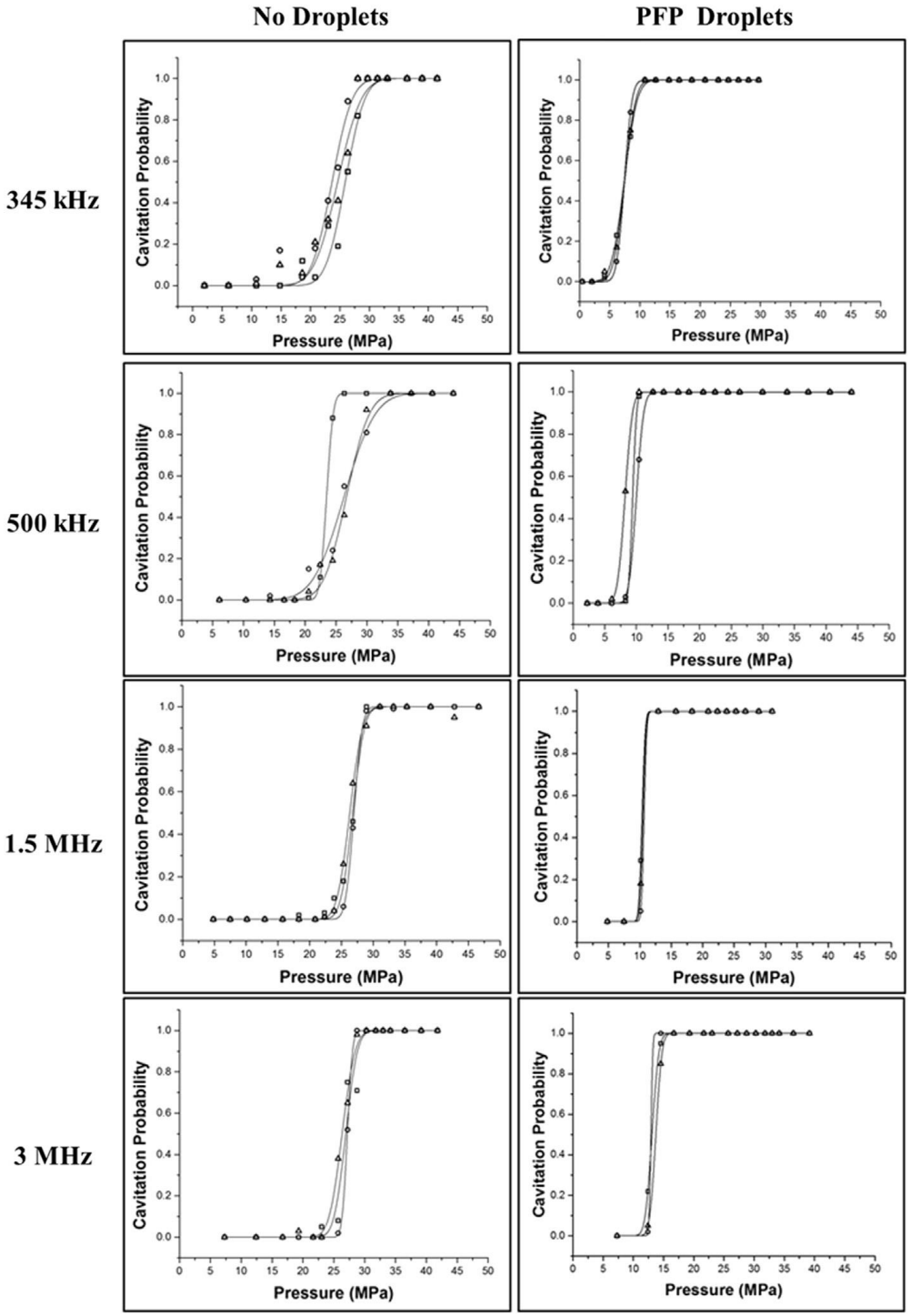

Figure A.5 Cavitation threshold curves. Probability curves for tissue phantoms with and without nanodroplets.

Results showed a significant decrease in the cavitation threshold with nanodroplets compared to controls. Results also showed a significant increase in the nanodroplet cavitation threshold with increasing frequency.

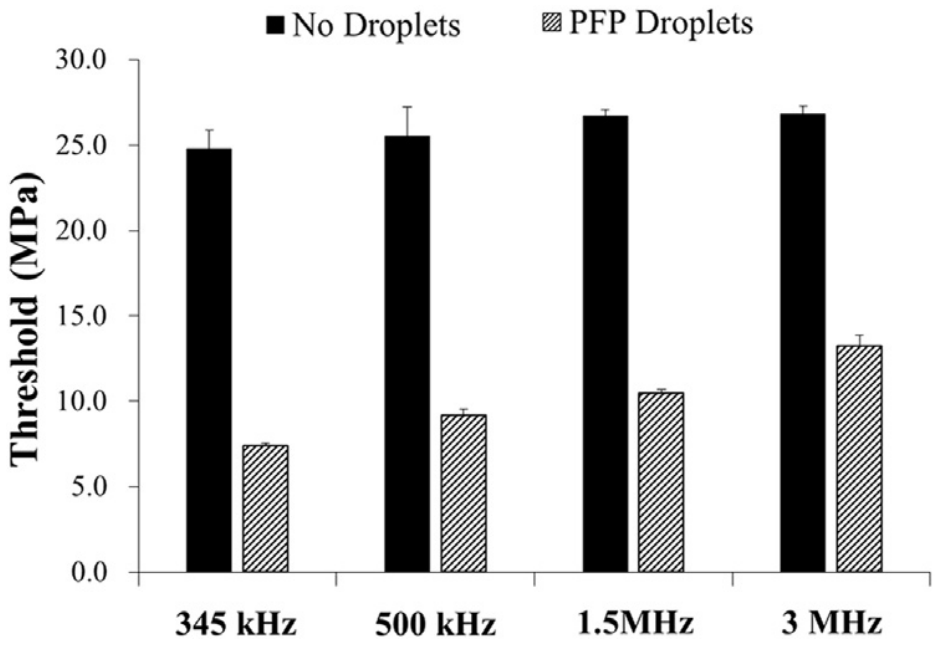

Figure A.6 Cavitation threshold results. Bar plots show the cavitation threshold results for tissue phantoms with and without perfluoropentane (PFP) nanodroplets at all frequencies studied in this work.

NMH Bubble Size

To study the effects of ultrasound frequency on the expansion of NMH bubbles, the maximum bubble radius, R_{max}, produced by 345 kHz, 500 kHz, 1.5 MHz, and 3 MHz histotripsy pulses was measured in phantoms with and without nanodroplets. The peak negative pressure used for each frequency was chosen to be slightly above the cavitation threshold at each frequency so that cavitation was always generated (P_{cav}=1). Optical imaging results demonstrated that NMH bubbles were significantly smaller than histotripsy bubbles generated above the intrinsic threshold (**Figure A.7**). Note that different image magnifications were used for each frequency for the images shown in **Figure A.7**, to provide a better image of the bubbles produced at each frequency.

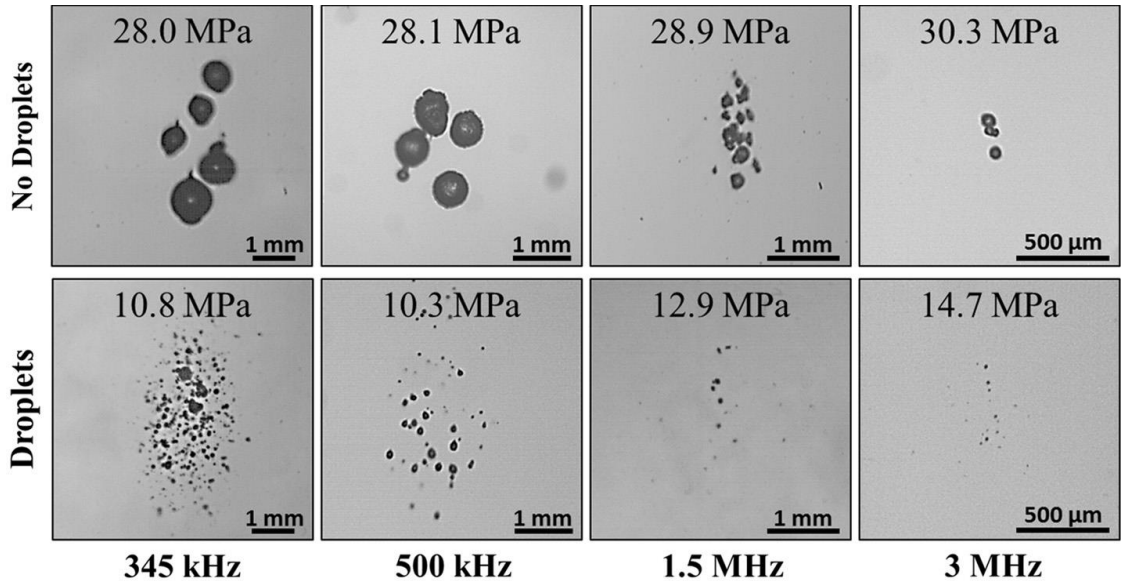

Figure A.7 Bubble R_{max} Images: Optical images of bubbles formed in tissue phantoms, with and without nanodroplets, by 345 kHz, 500 kHz, 1.5 MHz, and 3 MHz histotripsy pulses.

Results show a significant decrease in bubble size for nanodroplet-mediated histotripsy bubbles compared with control bubbles produced at the same frequency at higher pressure. Results further show a significant decrease in bubble size with increasing frequency. Note: Different image magnifications were used for the above images to better image the bubbles at each frequency.

At all frequencies, results showed that the R_{max} for NMH bubbles was between 30%-40% of the R_{max} measured for histotripsy bubbles produced above the intrinsic threshold (**Figure A.8**). Results further showed that larger bubbles were observed at lower frequency for both the histotripsy only and NMH conditions (**Figure A.8**). For example, R_{max} for NMH bubbles was shown to decrease from 126.7±47.5 µm at 345 kHz to 106.5±17.6 µm, 34.7±13.4 µm, and 12.9±5.3 µm at 500 kHz, 1.5 MHz, and 3 MHz, respectively (**Table A.1**). Comparing R_{max} for NMH and histotripsy bubbles showed that, although NMH bubbles were significantly smaller than histotripsy bubbles for all frequencies, NMH bubbles produced at the lower two frequencies (345 kHz, 500 kHz) grew larger than histotripsy bubbles produced at the two higher frequencies (1.5 MHz, 3 MHz). For example, the R_{max} of NMH bubbles produced at 345 kHz and 500 kHz (126.7±47.5 µm and 106.5±17.6 µm) were significantly larger than the R_{max} of histotripsy bubbles generated above the intrinsic

threshold at 1.5 MHz and 3 MHz (79.5±11.5μm and 34.3±8.5) (**Figure A.8**). The complete list of R_{max} results are listed in **Table 6.1** along with the peak negative pressure applied for each condition.

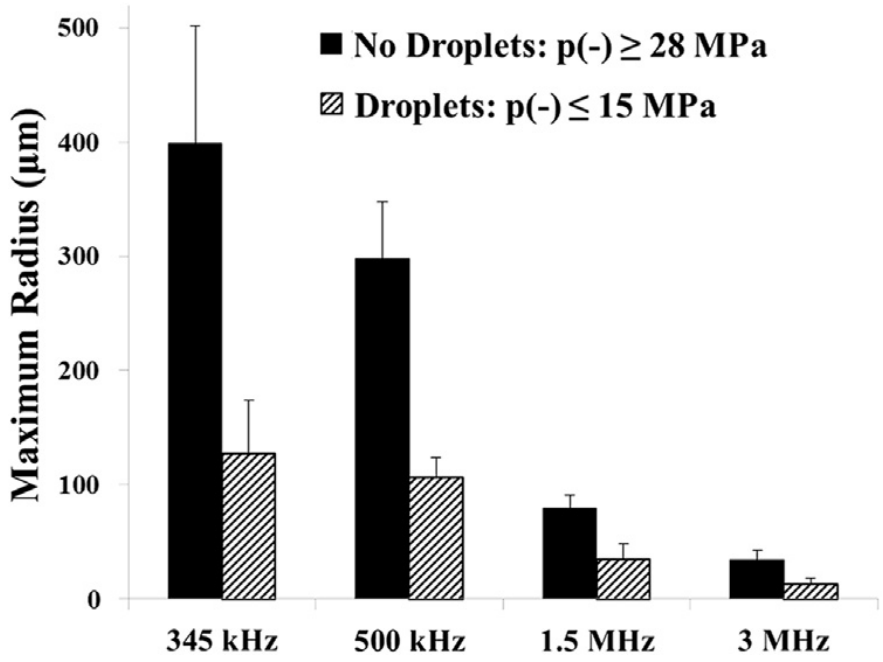

Figure A.8 Bubble R_{max} results. Plot shows a comparison of the maximum bubble radius produced in tissue phantoms with and without nanodroplets by 345 kHz, 500 kHz, 1.5 MHz, and 3 MHz histotripsy pulses.

The peak negative pressures *(p-)* applied for each condition are listed in Table 1.

NMH Multi-pulse Sustainability

To determine if nanodroplets are sustainable cavitation nuclei over multiple pulses, 1000 histotripsy pulses were applied to a single focal region in phantoms containing nanodroplets at a PRF of 1 Hz. Results demonstrated that a bubble cloud consisting of many bubbles was observed after the first pulse (**Figure A.9**). However, the number of bubbles observed inside the cloud significantly decreased with increasing number of pulses (**Figure A.9**).

Table A.1 Bubble R_{max} results. Table shows the maximum bubble radius produced in tissue phantoms with and without nanodroplets, along with the peak negative pressure (*p*-) applied for each condition. The *p*- for each condition was chosen to be slightly above the nanodroplet-mediated histotripsy (NMH) and intrinsic cavitation thresholds of the sample at each frequency.

Frequency	Sample	P- (MPa)	Max Radius (µm)
345 kHz			
	No Droplets	28	398.8±102.5
	Droplets	10.8	126.7±47.5
500 kHz			
	No Droplets	28.1	297.4±50.5
	Droplets	10.3	106.5±17.6
1.5 MHz			
	No Droplets	28.9	79.5±11.5
	Droplets	12.9	34.7±13.4
3 MHz			
	No Droplets	30.3	34.3±8.5
	Droplets	14.7	12.9±5.3

For example, for the 3 MHz sample shown in **Figure A.9**, only one bubble was observed after 5 pulses with no bubbles remaining after 10 pulses. At lower frequency, bubbles were generated for more pulses than at higher frequency, but still showed the same trend of decreasing number of bubbles with increasing pulse number (**Figure A.9**). It is likely that bubbles lasted for more pulses at lower frequency due to enhanced bubble expansion resulting in a larger population of residual nuclei and a corresponding increase in dissolution time. **Figure A.10** shows the number of pulses before cloud extinction, P_{Ext}, as a function of frequency (n=6). Results demonstrated a significant decrease ($p<0.05$) in P_{Ext} at higher frequencies, with P_{Ext} observed to decrease from 80.5±10.3 pulses at 345 kHz to 51.7±7.3 pulses, 15.7±4.8 pulses, and 5.5±1.9 pulses at 500 kHz, 1.5 MHz,

and 3 MHz, respectively (**Figure A.10**). For all frequencies, no bubbles were observed after 100 pulses were applied to the samples.

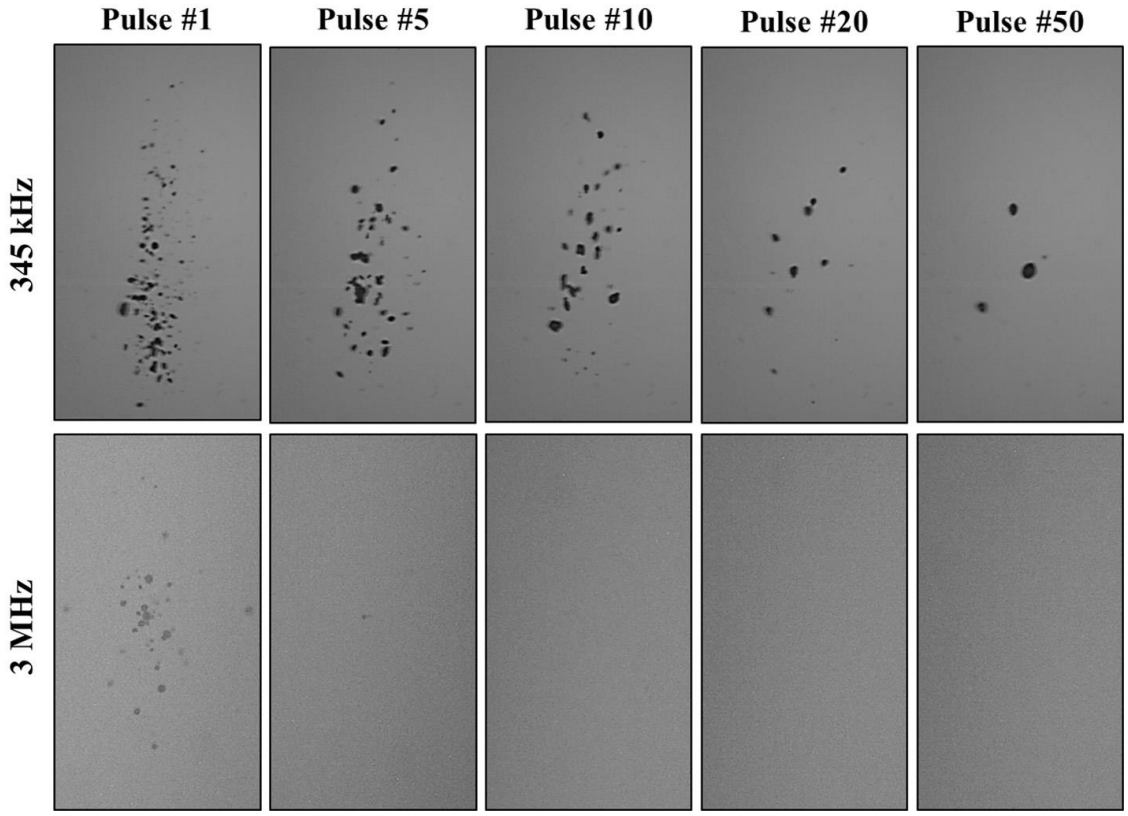

Figure A.9 Bubble cloud multi-pulse images. Optical images show NMH bubbles produced by 345 kHz (*p*-=10.8 MPa) and 3 MHz (*p*-=14.7 MPa) at a single focal point in tissue phantoms containing nanodroplets at a pulse repetition frequency (PRF) of 1 Hz.

Results showed a decrease in the number of bubbles observed at the focus with increasing pulse number.

Discussion

In this work, we investigated the effects of frequency on nanodroplet-mediated histotripsy (NMH) using our polymer encapsulated PFP nanodroplets [46]. This work builds upon two previous studies which demonstrated that NMH has the potential to be used for targeted tissue ablation by decreasing the pressure threshold required to generate histotripsy bubbles [46, 79]. In this study, we investigated the effects of frequency in order to optimize the acoustic parameters

used for NMH therapy. Since one of the goals of NMH therapy is to efficiently treat large and/or multi-focal tumor nodules, NMH parameters should be optimized to increase the size of the focal zone, decrease the NMH cavitation threshold, and increase NMH bubble expansion, all of which were improved at lower frequencies as shown in this study.

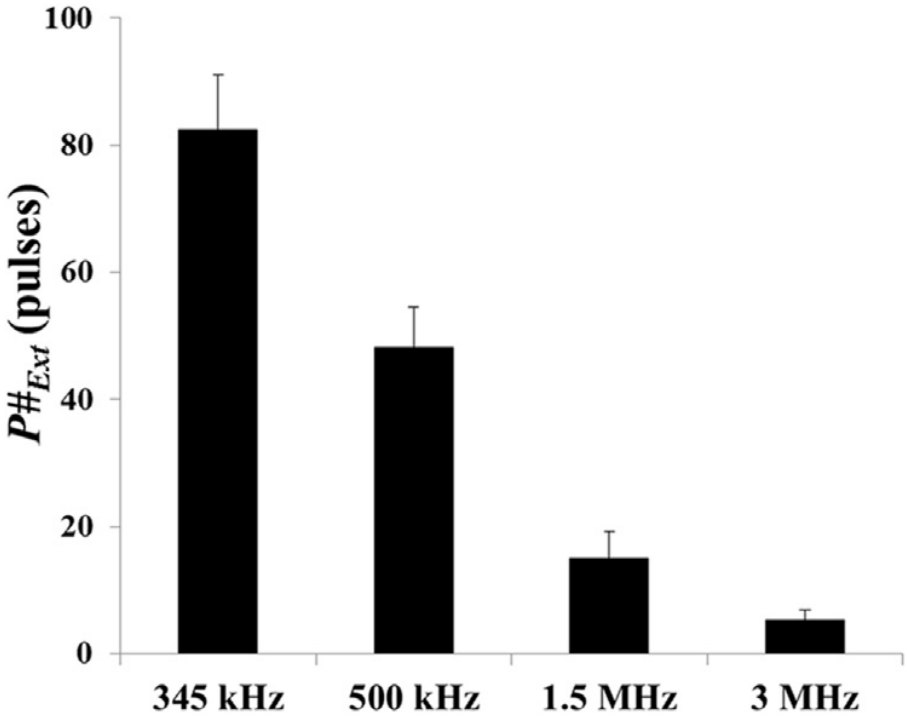

Figure A.10 Bubble cloud multi-pulse sustainability. Plot shows the number of pulses before cloud extinction, P_{Ext}, as a function of frequency.

Results demonstrated a significant decrease ($p<0.05$) in P_{Ext} with increasing frequency. A sample size of 6 tissue phantoms was used for each experimental condition.

In the first part of this study, the effects of frequency on the NMH cavitation threshold were investigated, with results demonstrating that PFP nanodroplets significantly reduced the cavitation threshold compared to the histotripsy intrinsic threshold. At all frequencies tested, the NMH threshold was significantly lower than the histotripsy intrinsic threshold, while maintaining a steep threshold behavior. This distinct threshold behavior is promising for the development of NMH therapy, in which the applied pressure must be chosen in the region above the NMH

threshold but below the histotripsy intrinsic threshold to ensure cavitation is only generated in regions containing nanodroplets. The results of this study suggest that all the frequencies investigated (345kHz-3MHz) could be used for NMH, with lower frequencies offering the largest drop in threshold compared to the histotripsy intrinsic threshold while maintaining the distinct threshold behavior.

The frequency dependence of the NMH cavitation threshold observed in this study is opposite to that reported in previous work on acoustic droplet vaporization (ADV) which showed that the ADV threshold decreases with increasing frequency [330-332]. However, those studies used larger droplets, higher frequency ranges, and/or longer duration exposures. Recent work has revealed that the decrease in the ADV threshold at higher frequencies is due to superharmonic focusing inside the droplet, which is significantly enhanced at higher frequencies and in larger droplets [333, 334]. These previous studies help to explain why the cavitation thresholds in this study do not follow the trends observed for ADV, since the extent of superharmonic focusing is negligible for the droplet size (<400 nm) and frequencies (≤3MHz) used in this study [334]. In contrast to those previous studies, the results of this work suggest that NMH bubbles are generated inside the droplets directly from the incident *p*- (tensile portion of the incident wave), similar to histotripsy bubbles generated above the intrinsic threshold [316]. This hypothesis is supported by the trends in the cavitation threshold with lower frequencies resulting in a lower cavitation threshold, likely due to the longer duration of the applied *p*- and the larger focal zone at lower frequencies, which increases the volume of PFP exposed to the *p*- and therefore increases the probability of nucleating cavitation inside the PFP nanodroplets. This would also imply that the NMH threshold will be affected by nanodroplet concentration, since a higher concentration of nanodroplets would result in a larger volume of PFP being exposed to the applied *p*-. This would

explain why a concentration of $2.0x10^8$ particles/mL was required in order to reduce the cavitation threshold in this study while concentrations $<\sim10^6$-10^7 particles/mL did not significantly reduce the cavitation threshold compared to the histotripsy intrinsic threshold. This threshold behavior suggests that the nanodroplets decrease the cavitation threshold by carrying a lower threshold media (PFP) rather than by acting as discrete nuclei as would be the case for gas-filled contrast agents. Future work will further investigate the role of droplet concentration on NMH therapy.

In the second part of this study, the effects of frequency on NMH bubble expansion were investigated, with results showing that lower frequencies facilitated larger bubble expansion. While it is likely that NMH will be able to fractionate tissue even at higher frequencies, the results of this study suggest that NMH will be more efficient at lower frequencies due to enhanced bubble expansion. A previous study investigating the effects of frequency on histotripsy bubble expansion demonstrated that the increase in bubble expansion at lower frequencies is due the increased duration of the applied rarefactional pressure [317]. This same effect likely explains the results of this study in which NMH bubbles at lower frequencies grew larger than bubbles produced by histotripsy without nanodroplets at higher frequencies, despite a >18 MPa decrease in the peak negative pressure of the applied pulses. For example, NMH bubbles produced at 345 kHz and 500 kHz grew larger than bubbles produced by histotripsy without nanodroplets at 1.5 MHz and 3 MHz, which have previously been shown capable of achieving tissue fractionation [324, 328]. This finding supports our hypothesis that NMH can be used to efficiently create histotripsy lesions when using lower frequencies.

In the final part of this work, the ability of PFP nanodroplets to act as sustainable cavitation nuclei over multiple pulses was investigated. In a previous study, nanodroplet-mediated histotripsy created consistent, well-defined fractionation at pressure levels (11-20 MPa) significantly below

the histotripsy intrinsic threshold (~26-30 MPa) in tissue phantoms at a PRF of 10 Hz by maintaining cavitation at over multiple pulses [79]. However, it is unclear whether the nanodroplets themselves or residual nuclei from previous pulses were responsible for seeding cavitation after the first few pulses. In this study, the PRF was kept low (1 Hz) to minimize the contributions of residual nuclei from a previous pulse, with results showing a significant reduction in the number of bubbles generated by NMH with increasing number of pulses. For all frequencies, no bubbles were observed in tissue phantoms after 100 pulses. These results suggest that the nanodroplets are destroyed by the cavitation process and only function as cavitation nuclei for the first few pulses, potentially due to the PFP being dissolved after undergoing the NMH cavitation process. This finding indicates that NMH will need to be applied at a higher PRF in order sustain cavitation for the duration of the treatment. It is also possible that nanodroplets containing a higher boiling point perfluorocarbon, such as perfluorohexane, would re-condense into a liquid and remain sustainable nuclei over multiple pulses, which would be a major benefit for NMH therapy, as previous work has shown a decrease in ablation efficiency for higher PRF treatments that rely on residual nuclei from previous pulses to maintain the cavitation bubble cloud [335]. However, higher boiling point droplets may also require a higher pressure in order to generate cavitation, which would not be desired for NMH therapy. Future work will investigate the possibility of using nanodroplets containing a higher boiling point perfluorocarbon for NMH therapy.

Conclusions

In this work, the effects of ultrasound frequency on nanodroplet-mediated histotripsy were investigated, with results supporting our hypothesis that using a lower frequency will improve NMH therapy. The results demonstrated that the NMH threshold was significantly reduced at lower frequencies, ranging from 7.4 MPa at 345 kHz to 13.2 MPa at 3 MHz. Furthermore, the

results demonstrated that NMH bubble expansion was enhanced at lower frequency, generating bubbles with a maximum radius >100 μm despite the reduced pressure applied. Finally, multi-pulse experiments demonstrated that nanodroplets are destroyed during the first few pulses at 1Hz PRF. Overall, the results of this study provide significant insight in the role of ultrasound parameters in NMH therapy and will provide a rational basis to specifically tailor acoustic parameters in order to improve NMH tissue fractionation.

Acknowledgements

We would like to thank Sonja Capracotta, PhD (Technical Specialist, Nano Sight, School of Public Health at the University of Michigan) for her help on NTA size and concentration measurements. This material is based upon work supported by a National Science Foundation Graduate Research Fellowship to Eli Vlaisavljevich. Omer Aydin acknowledges the support of the Turkish Republic the Ministry of National Education Fellowship Program (1416). This work was supported by a grant from the United States Department of Defense (W81XWH-11-PCRP-ID). Disclosure notice: Drs. Zhen Xu and Brian Fowlkes have financial interests and/or other relationship with HistoSonics Inc.

Appendix B

The Effects of Droplet Composition on Nanodroplet-Mediated Histotripsy

The material in this chapter is published from the following article: E. Vlaisavljevich, **O. Aydin,** Y. Y. Durmaz, K-W Lin, B. Fowlkes, Z. Xu, and M. ElSayed "The Effects of Droplet Composition on Nanodroplet-Mediated Histotripsy" *Ultrasound in Medicine and Biology* 42(4), 931, **2016**.

Introduction

Histotripsy is a noninvasive tissue ablation method that controllably fractionates soft tissue through cavitation generated by high pressure, short duration ultrasound pulses [49, 160, 336]. Histotripsy depends on the initiation and maintenance of a dense cavitation bubble cloud to produce mechanical tissue fractionation [314, 315]. Previous work has shown that, using a 1-2 cycle pulse with a single dominant negative pressure phase, cavitation bubbles can be reproducibly generated in tissue when the peak negative pressure (*p*-) is raised above the histotripsy intrinsic threshold of ~25-30 MPa [44, 337]. In order to effectively fractionate tissue into acellular debris, histotripsy requires a dense cavitation bubble cloud to be initiated and maintained over multiple pulses (often >100) until the tissue is completely fractionated into a liquid-appearing homogenate with no cellular structures remaining [49, 161, 336]. Histotripsy is currently being studied for many clinical applications where non-invasive tissue removal is desired including benign prostatic

hyperplasia [319], deep vein thrombosis [164], congenital heart disease [165, 166], and cancer [45, 167].

Although histotripsy has shown promise for many clinical applications including tumor ablation, this approach is limited to applications in which the target tissue can be identified and imaged prior to treatment, which is often not feasible in cancer patients with many small tumor nodules and micro-metastases. As a result, our group has developed a targeted ablation approach combining polymer encapsulated nanodroplets with histotripsy [46, 79, 338]. This nanodroplet-mediated histotripsy (NMH) approach takes advantage of the significantly reduced cavitation threshold of the nanodroplets, allowing for cavitation to be selectively generated only in regions where nanodroplets localize [79]. NMH has the potential for selective ablation of tumors given the small size (~100-400 nm) of the synthesized nanodroplets, which enables their diffusion across the leaky tumor vasculature and preferential accumulation in the tumor tissue [46, 79]. Previous work has demonstrated that NMH can be used to create well-defined ablation similar to histotripsy but at significantly lower pressure and has demonstrated the potential to use NMH for simultaneous multi-focal ablation [79]. Furthermore, a previous study by Yuksel Durmaz *et al* investigated the optimal characteristics of polymer encapsulated perfluoropentane (PFP) nanodroplets, with results showing optimal NMH ablation for nanodroplets with a shell-cross-linked triblock amphiphilic copolymer composed of a poly(ethylene glycol) (PEG) block that forms a biocompatible corona, a poly(acrylic acid) (PAA) middle block reacting with the cross-linker to form a flexible shell, and a poly(heptadecafluorodecyl methacrylate-*co*-methyl methacrylate) (P(HDFMA-co-MMA)) fluorinated hydrophobic block encapsulating 2% v/v PFP [46]. However, although this previous study determined the optimal conditions for PFP

nanodroplets, the effects of perfluorocarbon boiling temperature on NMH therapy have not been previously investigated.

In this study, we compare perfluoropentane (PFP, boiling point ~29°C) and perfluorohexane (PFH, boiling point ~56°C) nanodroplets for NMH therapy. Based on previous work comparing PFP and PFH droplets for acoustic droplet vaporization [339, 340], we hypothesize that PFH nanodroplets will have a slightly higher cavitation threshold than PFP droplets but the cavitation threshold of both droplets will be significantly lower than the histotripsy intrinsic threshold. To test this hypothesis, tissue phantoms containing PFP nanodroplets, PFH nanodroplets, and no nanodroplets were exposed to histotripsy pulses produced by 345 kHz, 500 kHz, 1.5 MHz, and 3 MHz custom-built histotripsy transducers. The probability of generating inertial cavitation from a single 1-2 cycle histotripsy pulse was measured, with the cavitation threshold defined as the peak negative pressure at which the probability of generating cavitation, p_{cav}, from a single histotripsy pulse was p_{cav}=0.5. In addition to the effects of droplet composition on the cavitation threshold, we also investigate the effects of droplet composition on cavitation sustainability over multiple histotripsy pulses. In previous studies, PFP nanodroplets were used to create consistent, well-defined fractionation at pressure levels (11-20 MPa) significantly below the histotripsy intrinsic threshold (~26-30 MPa) in tissue phantoms at a pulse repetition frequency (PRF) of 10 Hz by maintaining cavitation over multiple pulses [46, 79]. However, it was also observed that cavitation was not maintained over multiple pulses when ultrasound was applied at a lower PRF (1 Hz) [46, 79, 338]. A low PRF (1 Hz) has been shown to produce more efficient tissue fractionation and is not affected by the cavitation memory effect, in which residual gas bubbles from previous cavitation events function as nuclei for generating cavitation on a subsequent pulse [335]. This result suggests that PFP nanodroplets are destroyed during the first

few pulses, requiring cavitation on subsequent pulses to be generated from residual nuclei remaining from previous pulses. We hypothesize that, due to their higher boiling point, PFH nanodroplets will re-condense into a liquid after cavitation and remain as sustainable nuclei over multiple (>100) pulses, allowing cavitation to be maintained over multiple pulses even at low PRF. To test this hypothesis, 1000 histotripsy pulses were applied to a single focal zone tissue in phantoms containing PFP and PFH nanodroplets, and the number of NMH bubbles generated was compared after each pulse. In addition, tissue phantoms containing a layer of embedded red blood cells were used to compare the damage generated for NMH treatments using PFP and PFH droplets. Overall, these results will improve our understanding of the NMH process and help to determine the optimal nanodroplet characteristics for NMH therapy.

Materials

Methyl methacrylate (MMA, Sigma-Aldrich, 99 %), 3,3,4,4,5,5,6,6,7,7,8,8,9,9,10,10,10 heptadecafluorodecyl methacrylate (HDFMA, Sigma-Aldrich, 97 %), *tert*-butyl acrylate (*t*BA, Sigma-Aldrich, 98 %) and *N, N, N', N'', N''*-pentamethyldiethylenetriamine (PMDETA, Sigma-Aldrich, 99 %) were passed through a basic alumina column to remove the inhibitor. Copper (I) bromide (CuBr, Sigma-Aldrich, 99.9 %), 2-bromoisobutyryl bromide (Fluka, >97 %), tetrahydrofuran anhydrous (THF, Sigma-Aldrich, >99.9 %), *N,N'*-Dicyclohexylcarbodiimide (DCC, Sigma-Aldrich, 99 %), dimethylaminopyridine (DMAP, Acros, 99 %), 4-pentynoic acid (Sigma-Aldrich, 99 %), furan (Sigma-Aldrich, ≥99 %), maleic anhydride (Fluka, ≥99 %), 9 anthracene methanol (Aldrich, ≥ 99%), perfluoropentane (PFP, Alfa Aesar, 97% ca. 85% n isomer), perfluorohexane (PFH, SynQuest Lab, > 98%) *N*-hydroxy succinimide (NHS, Fluka, 97 %), *N*-(3-Dimethylaminopropyl)-*N* ethylcarbodiimide hydrochloride (EDC, Fluka >98 %),

poly(ethylene glycol) monomethylether (Me-PEG, M_n : 2000 g/mol, Sigma-Aldrich), sodium azide (NaN_3, Acros, 99 %), 2-(*N*-morpholino)ethanesulfonic acid monohydrate (MES, Acros, 99 %), triethylamine (TEA, Sigma-Aldrich, ≥ 99%), trifluoroacetic acid (TFA, Acros, 99 %), ethylene carbonate (Sigma-Aldrich, 98 %), 2,2`- (ethylenedioxy)-bis(ethylamine) (Sigma-Aldrich, 98%) agarose powder (Type VII, Sigma-Aldrich), citratephosphate-dextrose (CPD, Sigma-Aldrich), heptane fraction (Sigma-Aldrich, > 99%), dicholoromethane (DCM or CH_2Cl_2, Sigma-Aldrich, >99.5%) were used as received.

Methods

Nanodroplet Formulation and Characterization

A well-defined, triblock amphiphilic copolymer containing a hydrophilic poly(ethylene glycol) (PEG) block, a middle block poly(acrylic acid) (PAA) block, and a hydrophobic random copolymer of heptadecafluorodecyl methacrylate (HDFMA) and methyl methacrylate (MMA) was synthesized using a combination of atom transfer radical polymerization (ATRP) and "click" coupling techniques as previously described (**Figure 7.1**) [46]. The synthesized P($HDFMA_8$-*co*-MMA_{20})-*b*-PAA_{12}-*b*-PEG_{45} triblock amphiphilic copolymer was used to prepare PFP- and PFH-loaded nanodroplets. Briefly, the copolymers were dissolved in tetrahydrofuran (THF) (0.2% w/v) and cooled down to 0 °C before the addition of PFP (2% v/v) or PFH (2% v/v) while vigorously stirring the copolymer-perfluorocarbon mixture. An equal amount of deionized water was added drop-wise to this solution mixture to initiate micelle formation and the mixture was stirred for 1h in an ice bath. The micelles solution was transferred into a dialysis bag (MWCO of 1 KDa, Spectrum, Rancho Dominguez, CA) and dialyzed overnight against ice-cold MES solution (pH 5.5) to remove the THF and get a milky solution of non-cross-linked PFP-loaded nanodroplets and

non-cross-linked PFH-loaded nanodroplets. The milky nanodroplets solutions were transferred to round bottom flasks and mixed with the 2,2`-(ethylenedioxy)-bis(ethylamine) cross-linker, which reacts with the carboxyl groups of the central PAA block in the copolymer via NHS/EDC coupling chemistry forming cross-linked nanodroplets with a flexible polymer shell. Shell cross-linked nanodroplets were dialyzed against ice-cold water for 12 hours to remove unreacted cross-linker and reaction byproducts.

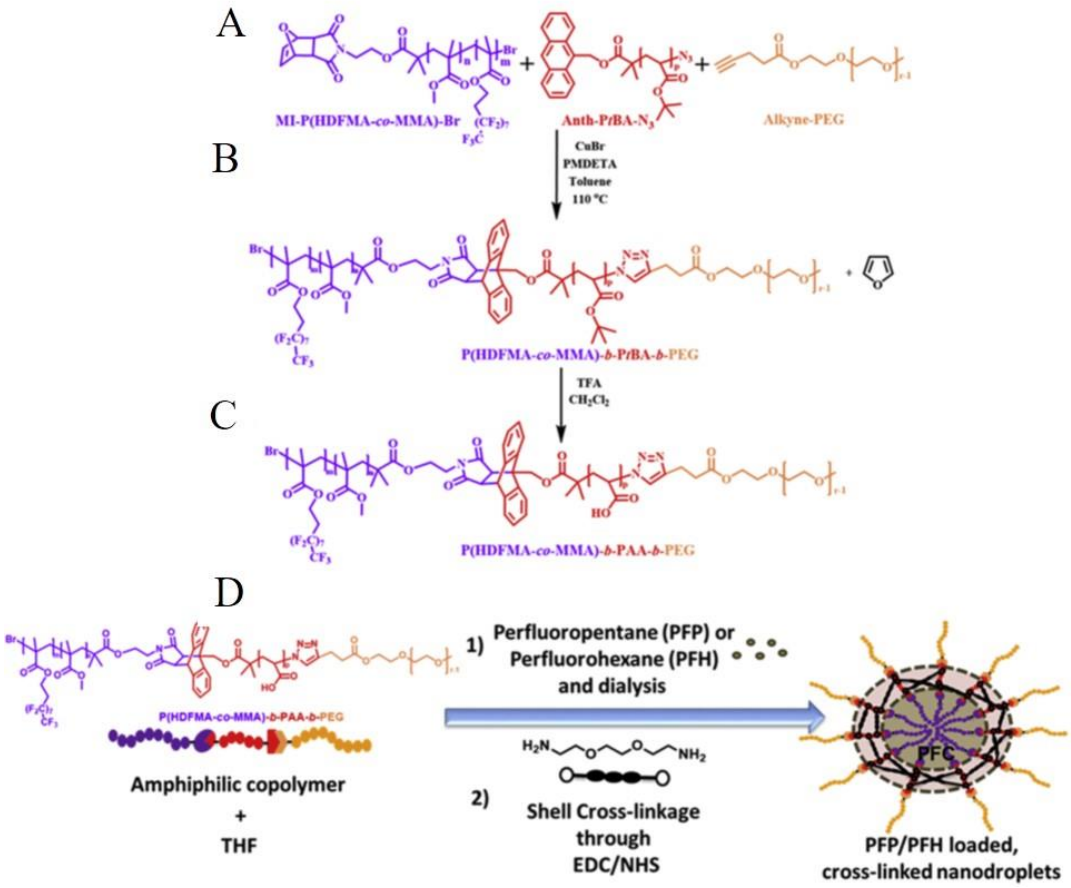

Figure B.1 Synthesis of the P(HDFMA-*co*-MMA)-*b*-P*t*BA-*b*-PEG triblock copolymer and formulation of PFP- and PFH-loaded nanodroplets

(A) The chemical structure of each block and (B) the one-pot "click" reaction to obtain P(HDFMA-*co*-MMA)-*b*-P*t*BA-*b*-PEG copolymer. (C) Hydrolysis of the *t*BA group to obtain the P(HDFMA-*co*-MMA)-*b*-PAA-*b*-PEG polymer. (D) Formulation of the P(HDFMA-*co*-MMA)-*b*-P*t*BA-*b*-PEG polymer into PFP- and PFH-loaded nanodroplets.

Concentration and size distribution of the nanodroplets were measured using Nanoparticle Tracking Analysis (NTA). Briefly, the NanoSight™ LM10 (Malvern Instruments, Amesbury, UK), equipped with a temperature-controlled 405 nm laser module, high sensitivity scientific Complementary Metal–Oxide–Semiconductor (sCMOS) camera (Hamamatsu, Orca, Hamamatsu City, Japan), and a syringe pump was used for the collection of NTA data. Upon diluting the nanodroplets solution to the appropriate particle concentration with deionized water, image capture and analysis was carried out using the NTA software (Version 3.0, Build 0066) at 37 °C. Concentration and size distribution of the nanodroplets in each sample were analyzed using 5 videos per sample each lasting 60s. Based on these videos, nanodroplet concentration was plotted as a function of droplet size, with the error bars representing the standard deviation of the repeat measurements of each sample. The mean size and standard deviation values obtained by the NTA software correspond to arithmetic values calculated with the sizes of all particles analyzed for each sample (n=5).

Preparation of Tissue Phantoms

Agarose phantoms were used to provide a well-controlled viscoelastic medium for this study. Tissue phantoms containing 1% agarose w/v were prepared by slowly mixing agarose powder (Agarose Type VII; Sigma-Aldrich, St. Louis, MO, USA) into saline solution (0.9% sodium chloride; Hospira, Lake Forest, Illinois, USA) heated to boiling temperature. The solution was stirred on a hot plate until the gel turned completely transparent and then allowed to boil for ten minutes. After boiling, solutions were allowed to cool and were degassed under a partial vacuum (~20 kPa, absolute) for 30 minutes. After degassing, phantoms containing nanodroplets were prepared by slowly adding the nanodroplets (2.0×10^8 particles/ml) into the agarose solution while stirring. The agarose mixtures were poured into rectangular polycarbonate holders with

acoustic windows and placed in a refrigerator at 4°C to allow the solution to solidify, forming tissue phantoms with embedded PFP nanodroplets, PFH nanodroplets, or without nanodroplets (control). The temperature of the agarose was ~40 °C when the nanodroplets were added. As this temperature is close to the temperature at which the NTA analysis was performed (37°C), it is expected that the size and concentration of nanodroplets was not be significantly affected by the casting process. This hypothesis is further supported by previous studies showing that PFP and PFH nanodroplets have vaporization temperatures much higher than their reported boiling points. For example, the vaporization temperatures of PFP and PFH nanodroplets between 250-350 nm have been reported to be higher than 80°C and 140 °C, respectively, suggesting that the droplets will remain stable during the casting process (40 °C) and experimental temperatures (37 °C) [341, 342].

For cell fractionation experiments, tissue phantoms with a red blood cell (RBC) layer were prepared using porcine RBCs in 0.9% isotonic saline and 1% agarose solutions with PFP or PFH nanodroplets. Fresh porcine blood was obtained from research subjects in an unrelated study and added to an anticoagulant solution of citratephosphate-dextrose (CPD) (Sigma-Aldrich Co., St. Louis, MO) with a CPD-to-blood ratio of 1:9 mL. Whole blood was separated in a centrifuge at 3000 rpm for 10 min. The plasma and white buffy coat were removed, and the RBCs were saved for addition to the phantom. To prepare the RBC phantom, an initial layer of 1% agarose mixture (with PFP or PFH nanodroplets) was poured into a rectangular polycarbonate housing to fill half of it at 40°C. The housing was placed in a refrigerator at 4 °C to allow the agarose to cool and solidify. The remaining solution was kept at 40 °C. A small amount of agarose solution was mixed with the RBCs (5% RBCs v/v). The frame with solidified agarose was removed from refrigeration, and a thin layer of the RBC-agarose solution was poured onto the gel surface to allow the entire

surface to coat in a thin layer. After 5 min, the RBC-agarose layer was solidified, and the remaining agarose solution without RBCs was poured to completely fill the frame. This procedure created a thin layer of RBCs suspended in the center of the agarose phantom.

Histotripsy Pulse Generation

Histotripsy pulses were generated at four ultrasound frequencies (345 kHz, 500 kHz, 1.5 MHz, and 3 MHz) using three custom-built histotripsy transducers. The 345 kHz pulses were generated by a twenty-element array transducer with a geometric focus of 150 mm, an aperture size of 272 mm, and an effective f-number of 0.55. The 1.5 MHz pulses were generated by a six-element array transducer with a geometric focus of 55 mm, an aperture of 79 mm in the elevational direction and 69 mm in the lateral direction, and effective f-numbers of 0.7 and 0.8 in the elevational and lateral directions, respectively. The 500 kHz and 3 MHz pulses were generated by a dual frequency array transducer that consisted of twelve 500-kHz elements and seven 3-MHz elements. For the 500 kHz elements, the geometric focus was 40 mm, the aperture size was 71 mm, and the effective f-number was 0.56. For the 3 MHz elements, the geometric focus was 40 mm, the aperture size was 80 mm, and the effective f-number was 0.5. The design of the dual frequency transducer has been described in detail in a previous study [328].

To compare the NMH cavitation threshold with the histotripsy intrinsic threshold, short pulses with a single dominant negative pressure half-cycle were applied to the tissue phantoms with and without nanodroplets inside a water bath heated to at 37 °C. To generate a short therapy pulse, a custom high-voltage pulser developed in-house was used to drive the transducers. The pulser was connected to a field-programmable gate array (FPGA) board (Altera DE0-Nano Terasic Technology, Dover, DE, USA) specifically programmed for histotripsy therapy pulsing. This setup allowed the transducers to output short pulses of less than two cycles. A fiber-optic probe

hydrophone built in-house [172] was used to measure the acoustic output pressure of the transducers. At higher pressure levels (p- > 23 MPa), the acoustic output could not be directly measured due to cavitation at the fiber tip. These pressures were estimated by a summation of the output focal p- values from individual transducer elements. This approximation assumes minimal nonlinear distortion of the waveform occurs within the focal region. In a previous study [44], this estimated p- was found to be accurate within 15% compared to direct focal pressure measurements in water and in a medium (1,3 butanediol) with a higher cavitation threshold. Sample acoustic waveforms produced by the four frequency transducers are shown in **Figure B.2A**.

Optical Imaging and Image Processing

High speed optical imaging was used to capture images of the focal zone after the propagation of each pulse through the focus using two high speed cameras (**Figure B.2B**). For experiments with the 345 kHz and 1.5 MHz transducers, a high-speed, 1 megapixel CCD camera (Phantom V210, Vision Research, Wayne, NJ, USA) was aligned with the transducer and backlit by a continuous white-light source. The camera was focused using a macro-bellows lens (Tominon, Kyocera), giving the captured images a resolution of approximately 5.9 μm per pixel and 3.4 μm per pixel for 345 kHz and 1.5 MHz, respectively. For experiments with the 500 kHz and 3 MHz dual frequency transducer, a digital, 1.3-megapixel CCD camera (PN: FL3-U3-13Y3M-C, Flea® 3, PointGrey, Richmond, BC, Canada) was positioned perpendicularly to the dual-frequency array transducer facing one of the transducer's optical windows. A Nikon 4X objective was attached to the camera with extension tubes to magnify the image plane, giving the captured images a resolution of approximately 2.5 μm per pixel. A pulsed white-light LED was placed on the diametrically-opposed optical window of the dual-frequency array transducer, which provided back-lit illumination. The cameras were triggered to record one image for each applied

pulse. After acquisition, shadowgraph images were converted from grayscale to binary by an intensity threshold determined by the background intensity using image processing software (MATLAB, The Mathworks, Natick, MA, USA), as described in a previous study [44].

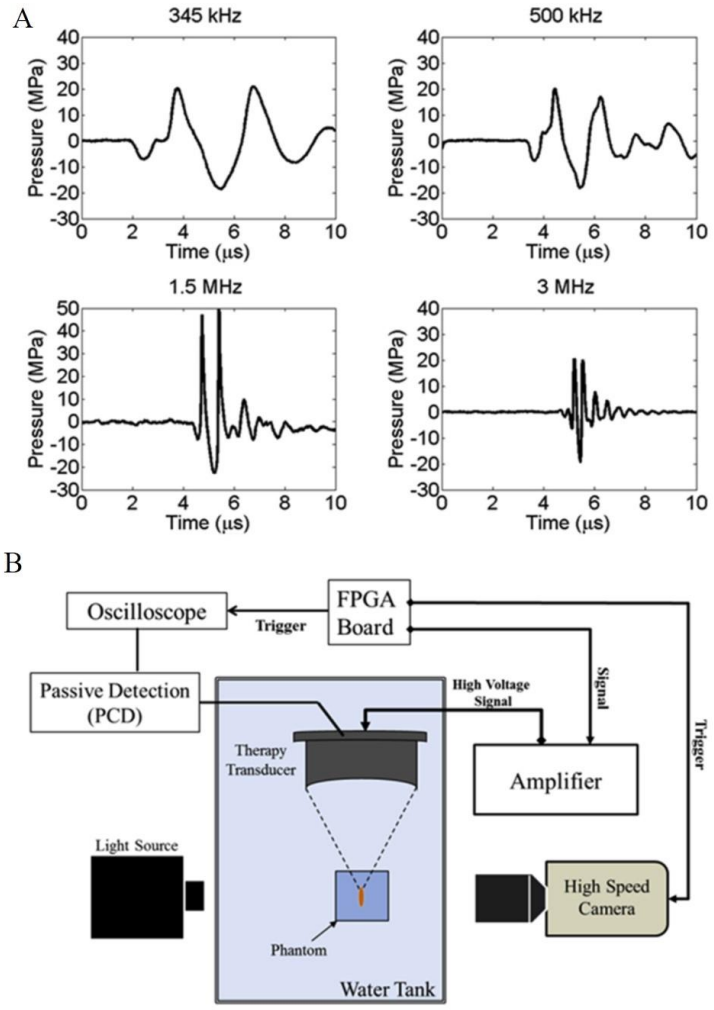

Figure B.2 (A) Example waveforms for 2-cycle histotripsy pulses generated by custom-built 345 kHz, 500 kHz, 1.5 MHz, and 3 MHz transducers. (B) Experimental set-up showing the focus of the histotripsy transducers aligned inside tissue phantoms containing PFP, PFH, or no nanodroplets.

Cavitation was monitored using high speed optical imaging and passive cavitation detection using one of the therapy elements.

Bubbles were indicated as any black regions >5 pixels. By this criterion, the minimum resolvable bubble radius was 14.75 μm, 6.25 μm, 8.5 μm, and 6.25 μm for the 345 kHz, 500 kHz, 1.5 MHz, and 3 MHz transducers, respectively.

Passive Cavitation Detection (PCD)

In addition to high speed imaging, an acoustic method was used to identify cavitation in the focal zone for cavitation threshold experiments. For each experiment, one of the transducer's therapy elements was also used for PCD to detect the presence of cavitation in the focal region (**Figure 7.2B**). The PCD signal was connected to an oscilloscope (LT372; Lecroy, Chestnut Ridge, NY, USA) with the time window selected to record the backscattering of the therapy pulse from cavitation bubbles [44, 323, 337]. To determine whether cavitation occurred during a pulse, the signal generated by backscattering of the incident pulse from the focus was analyzed following the method used in previous studies [44, 337]. A significant fraction of the incident wave energy is scattered when a cavitation bubble expands, greatly increasing the backscattered pressure amplitude received by the PCD. This signal appeared on the PCD at the time point corresponding to two times the time of flight for the focal length of the respective transducers. The integrated frequency power spectrum (S_{PCD}) of the backscatter signal was used as a measure of whether cavitation occurred according to the method previously described by Maxwell *et al* [44].

NMH Cavitation Threshold

For cavitation threshold experiments, 100 pulses were applied to each sample inside a water bath heated to 37 °C at each pressure level at a pulse repetition frequency (PRF) of 0.5 Hz. The PRF was kept low to minimize the possibility that cavitation from one pulse would change the probability of cavitation on a subsequent pulse. In a previous study, it was demonstrated that cavitation during a pulse increased the likelihood of cavitation on a following pulse for PRFs > 1 Hz, , but this effect was not observed for PRFs < 1 Hz [44]. In addition to this low PRF, the focus was translated for each pulse by 1 mm transverse to the acoustic propagation direction in a 10 × 10 grid in order to minimize the effects of cavitation damage to the nanodroplets or tissue phantoms from altering the probability of cavitation. For each pulse, cavitation was monitored using both

high speed imaging and PCD, and the fraction of total pulses (out of 100) for which cavitation was detected was determined as the cavitation probability.

The probability of observing cavitation followed a sigmoid function, given by

$$P(p_-) = \frac{1}{2} + erf\left(\frac{p_- - p_t}{\sqrt{2\sigma^2}}\right) \text{ Eq. 7.1}$$

where *erf* is the error function, p_t is the negative pressure at which the probability p_{cav}=0.5, σ is a variable related to the width of the transition between p_{cav}=0 and p_{cav}=1, with ± σ giving the difference in pressure from about p_{cav}=0.15 to p_{cav}=0.85 for the fit [44]. The cavitation threshold for each sample, p_t, is defined as the *p*- corresponding to p_{cav}=0.5 as calculated by the curve fit. Curve fitting for all data sets was performed using an OriginLab curve fitting program (OriginPro 9.1; OriginLab Corporation, Northampton, MA, USA). The fit curves for all samples were analyzed statistically to determine whether the differences in the values of p_t were significantly different from each other. The standard errors for p_t were estimated by a covariance matrix using the delta method [329]. The curves were compared using a two-sample t-test with statistic $t\left(p_{int1} - p_{int2}, \sqrt{SE_1^2 + SE_2^2}\right)$ at a 95% confidence interval. Results were considered statistically significant for $p<0.05$. Note that the standard error does not include the uncertainty in absolute pressure from the hydrophone measurement, only the uncertainty in the fit. A sample size of 3 tissue phantoms was used for each experimental condition (i.e. PFP nanodroplets, PFH nanodroplets, or no nanodroplets).

NMH Multi-pulse Sustainability

To test the hypothesis that PFH nanodroplets will remain sustainable cavitation nuclei over multiple pulses while PFP nanodroplets will be destroyed during the first few pulses, 1000 ultrasound pulses were applied to a single focal region in tissue phantoms containing PFP and PFH

nanodroplets inside a water bath heated to 37 °C. Pulses were applied at a PRF of 1 Hz and peak negative pressures of 11.8 MPa (345 kHz), 12.6 MPa (500 kHz), 14.3 MPa (1.5 MHz), and 15.6 MPa (3 MHz). The PRF in this study was kept low (1 Hz) to minimize the contributions of residual nuclei from a previous pulse from effecting cavitation generation on a subsequent pulse in order to determine if PFP and PFH nanodroplets continue to function as viable cavitation nuclei after the first few pulses or if the nanodroplets are destroyed in the cavitation process. Furthermore, a PRF of 1 Hz was also chosen as previous work has shown an increase in ablation efficiency for 1 Hz treatments in comparison to higher PRF treatments that rely on residual nuclei from previous pulses to maintain the cavitation bubble cloud [335, 343]. Cavitation was monitored using high speed optical imaging, and the number of bubbles produced by each pulse was compared for 1000 histotripsy pulses in each sample.

NMH RBC Phantom Ablation

Agarose gel phantoms with an embedded RBC layer were used to characterize cell fractionation induced by NMH. Fractionation of the RBCs turns the color of the embedded cell layer from opaque red to translucent as the RBCs are lysed, which allows direct visualization of the histotripsy-induced fractionation process [344]. Previous studies have also shown that the lesion visualized in RBC phantoms is similar to the lesion generated in tissue identified by histology [344]. For RBC experiments, 2000 histotripsy pulses were applied to the center of the red blood cell phantom layer at PRFs of 1 Hz and 10 Hz (n=4). The bubble cloud and resulting cell fractionation were recorded by high-speed optical imaging after each pulse. Cell fraction was compared between RBC phantoms with PFP and PFH nanodroplets.

Results

Nanodroplets Characterization

In this study, we aimed to encapsulate PFH into the triblock amphiphilic P(HDFMA$_8$-*co*-MMA$_{20}$)-*b*-PAA$_{12}$-*b*-PEG$_{45}$ copolymer in order to compare the cavitation ability of PFH-loaded nanodroplets with PFP-loaded nanodroplets. In our previous study, we demonstrated that PFP can be encapsulated in the fluorinated copolymer, forming nanodroplets containing an elastic shell with an average size of ~100-400 nm [46]. In contrast to PFP, the solubility of PFH is limited in most common polar solvents as well as water. Moreover, PFH is not miscible with any of these solvents and exhibits a clear phase separation from organic solvents. In this study, we hypothesized that PFH could be encapsulated by the P(HDFMA$_8$-*co*-MMA$_{20}$)-*b*-PAA$_{12}$-*b*-PEG$_{45}$ copolymer forming nanodroplets with similar size and characteristics to the PFP droplets described in our previous study [46]. Results demonstrate that both PFP and PFH encapsulated into stable nanodroplets in the desired size range (100-600 nm). NTA size analysis showed similar characteristics for the PFP and PFH droplets (**Figure B.3**). PFP-loaded nanodroplets size ranged from 100-450 nm with the major peak <300 nm. The size distribution of PFH-loaded nanodroplets was slightly larger than the PFP-loaded ones, ranging from 100-600 nm. Three additional high-intense peaks in the range of 200-300 nm, 300-450 nm, and 450-600 nm were observed in the large size portion of the PFH nanodroplet size plot (**Figure B.3B**). The larger size of the PFH-loaded

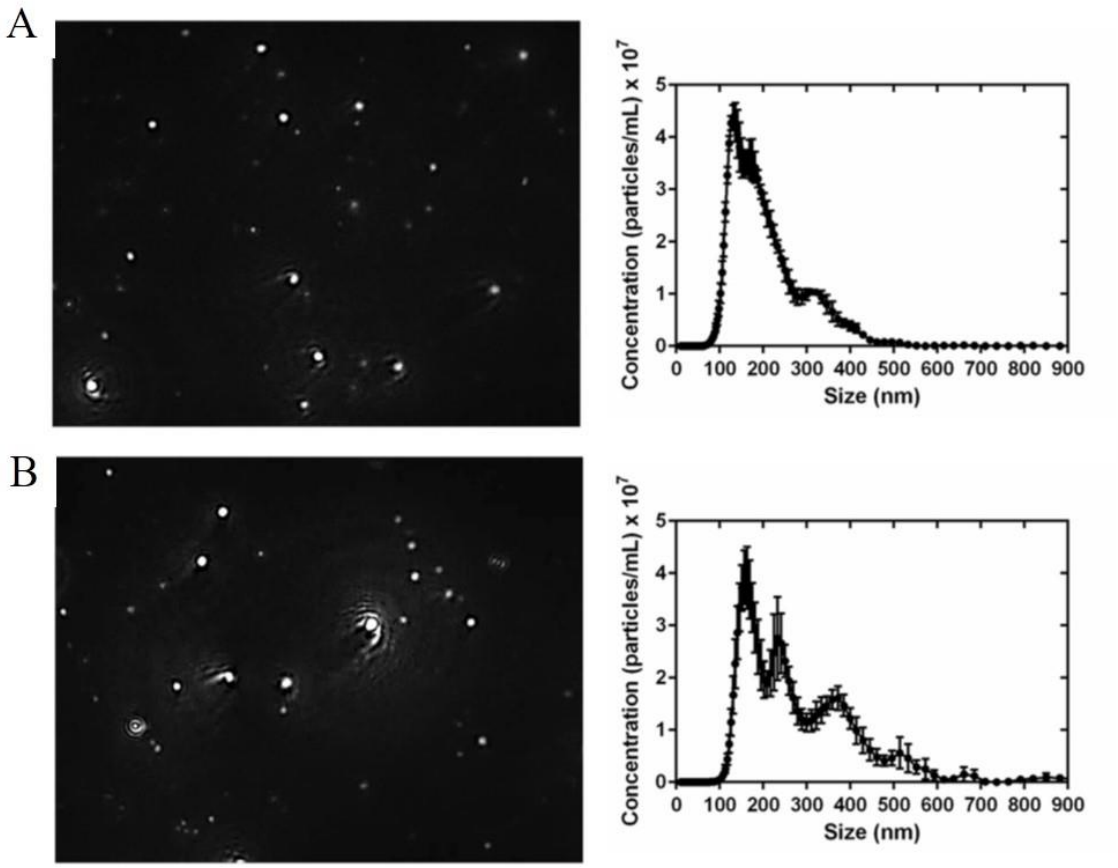

Figure B.3 Nanoparticle Tracking Analysis (left) demonstrated similar characteristics for

(A) PFP- and (B) PFH-loaded nanodroplets. Size distribution plots (right) show the average size of the droplets was 177.9±1.9 nm and 233.9±3.9 nm for PFP and PFH nanodroplets, respectively.

nanodroplets is possibly due to the difference in PFH miscibility with the THF/copolymer mixture compared to PFP. For example, PFP was observed to homogenously disperse in the THF/copolymer mixture in the beginning of droplets formulation, whereas PFH remained separate from the mixture on the bottom of the round-bottom flask. This energetically-favored phase separation was broken up by drop-wise addition of water to trigger the micellization process of the amphiphilic copolymer under vigorous stirring. This strategy allowed for uniform mixing of the PFH and efficient encapsulation in the droplets core. Both types of droplets were dispersed throughout the aqueous solution without aggregation or settling down in solution due to the hydrophilic PEG corona. PFP- and PFH-loaded nanodroplets exhibited similar concentrations and

size distribution (**Figure B.3**). The error bars on the size distribution plots represent the standard deviation of the repeat measurements of each sample. The mean size and standard deviation values obtained by the NTA software correspond to arithmetic values calculated with the sizes of all particles analyzed for each sample (n=5). Results from all samples demonstrated an average size of 177.9±1.9 nm and 233.9±3.9 nm for PFP and PFH nanodroplets, respectively.

NMH Cavitation Threshold

To investigate the effects of nanodroplet composition on the NMH threshold, histotripsy pulses were applied to tissue-mimicking agarose phantoms with PFP nanodroplets, PFH nanodroplets, and no nanodroplets using the 345 kHz, 500 kHz, 1.5 MHz, and 3 MHz histotripsy transducers. For all experimental conditions, cavitation bubbles were observed on the high-speed camera in an increasingly larger area with increasing pressure once a certain negative pressure was exceeded, with complete agreement between optical imaging and PCD detection methods (**Figure B.4**), as seen in previous studies [44, 337]. Plotting the probability of cavitation as a function of peak negative pressure demonstrated a significant decrease in the cavitation threshold with both PFP and PFH nanodroplets compared to controls at all frequencies (**Figure B.5**). Additionally, results showed a slight increase in the nanodroplet cavitation threshold for PFH nanodroplets compared to PFP nanodroplets (**Figure B.5**). Cavitation threshold results for all experimental conditions are listed in **Table B.1**. Comparing the threshold results for phantoms containing PFH nanodroplets with control phantoms demonstrated that the cavitation threshold was decreased by 14.4 MPa, 15 MPa, 13.7 MPa, and 11.9 MPa at 345 kHz, 500 kHz, 1.5 MHz, and 3 MHz, respectively (**Figure B.6**).

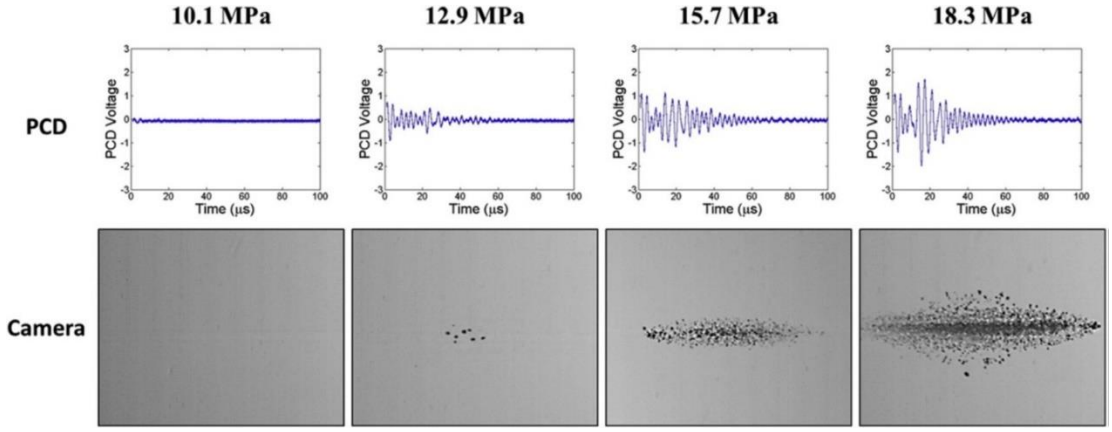

Figure B.4 Sample PCD signals (top) and high speed optical imaging (bottom) were used for cavitation detection for cavitation threshold experiments.

Results showed good agreement between the two methods. Representative images shown above are from 1.5 MHz histotripsy pulses applied to tissue phantoms containing PFH nanodroplets.

Table B.1 Threshold results. Table shows the values for the peak negative pressure, pt, at which the fit curve set Pcav = 0.5 for each sample as well as the mean values for pt and σ. A two-way ANOVA showed all differences in pt_mean between samples were statistically significant ($p<0.05$).

Frequency	Material	P_t (1)	P_t (2)	P_t (3)	P_t (mean)	σ(mean)
345 kHz	**No Droplets**	25.9	23.7	24.7	24.8	2.0
	PFP Droplets	7.3	7.4	7.4	7.4	1.4
	PFH Droplets	10.5	10.1	10.6	10.4	0.9
500 kHz	**No Droplets**	23.5	26.3	26.7	25.5	1.8
	PFP Droplets	9.4	10.0	8.2	9.2	0.8
	PFH Droplets	10.4	10.8	10.3	10.5	0.8
1.5 kHz	**No Droplets**	26.8	27.0	26.3	26.7	1.0
	PFP Droplets	10.3	10.7	10.5	10.5	0.4
	PFH Droplets	12.8	13.0	13.1	13.0	0.3
3 MHz	**No Droplets**	26.9	27.2	26.3	26.8	0.9
	PFP Droplets	13.1	12.9	13.7	13.2	0.6
	PFH Droplets	14.6	14.6	15.4	14.9	0.4

When comparing phantoms containing PFP and PFH nanodroplets (**Figure B.6**), a decrease of 3 MPa, 1.3 MPa, 2.5 MPa, and 1.7 MPa was observed for PFP phantoms at 345 kHz, 500 kHz, 1.5 MHz, and 3 MHz, respectively (**Figure B.6**). For all experimental conditions, the cavitation threshold was observed to decrease at lower frequency, as has been observed in previous studies (**Figure B.6**) [79, 337]. A two-way ANOVA was performed on the data shown in **Figure B.6**,

demonstrating all differences between the cavitation threshold in PFP, PFH, and control phantoms were significant ($p<0.05$).

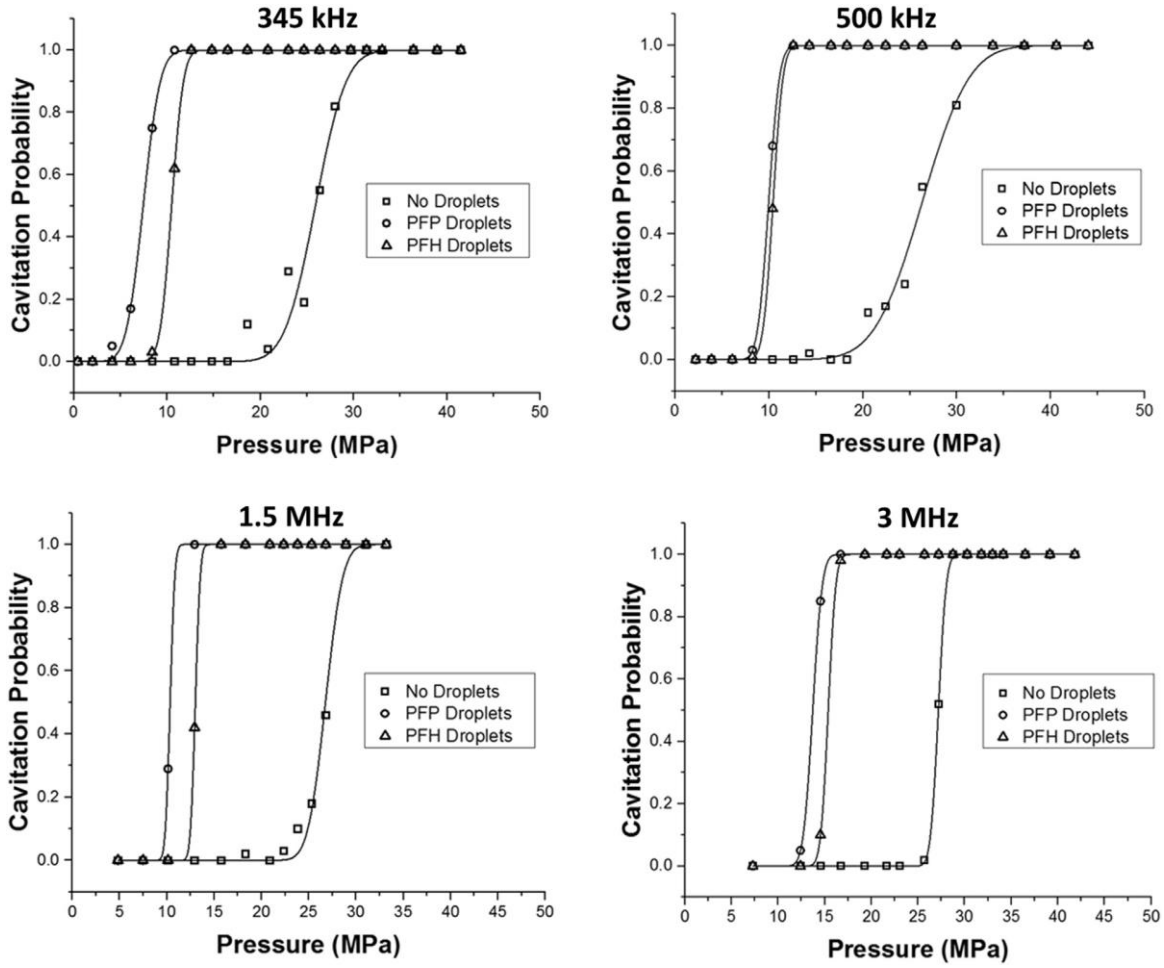

Figure B.5 Plots show sample cavitation probability curves for tissue phantoms containing PFP nanodroplets, PFH nanodroplets, and no nanodroplets at 345 kHz, 500 kHz, 1.5 MHz, and 3 MHz.

At all frequencies, results showed a significant decrease in the cavitation threshold with both PFP and PFH nanodroplets compared to controls. Results also showed a slight increase in the nanodroplet cavitation threshold for PFH nanodroplets compared to PFP nanodroplets.

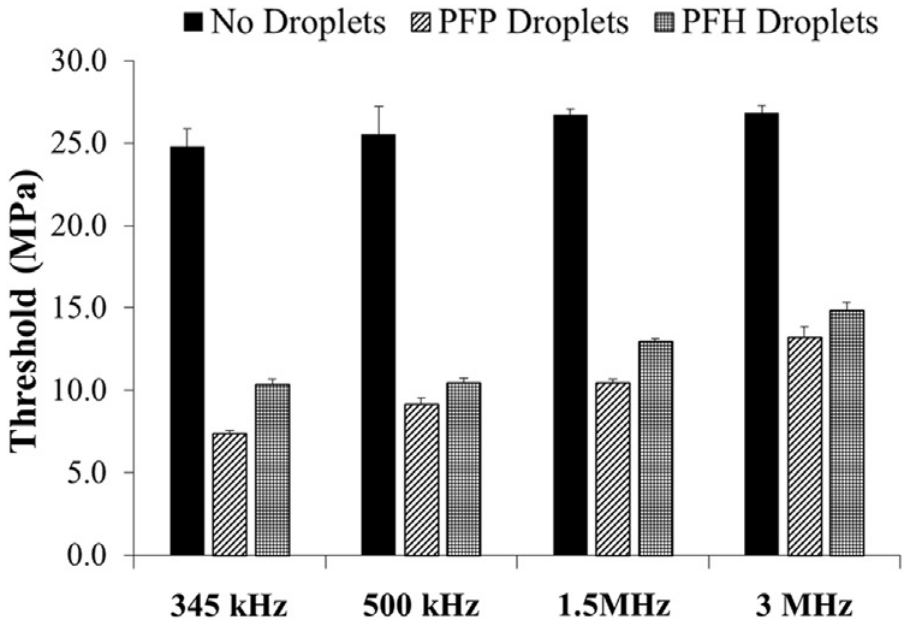

Figure B.6 Bar plots show the complete cavitation threshold results for tissue phantoms containing PFP nanodroplets, PFH nanodroplets, and no nanodroplets.

All differences in the cavitation threshold between samples were statistically significant ($p<0.05$).

NMH Multi-pulse Sustainability

To compare the ability of nanodroplets to act as sustainable cavitation nuclei over multiple pulses, 1000 histotripsy pulses were applied to a single focal region in phantoms containing PFP and PFH nanodroplets at a PRF of 1 Hz. Results demonstrated that a bubble cloud consisting of many bubbles was observed after the first pulse for both types of droplets (**Figure B.7**). However, the bubble cloud generated in PFH phantoms was a more well-defined bubble cloud, similar to those previously observed for histotripsy above the intrinsic threshold [337, 345]. At all frequencies, over all 1,000 pulses, a dense bubble cloud was produced in PFH phantoms, with the bubbles more tightly confined inside the focal region and no significant change in the number of bubbles inside the cloud (**Figure B.7 and B.8**). In comparison, after the first pulse, the bubble cloud generated in the PFP phantom is sparsely populated (**Figure B.7 and B.8**). At all frequencies, the number of bubbles observed inside PFP phantoms significantly decreased with

increasing number of pulses, and bubbles distinguished after ~5-50 pulses. At a higher frequency, the bubble cloud distinguished with fewer pulses. For example, no bubbles were observed after ~50 pulses in PFP phantoms exposed to 500 kHz (p-=12.6 MPa) pulses and after ~5 pulses exposed to 3 MHz (p-=15.6 MPa) pulses.

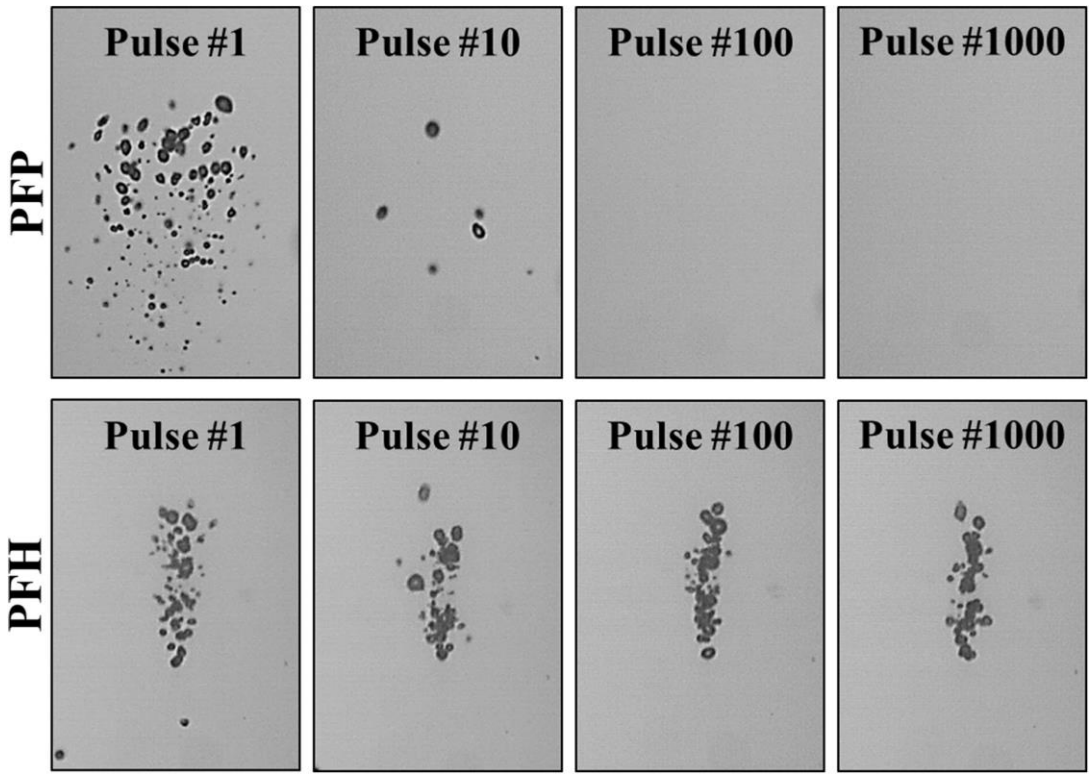

Figure B.7 Optical images show NMH bubbles produced by 500 kHz (p-=12.6 MPa) pulses at a single focal point in tissue phantoms containing PFP and PFH nanodroplets at a PRF of 1 Hz.

Results for PFP phantoms showed a decrease in the number of bubbles observed at the focus, with increasing pulse number, with no bubble observed after ~50 pulses. PFH phantom results demonstrated no significant decrease in the number of bubbles observed at the focus with increasing pulse number, with well-defined dense bubble clouds still observed after 1,000 pulses.

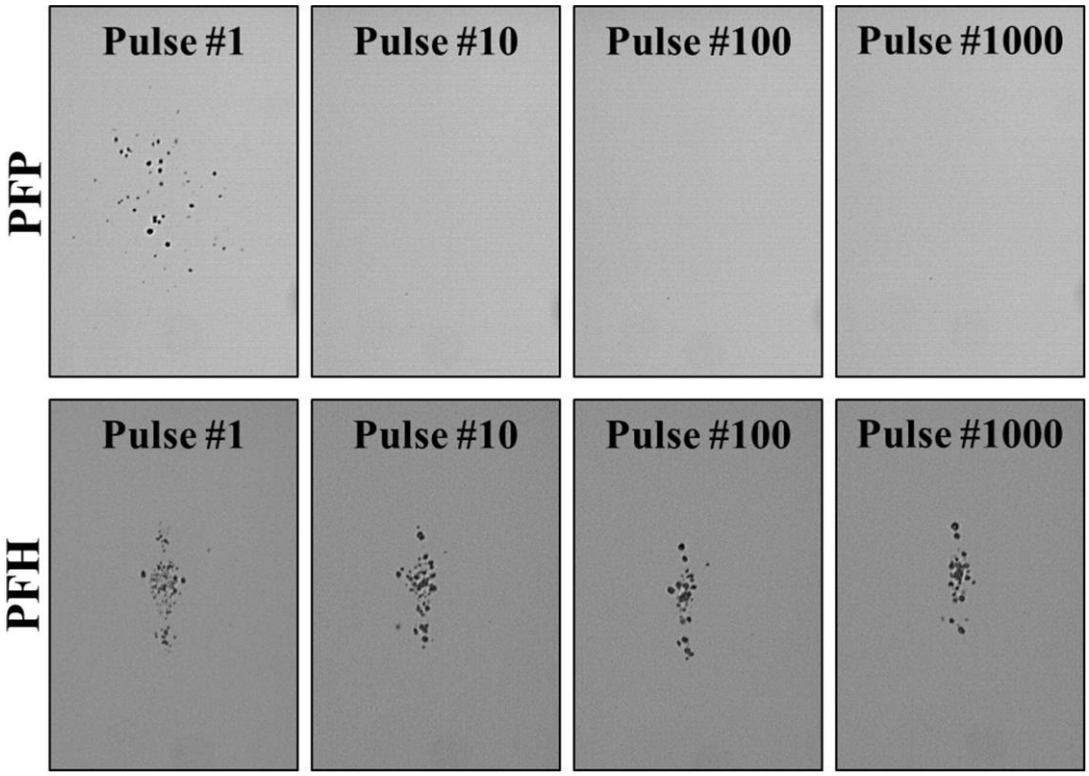

Figure B.8 Optical images show NMH bubbles produced by 3 MHz (p-=15.6 MPa) pulses at a single focal point in tissue phantoms containing PFP and PFH nanodroplets at a PRF of 1 Hz. Results for PFP phantoms showed a decrease in the number of bubbles observed at the focus, with increasing pulse number, with no bubble observed after ~5 pulses. PFH phantom results demonstrated well-defined NMH bubble clouds were still observed after 1,000 pulses.

NMH RBC Phantom Ablation

Agarose tissue phantoms embedded with RBC layers were used to compare NMH ablation for phantoms containing PFP and PFH nanodroplets. Results demonstrated that NMH generated consistent, well-defined lesions for RBC phantoms containing PFH nanodroplets, with the results being consistent for NMH treatments applied at 1 Hz and 10 Hz PRF. For example, **Figures B.9 and B.10** show images of NMH lesions generated inside RBC phantoms containing PFH droplets using the 345 kHz (**Figure B.9**) and 1.5 MHz (**Figure B.10**) transducers.

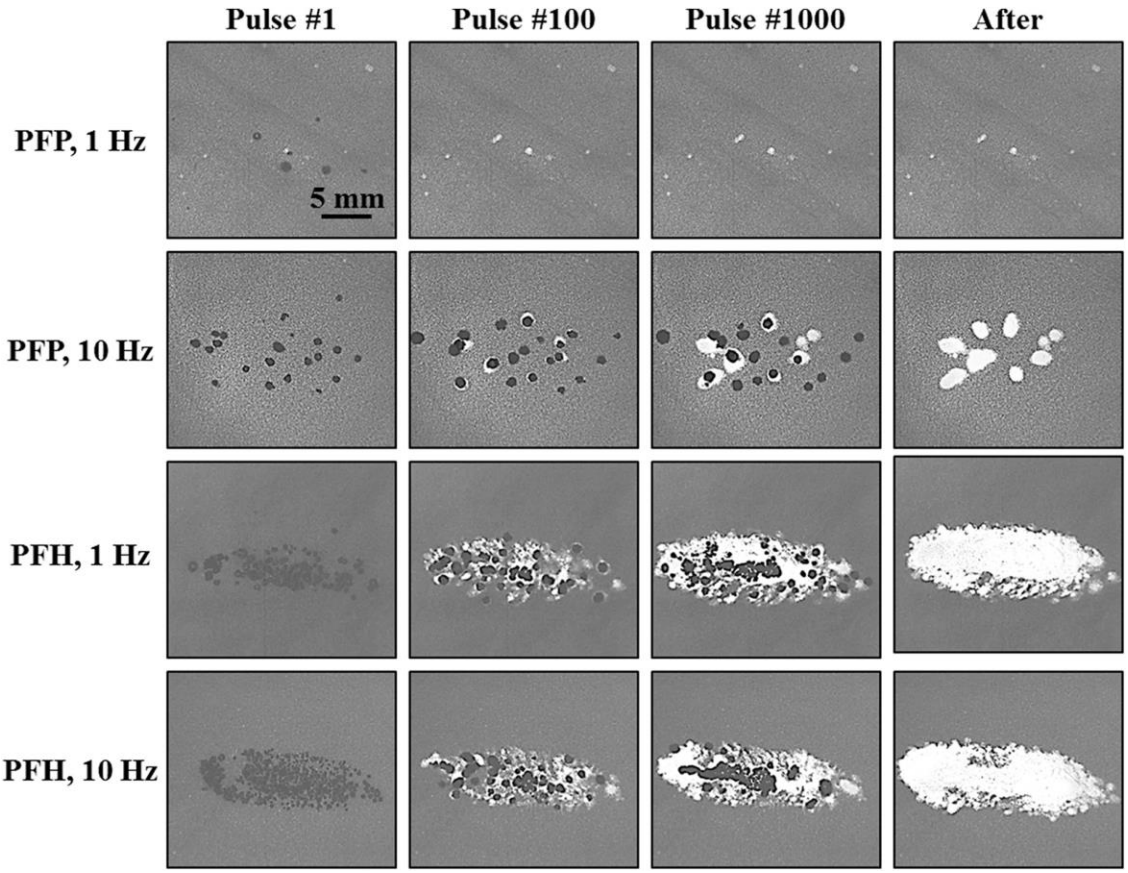

Figure B.9 Optical images show NMH fractionation produced by 345 kHz (p-=12.6 MPa) pulses in RBC phantoms containing PFP and PFH nanodroplets at PRFs of 1 Hz and 10 Hz.

Results showed significantly larger and more well-defined lesions generated inside the PFH tissue phantoms, compared to the sparse lesions inside the PFP tissue phantoms.

For all cases, dense cavitation bubble clouds were generated inside the PFH phantom on every pulse, resulting in sharp lesions with well-defined boundaries between the fractionated lesion and intact RBCs (**Figure B.9 and B.10**). In contrast, only sparse lesions were formed inside the PFP phantoms. For example, for the 10 Hz PRF treatments using the 345 kHz transducer, sparse cavitation bubble clouds were observed over the course of the treatment, with the location of the bubbles remaining consistent from pulse to pulse inside the PFP phantoms, resulting in sparse lesions (**Figure B.9**). For the 1 Hz treatments inside the PFP phantoms using the 345 kHz

transducer, cavitation was only observed on the initial pulses (<10 pulses) and was not maintained for the duration of the treatment, resulting in very small lesions after treatment (**Figure B.9**).

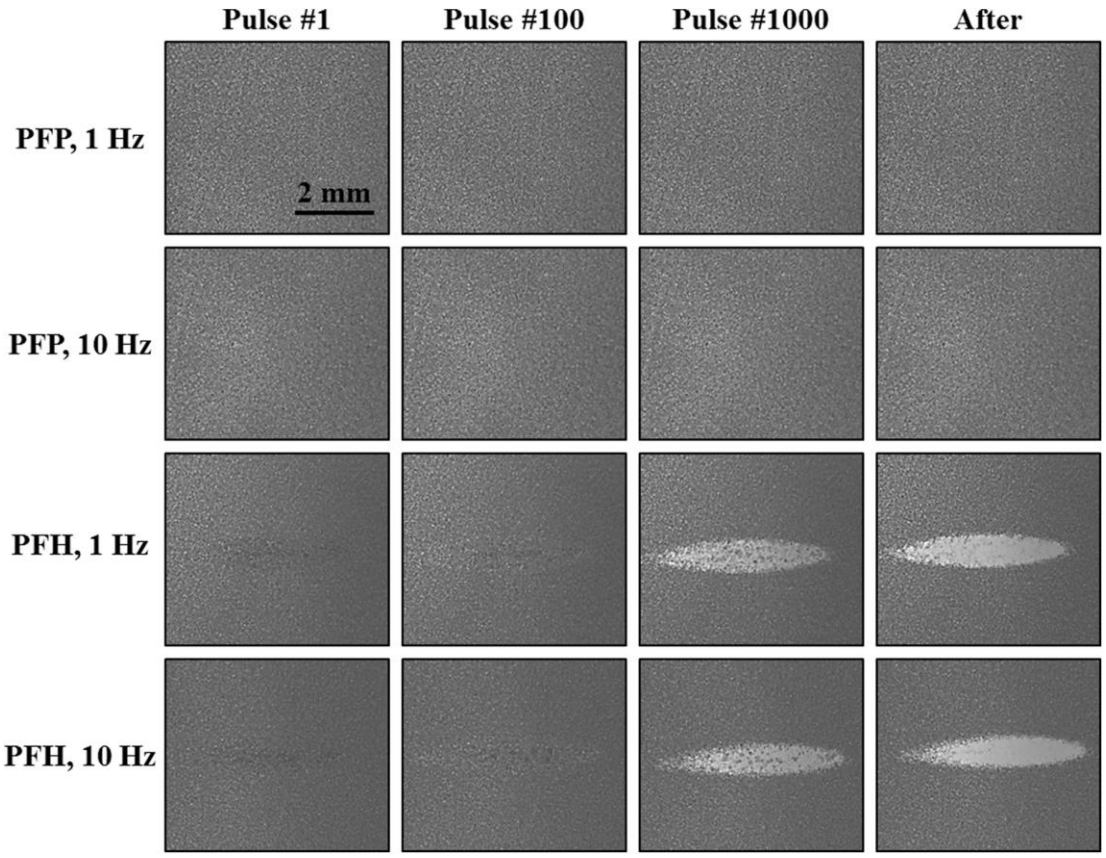

Figure B.10 Optical images show NMH fractionation produced by 1.5 MHz (p-=15.7 MPa) pulses in RBC phantoms containing PFP and PFH nanodroplets at PRFs of 1 Hz and 10 Hz.

Results showed well-defined lesions generated inside the PFH tissue phantoms. No visible lesions were observed for treatments applied to tissue phantoms containing PFP droplets.

At higher frequency (i.e. 1.5 MHz), no visible lesions were observed in the PFP phantoms for either 1 Hz or 10 Hz treatments, with bubbles only visible on the first pulse (**Figure B.10**). Quantifying the lesions areas for RBC phantoms (n=4) demonstrated a significant decrease in lesion size for phantoms containing PFP droplets in comparison to PFH phantoms. For example, at 345 kHz the lesion areas inside the PFH phantoms were 14.35±1.13 mm^2 (1 Hz) and 15.01±1.61 mm^2 (10 Hz), which were significantly larger than the lesion areas inside the PFP phantoms of

0.05±0.04 mm^2 (1 Hz) and 3.24±0.29 mm^2 (10 Hz). At 1.5 MHz, the lesion areas inside the PFH phantoms were 1.31±0.09 mm^2 (1 Hz) and 1.17±0.13 mm^2 (10 Hz), which were significantly larger than the lesion areas inside the PFP phantoms of 0.00±0.00 mm^2 (1 Hz, 10 Hz).

Discussion

In this study, the effects of droplet composition on NMH therapy were investigated using perfluoropentane (boiling point~29°C, surface tension~9.5 mN/m) and perfluorohexane (boiling point~56°, surface tension~11.9 mN/m) nanodroplets. In the first part of this study, PFP and PFH droplets were synthesized using a previous developed method [46]. The results from the nanodroplet characterization suggest that the droplet preparation method described by Durmaz *et al* can be used to create nanodroplets with similar surface characteristics within the media while the composition of the encapsulated perfluorocarbon can be modulated as desired [46]. The design of the triblock amphiphilic copolymer acts to increase the particle's solubility in aqueous environments due the hydrophilic character of the outer PEG block while also improving hemocompatibility (i.e. no protein adsorption on the particles, no macrophage recognition, and minimum interaction with blood cells during blood circulation) [46, 247, 249]. The results of this study suggest that the PFC inside the nanodroplets can be easily modified to take advantage of perfluorocarbons with different boiling points without losing the benefits of the functionalized polymer shell.

In the second part of this study, the effects droplet composition on the histotripsy cavitation threshold were investigated, with resulting showing a significant decrease in the cavitation threshold for both types of nanodroplets compared to controls, with a slightly lower threshold observed for PFP phantoms, likely due to the decrease in surface tension for PFP. These results

support our hypothesis that both PFP and PFH nanodroplets can be used to significantly reduce the pressure required to generate histotripsy bubbles for NMH therapy. At all frequencies tested, the NMH threshold for both types of droplets was significantly lower (>10 MPa decrease) than the histotripsy intrinsic threshold, while maintaining a steep threshold behavior. In fact, the σ_{mean} values calculated by the curve fit decreased (i.e. sharper threshold curve) for phantoms containing nanodroplets, with the lowest σ_{mean} values observed for phantoms containing PFH droplets (**Table B.1**). This distinct threshold behavior is promising for the development of NMH therapy in which the applied pressure must be chosen in the region above the NMH threshold but below the histotripsy intrinsic threshold to ensure cavitation is only generated in regions containing nanodroplets. The results of these threshold experiments suggest that both PFP and PFH nanodroplets could be used for NMH, with PFP droplets offering a slightly lower threshold (~1-3 MPa decrease). With everything else equal, one might expect a lower cavitation threshold for the larger PFH droplets (233.9±3.9 nm) compared to PFP droplets (177.9±1.9 nm). It is possible that the slight decrease in threshold for PFP droplets is due to the lower surface tension of PFP (9.5 mN/m) compared to PFH (11.9 mN/m), as previous work has demonstrated that the cavitation threshold is highly dependent upon the surface tension of the media (i.e. bulk fluid inside the droplet) when using the 1-2 cycle pulses used in this study [44, 337]. These results suggest that the nanodroplets may actually decrease the cavitation threshold by carrying a lower threshold medium, rather than each droplet acting as single cavitation nuclei as would be the case for an air contrast agent. Based on this finding, the results of this work suggest that the NMH threshold can be selectively modulated by changing the droplet composition, with lower surface tension/boiling point droplets resulting in a decreased cavitation threshold. The finding that the NMH threshold can be finely tuned by changing droplet composition while maintaining the distinct threshold

behavior is a significant benefit for the development of NMH therapy as well as for other nanodroplet applications such as selective drug delivery [346].

In the final part of this study, the effects of droplet composition on cavitation sustainability and tissue fractionation were investigated, with results showing that PFH nanodroplets were sustainable cavitation nuclei over multiple pulses, while PFP nanodroplets were destroyed during the initial pulses. This effect resulted in well-defined lesions being generated inside the red blood cell phantom containing PFH droplets under all treatment conditions. In contrast, only sparse lesions were formed inside the PFP phantoms for the 345 kHz treatments applied at 10 Hz PRF, with no visible lesions observed at higher frequency (i.e. 1.5 MHz) or lower PRF (i.e. 1 Hz). The increased cavitation sustainability of the PFH droplets is most likely due to the re-condensing of PFH droplets into a liquid after the cavitation event occurs, due to the higher boiling point of the PFH droplets. The finding that PFH nanodroplets act as sustainable cavitation nuclei over multiple pulses, while PFP droplets are destroyed during the initial pulses, supports our hypothesis that using droplets with a higher boiling point is advantageous for NMH therapy. Results suggest that PFH droplets may re-condense into a liquid after the collapse of the cavitation bubble while the PFP bubbles are destroyed by the cavitation process (i.e. do not return to liquid form). These results suggest that higher boiling point droplets can be used to significantly reduce the nucleation threshold for generating cavitation bubbles over multiple pulses, allowing NMH therapy to be applied for multiple pulses until the targeted tissue is completely fractionated, even at low PRF. In contrast, due to the lower boiling point, PFP nanodroplets are only capable of reducing the cavitation threshold on the initial pulses, requiring cavitation on subsequent pulses to be generated from residual nuclei remaining in the focal region from previous pulses. The finding that higher boiling point droplets can serve as functional cavitation nuclei over multiple pulses is therefore a

major benefit for NMH therapy, as previous work has shown a decrease in ablation efficiency for higher PRF treatments that rely on residual nuclei from previous pulses to maintain the cavitation bubble cloud [335].

In addition to the finding that PFH droplets acted as sustainable cavitation nuclei over multiple pulses, it was also observed that the NMH bubble clouds produced from PFH droplets were more well-defined and densely populated compared to the sparse bubble clouds produced by the PFP droplets, even when comparing bubble clouds produced on the first pulse. The well confined, dense bubble clouds produced inside the PFH phantoms closely match the behavior of bubble clouds previously observed for histotripsy treatments above the intrinsic threshold, which have been shown to be efficient and precise at fractionating the target tissue [44, 337, 343, 345]. In contrast, the more sparse bubble clouds produced inside the PFP phantoms resemble bubble clouds generated at higher PRF or bubble clouds that rely upon residual nuclei in order to maintain cavitation, which have been shown to be less efficient at fractionating tissue while increasing collateral damage to surrounding tissue [335]. This observation suggested that NMH bubble clouds produced using PFH droplets will be more efficient at fractionating tissue and provide less collateral damage to surrounding tissue compared to NMH therapy using PFP droplets, which was validated by the final set of experiments in this study comparing NMH ablation in red blood cell phantoms.

Conclusion

In this work, the effects of droplet composition on NMH therapy were investigated using perfluoropentane (boiling point~29°C, surface tension~9.5 mN/m) and perfluorohexane (boiling point~56°, surface tension~11.9 mN/m) droplets. The results demonstrated a significant decrease

in the cavitation threshold for both types of nanodroplets compared to controls, with a slightly lower threshold observed for PFP phantoms, likely due to the decrease in surface tension for PFP. Results further demonstrated that PFH nanodroplets were sustainable cavitation nuclei over multiple pulses, while PFP nanodroplets were destroyed during the initial pulses. This effect is most likely due to the re-condensing of PFH droplets into a liquid after the cavitation event occurs, due to the higher boiling point of the PFH droplets. In the final part of this study, tissue phantoms containing a layer of embedded red blood cells were used to compare the damage generated for NMH treatments using PFP and PFH droplets, with results showing PFH nanodroplets significantly improved NMH ablation, allowing for well-defined lesions to be generated at all frequencies and PRFs tested. The results of this study suggest that NMH therapy can be significantly enhanced by modulating droplet composition in order to optimize the cavitation threshold (decrease droplet surface tension) and increase the multi-pulse sustainability (increase droplet boiling point). Overall, the results of this study provide significant insight in the role of droplet composition in NMH therapy and will provide a rational basis to specifically tailor droplet parameters in order to improve NMH tissue fractionation.

Acknowledgements

We would like to thank Sonja Capracotta, PhD (Technical Specialist, Nano Sight, School of Public Health at the University of Michigan) for her help on NTA size and concentration measurements. This material is based upon work supported by a National Science Foundation Graduate Research Fellowship to Eli Vlaisavljevich. Omer Aydin acknowledges the support of the Turkish Republic the Ministry of National Education Fellowship Program (1416). This work was supported by a grant from the United States Department of Defense (W81XWH-11-PCRP-ID).

Disclosure notice: Drs. Eli Vlaisavljevich, Kuang-Wei Lin, Brian Fowlkes, and Zhen Xu have financial interests and/or other relationship with HistoSonics Inc.

Appendix C

The Role of Positive and Negative Pressure on Cavitation Nucleation in Nanodroplet-Mediated Histotripsy

The material in this chapter is published from the following article: E. Vlaisavljevich, **O. Aydin,** Y. Y. Durmaz, K-W Lin, B. Fowlkes, M. ElSayed, and Z. Xu "The Role of Positive and Negative Pressure on Cavitation Nucleation in Nanodroplet-Mediated Histotripsy" *Phys. Med. Biol, 30, 61(2), 663-682, **2015**.*

Introduction

Histotripsy is a noninvasive tissue ablation method that controllably fractionates soft tissue through cavitation generated by high pressure, short duration ultrasound pulses [49, 313, 336]. Histotripsy is currently being studied for many clinical applications where non-invasive tissue removal is desired including benign prostatic hyperplasia [319], deep vein thrombosis [164], congenital heart disease [165, 166], fetal interventions [347, 348], and cancer [45, 167]. Although histotripsy has shown promise for many clinical applications including tumor ablation, this approach is limited to applications in which the target tissue can be identified and imaged prior to treatment, which is often not feasible in cancer patients with many small tumor nodules and micro-metastases. Histotripsy also requires very high pressure (P–>20MPa), which may not be achievable in some target tissues with limited acoustic access. Due to these limitations, our group has recently developed a targeted ablation approach combing polymer encapsulated nanodroplets

with histotripsy [46, 79]. Nanodroplet-mediated histotripsy (NMH) takes advantage of the significantly reduced cavitation threshold of the nanodroplets, allowing for cavitation to be selectively generated only in regions containing nanodroplets [79]. By synthesizing nanodroplets in a size range (~100-400 nm) in which they can diffuse through the leaky tumor vasculature and preferentially accumulate in the tumor, NMH has the potential for selective ablation of tumors [46, 79]. Previous work has demonstrated that NMH can be used to create well-defined ablation similar to histotripsy but at significantly lower pressure and has the potential to be used for simultaneous multi-focal ablation [79].

Understanding the physical mechanisms underlying the NMH cavitation process is essential for the development of NMH therapy. Previous studies on acoustic droplet vaporization (ADV) have shown that the ADV vaporization thresholds do not appear to follow the trends predicted by classical nucleation theory (CNT), which predicts that cavitation will be nucleated inside the droplets directly from the applied negative pressure (*p*-) [330-332, 349-354]. These studies have led to the hypothesis that nanodroplet nucleation in ADV is caused by a different mechanism than what is predicted by CNT, such as droplet deformation, hydrodynamic cavitation, or acoustic heating [330, 353, 354]. However, these ADV studies used larger droplets, higher frequency ranges, and pulses with more acoustic cycles than those used in NMH therapy [46, 79, 80, 330-332, 353-355]. Furthermore, recent work reveals that the decrease in the ADV threshold at higher frequencies is due to superharmonic focusing, which significantly increases the amplitude of the *p*- inside the droplet and is enhanced at higher frequencies and in larger droplets [333, 334]. Therefore, it is possible that ADV nucleation does in fact follow the predictions of CNT, once the effects of pressure focusing are accounted for.

In NMH, cavitation bubbles are generated from nanodroplets <600 nm in diameter using single-cycle ultrasound pulses at frequencies in the hundreds of kHz to low MHz range, resulting in cavitation thresholds significantly higher than the vaporization thresholds previously measured for ADV [46, 79, 80, 353, 355], with the trends appearing the follow the predictions of CNT [337, 349-352]. For example, previous work has demonstrated a significant reduction in the histotripsy cavitation threshold for both perfluoropentane (PFP) and perfluorohexane (PFH) nanodroplets exposed to single cycle histotripsy pulses [44, 80, 337, 355, 356]. The NMH cavitation threshold decreases at lower frequencies [80, 355], in contrast to the increasing ADV threshold with higher frequency observed using micron sized droplets [330-332, 353]. The NMH frequency dependence appears to agree with CNT, which predicts that lower frequency will decrease the cavitation threshold due to the longer duration of the applied *p*- and the larger focal zone at lower frequencies [80, 337, 349-352, 355]. Furthermore, a slight increase in the NMH cavitation threshold has been observed for PFH nanodroplets compared to PFP droplets due to the increase in the surface tension and boiling point of PFH, which also agrees with the predictions of CNT [80, 337, 349-352, 355].

Based on these previous studies, we hypothesize that NMH bubbles are generated after cavitation is nucleated inside the droplets directly from the incident *p*- (tensile portion of the incident wave), similar to histotripsy bubbles generated without nanodroplets when the negative pressure directly exceeds the intrinsic threshold [44, 337, 357]. In order to test this hypothesis, in this study we separate the effects of negative and positive pressure on NMH cavitation nucleation using near half-cycle ultrasound pulses with dominant negative (negative-polarity pulses) or positive (positive-polarity pulses) pressure phases. This paper reports the first study that separately investigates the effects of negative and positive pressure on the NMH cavitation process. The generation of near monopolar pulses was made possible by using a frequency compounding

transducer recently developed in our lab, which aligns the positive or negative phases of multiple-frequency components while destructive interference occurs elsewhere in space and time, leading to pulses with a single dominant negative or positive pressure phase [357]. Tissue phantoms containing PFH nanodroplets and control phantoms without droplets were exposed to negative-polarity and positive-polarity pulses, and optical imaging was used to measure the NMH cavitation threshold as a function of peak negative (P–) and peak positive (P+) pressure. The NMH cavitation threshold definition is similar to the ADV threshold, with the difference being in the type of bubble that is generated from the nanodroplets (i.e. transient cavitation bubble vs. stable ADV bubble). Finally, to help explain the experimental results, CNT was used to theoretically investigate the expected cavitation thresholds for samples with and without PFH nanodroplets, with the CNT results compared to the experimentally observed thresholds. Overall, the results of this study will improve our understanding of the physical mechanisms underlying the NMH cavitation process, which is essential for the development of NMH therapy.

Methods

Nanodroplet Formulation and Characterization

Polymer encapsulated perfluorohexane (PFH, SynQuest Lab, > 98%) nanodroplets were used for this study based on recent work demonstrating that PFH droplets have many benefits for NMH therapy [355]. A PEG_{45}-*b*-PAA_{12}-*b*-P($HDFMA_8$-*co*-MMA_{20}) triblock copolymer was synthesized using a combination of atom transfer radical polymerization (ATRP) and "click" coupling chemistry to prepare PFH-loaded nanodroplets following our published method [46]. Formulation of PFH-loaded nanodroplets started by dissolving the polymer in tetrahydrofuran (THF) (0.2% w/v) and cooling the solution down to 0^{o}C before adding PFH (2% v/v) while

vigorously stirring the reaction mixture. An equal volume of deionized water was added drop-wise to this solution to initiate micelle formation and the mixture was stirred for 1 hour in an ice bath. The micelles solution was transferred to a dialysis bag (MWCO of 1 KDa, Spectrum, Rancho Dominguez, CA) and dialyzed overnight against ice-cold MES buffer solution (pH 5.5) to remove the THF solvent and get a milky solution of non-cross-linked PFH-loaded nanodroplets. The milky nanodroplets solution was transferred to a round bottom flask and mixed with the 2,2`-(ethylenedioxy)-bis(ethylamine) cross-linker to react with the carboxyl groups of the central PAA block in the polymer backbone via NHS/EDC coupling chemistry forming cross-linked nanodroplets with a flexible polymer shell. Shell cross-linked nanodroplets were dialyzed against ice-cold water for 12 hours to remove unreacted cross-linker and reaction byproducts.

Concentration and size distribution of the nanodroplets were measured using Nanoparticle Tracking Analysis (NTA). Briefly, the NanoSight™ LM10 (Malvern Instruments, Amesbury, UK), equipped with a temperature-controlled 405 nm laser module, high sensitivity Scientific Complementary Metal–Oxide–Semiconductor (sCMOS) camera (Hamamatsu, Orca, Hamamatsu City, Japan), and a syringe pump was used for the collection of NTA data. Upon diluting the nanodroplet solution to the appropriate particle concentration with deionized (DI) water (Thermo Scientific, GenPure, Waltham, MA, USA), image capture and analysis was carried out using the NTA software (Version 3.0, Build 0066, Malvern Instruments, Amesbury, UK) at 37°C. The samples were measured by capturing 60s videos (5 videos per each sample). These values were determined in order to collect sufficient data such that the shape of the histogram no longer changed significantly with additional data (i.e. NTA analyzed hundreds or thousands of particles in order to calculate a representative particle size distribution). **Figure C.1** is a representative plot showing the size distribution of the PFH nanodroplets. The error bars represent the standard

deviation of the repeat measurements of each sample. The mean size and standard deviation values obtained by the NTA software correspond to arithmetic values calculated with the sizes of all particles analyzed for each sample (n=5). Results from all samples demonstrated that the average size of the nanodroplets (NDs) was 233±3.9 nm with 10% of NDs have a diameter ≤ 135.3±2.6 nm, 50% of the NDs have a diameter ≤ 192.7±5.3 nm, 90% of the NDs have a diameter ≤ 373.7±7.2 nm, and >99% of the NDs are ≤ 600 nm.

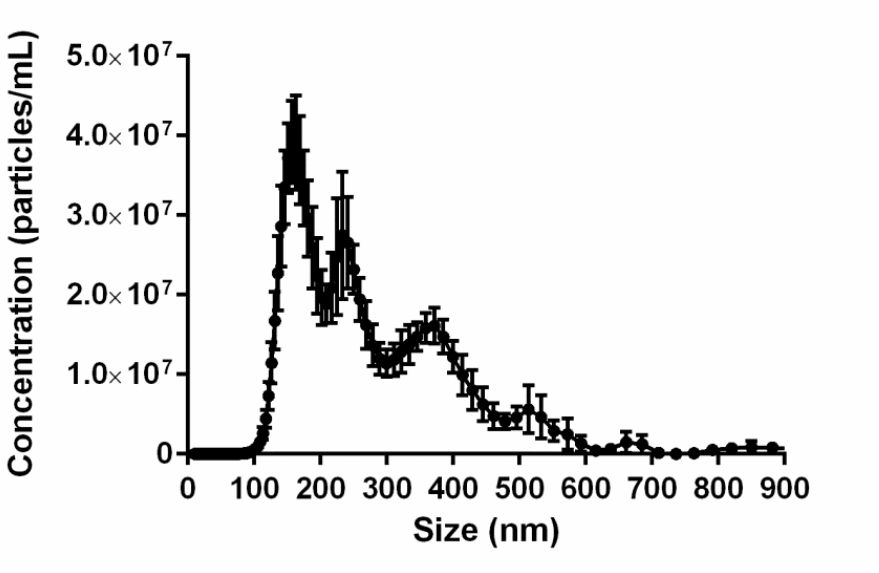

Figure C.11 Nanodroplet characterization. Nanoparticle Tracking Analysis demonstrated PFH nanodroplets had an average size of 233.9±3.9 nm.

Preparation of Tissue Phantoms

Agarose phantoms were used to provide a well-controlled viscoelastic medium for this study. Tissue phantoms containing 1% agarose w/v were prepared by slowly mixing agarose powder (Agarose Type VII; Sigma-Aldrich, St. Louis, MO, USA) into saline solution (0.9% sodium chloride; Hospira, Lake Forest, Illinois, USA) heated to boiling temperature. The solution was stirred on a hot plate until the gel turned completely transparent and then allowed to boil for

ten minutes. After boiling, solutions were allowed to cool and were degassed under a partial vacuum (~20 kPa, absolute) for 30 minutes. After degassing, phantoms containing nanodroplets were prepared by slowly adding the nanodroplets (2.0×10^8 particles/ml) into the agarose solution while stirring. The agarose mixtures were poured into polycarbonate holders and placed in a refrigerator at 4°C to allow the solution to solidify, forming tissue phantoms with embedded PFH nanodroplets and without nanodroplets (control). Tissue phantoms containing PFH nanodroplets were assumed to have a nearly uniform distribution of droplets throughout the phantom, which is supported by the observations in previous NMH studies which showed similar cavitation thresholds and bubble activity for treatments applied throughout all regions of these tissue phantoms [46, 79, 80]. The attenuation coefficients of the agarose tissue phantoms with and without PFH droplets were measured to be <0.1 dB/cm for the pulses used in this study. These values, along with the short propagation distance through the phantom (<2 cm), suggest that attenuation from the tissue phantoms will have a negligible impact on the reported pressure values which were measured in free field.

Histotripsy Pulse Generation

Histotripsy pulses with dominant negative (negative-polarity pulse) and positive (positive-polarity pulse) pressure phases were generated used a frequency compounding transducer, adapted from a previous study [357]. The frequency-compounding transducer was composed of 12 elements (20 mm in diameter) with various resonant frequencies: 500 kHz (three elements), 1 MHz (two elements), 1.5 MHz (two elements), 2 MHz (two elements), and 3 MHz (three elements) [357]. The elements had a common geometric focus at 40 mm and were populated in a scaffold in a specific order to ensure that adjacent elements did not have the same frequency. This was done to reduce nonlinear propagation effects that occur when acoustic waves of the same frequency

propagate closely in space and interfere constructively. Additionally, the frequency-compounding transducer has two diametrically opposed optical windows to allow for optical imaging at the geometric focus. The design of the frequency compounding transducer has been described in detail in a previous study [357].

A custom high voltage pulser with 12 parallel channels was used to drive the frequency-compounding transducer. The pulser was connected to a field-programmable gated array (FPGA) development board (Altera DE1, Terasic Technology, Dover, DE, USA) specifically programmed for frequency compounding pulse generation. This setup allowed each element to individually output short pulses with only one large negative or positive pressure phase. The generation of negative-polarity pulses was achieved by adjusting the arrival times of individual frequency components to allow their principal negative phase peaks to arrive at the focus of the transducer concurrently (**Figure C.2A**). In this situation, destructive interference occurs elsewhere in space and time, leading to a diminution of the peak positive pressure of the combined ultrasound pulse (**Figure C.2A**). For the generation of positive-polarity pulses, the driver pulses for the individual elements were inverted, resulting in ultrasound pulses with a single principal positive phase from each element. The arrival times of individual frequency components were then adjusted to allow their principal positive phase peaks to arrive at the focus concurrently (**Figure C.2B**).

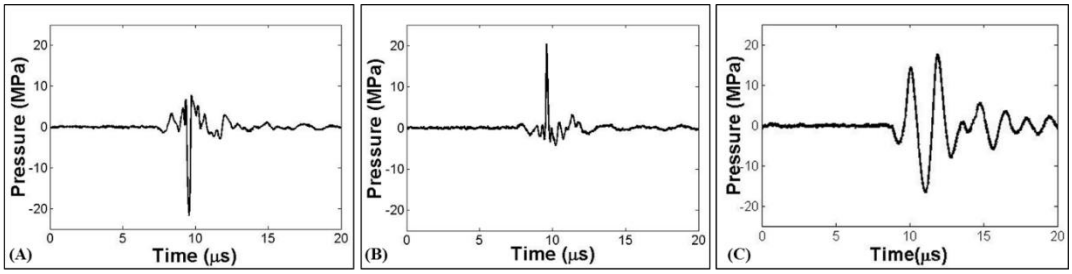

Figure C.12 Acoustic waveforms.

Example of (A) negative-polarity and (B) positive-polarity pulses produced by the frequency compounding transducer compared with a (C) dual-polarity pulse (500 kHz) previously used in NMH therapy.

A fiber-optic probe hydrophone (FOPH) built in-house [172] was used to calibrate and measure the acoustic output of the frequency-compounding transducer, with example waveforms shown in **Figure C.2**. For threshold experiments, the probability of cavitation (measured by optical imaging) was plotted as a function of both the peak negative (P–) and peak positive (P+) pressure. In order to determine the peak pressure values for the negative and positive polarity pulses, 2D spatial pressure fields were directly measured using the FOPH in order to identify the locations corresponding to the P– and P+ in the focal region. The ratio of P– to P+ measured for the negative-polarity pulses in this location was between 2.9-3.7 for the pressure ranges used in this study. For the positive-polarity pulses, the 2D spatial pressure fields measured by the FOPH demonstrated the location of the P– in the focal region occurred ~0.5 mm away from the geometric focus, while the location of the P+ remained near the geometric focus (**Figure C.3**). This effect is due to the temporal alignment of the principle peak positive peaks of the individual frequency components at the geometric focus, which resulted in a near monopolar positive pulse at the geometric focus with two low-negative-pressure lobes outside of the focal region. The ratio of P+ to P– for the positive-polarity pulses was measured to be between 3.2-3.9 for the pressure ranges used in this study using the P+ and P– measured at the maximum locations in the field. For the positive polarity

pulses, the pressure was directly measured up to the maximum output of the transducer, P–/P+=16.3/55.1 MPa. For the negative polarity pulses, the pressure at the focus could only be directly measured up to P–/P+=21.5/7.6 MPa due to cavitation at the fiber tip at higher pressures. The pressures above this value were estimated using a linear summation of the pressures measured for individual elements, as outlined in previous studies [44, 337, 345, 357].

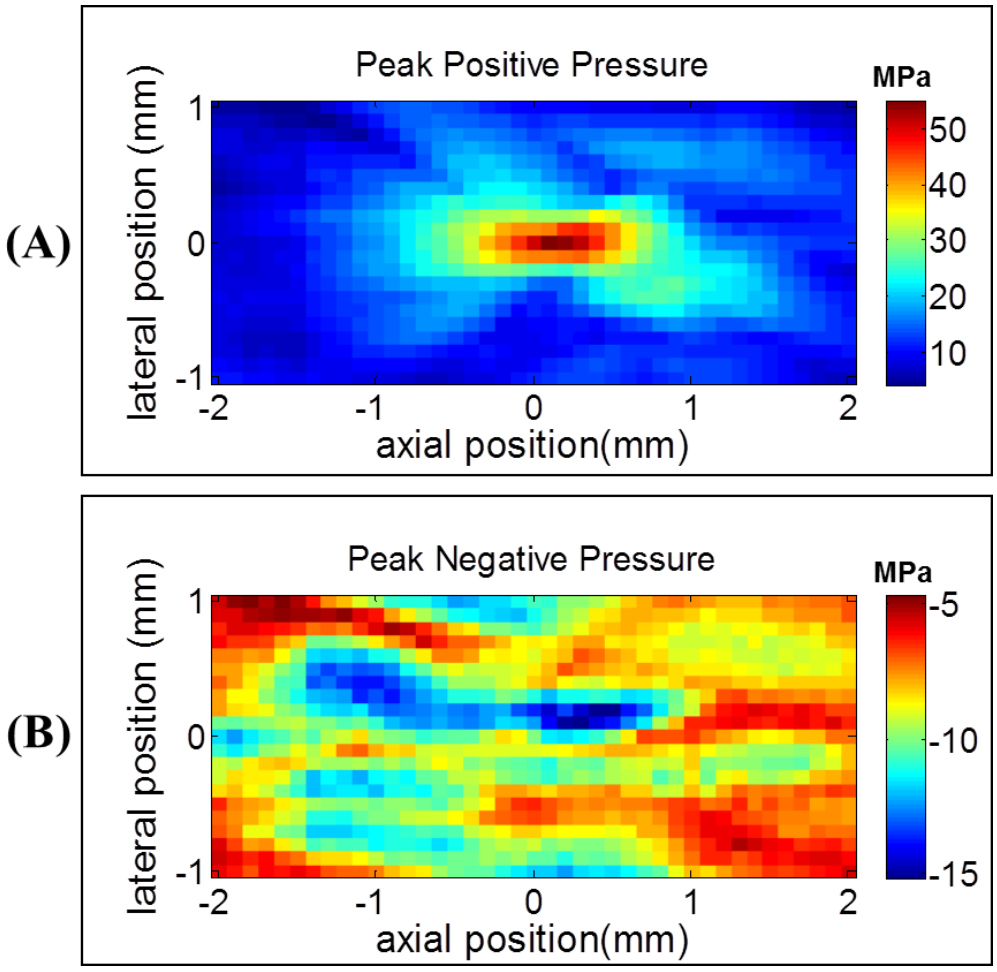

Figure C.13 Positive-polarity Pulse: Pressure Fields. 2D spatial pressure fields were measured by the FOPH for a positive-polarity pulse.

(A) Results demonstrated the location corresponding to the highest positive pressure was near the geometric focus. (B) The location corresponding to the highest negative pressure was ~0.5 mm away from the geometric focus in the axial direction.

Optical Imaging and Image Processing

High speed optical imaging was used to capture images of the focal zone after the propagation of each pulse through the focus. The frequency compounding transducer was placed on the bottom of a tank of degassed water, and a tissue phantom attached to a 3-axis motorized positioning system was lowered into the focus of the transducer (**Figure C.4**). A digital, 1.3-megapixel CCD camera (PN: FL3-U3-13Y3M-C, Flea® 3, PointGrey, Richmond, BC, Canada) was positioned perpendicularly to the frequency compounding transducer facing one of the transducer's optical windows (**Figure C.4**).

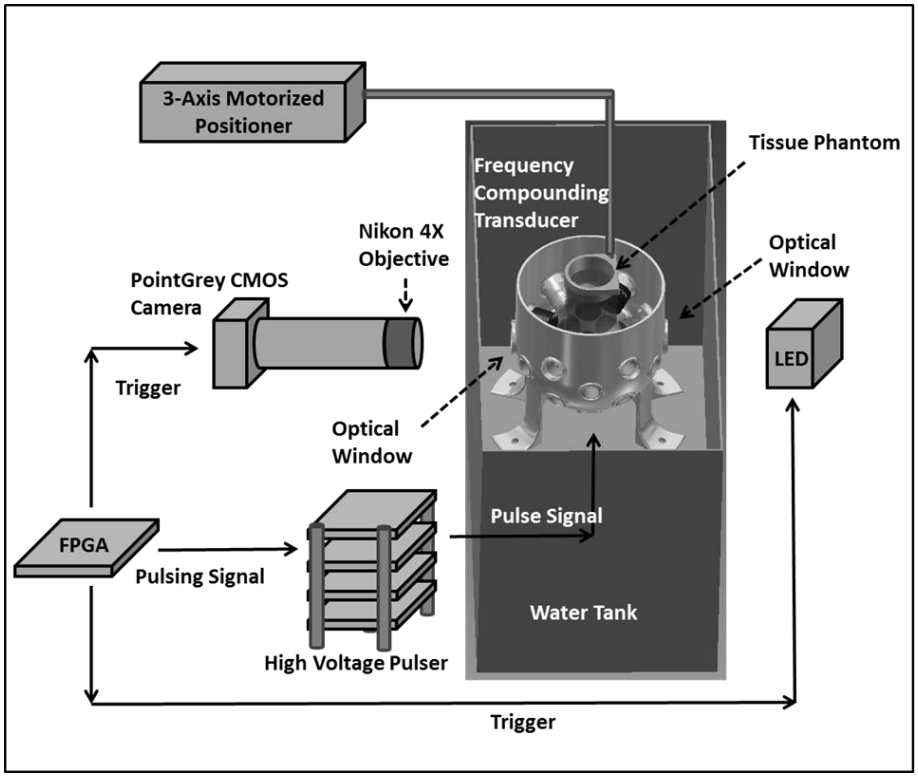

Figure C.14 Experimental set-up.

Tissue phantoms with and without PFH nanodroplets were placed at the focus of the frequency-compounding transducer [357] for cavitation threshold experiments. Cavitation was monitored using high-speed optical imaging through the transducer's optical windows.

A Nikon 4X objective was attached to the camera with extension tubes to magnify the image plane, giving the captured images a resolution of approximately 3.6 μm per pixel. A pulsed white-light LED was placed on the diametrically-opposed optical window of the dual-frequency array transducer, which provided back-lit illumination. The cameras were triggered to record one image after the passage of each pulse at a time point approximately corresponding to the maximum bubble expansion. This time point was determined for the negative-polarity and positive-polarity pulses prior to experiments by changing the delay time on the camera to identify the time corresponding to maximum bubble expansion, as described in previous studies [80, 337, 345]. After acquisition, shadowgraph images were converted from grayscale to binary by an intensity threshold determined by the background intensity using image processing software (MATLAB, The Mathworks, Natick, MA, USA), as described in a previous study [44]. Bubbles were indicated as any black regions greater than 5 pixels in diameter. By this criterion, the minimum resolvable bubble radius was 9 μm.

NMH Cavitation Threshold

For cavitation threshold experiments, 100 pulses were applied inside each sample at each pressure level at a pulse repetition frequency (PRF) of 0.5 Hz. The PRF was kept low to minimize the possibility that cavitation from one pulse would change the probability of cavitation on a subsequent pulse. In a previous study, it was demonstrated that cavitation during a pulse increased the likelihood of cavitation on a following pulse for PRFs > 1 Hz, but this effect was not observed for PRFs < 1 Hz [44]. In addition to this low PRF, the phantom sample was translated for each pulse by 1 mm transverse to the acoustic propagation direction in a 10 × 10 grid in order to minimize the effects of cavitation damage to the nanodroplets from altering the probability of cavitation. Using this method, each point in the tissue phantom was exposed to a single pulse at a

single pressure amplitude. For each pulse, cavitation was monitored using high speed imaging, and the fraction of total pulses at a given pressure level (out of 100) for which cavitation was detected was determined as the cavitation probability.

The probability of observing cavitation followed a sigmoid function, given by

$$P(p) = \frac{1}{2} + erf\left(\frac{p - p_t}{\sqrt{2\sigma^2}}\right) \quad \text{Eq. 8.1}$$

where *erf* is the error function, p_t is the pressure at which the probability p_{cav}=0.5, σ is a variable related to the width of the transition between p_{cav}=0 and p_{cav}=1, with ± σ giving the difference in pressure from about p_{cav}=0.15 to p_{cav}=0.85 for the fit [44]. The cavitation threshold for each sample, p_t, is defined as the pressure, p, corresponding to p_{cav}=0.5 as calculated by the curve fit. Curve fitting for all data sets was performed using an OriginLab curve fitting program (OriginPro 9.1; OriginLab Corporation, Northampton, MA, USA). The fit curves for all samples were analyzed statistically to determine whether the differences in the values of p_t were significantly different from each other. The standard errors for p_t were estimated by a covariance matrix using the delta method [329]. The curves were compared using a two-sample t-test with statistic $t\left(p_{int1} - p_{int2}, \sqrt{SE_1^2 + SE_2^2}\right)$ at a 95% confidence interval. Results were considered statistically significant for $p<0.05$. Note that the standard error does not include the uncertainty in absolute pressure from the hydrophone measurement, only the uncertainty in the fit, because the values p_t are relative. For each sample, the curves were analyzed as a function of both positive and negative pressure, with the corresponding cavitation threshold values calculated as $p_t(+)$ and $p_t(-)$, respectively. A sample size of 3 tissue phantoms was used for each experimental condition (i.e. phantoms containing PFH nanodroplets or no nanodroplets exposed to negative-polarity or positive-polarity pulses).

Classical Nucleation Theory Simulation

A theoretical analysis was performed based on classical nucleation theory (CNT) in order to theoretically investigate the expected cavitation thresholds [349, 350, 352, 358]. Previous studies using CNT suggest that the cavitation threshold is dependent upon the properties of the media (i.e. temperature, surface energy) as well as the spatial and temporal distribution of the applied *p*- [349, 358]. In this study, CNT was used to calculate the theoretical cavitation thresholds for samples with and without PFH nanodroplets. The CNT results were then compared to the experimental thresholds measured for the near monopolar pulses used in this study as well as for dual polarity pulses at frequencies ranging from 345 kHz to 3 MHz used in previous studies [80, 337]. The threshold predicted by CNT, p_{CNT}, was calculated as

$$p_{CNT} = \left(\frac{16\pi\alpha^3}{3k_bT * \ln\frac{\Gamma_0 V_f \tau_f}{\ln 2}} \right)^{0.5} \quad \text{Eq. 8.2}$$

where α is the surface energy, k_b is the Boltzmann's constant, T is temperature in Kelvin, Γ_0 is a prefactor, V_f is the focal volume for a given frequency, and τ_f is the time the focal volume is above a given pressure [349-352, 358]. Γ_0 was set to $\Gamma_0=10^{33}$ similar to previous work [337, 358]. V_f and τ_f were modified for each frequency with τ_f set to one fourth of the acoustic period and V_f representing the volume of fluid exposed to the applied pressure. An effective frequency of 1.8 MHz was used for the frequency compounding transducer, as calculated based on the duration of the applied *p*- pressure cycle shown in **Figure C.2A**. The values of V_{f_water} were calculated from the -6 dB FWHM beam profiles of the transducers assuming an ellipsoidal focus, and were 47.07 mm^3, 7.89 mm^3, 2.30 mm^3, 0.072 mm^3, and 1.04 mm^3 for 345 kHz, 500 kHz, 1.5 MHz, 3 MHz, and the frequency compounding transducer (1.8 MHz), respectively. For simulations of the cavitation threshold without droplets, the surface energy of water, α_w, was set to 19 mN/m, ~25%

of the macroscopic surface tension of water, based on previous work showing this value provides a more reasonable agreement with experimentally observed cavitation thresholds [337, 349, 352].

To theoretically investigate the cavitation threshold in phantoms containing PFH droplets, the CNT simulation was modified to account for the lower surface energy of PFH, α_{PFH}, which was set to 11.9 mN/m. In addition, the PFH threshold simulation was corrected to account for only the volume of PFH within the focal region. The volume of PFH in the focal region, V_{f_PFH}, was calculated by multiplying V_{f_water} by the amount of PFH in a unit volume of water, as calculated from the particle concentration and size distribution data shown in **Figure C.1**. The resulting values of V_{f_PFH} were 0.31 mm^3, 0.051 mm^3, 0.015 mm^3, 0.00046 mm^3, and 0.0068 mm^3 for 345 kHz, 500 kHz, 1.5 MHz, 3 MHz, and the frequency compounding transducer (1.8 MHz), respectively.

Results

NMH Cavitation Threshold: Negative-Polarity Pulse

In the first set of experiments, the histotripsy cavitation threshold was measured for agarose tissue phantoms with and without PFH nanodroplets exposed to negative-polarity pulses (**Figure C.2A**). For both types of phantoms, cavitation bubbles were only observed on the high-speed camera once a certain pressure threshold was exceeded (**Figure C.5**), as seen in previous studies [44, 80, 337, 355]. As the pressure was further raised above this threshold value, cavitation was observed in an increasingly larger region of the focal area, forming well-defined histotripsy bubble clouds similar to those observed in previous work using dual-polarity pulses at various frequencies [44, 80, 337, 345, 355]. Plotting the probability of cavitation as a function of P– demonstrated a significant decrease in $p_t(-)$ for tissue phantoms containing nanodroplets compared to control

phantoms (**Figure C.6A and C.6B**), with the P– threshold measured to be $p_{t\_}(–)$ = 29.8±0.3 MPa, with σ_{mean} = 0.7 MPa for control phantoms without nanodroplets and $p_t(–)$ = 11.7±0.2 MPa, with σ_{mean} = 0.4 MPa for PFH phantoms. These results closely matched the P– thresholds measured in previous studies using single-cycle dual-polarity pulses with center frequencies ranging from 345kHz to 3MHz (**Table C.1**).

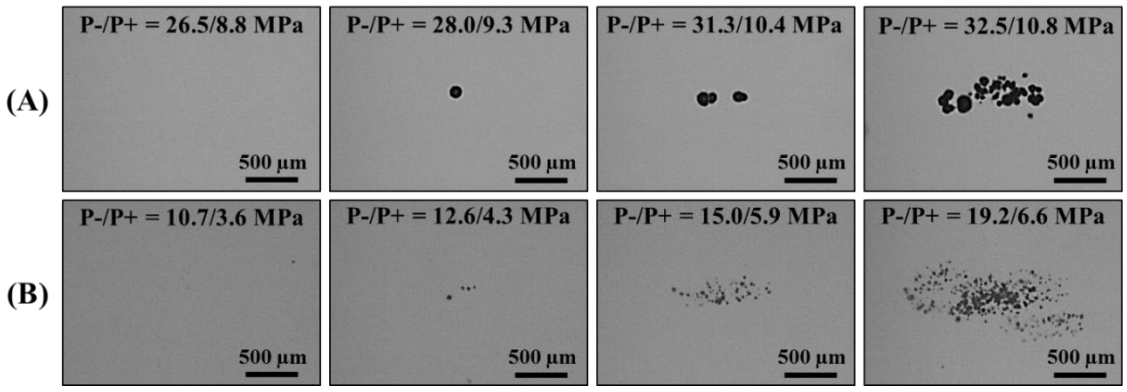

Figure C.15 Bubble Images: Negative-polarity Pulses. Optical Images of cavitation bubbles generated from negative-polarity pulses inside (A) control phantoms and (B) PFH phantoms.

The single-cycle dual-polarity pulses commonly used in histotripsy studies contain both high amplitude positive and negative pressure phases (**Figure C.2C**). The P– thresholds for generating cavitation previously measured with the dual-polarity pulse were 24 MPa–27 MPa without nanodroplets and 10 MPa–15 MPa with PFH nanodroplets (**Table C.1**) [80, 337, 355]. Plotting the probability of cavitation for the negative-polarity pulses as a function of P+ demonstrated a significant decrease in $p_t(+)$ for tissue phantoms containing nanodroplets compared to control phantoms (**Figure C.7A and C.7B**), with the P+ threshold measured to be $p_{t\_}(+)$ = 9.9±0.1 MPa, with σ_{mean} = 0.2 MPa for control phantoms and $p_t(+)$ = 4.0±0.1 MPa, with σ_{mean} = 0.2 MPa for PFH phantoms. The P+ threshold results measured for the negative-polarity pulses were significantly different than the P+ thresholds measured in previous studies using dual-polarity

pulses, which ranged from $p_t(+)$ = 28.1 MPa–51.2 MPa and $p_t(+)$ = 10.2 MPa–15.8 MPa for control and PFH phantoms, respectively (**Table C.1**).

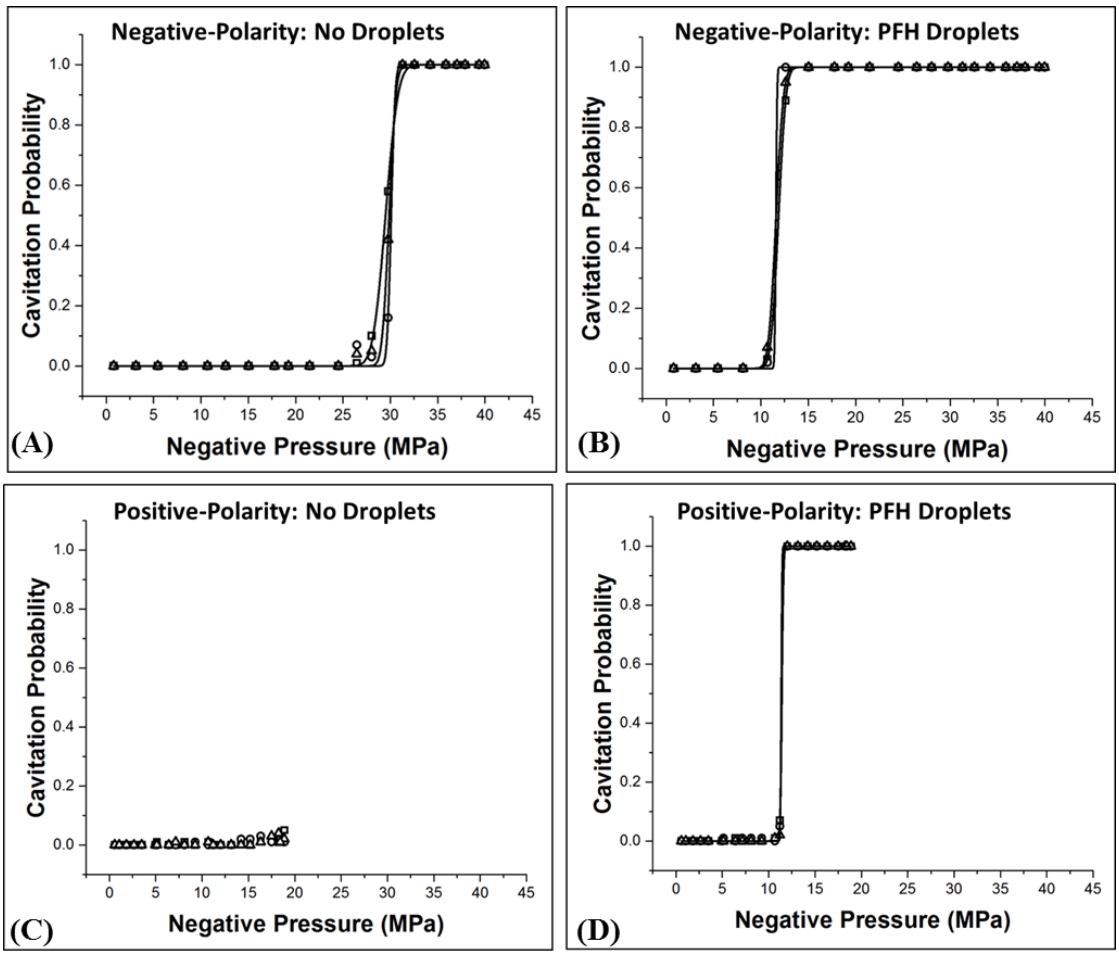

Figure C.16 Cavitation Probability vs. Negative Pressure. Plots show the cavitation probability as a function of negative pressure for (A, C) control and (B, D) PFH phantoms exposed to (A, B) negative-polarity pulses and (C, D) positive-polarity pulses.

The P– threshold measured for the negative-polarity and positive-polarity pulses showed close agreement for PFH phantoms. Cavitation couldn't be generated in control phantoms exposed to positive-polarity pulses (Max P–=18.4 MPa).

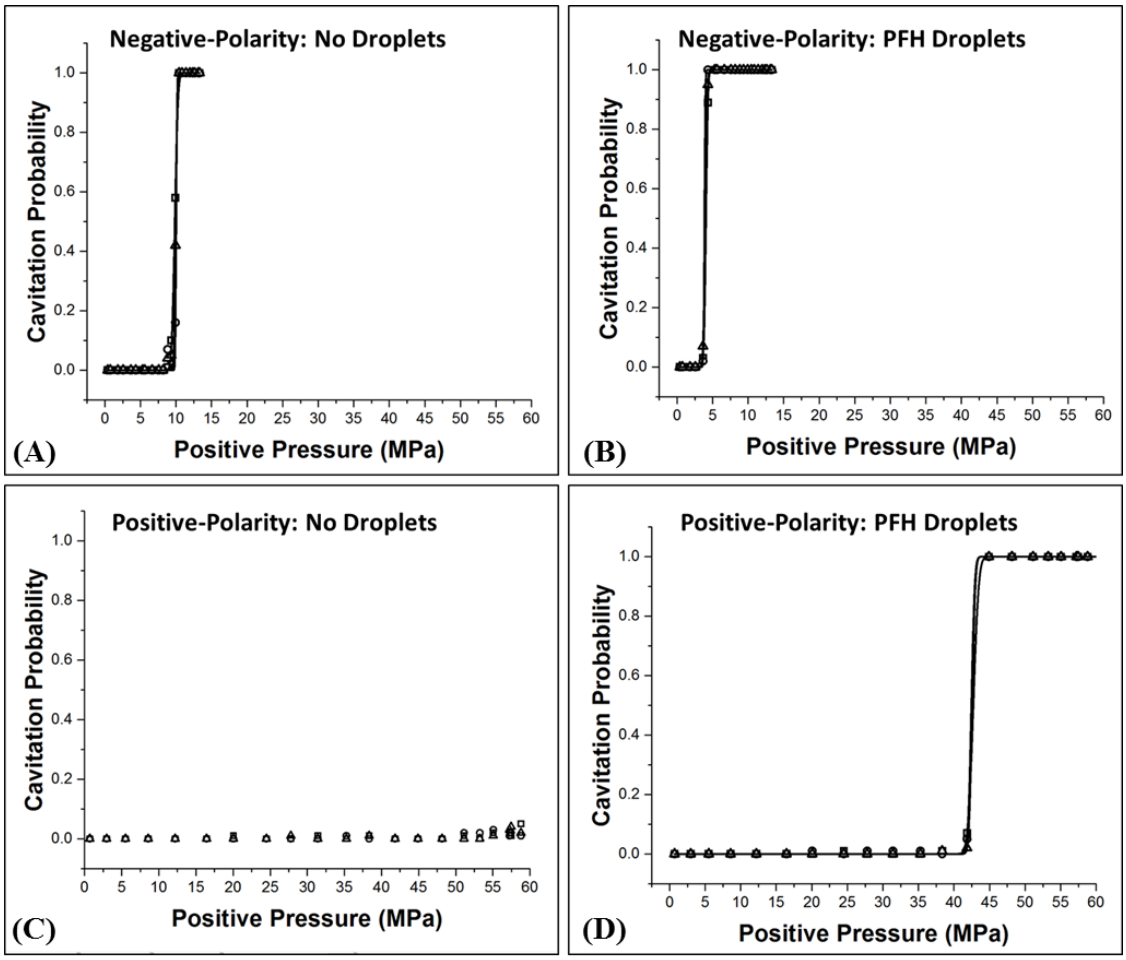

Figure C.17 Cavitation Probability vs. Positive Pressure.

Plots show the cavitation probability as a function of positive pressure for (A, C) control and (B, D) PFH phantoms exposed to (A, B) negative-polarity pulses and (C, D) positive-polarity pulses. A significant increase in the P+ threshold was observed for both control and PFH phantoms exposed to the positive-positive polarity pulses.

Table C.2 Threshold Results Comparison. Table shows the values for the P– and P+ thresholds measured for control and PFH phantoms exposed to the negative-polarity and positive-polarity pulses generated by the frequency compounding transducer along with the thresholds previously measured using dual-polarity pulses at 345 kHz, 500 kHz, 1.5 MHz, and 3 MHz [80, 337, 355]. Note: *Italics* represents data taken from previous studies.

Sample	Pulse Characteristics	P- Threshold (MPa)	P+ Threshold (MPa)
No Droplets	***Dual-Polarity: 345 kHz***	24.8±1.1	31.4±1.5
	Dual-Polarity: 500 kHz	25.5±1.7	28.1±1.9
	Dual-Polarity: 1.5 MHz	26.7±0.4	51.2±2.3
	Dual-Polarity: 3 MHz	26.8±0.5	29.4±29.4
	Negative-Polarity	29.8±0.3	9.9±0.1
	Positive-Polarity	>18.4	>61.1
		P- Threshold (MPa)	**P+ Threshold (MPa)**
PFH Droplets	***Dual-Polarity: 345 kHz***	10.4±0.3	10.2±0.2
	Dual-Polarity: 500 kHz	10.5±0.2	10.7±0.2
	Dual-Polarity: 1.5 MHz	13.0±0.1	14.1±0.2
	Dual-Polarity: 3 MHz	14.9±0.4	15.8±0.4
	Negative-Polarity	11.7±0.2	4.0±0.1
	Positive-Polarity	11.4±0.1	42.6±0.2

NMH Cavitation Threshold: Positive-Polarity Pulse

In the second set of experiments, the histotripsy cavitation threshold was measured for tissue phantoms with and without PFH nanodroplets exposed to positive-polarity pulses (**Figure C.2B**). For control phantoms without nanodroplets, cavitation bubbles were not consistently observed in the focal region at any of the pressure levels tested (**Figure C.8**). Plotting the probability of cavitation as a function of P– (**Figure C.6C**) and P+ (**Figure C.7C**) for control phantoms without nanodroplets demonstrated that the cavitation threshold was not reached even when the frequency compounding transducer was driven at its maximum output pressure for the positive-polarity pulses (P–/P+=18.4/61.1 MPa). This finding matched previous work studying the histotripsy intrinsic threshold which has shown that cavitation is only generated when the P– is raised above the intrinsic threshold (~25-30 MPa) [44, 337, 343, 357].

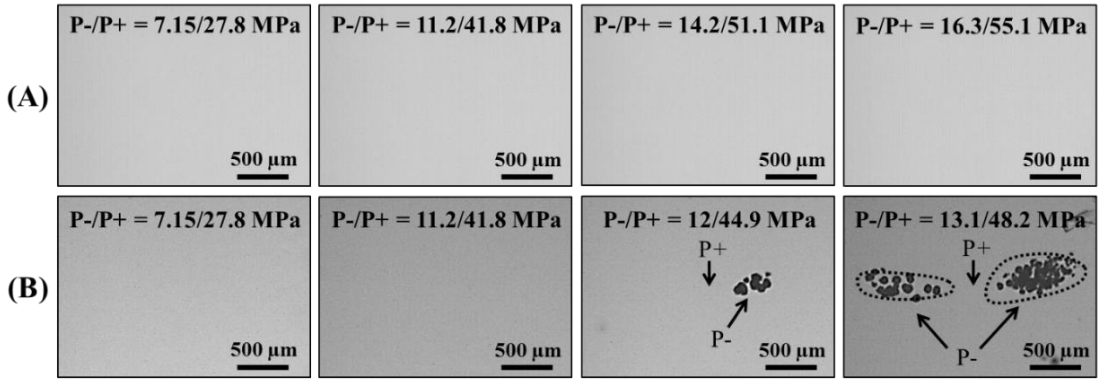

Figure C.18 Bubble Images: Positive-polarity Pulses.

Optical Images of cavitation bubbles generated from positive-polarity pulses inside (A) control phantoms and (B) PFH phantoms. Arrows on the plot indicate the locations in the focal region corresponding to the highest positive (P+) and negative (P–) pressures as measured by the FOPH (Figure 8.3). Dashed lines correspond to the approximate regions with a P– above ~12 MPa (Figure 8.3).

For PFH phantoms exposed to the positive-polarity pulses, cavitation was observed once a certain pressure threshold was exceeded (**Figure C.8**). However, cavitation did not occur at the geometric focus of the transducer. Instead, the location of the cavitation was ~0.5 mm from the geometric focus, closely matching the location in the field with the highest P– (**Figure C.3**). As the pressure was further increased above the NMH cavitation threshold, two separate regions containing cavitation were observed in the PFH phantoms (**Figure C.7**), with these locations closely corresponding to the two regions of highest P– as measured by the FOPH (**Figure C.3**). The probability of cavitation for PFH phantoms exposed to positive-polarity pulses was plotted as a function of P– (measured at the location corresponding to the highest P–), with the results demonstrating $p_t(–)$ = 11.4±0.1 MPa, with σ_{mean} = 0.1 MPa (**Figure C.5D**). This P– threshold closely matched the P– threshold for the negative-polarity pulses as well as the P– thresholds previously measured using dual-polarity pulses (**Table C.1**). Plotting the probability of cavitation for PFH phantoms exposed to positive-polarity pulses as a function of P+ resulted in a P+ threshold of $p_t(+)$ = 42.6±0.2 MPa, with σ_{mean} = 0.4 MPa (**Figure C.6D**). This P+ threshold was significantly

different than the P+ thresholds measured for the negative-polarity pulses as well as the P+ thresholds previously measured for dual-polarity pulses (**Table C.1**). **Figure C.9** shows a comparison of the P– and P+ thresholds measured for PFH phantoms exposed to the positive-polarity and negative polarity pulses generated in this study as well as dual-polarity pulses at various frequencies (345 kHz–3MHz) measured in a previous study [355], with results strongly suggesting that the NMH threshold is a function of the applied P–.

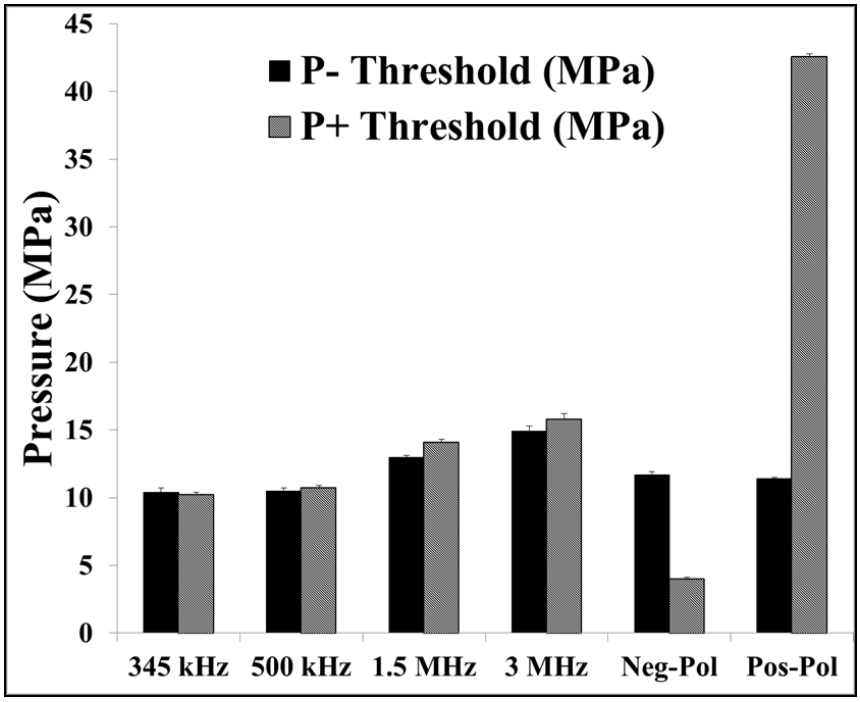

Figure C.19 NMH Threshold Results Comparison.

Plot compares the P– and P+ thresholds measured for PFH phantoms in this study (negative-polarity and positive-polarity pulses) with the thresholds previously measured using dual-polarity pulses (f=345kHz, 500kHz, 1.5MHz, 3 MHz) [355]. Results suggest NMH cavitation is generated directly from the P– of the incident wave.

Classical Nucleation Theory Simulation

A theoretical analysis was performed based on classical nucleation theory (CNT) in order to theoretically investigate the expected cavitation thresholds for phantoms with and without PFH nanodroplets. **Figure C.10** shows p_{CNT} compared with the average $p_t(-)$ measured for the near

monopolar pulses used in this study as well as for dual polarity pulses at frequencies ranging from 345 kHz to 3 MHz used in previous studies [80, 337]. The CNT results predicted a significant decrease in the cavitation threshold for phantoms containing PFH nanodroplets, with the results closely matching the thresholds measured experimentally (**Figure C.10**).

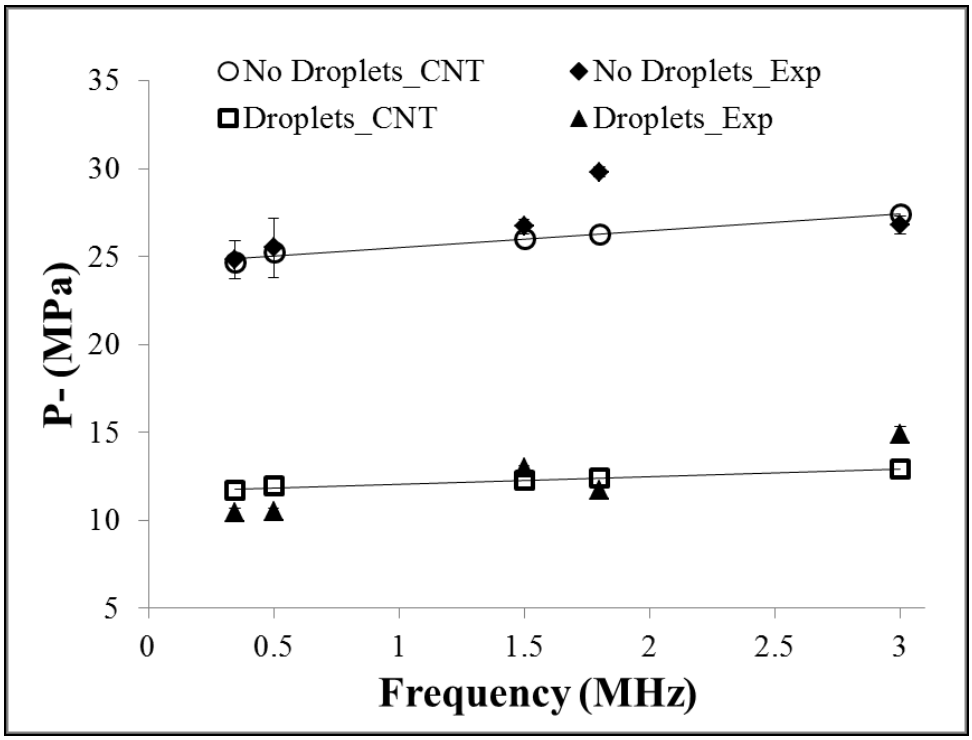

Figure C.20 CNT Simulation.

Classical nucleation theory was used to predict the cavitation thresholds for histotripsy pulses applied to phantoms with and without PFH nanodroplets. Results showed close agreement between the CNT simulation and the experimentally measured thresholds. Note that the waveforms produced by the frequency compounding transducer are plotted as an effective frequency of 1.8 MPa.

For example, the predicted P- cavitation threshold for PFH phantoms exposed to the negative-polarity pulses used in this study was calculated to be p_{CNT_PFH} = 12.4 MPa, which was close to the experimental measured threshold of $p_t(-)$ = 11.7±0.2 MPa. The CNT results also predicted a slight increase (~1-3 MPa) in p_{CNT} with increasing frequency, once again matching the trends observed experimentally (**Figure C.10**). This slight increase in threshold at higher

frequency is due to the smaller focal zone and shorter duration of the applied *p*-. In fact, since bubbles are generated directly from the single *p*- phase of the incident wave, the results of this study suggest that it is more appropriate to use the duration of the applied *p*- as a metric to predict the probability of generating cavitation from these single cycle pulses. The only significant deviation between the experimental and CNT results was observed for phantoms without nanodroplets exposed to the negative-polarity pulses, with the experimental results measuring a threshold ~3.5 MPa greater than predicted by CNT. This difference is likely explained by inaccuracies in the reported pressure values for high pressures (P–>21.5), which were estimated using a linear summation of individual elements as described in the Methods.

Discussion

In this work, we were able to generate pulses with dominant negative and positive pressure phases, which allowed us to investigate the effects of positive and negative pressure on the NMH cavitation threshold separately. The results supported our hypothesis that NMH bubbles are generated after cavitation is nucleated inside the droplets directly from the incident *p*- (tensile portion of the incident wave), similar to histotripsy bubbles generated without nanodroplets when the *p*- directly exceeds the intrinsic threshold of the target media. Results showed close agreement in the P– threshold for PFH phantoms exposed to negative-polarity (11.4±0.1 MPa), positive-polarity (11.7±0.2 MPa), and dual-polarity (10-15 MPa) pulses. The P+ thresholds, in contrast, were measured to be significantly different for PFH phantoms exposed to negative-polarity (4.0±0.1 MPa), positive-polarity (42.6±0.2 MPa), and dual-polarity (10–16 MPa) pulses. These results support our hypothesis that NMH cavitation is purely dependent upon the applied *p*-. This hypothesis was further supported by the observation that exposing PFH phantoms to positive-

polarity pulses resulted in cavitation only being generated in the regions with the highest P– (**Figure C.8**), as measured by the FOPH (**Figure C.3**).

The results of this study provide significant insight into the nanodroplet nucleation process and support the hypothesis that the nucleation in NMH can be explained by classical nucleation theory (CNT). The ADV literature has hypothesized that droplet nucleation in ADV is caused by a different mechanism than what is predicted by classical nucleation theory (CNT), based on previous studies showing that the ADV threshold decreases with increasing frequency [330-332, 353, 354]. Many alternative mechanisms have been proposed to explain the discrepancy between the trends predicted by CNT and the experimental trends observed for ADV including droplet deformation, hydrodynamic cavitation, or acoustic heating [330, 353, 354]. The results of this study, however, suggest that the nucleation process involved in NMH does in fact follow the mechanism described by CNT, which predicts that cavitation is nucleated inside the droplets directly from the applied *p*-. These results suggest that nanodroplets reduce the cavitation threshold by carrying a lower threshold medium, with the probability of nucleation being a function of the *p*- exposed to the PFC. We think this theory can also be extended to explain the nucleation mechanism for ADV using multi-cycle pulses and various droplet sizes, as recent work has revealed that the decrease in the ADV threshold at higher frequencies is due to superharmonic focusing, which significantly increases the amplitude of the *p*- inside the droplet and is enhanced at higher frequencies and in larger droplets [333, 334]. It is likely that the probability of nucleation in ADV will still follow the trends predicted by CNT once the pressure focusing effects are accounted for.

Although the results of this work and previous ADV studies suggest that the same nucleation process may be responsible in ADV and NMH, it is important to note that the resulting

bubble dynamics are significantly different in these two cases. For example, stable bubbles are formed in ADV [330, 353, 359-363] while NMH produces cavitation bubbles that rapidly expand and then violently collapse [46, 79, 80, 348]. There are many factors determining the resulting bubble behavior after nucleation, including the ultrasound pulse parameters, initial droplet characteristics, and the properties of the surrounding microenvironment. For example, the higher frequencies and multi-cycle pulses commonly used in ADV result in oscillatory bubble growth, which allows ADV bubbles to stabilize [359, 361]. In contrast, NMH bubbles are exposed to a single large *p*- at lower frequencies, producing bubbles that rapidly expand to sizes much larger (R_{max}~10-150 μm) than those observed for nanodroplet ADV (R_{max}~1-10 μm), followed by the violent collapse of the NMH bubbles [46, 79, 80, 359]. In addition to the effects of ultrasound parameters, the resulting bubble behavior is dependent upon the droplet properties (i.e. size, concentration, and PFC boiling point) [359-361]. Finally, the bubble behavior will also be highly dependent upon the properties of the surrounding media including the temperature, Young's modulus, viscosity, surface tension, and gas concentration [79, 80, 345, 359-361]. It is therefore important to understand the impact of these properties on the resulting bubble dynamics of ADV or NMH therapies, even though the underlying nucleation process is likely the same for these two approaches.

The finding that the nanodroplet nucleation thresholds are determined by the applied P- and exhibit a distinct threshold behavior is promising for the development of NMH. This distinct P- threshold is dependent upon the droplet properties and can be changed by modulating droplet composition (i.e. changing droplet surface tension to modulate the nucleation threshold) [355]. With knowledge of the applied pressure fields and droplet characteristics (i.e. size, composition, concentration), predictable and reliable NMH therapy strategies can be developed. For example,

the applied P– in NMH therapy must be chosen in the region above the NMH threshold but below the histotripsy intrinsic threshold to ensure cavitation is only generated in regions containing nanodroplets. This approach also suggests that NMH therapy will share the same advantages of histotripsy treatments performed above the intrinsic threshold, such as the generation of precise lesions matching the portion of the beam profile above the P– threshold as well as the ability to manipulate bubble dynamics by changing the pulse parameters [44, 337, 343, 345]. Furthermore, the sharp P– threshold behavior observed in this study suggests that generating cavitation from nanodroplets is more predictable and reproducible than generating cavitation from micron-sized air contrast agents, which do not require nucleation (i.e. phase transition) in order to initiate the cavitation process and therefore do not show the same distinct threshold behavior [337, 364, 365]. Overall, the results of this study improve our understanding of the physical mechanisms underlying the nanodroplet nucleation process, which will help to guide the development of NMH therapy.

Conclusion

In this work, the effects of positive and negative pressure on the NMH cavitation threshold were investigated separately, with results supporting our hypothesis that the NMH cavitation threshold is determined by the incident *p*-. Close agreement was observed for the P– thresholds measured for PFH tissue phantoms exposed to negative-polarity (11.4±0.1 MPa) and positive-polarity (11.7±0.2 MPa) pulses. The P+ thresholds, in contrast, were significantly different for the negative-polarity (4.0±0.1 MPa) and positive-polarity (42.6±0.2 MPa) pulses. Furthermore, the positive-polarity pulse experiments demonstrated that cavitation was preferentially generated in the regions with the largest P–. In the final part of this study, the experimental results were compared to the cavitation thresholds predicted by classical nucleation theory (CNT), with results

showing close agreement between simulations and experiments. Overall, the results of this study support our hypothesis that nanodroplet nucleation is determined by the applied *p*- and provide significant insight into the physical mechanisms underlying the NMH process.

Acknowledgements

We would like to thank Sonja Capracotta, PhD (Technical Specialist, Nano Sight, School of Public Health, University of Michigan) for her help on NTA size and concentration measurements. This material is based upon work supported by a National Science Foundation Graduate Research Fellowship to Eli Vlaisavljevich. Omer Aydin acknowledges the support of the Turkish Republic the Ministry of National Education Fellowship Program (1416). This work was supported by a grant from the United States Department of Defense (W81XWH-11-PCRP-ID). Disclosure notice: Drs. Zhen Xu, Brian Fowlkes, and Kuang-Wei Lin have financial interests and/or other relationship with HistoSonics Inc.

Appendix D

Supplementary of Chapter 3

The material in this chapter is published from the following article: **O. Aydin,** I. Youssef, Y. Y. Durmaz, G. Tiruchinapally, and M. E. H. ElSayed, "Formulation of Acid-Sensitive Micelles for Delivery of Cabazitaxel into Prostate Cancer Cells" *Molecular Pharmaceutics*, **2016**, *13* (4), 1413–1429 **(2016)**.

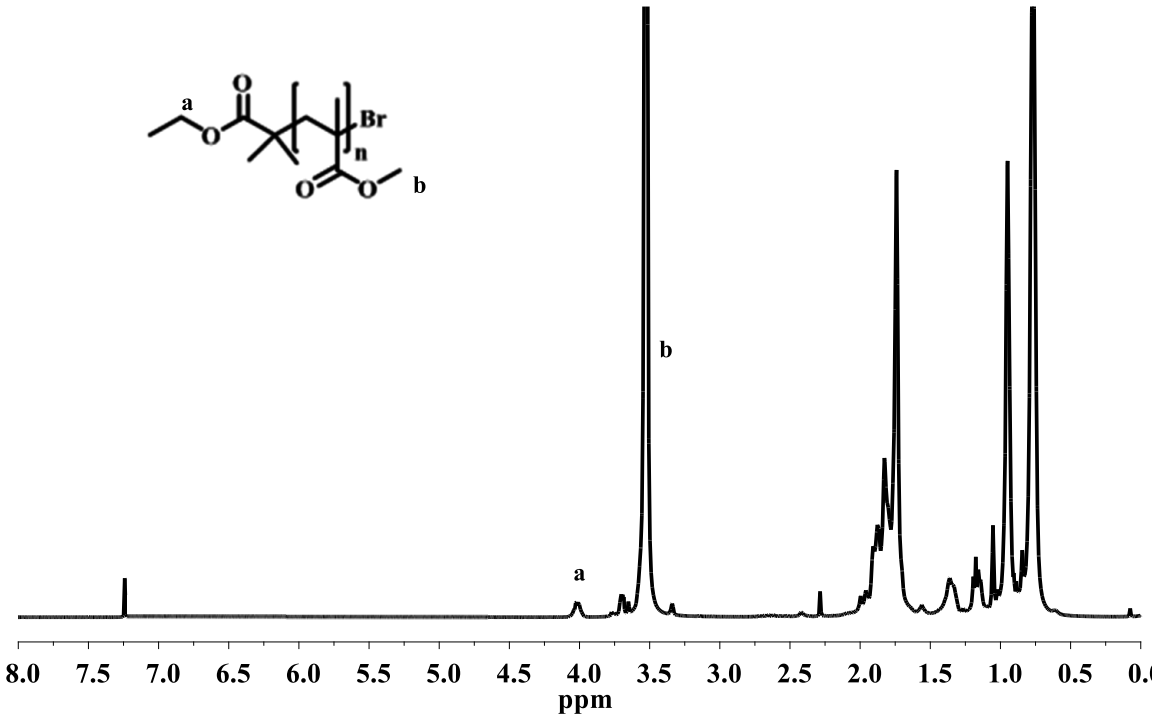

Figure D.1 ^{1}H NMR spectrum of PMMA in $CDCl_3$

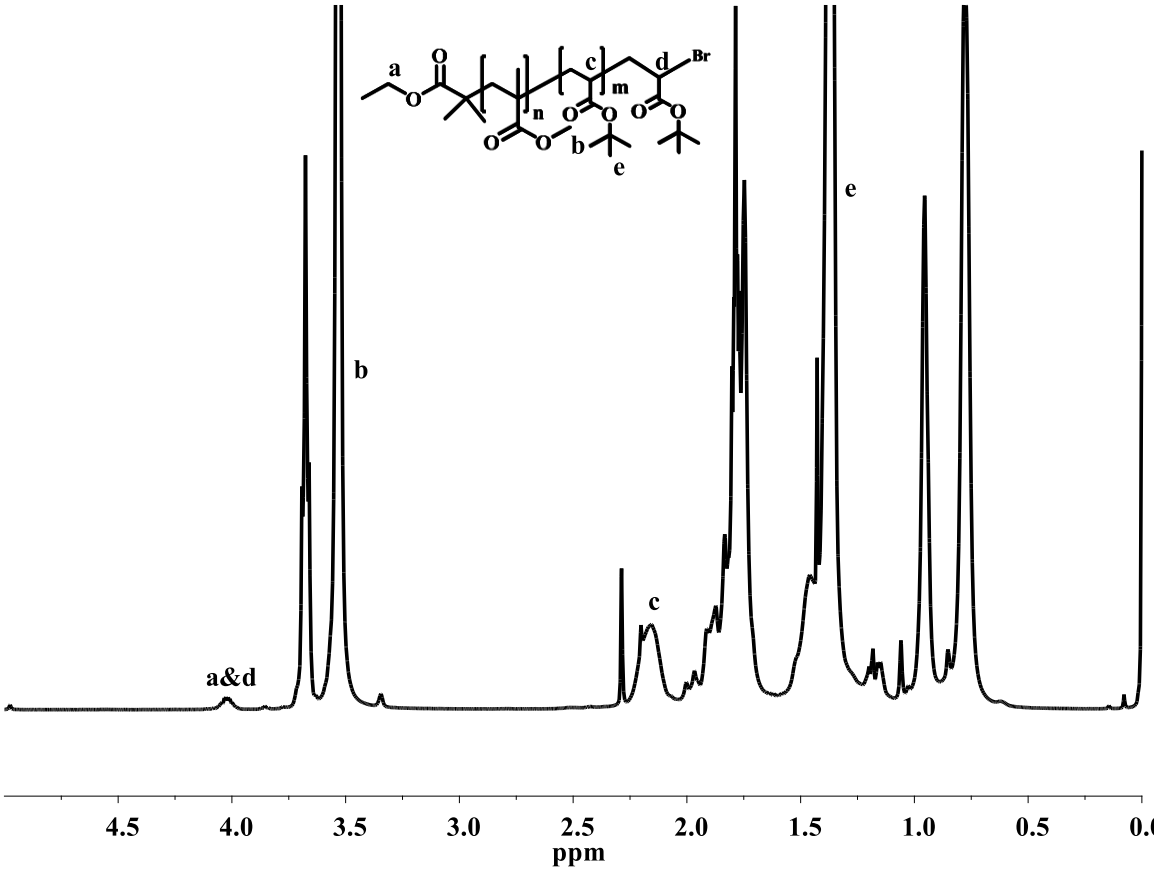

Figure D.2 ^{1}H NMR spectrum of PMMA-*b*-P*t*BA-Br in $CDCl_3$.

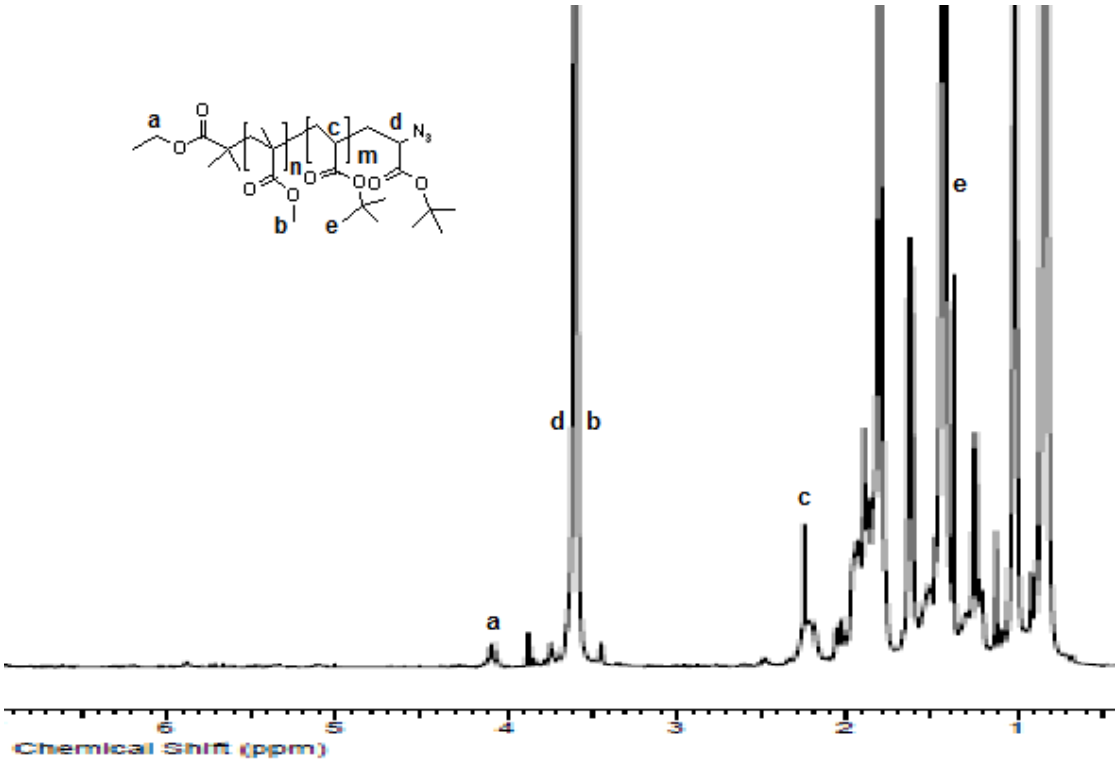

Figure D.3 ^{1}H NMR spectrum of PMMA-*b*-P*t*BA-N_3 in $CDCl_3$.

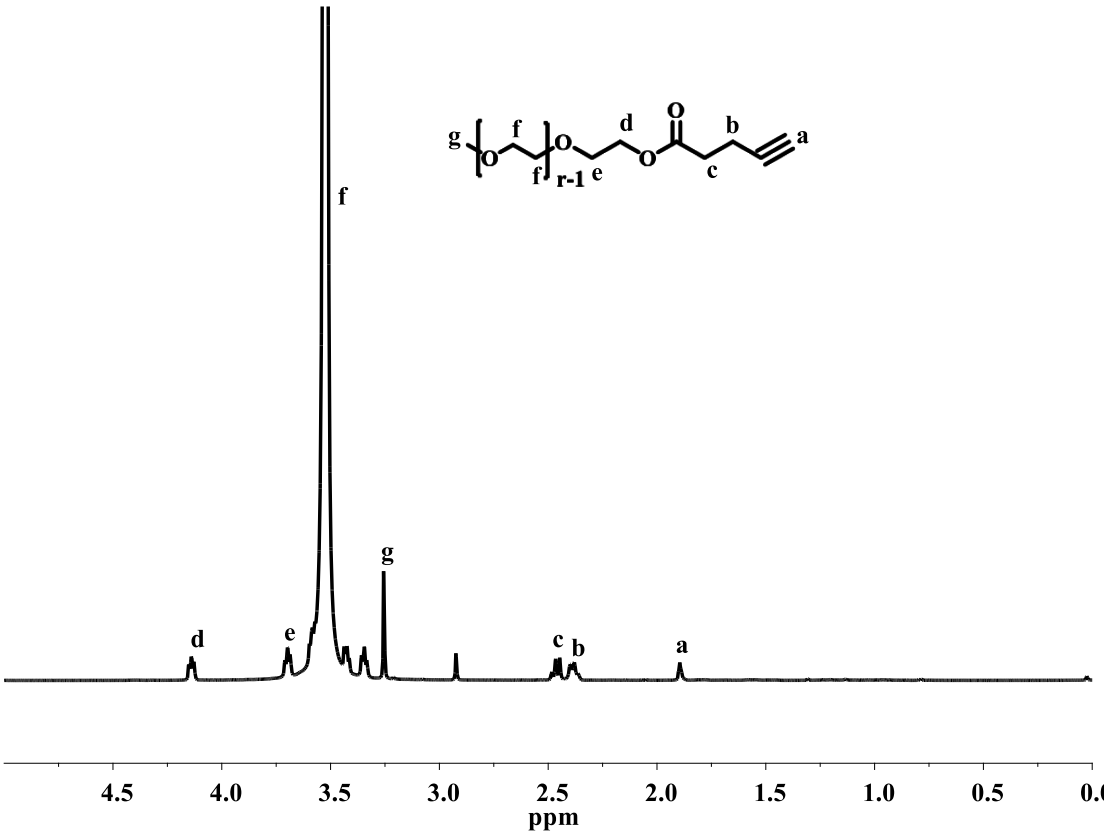

Figure D.4 ^{1}H NMR spectrum of alkyne-PEG in $CDCl_3$.

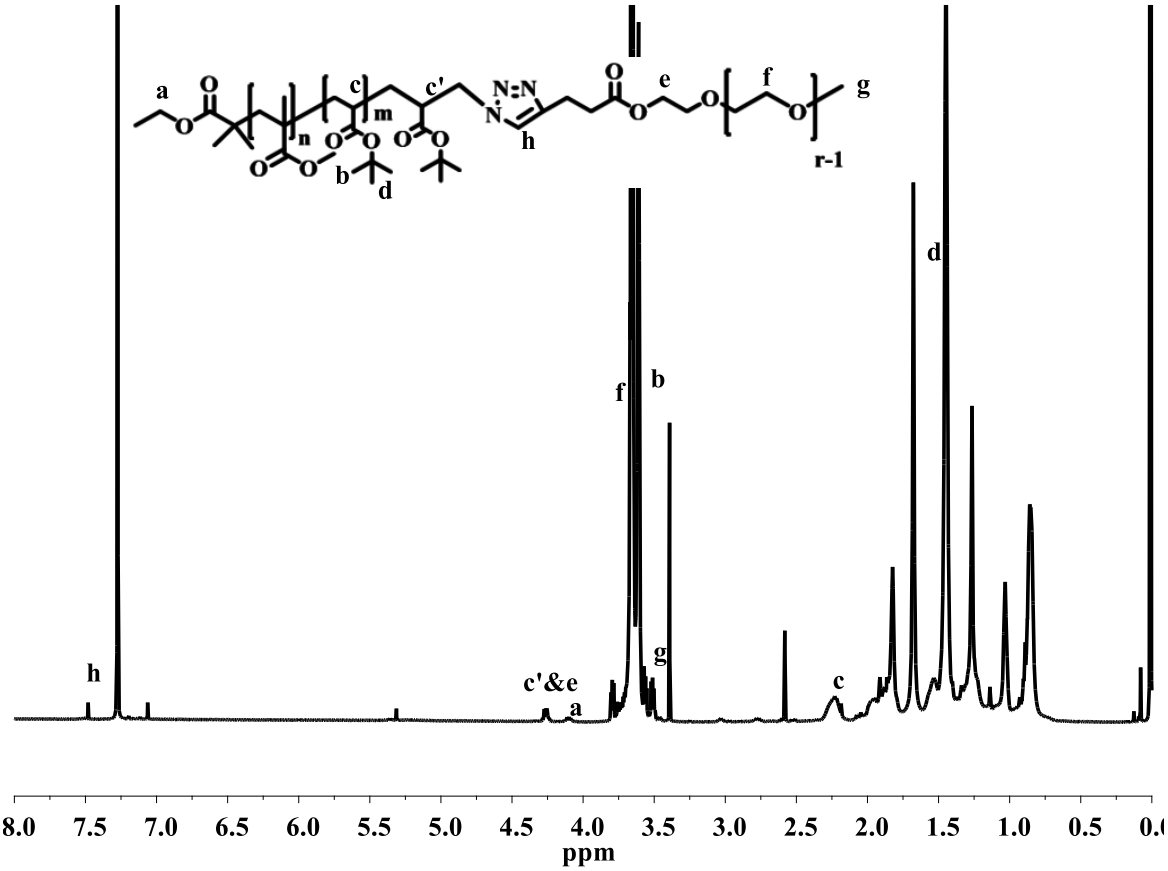

Figure D.5 ^{1}H NMR spectrum of PMMA-*b*-P*t*BA-*b*-PEG in $CDCl_3$.

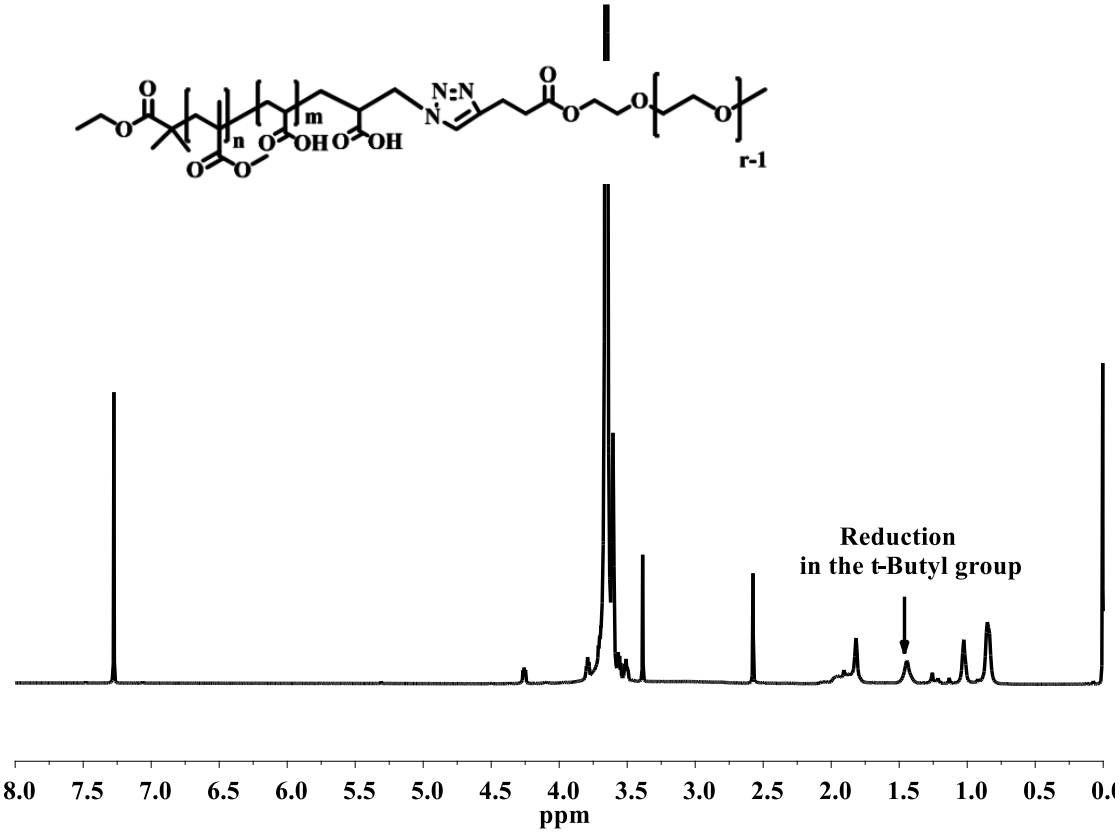

Figure D.6 ^{1}H NMR spectrum of PMMA-*b*-PAA-*b*-PEG in $CDCl_3$.

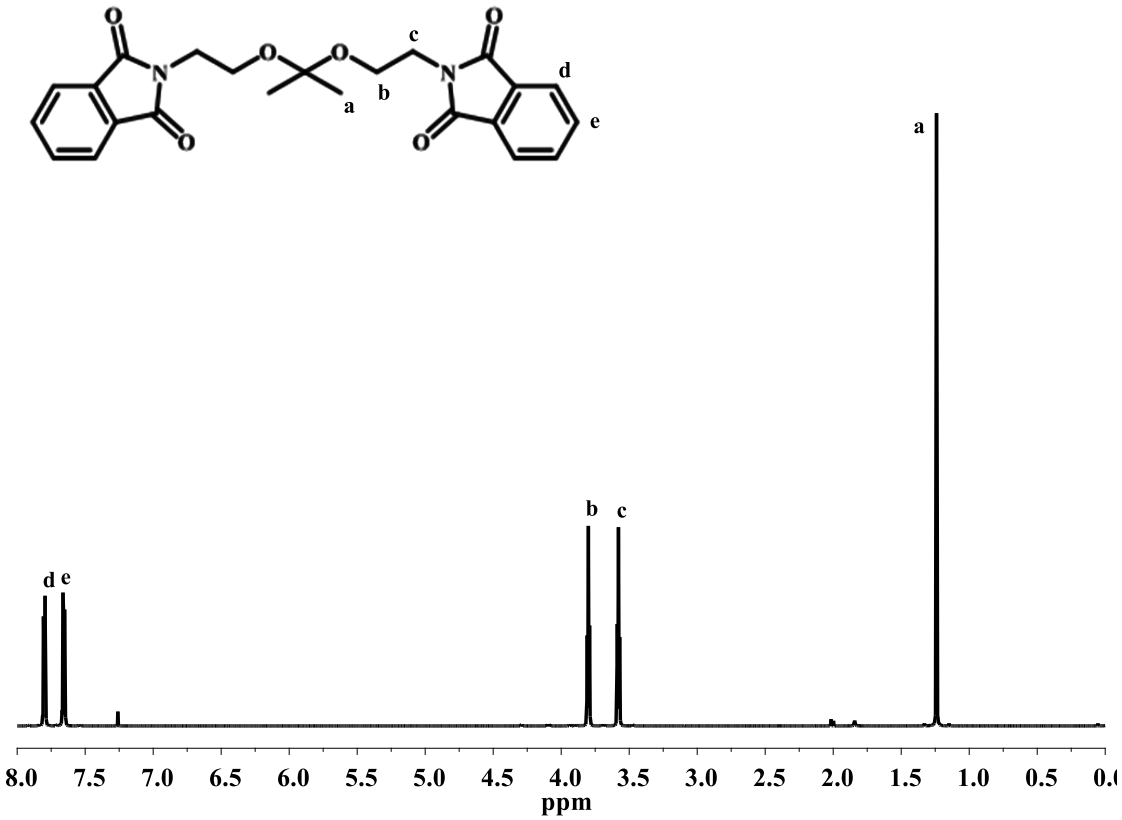

Figure D.7 ^{1}H NMR of Compound X 2,2'-(Propane-2,2-diylbis(oxy))bis(diethane-2,1diyl)bis(isoindoline-1,3-dione) in $CDCl_3$.

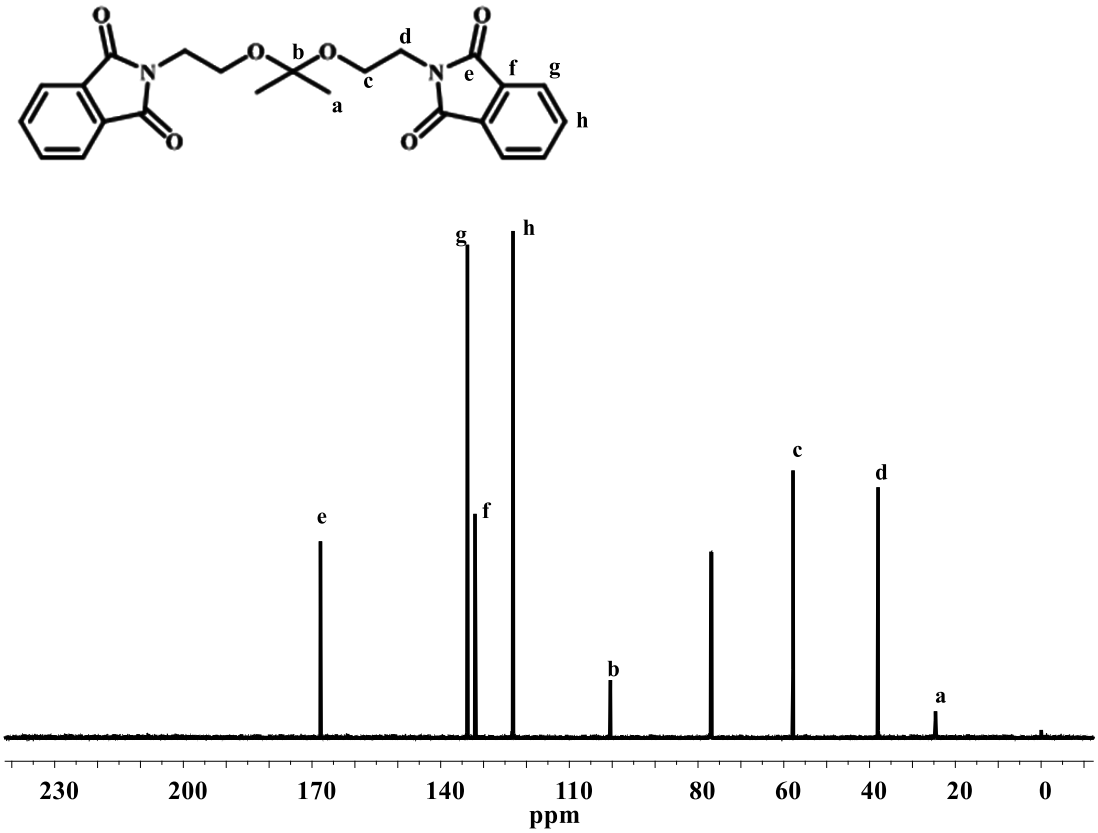

Figure D.8 ^{13}C NMR of Compound X 2,2'-(Propane-2,2-diylbis(oxy))bis(diethane-2,1diyl)bis(isoindoline-1,3-dione) in $CDCl_3$.

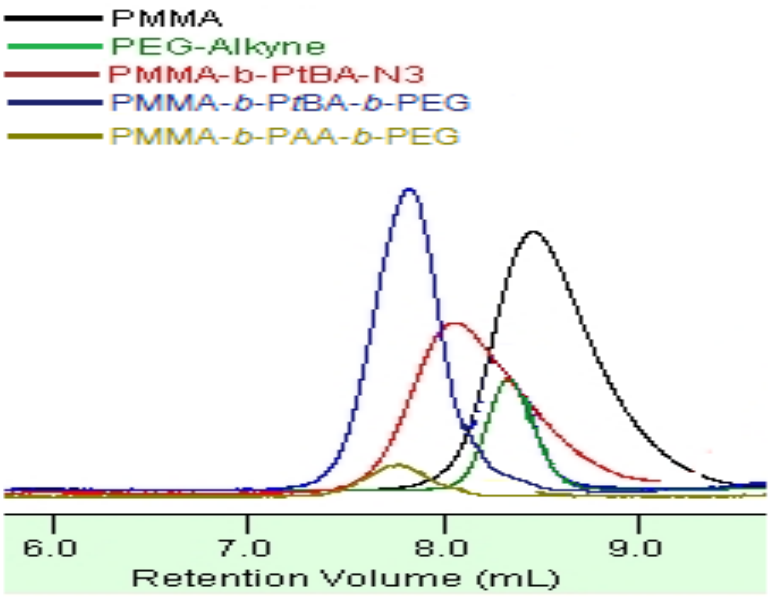

Figure D.9 GPC results of PEG-*b*-PAA-*b*-PMMA block copolymer and its precursors.

Appendix E

Supplementary of Chapter 4

The material in this chapter is submitted to the following journal: **O. Aydin,** I. Youssef, G. Tiruchinapally, H. Ramaraju, Y. Y. Durmaz, K. Kozloff, D. H. Kohn, and M. ElSayed "Differential Targeting of Prostate Cancer Cells, Osteoblasts, and Osteoclasts using pVTK Peptide- and Bisphosphonate-Functionalized Micelles", *Biomaterials.*

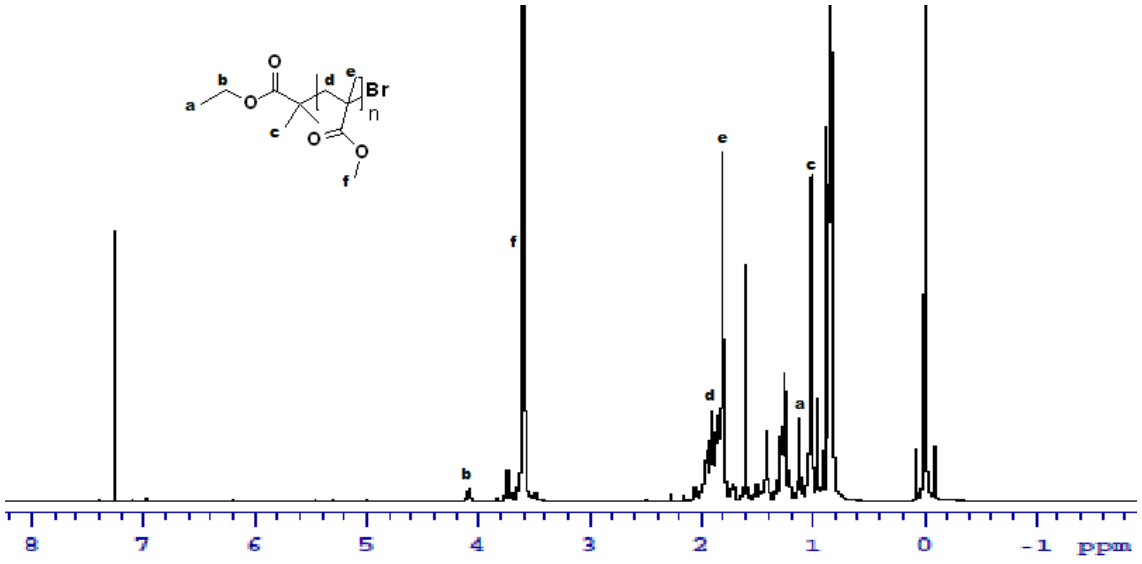

Figure E.1 ^{1}H NMR of compound 1 in $CDCl_3$.

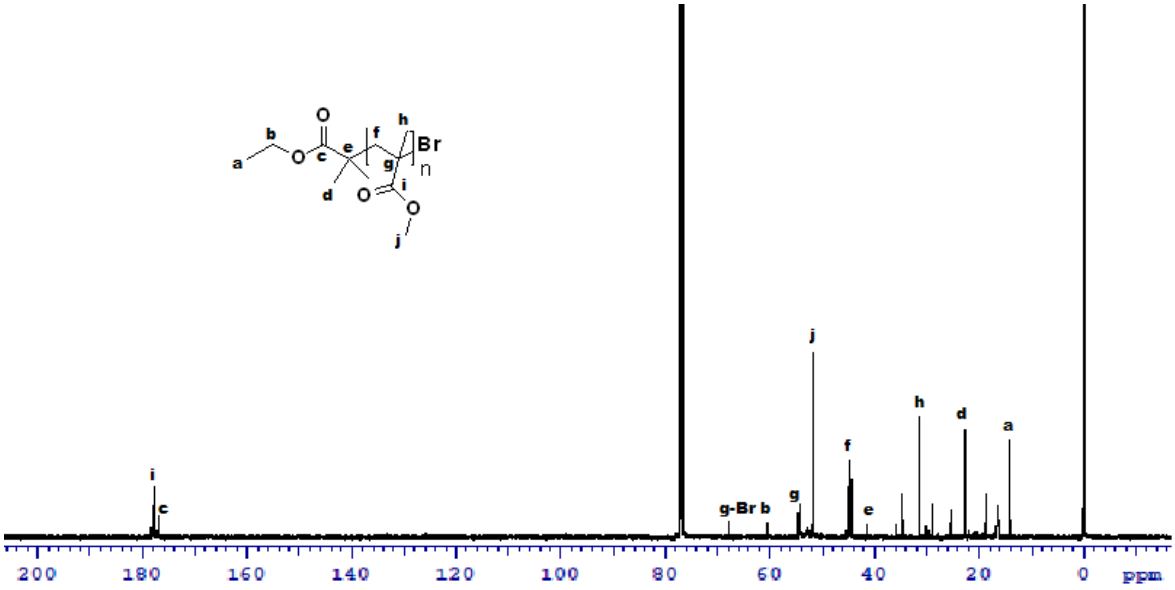

Figure E.2 ^{13}C NMR of compound 1 in $CDCl_3$.

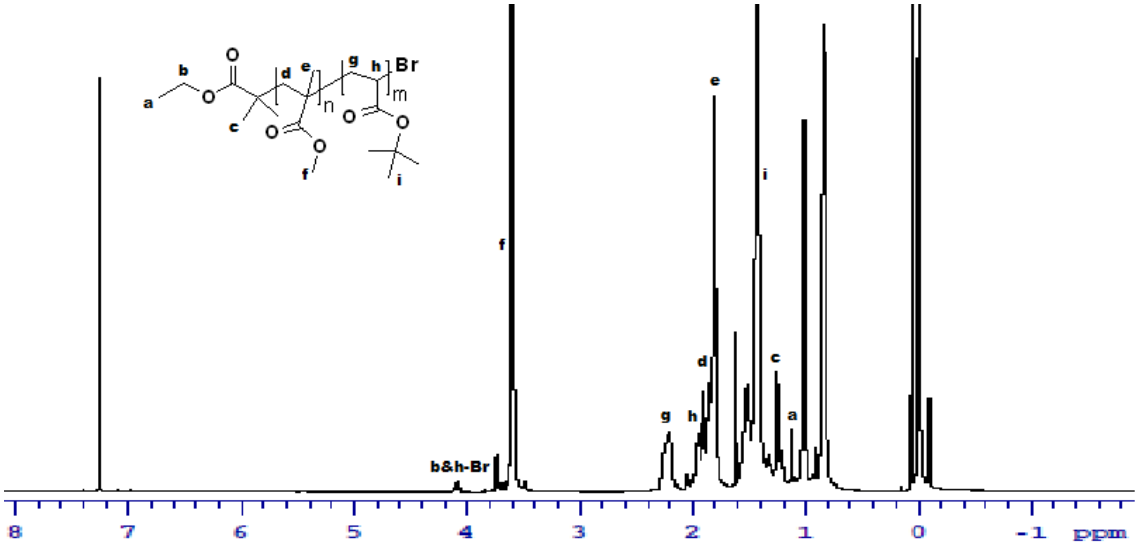

Figure E.3 ^{1}H NMR of compound 2 in $CDCl_3$.

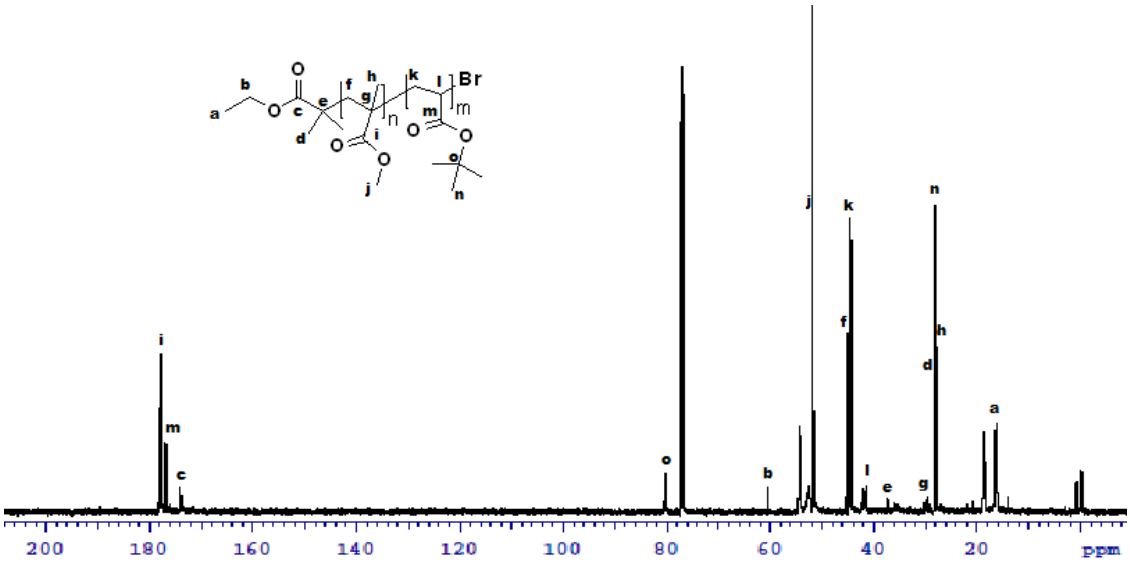

Figure E.4 ^{13}C NMR of compound 2 in $CDCl_3$.

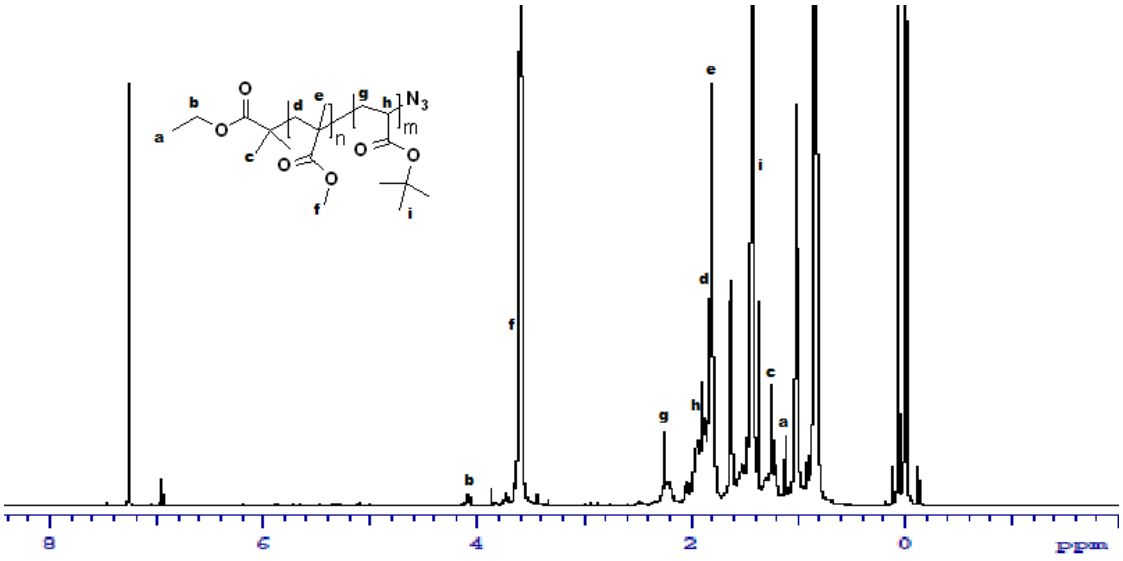

Figure E.5 ^{1}H NMR of compound 3 in $CDCl_3$.

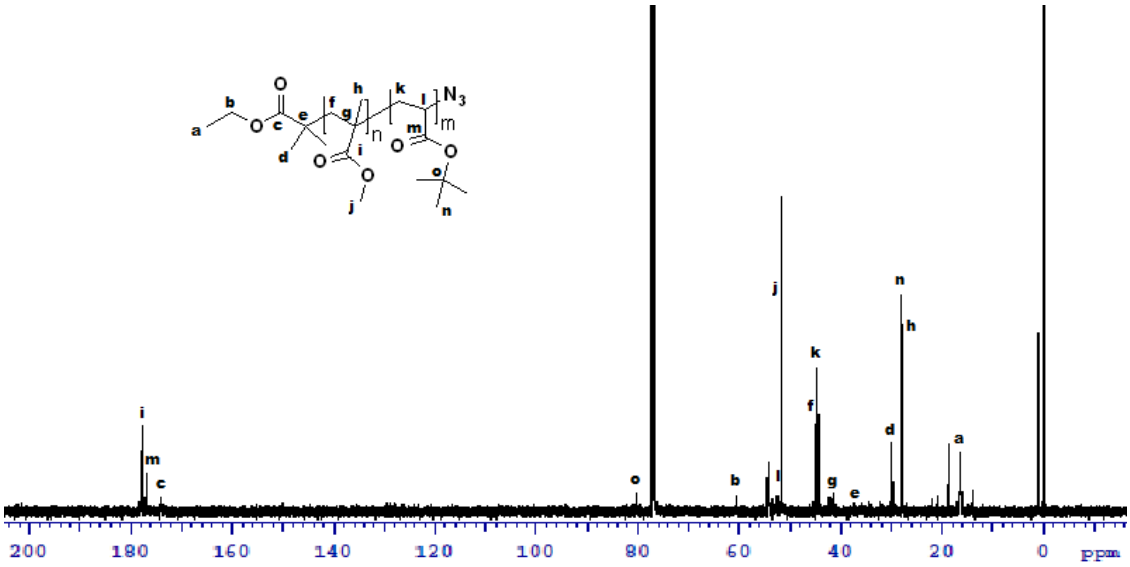

Figure E.6 ^{13}C NMR of compound 3 in $CDCl_3$.

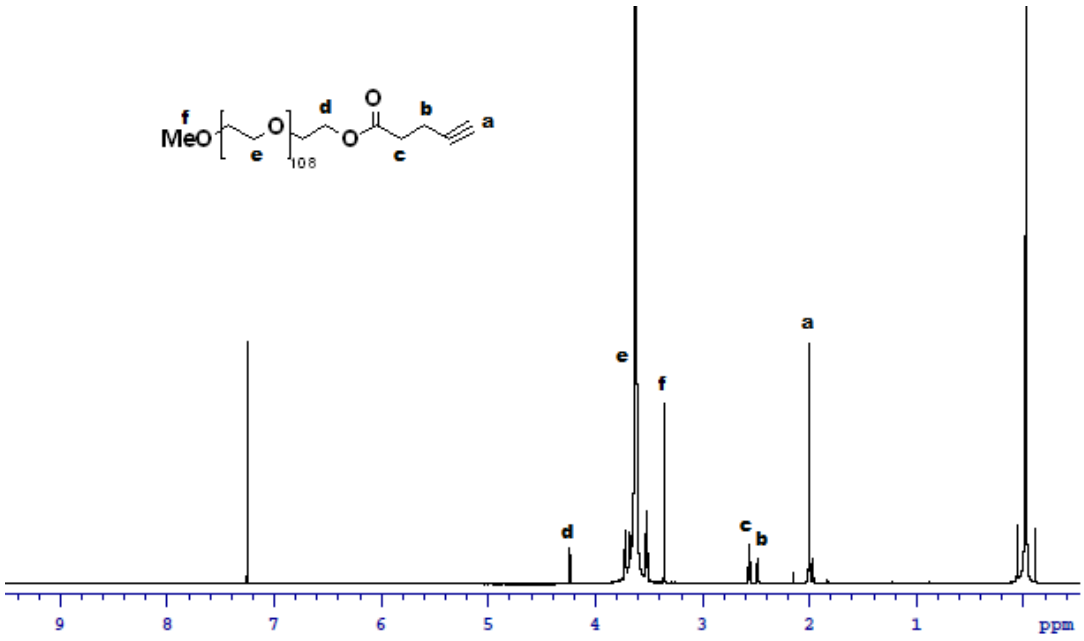

Figure E.7 ^{1}H NMR of compound 3a in $CDCl_3$.

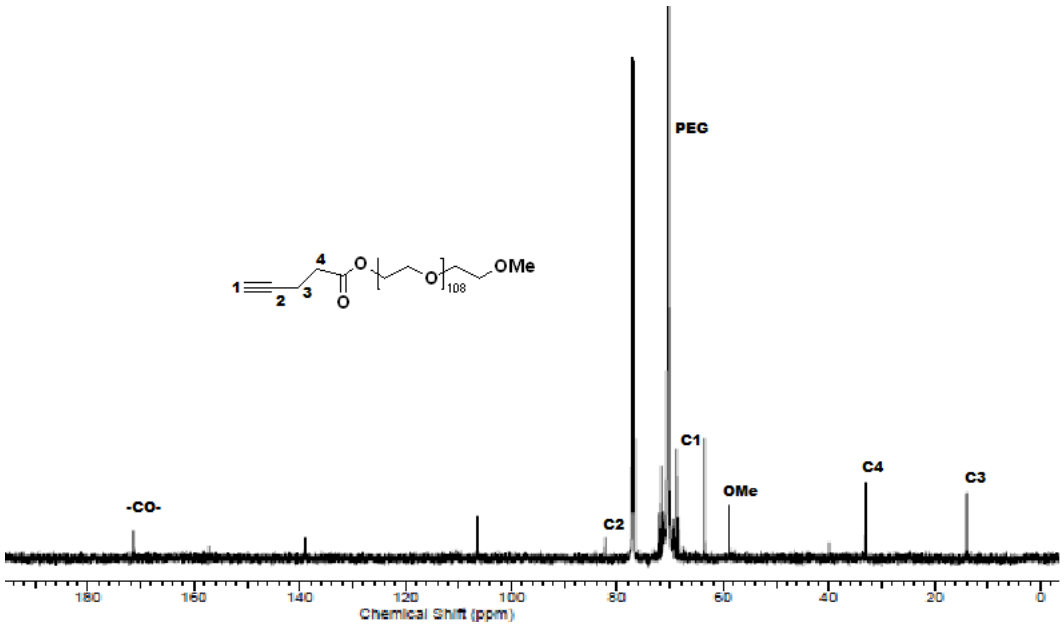

Figure E.8 ^{13}C NMR of compound 3a in $CDCl_3$.

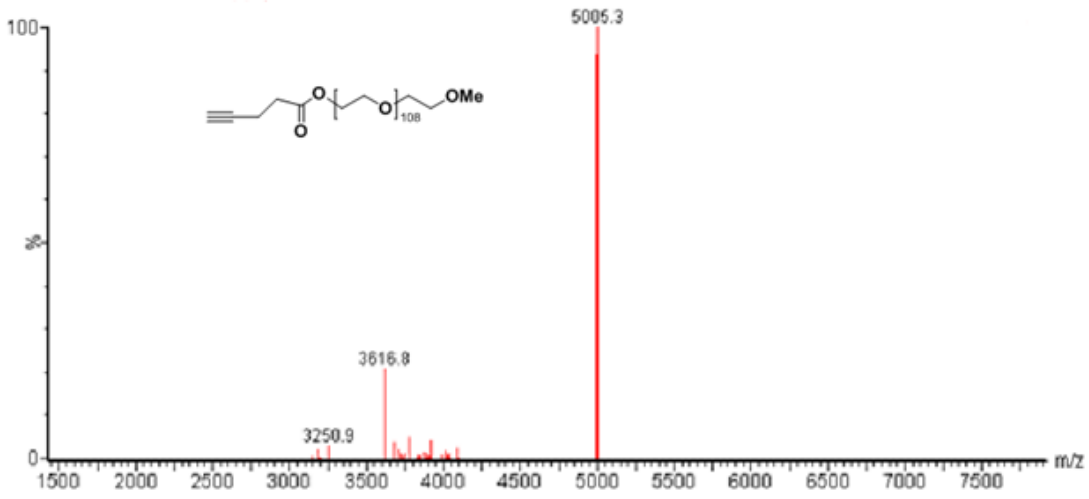

Figure E.9 MALDI-TOF of Compound 3a (Alkyne-PEG).

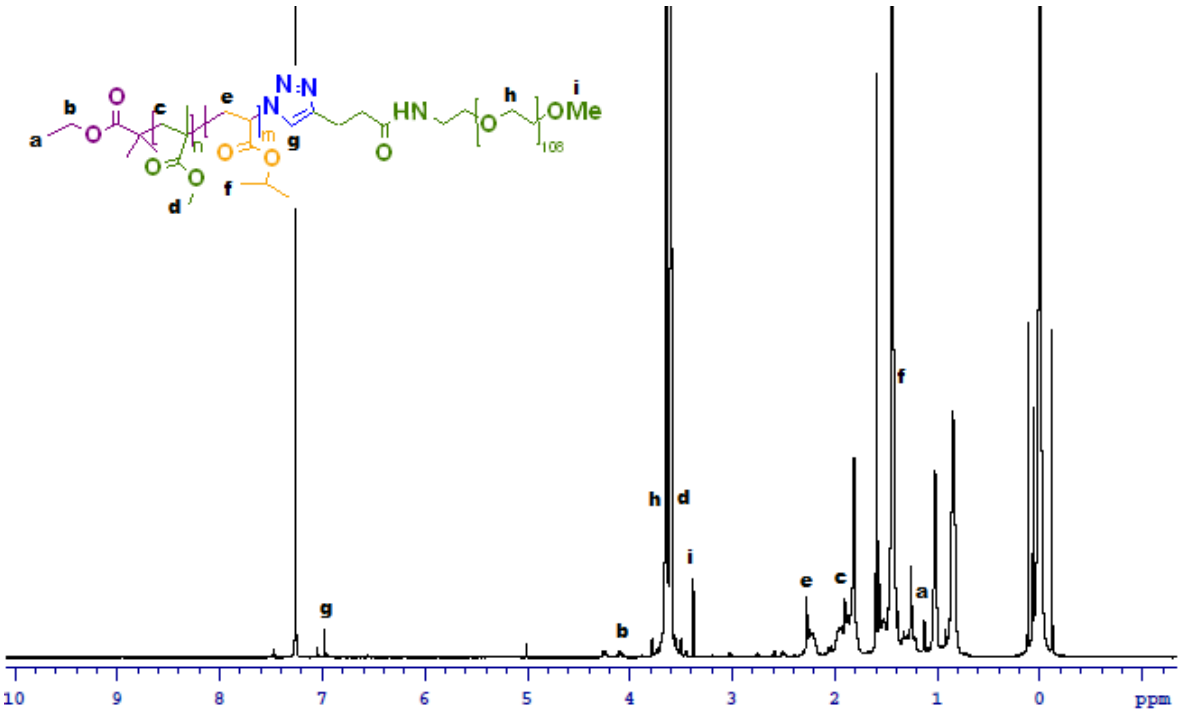

Figure E.10 ^{1}H NMR of Compound 4 (PMMA-*b*-P*t*BA-PEG) in $CDCl_3$.

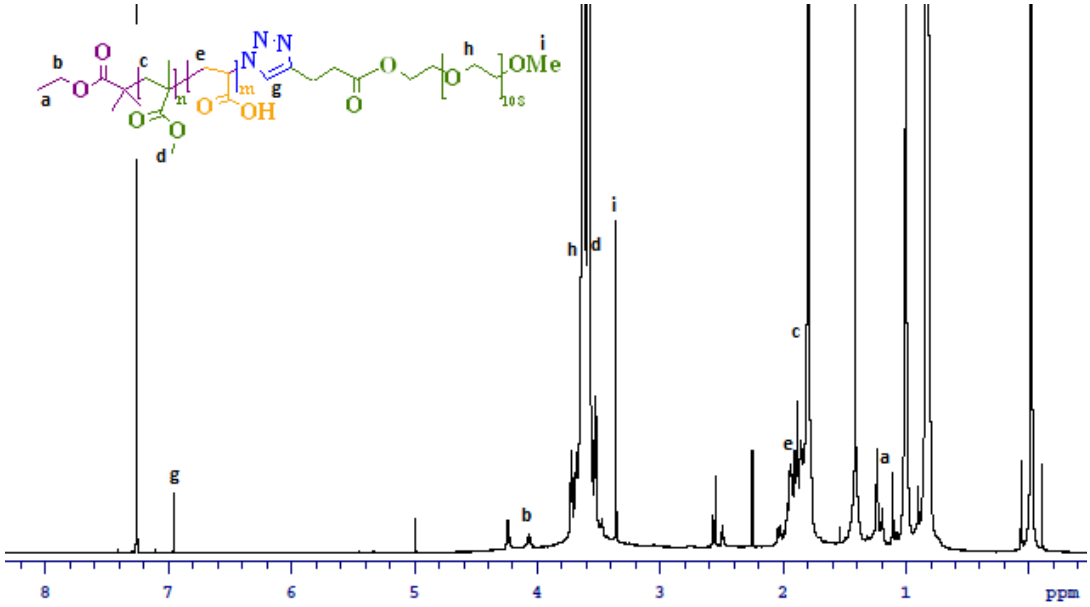

Figure E.11 ^{1}H NMR of Compound 5 (PMMA-*b*-PAA-*b*-PEG) in $CDCl_3$.

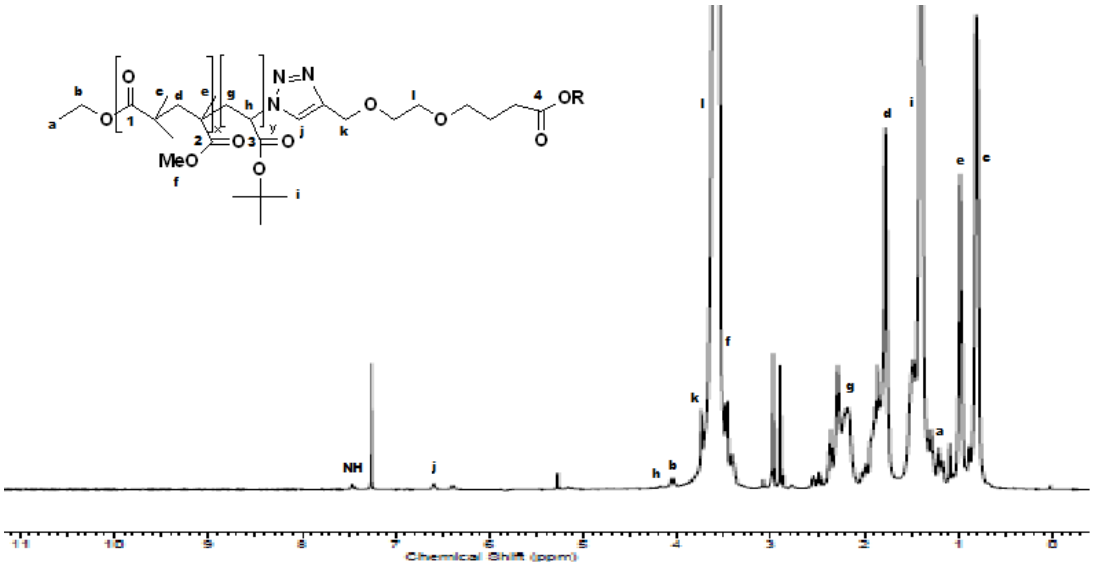

Figure E.12 ^{1}H NMR spectrum of compound 6 in $CDCl_3$.

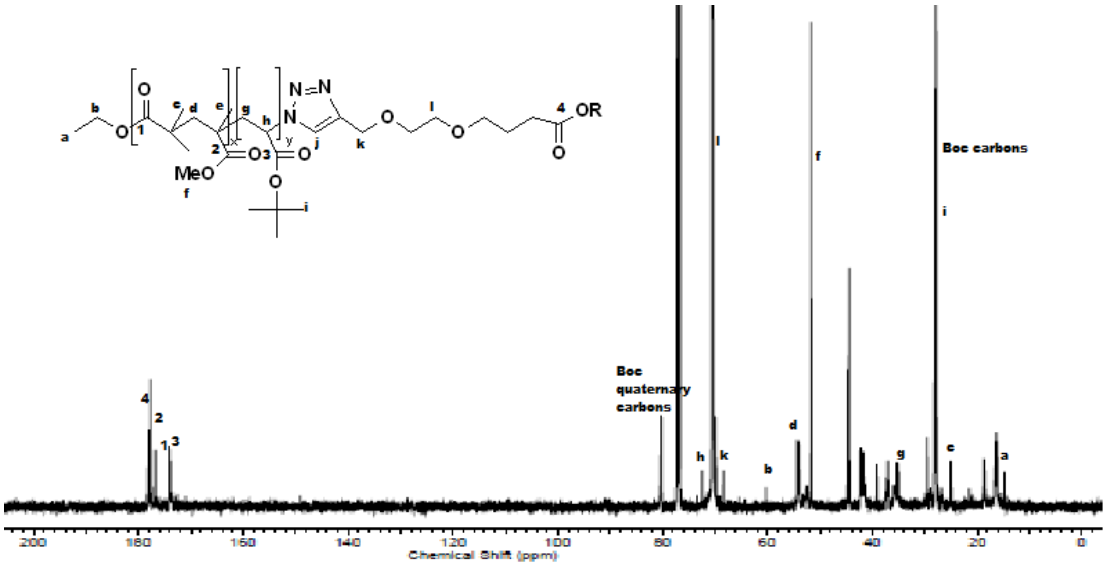

Figure E.13 ^{13}C NMR spectrum of compound 6 in $CDCl_3$.

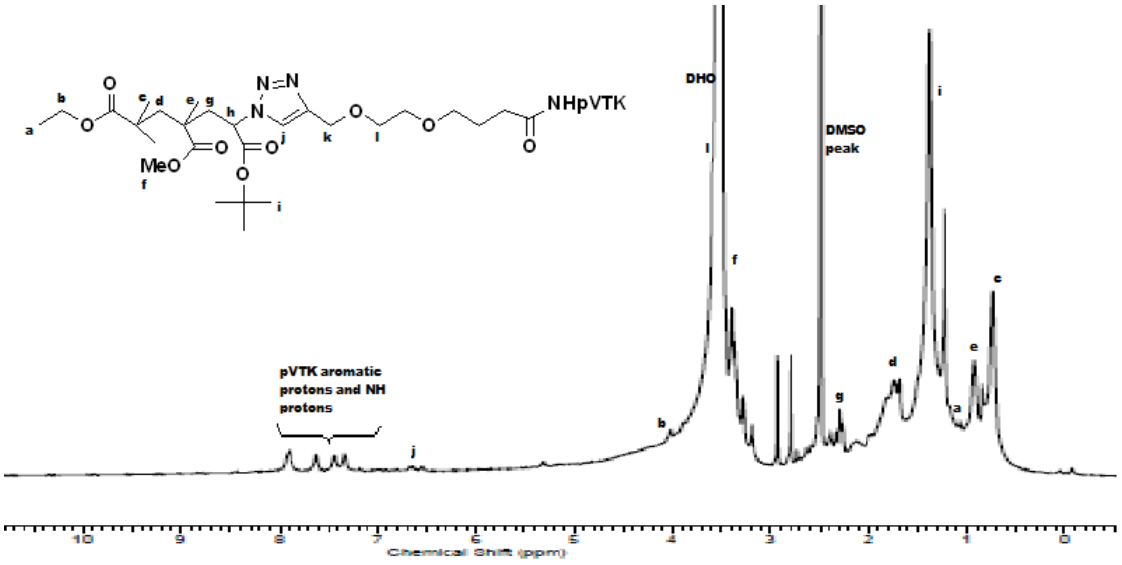

Figure E.14 ^{1}H NMR spectrum of compound 7 in DMSO-d6.

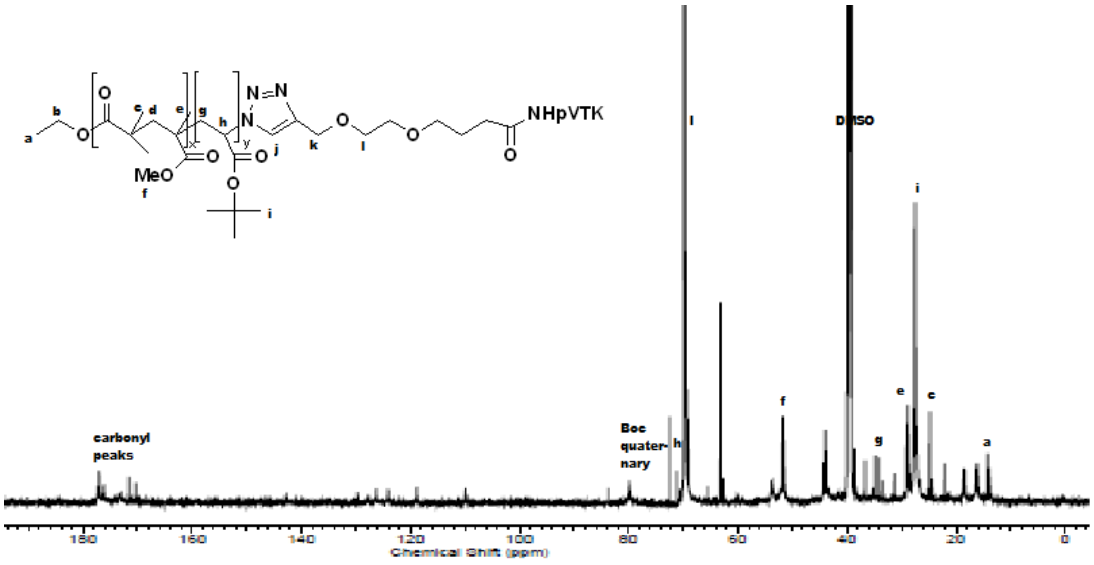

Figure E.15 ^{13}C NMR spectrum of compound 7 in DMSO-d6.

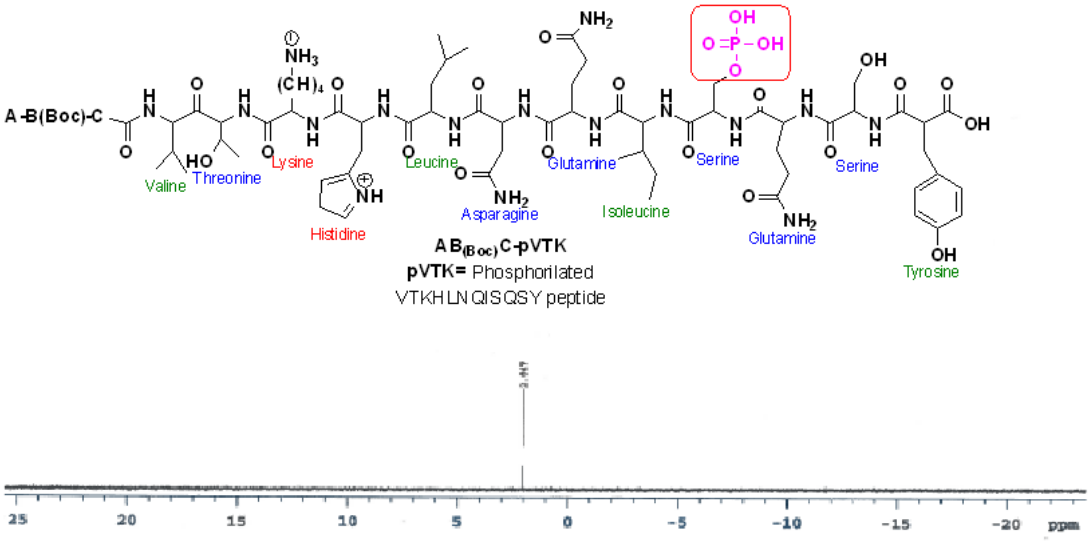

Figure E.16 ^{31}P NMR spectrum of compound 7 in DMSO-d6.

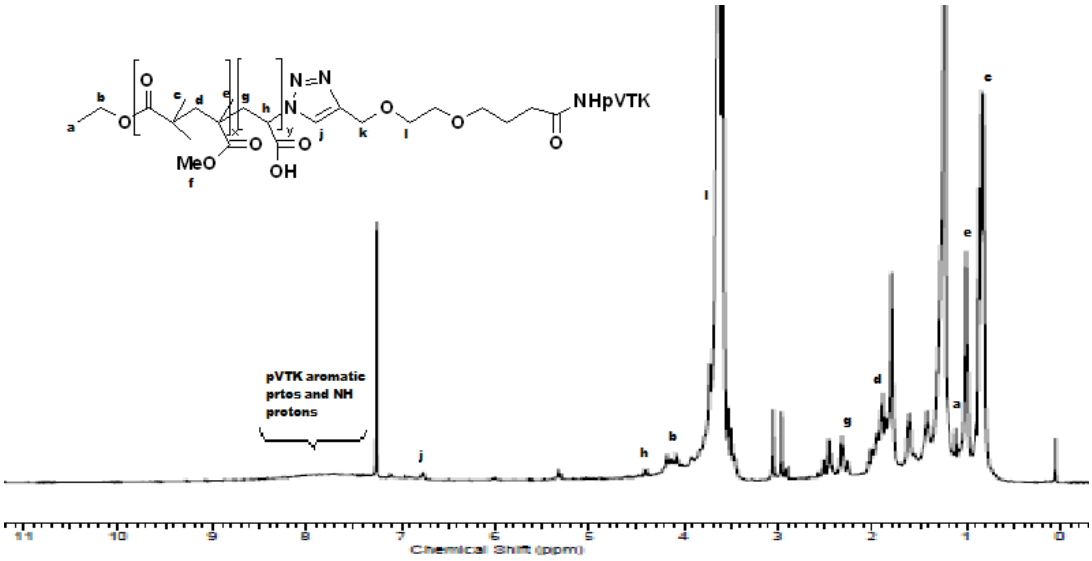

Figure E.17 ^{1}H NMR spectrum of compound 8 in $CDCl_3$.

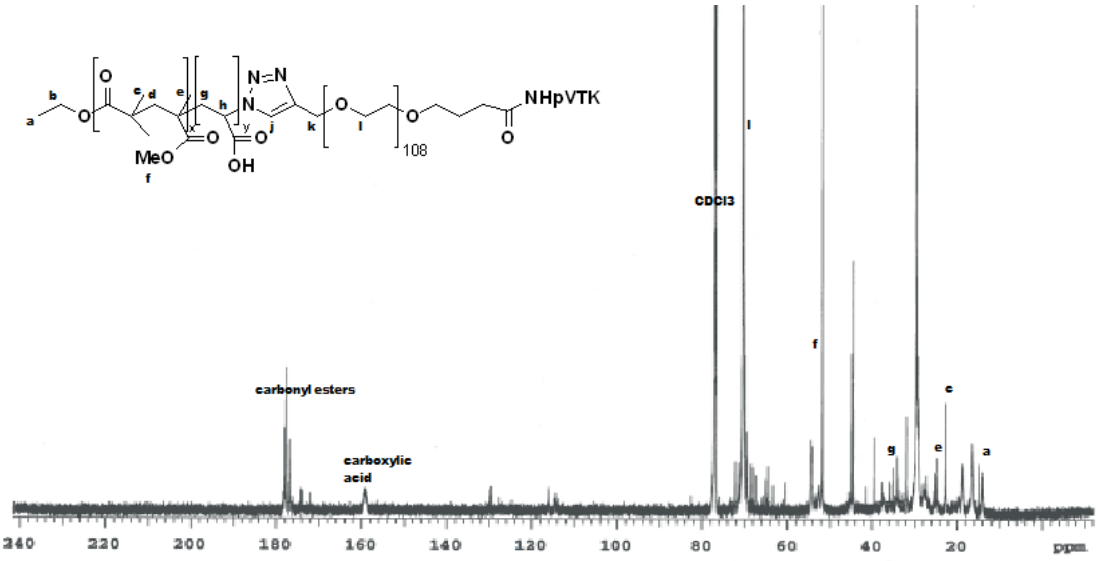

Figure E.18 ^{13}C NMR spectrum of compound 8 in $CDCl_3$.

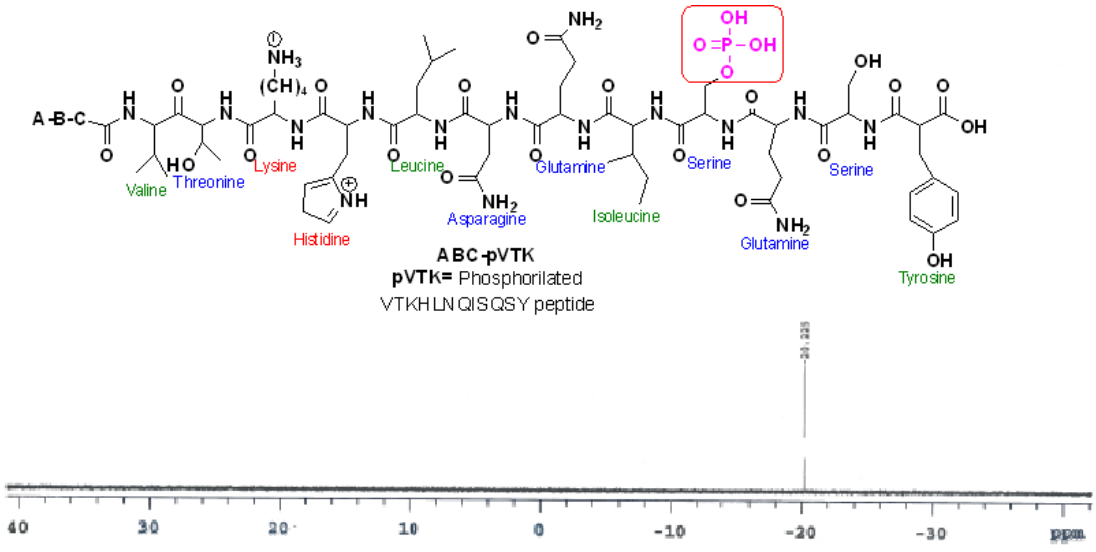

Figure E.19 ^{31}P NMR spectrum of compound 8 in $CDCl_3$.

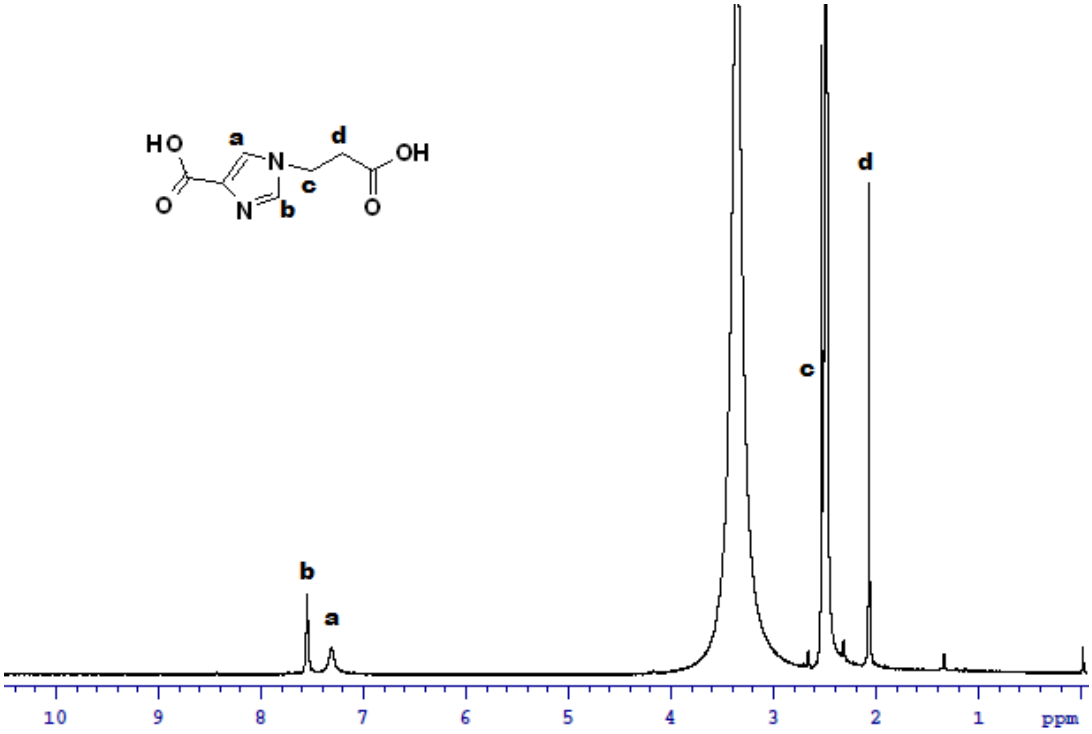

Figure E.20 ^{1}H NMR of compound 9a in DMSO-d6.

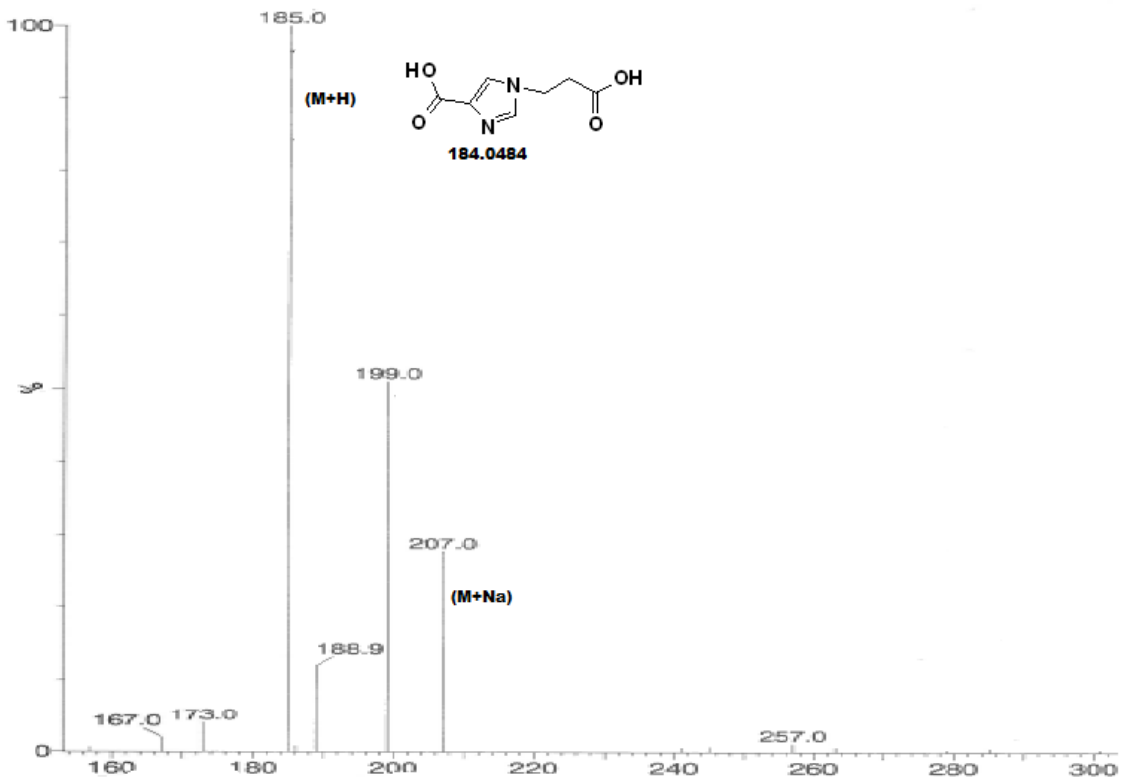

Figure E.21 ESI-MS of compound 9a.

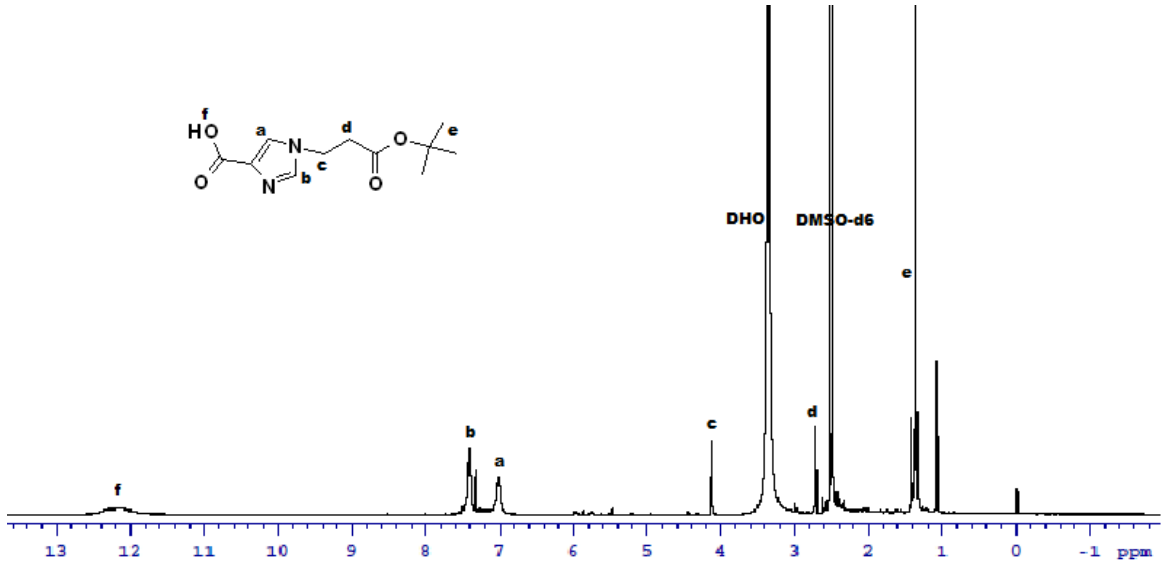

Figure E.22 ^{1}H NMR of compound 9 in DMSO-d6 (before purification).

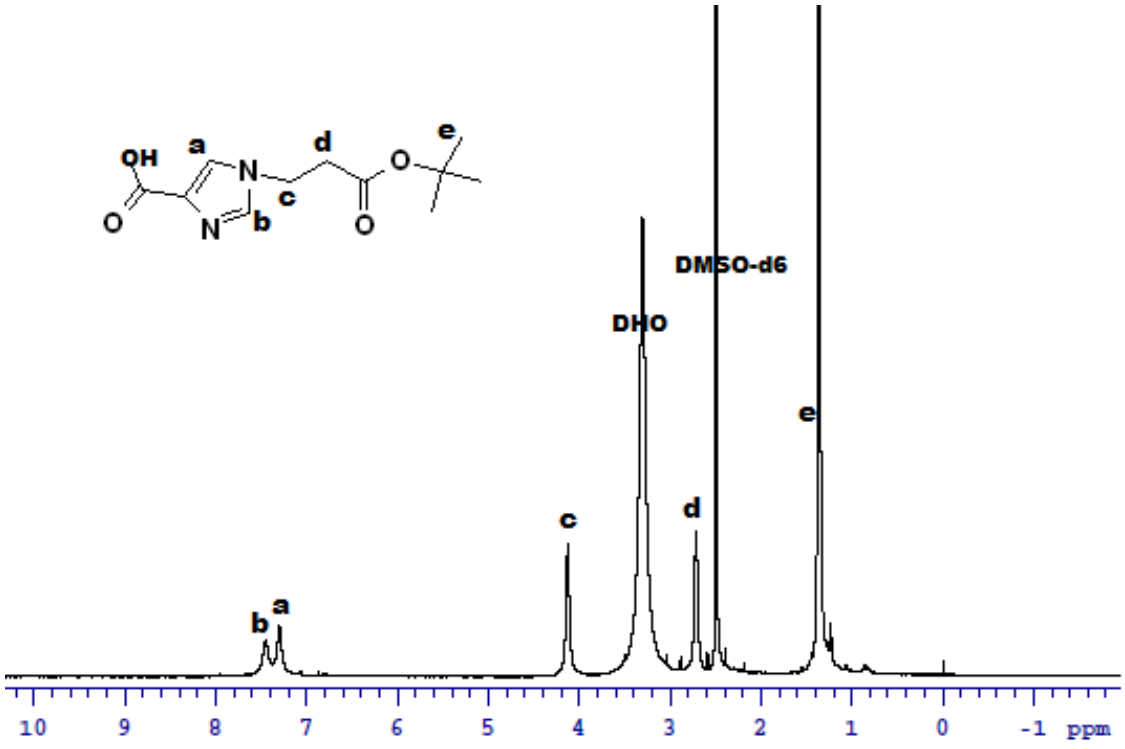

Figure E.23 ^{1}H NMR of compound 9 in DMSO-d6 (after purification).

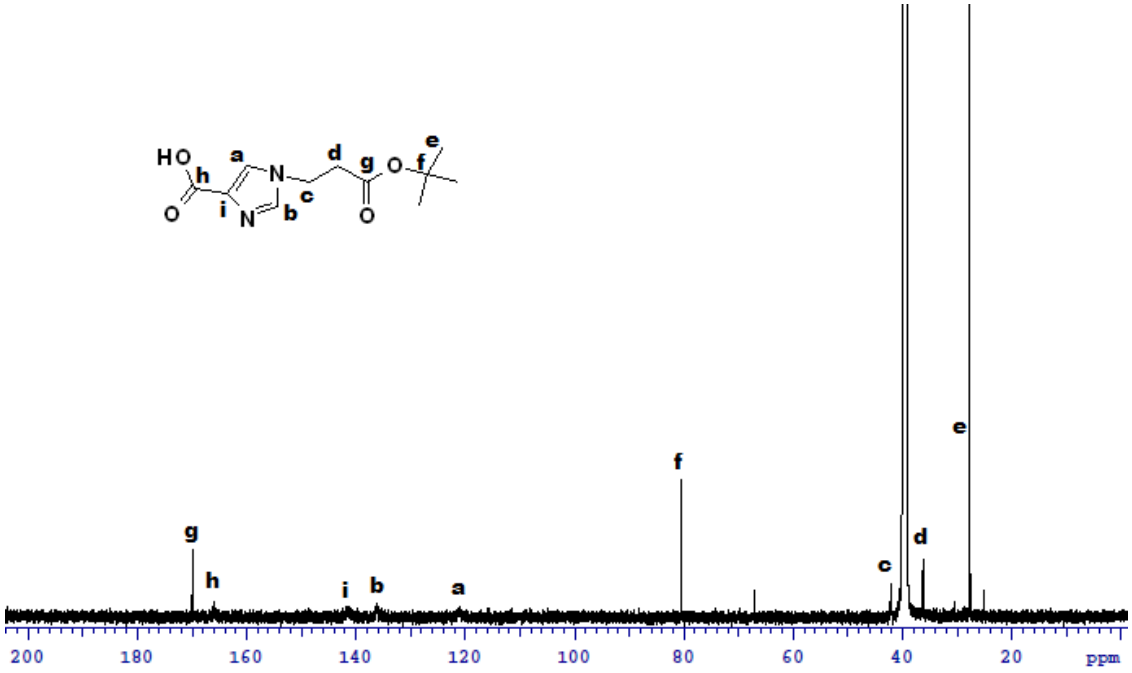

Figure E.24 ^{13}C NMR of compound 9 in DMSO-d6.

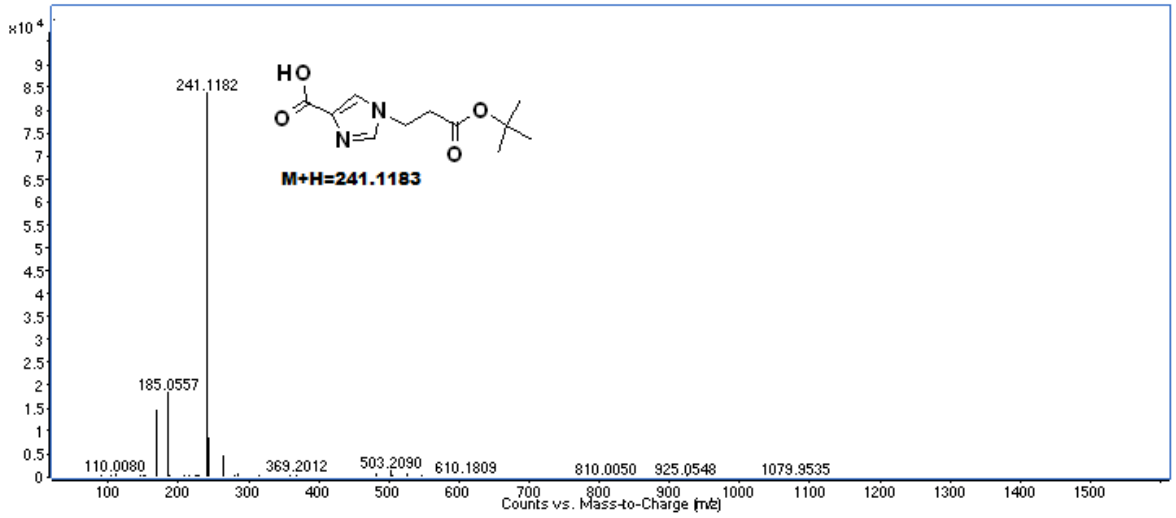

Figure E.25 HR-MS (ESI-MS) of compound 9.

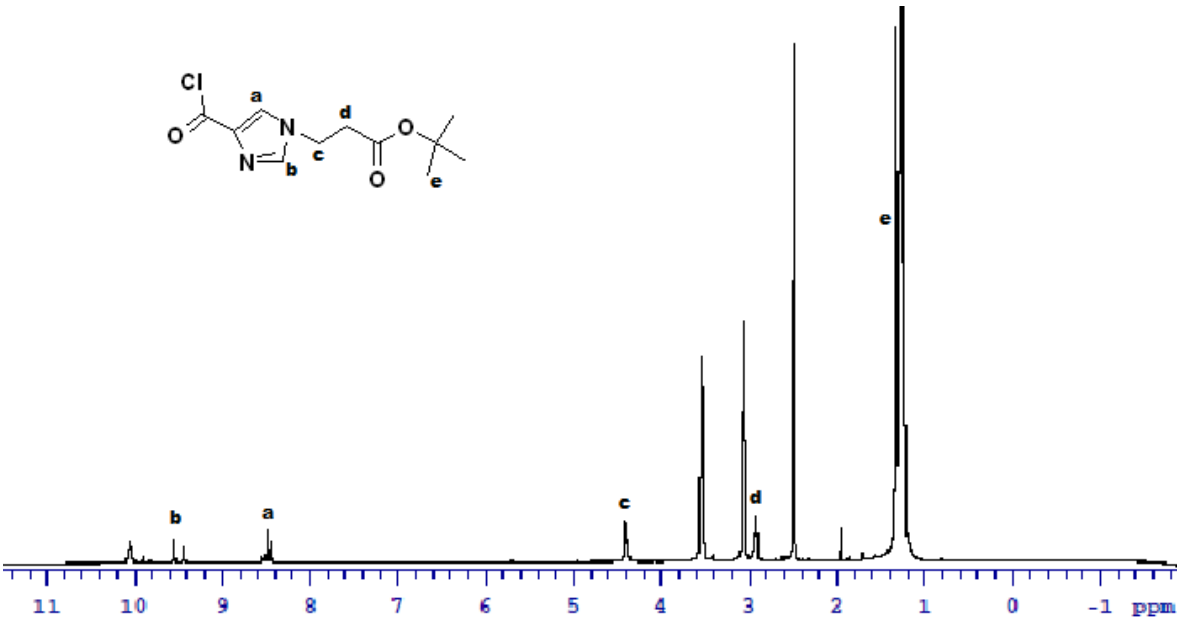

Figure E.26 ^{1}H NMR of compound 10 in DMSO-d6 (DIPEA in DMSO-d6, non-purified material).

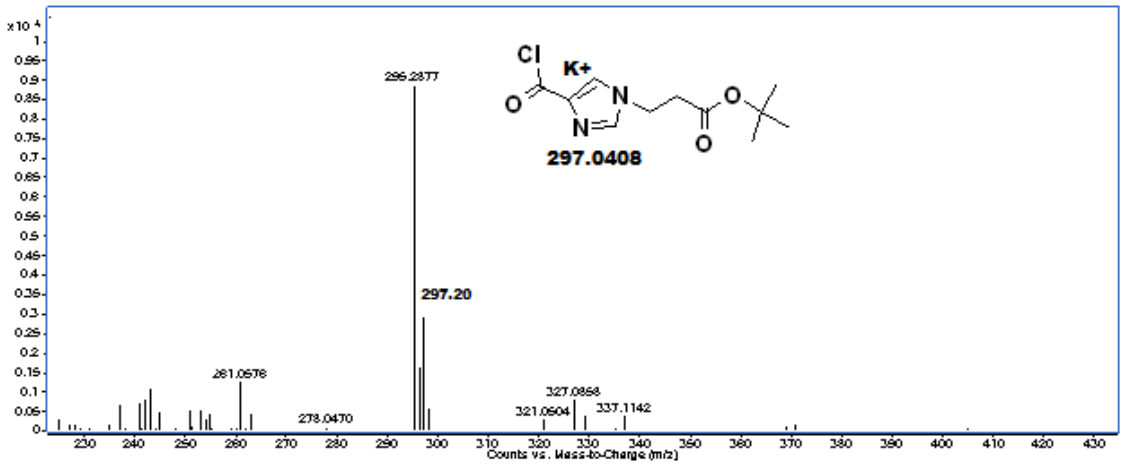

Figure E.27 ESI-MS of compound 10.

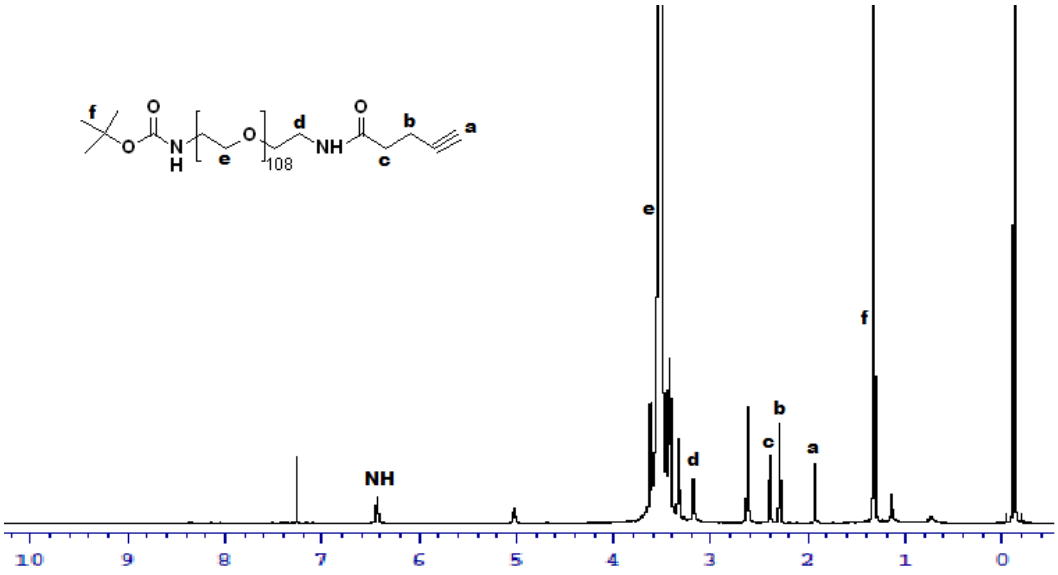

Figure E.28 ^{1}H NMR of compound 11 in $CDCl_3$.

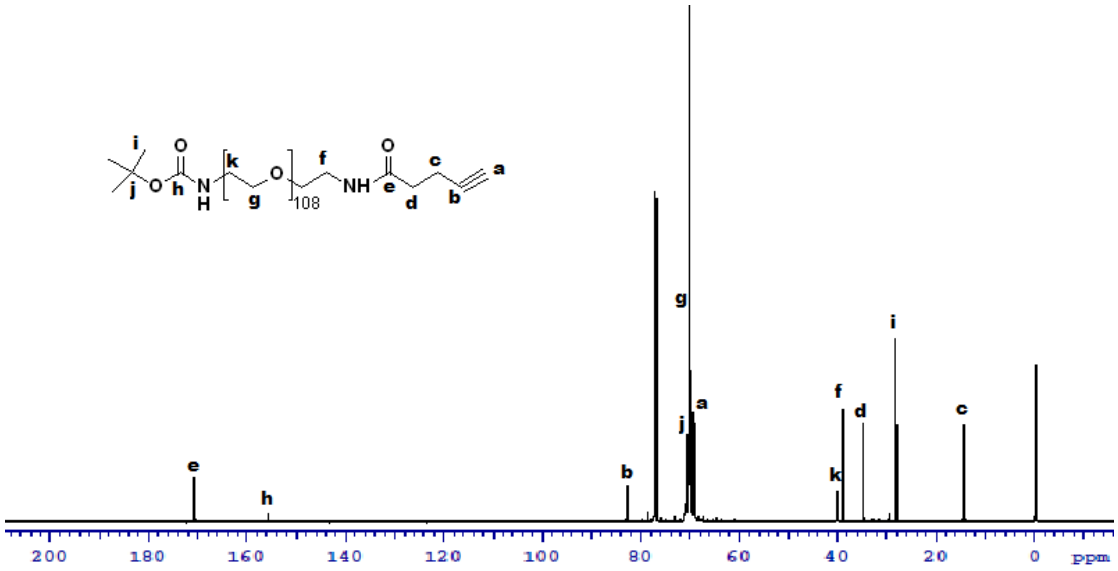

Figure E.29 ^{13}C NMR of compound 11 in $CDCl_3$.

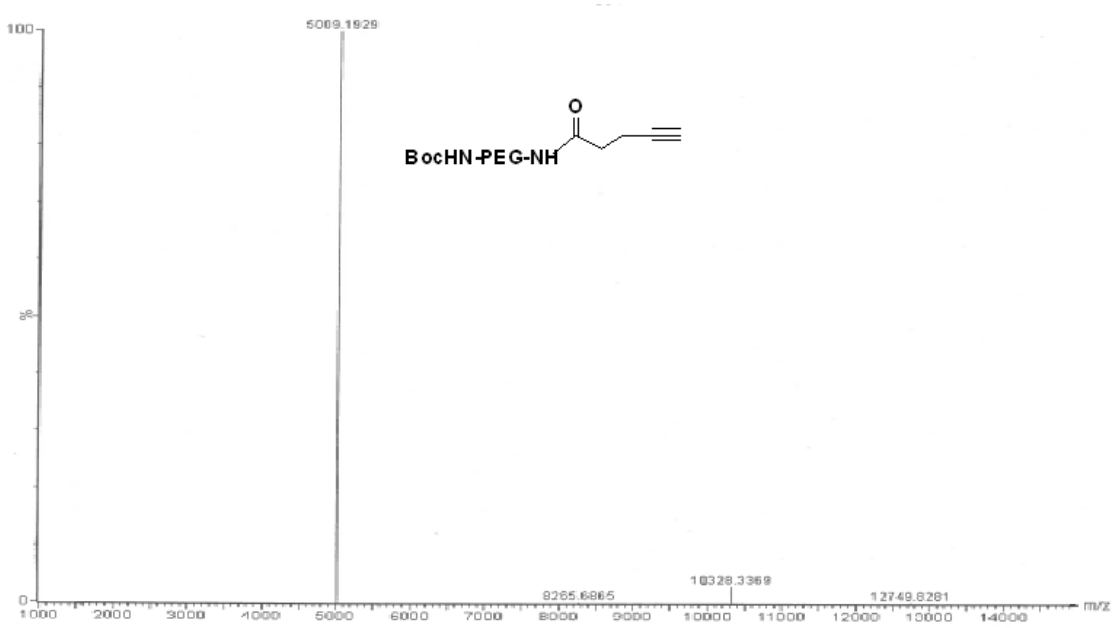

Figure E.30 MALDI-spectrum of compound 11.

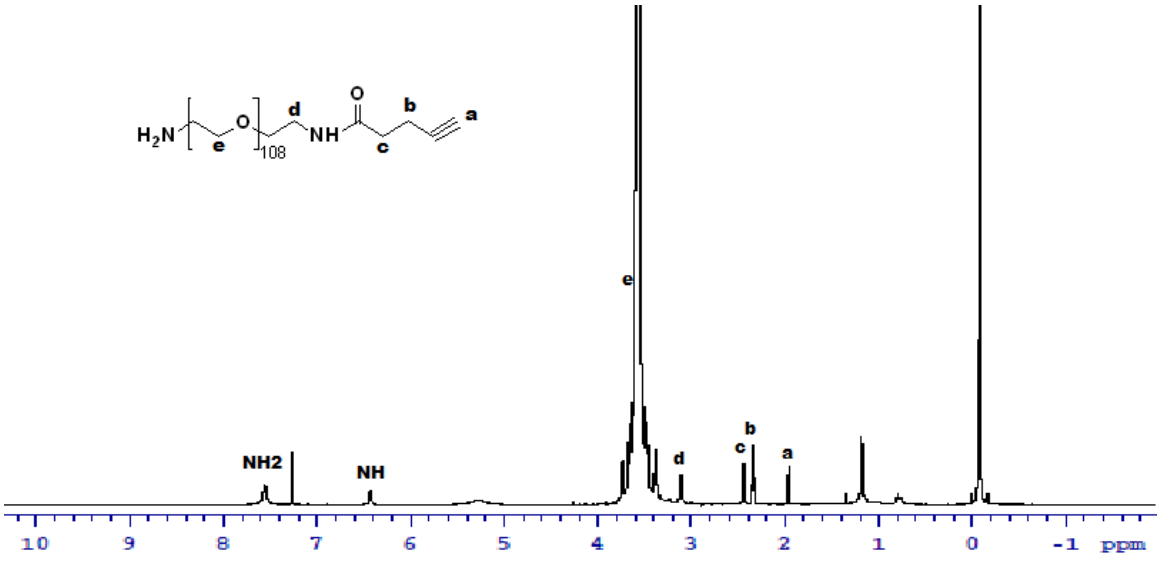

Figure E.31 ^{1}H NMR of compound 12 in $CDCl_3$.

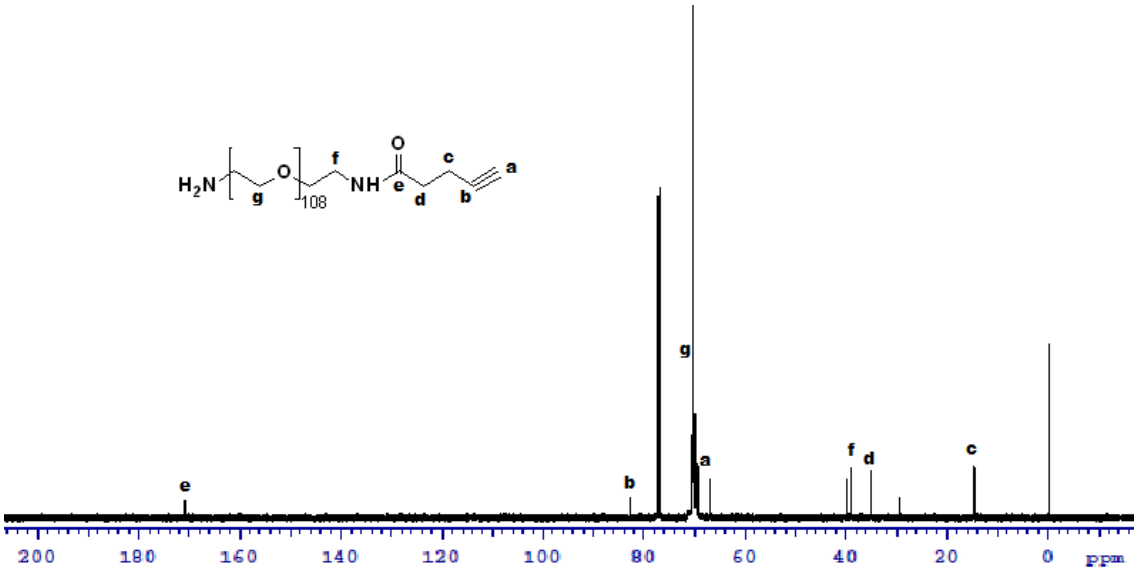

Figure E.32 ^{13}C NMR of compound 12 in $CDCl_3$.

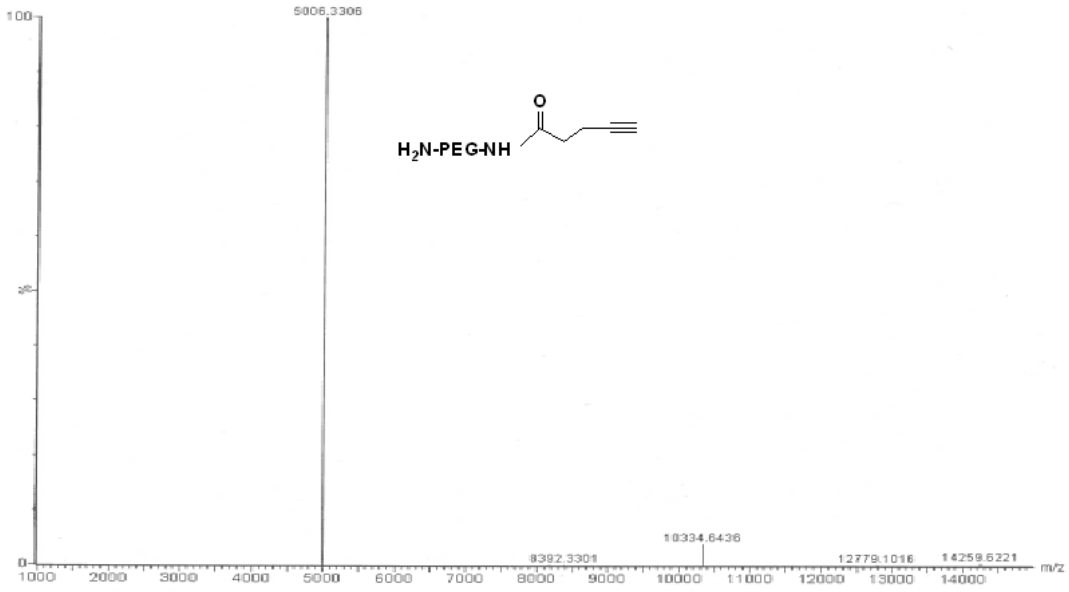

Figure E.33 MALDI-spectrum of compound 12.

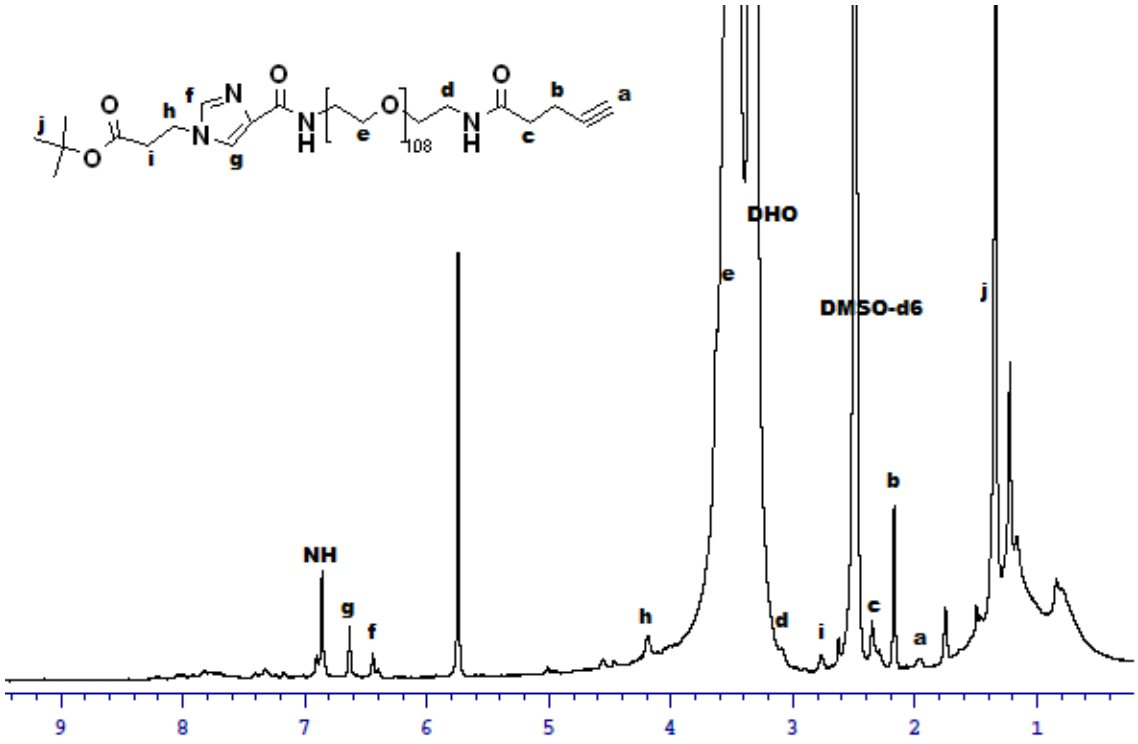

Figure E.34 ^{1}H NMR of compound 13 in $CDCl_3$.

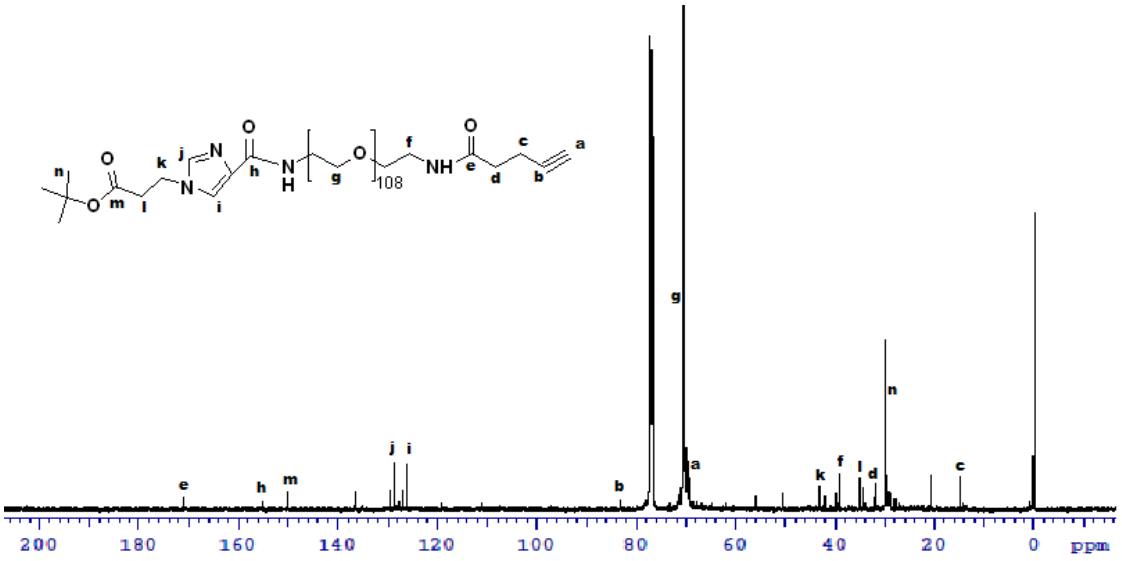

Figure E.35 ^{13}C NMR of compound 13 in $CDCl_3$.

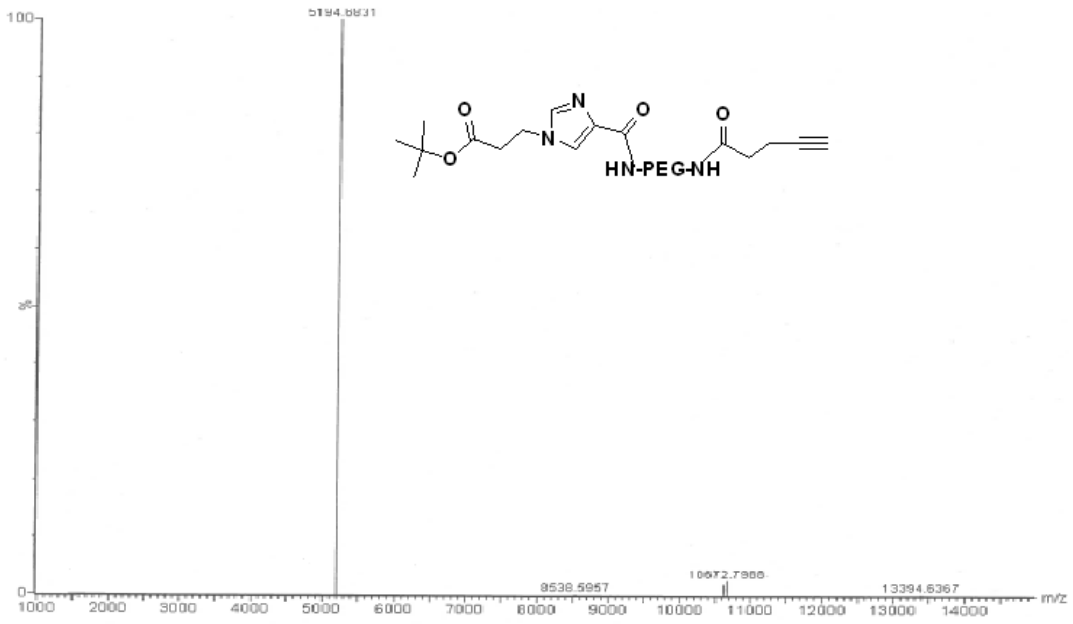

Figure E.36 MALDI-spectrum of compound 13.

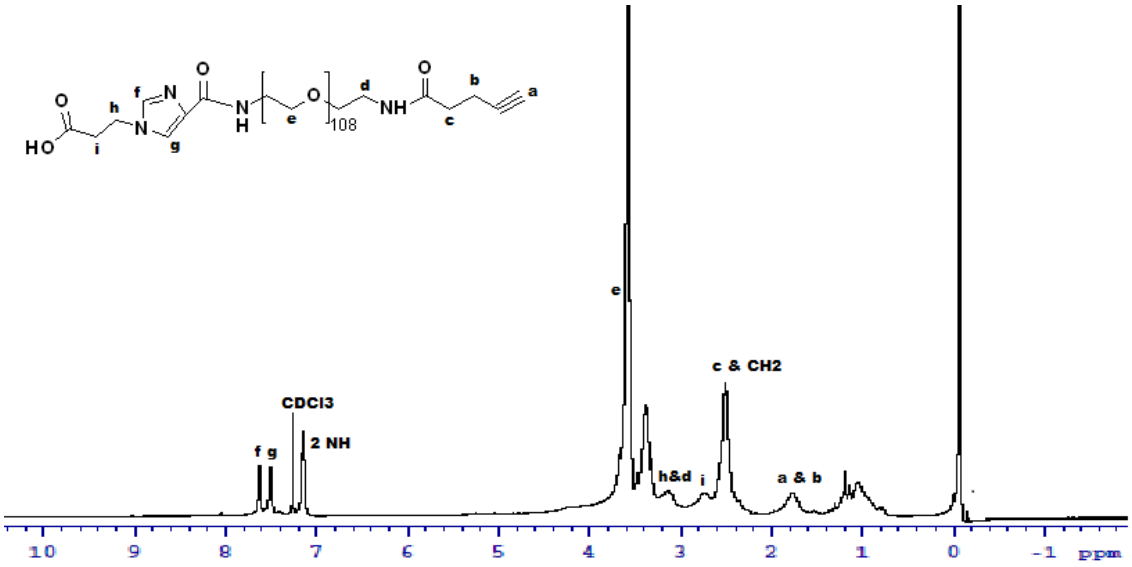

Figure E.37 ^{1}H NMR of compound 14 in $CDCl_3$.

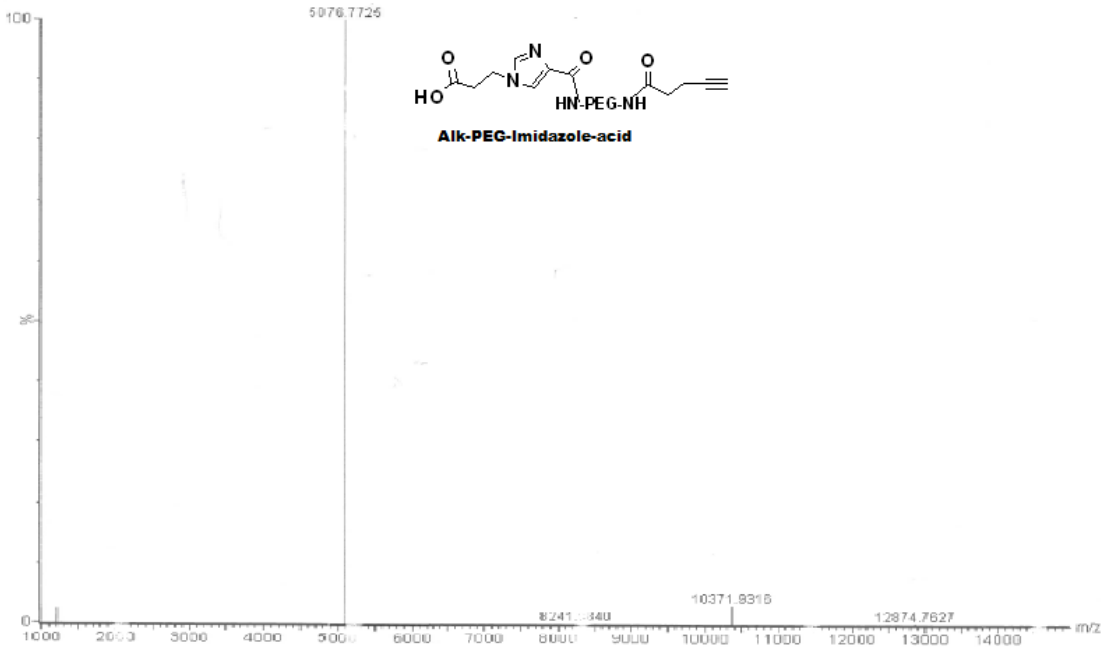

Figure E.38 MALDI-spectrum of compound 14.

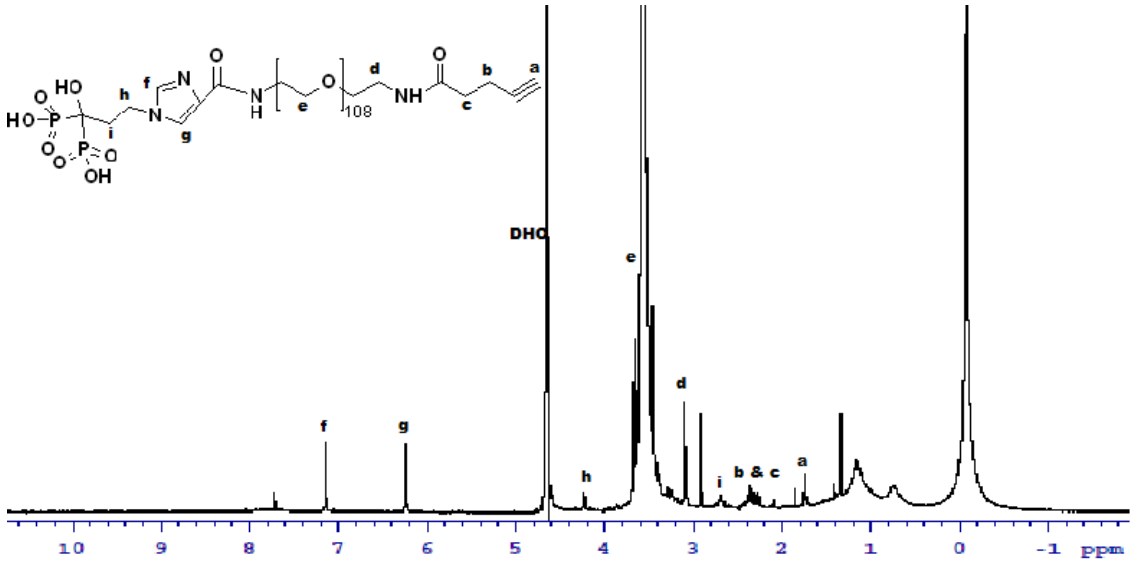

Figure E.39 ^{1}H NMR of compound 15 in D_2O.

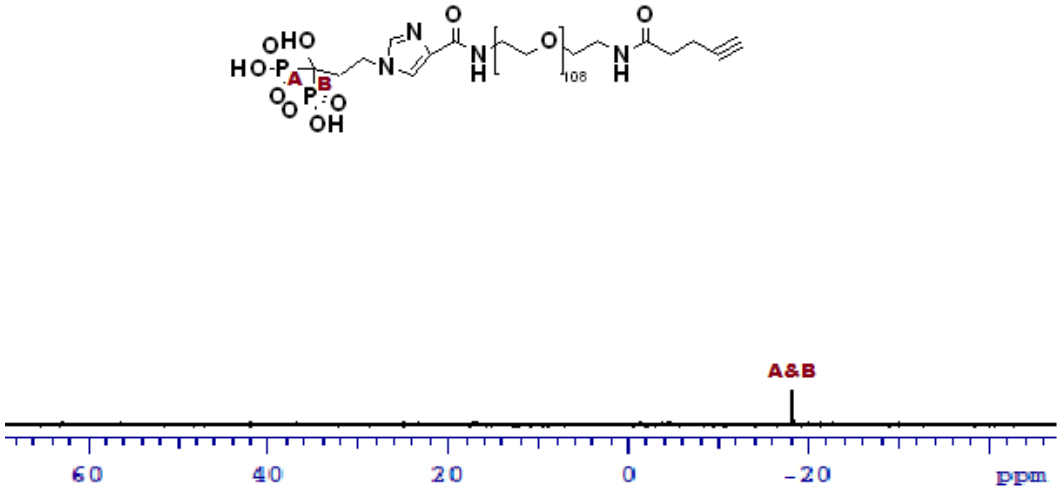

Figure E.40 ^{31}P NMR of compound 15 in D_2O.

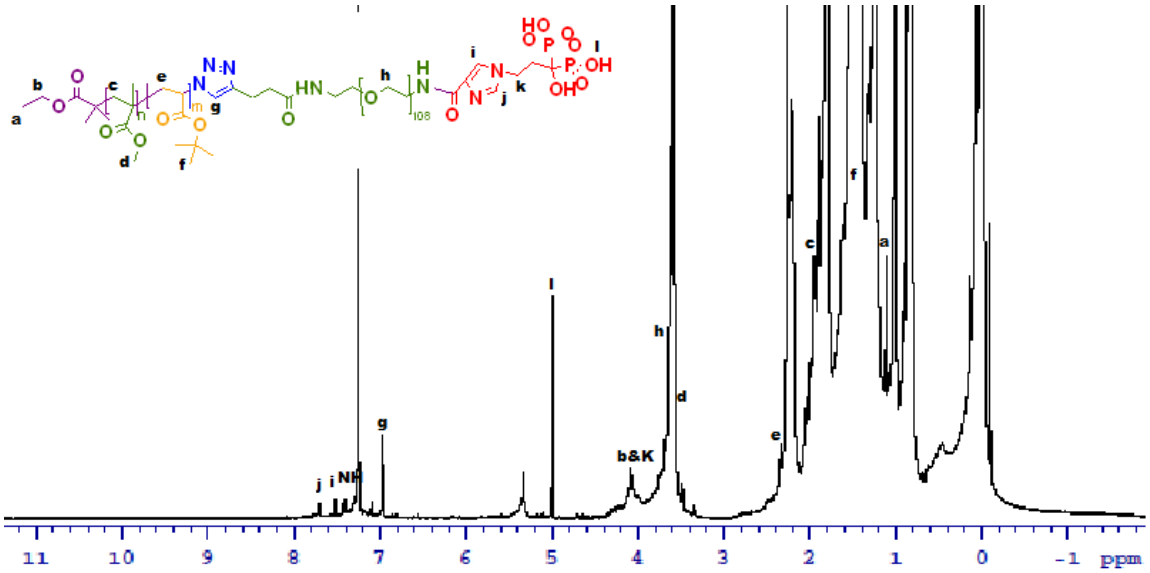

Figure E.41 ^{1}H NMR of compound 16 in $CDCl_3$.

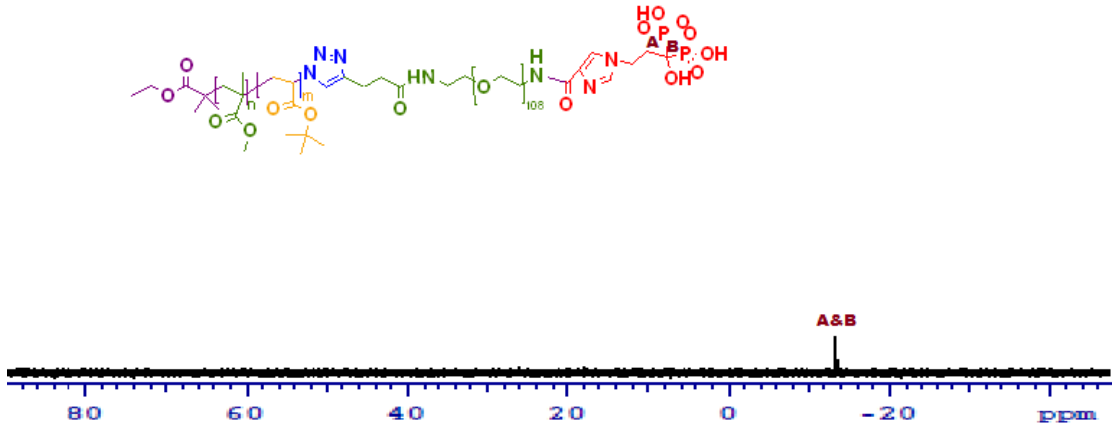

Figure E.42 ^{31}P NMR of compound 16 in D_2O.

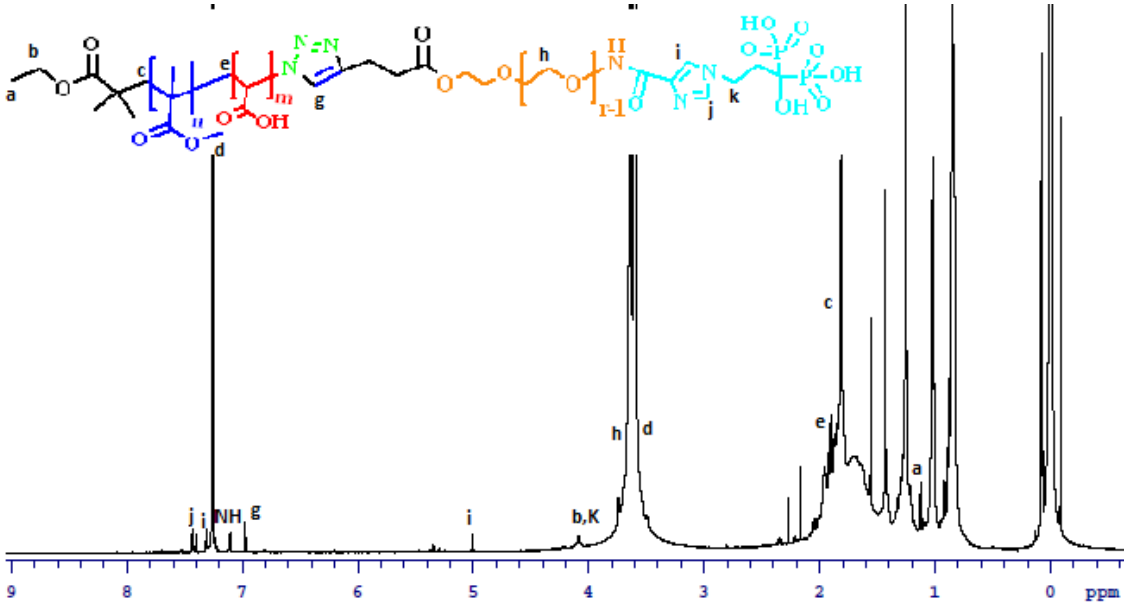

Figure E.43 ^{1}H NMR of compound 17 in $CDCl_3$.

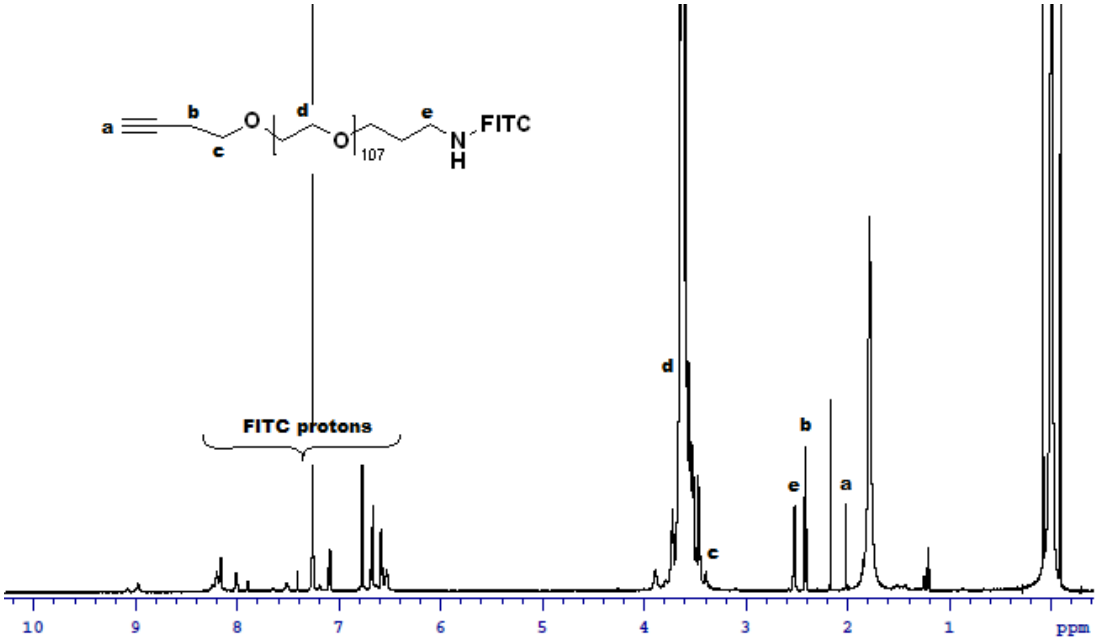

Figure E.44 ^{1}H NMR of compound 18 in $CDCl_3$.

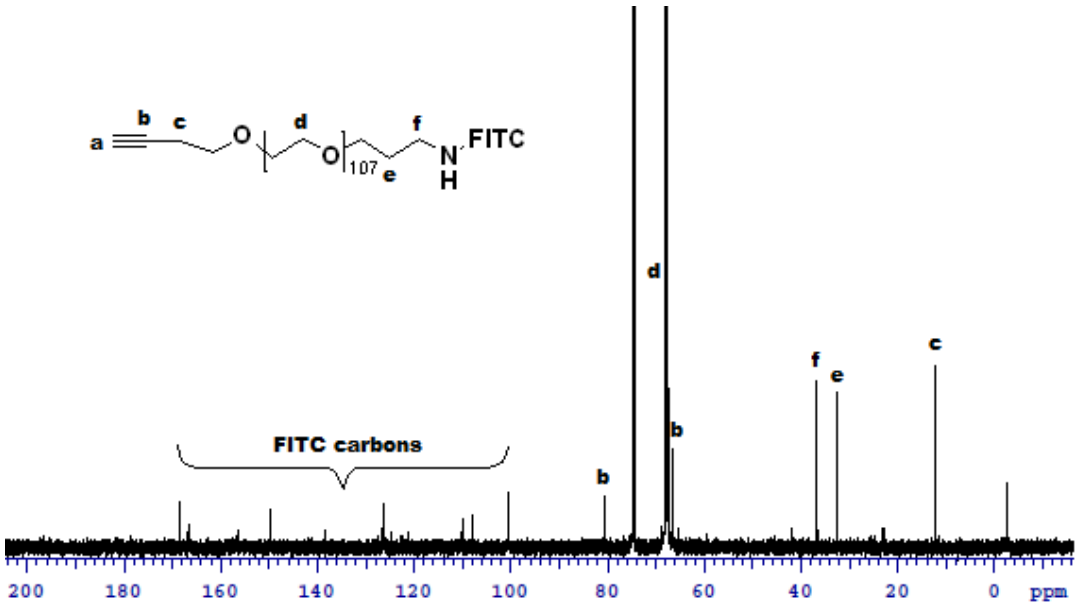

Figure E.45 ^{13}C NMR of compound 18 in $CDCl_3$.

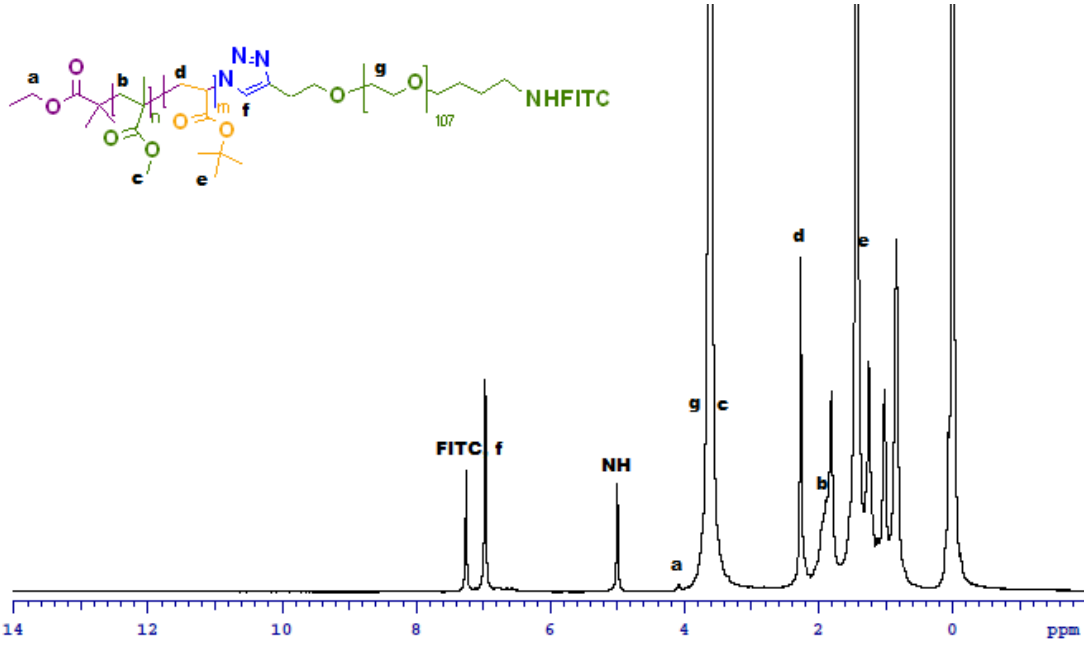

Figure E.46 ^{1}H NMR of Compound 19 (PMMA-*b*-P*t*BA-*b*-PEG-NHFITC) in $CDCl_3$.

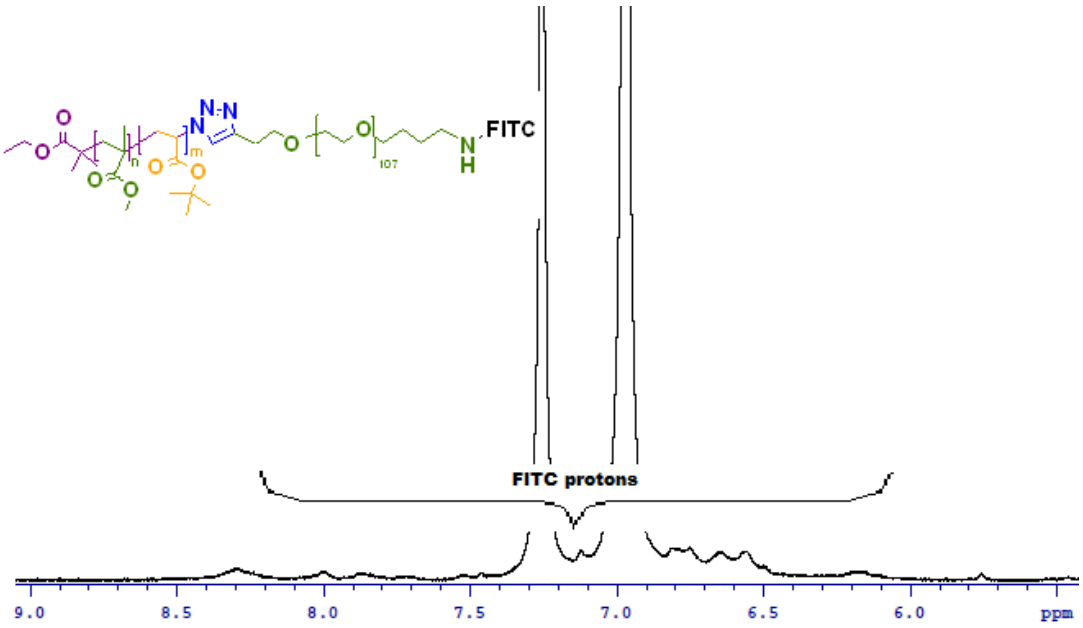

Figure E.47 expanded ^{1}H NMR of Compound 19 (PMMA-*b*-P*t*BA-*b*-PEG-NHFITC, (5.5-9.0 ppm) in $CDCl_3$.

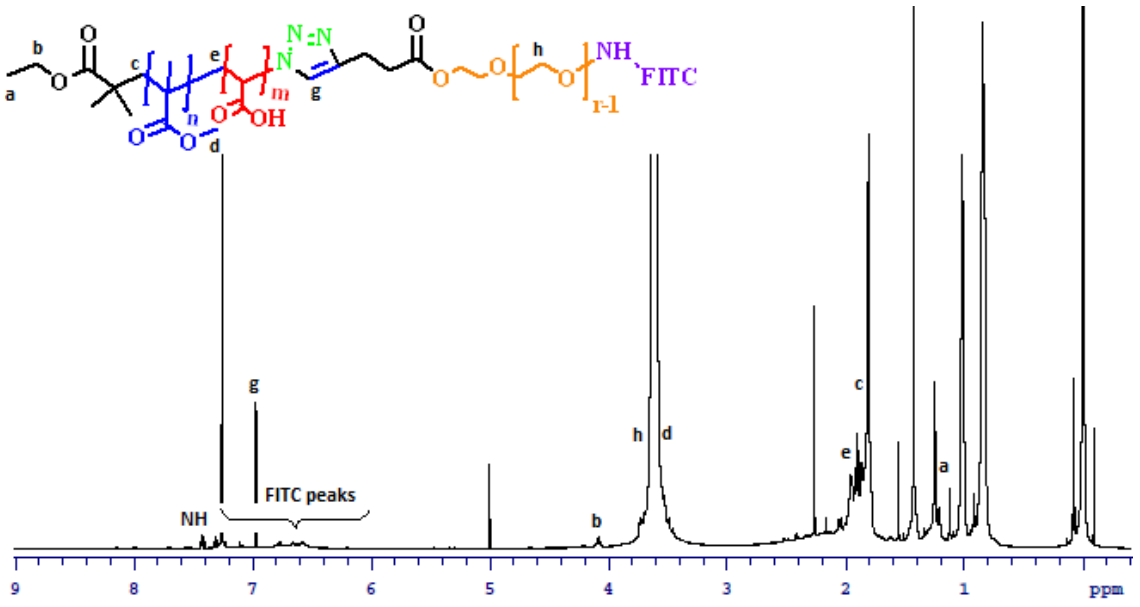

Figure E.48 ^{1}H NMR of Compound 20 (PMMA-*b*-PAA-*b*-PEG-NHFITC) in $CDCl_3$.

References

[1] Society AC. What are the key statistics about prostate cancer? : American Cancer Society; 2016.

[2] McPhail S. SWPHO Briefing 4: Prostate cancer survival by stage. In: Health SWP, editor.: Cancer Analysis Team, South West Public Health Observatory; 2008.

[3] Bauer RM, Mayer ME, Gratzke C, Soljanik I, Bastian PJ, Stief CG, et al. [Urinary incontinence after radical prostatectomy]. Urologe A. 2009;48:1044, 6, 8-9.

[4] Becker AJ, Stief CG, Stadler TC. [Erectile dysfunction after radical prostatectomy]. Aktuelle Urol. 2009;40:289-93.

[5] Steyerberg EW, Roobol MJ, Kattan MW, van der Kwast TH, de Koning HJ, Schroder FH. Prediction of indolent prostate cancer: validation and updating of a prognostic nomogram. J Urol. 2007;177:107-12; discussion 12.

[6] Duffield AS, Lee TK, Miyamoto H, Carter HB, Epstein JI. Radical prostatectomy findings in patients in whom active surveillance of prostate cancer fails. J Urol. 2009;182:2274-8.

[7] Brawer MK. Hormonal therapy for prostate cancer. Rev Urol. 2006;8 Suppl 2:S35-47.

[8] Smith JA, Jr. Management of hot flushes due to endocrine therapy for prostate carcinoma. Oncology (Williston Park). 1996;10:1319-22; discussion 24.

[9] Gravis G, Fizazi K, Joly F, Oudard S, Priou F, Esterni B, et al. Androgen-deprivation therapy alone or with docetaxel in non-castrate metastatic prostate cancer (GETUG-AFU 15): a randomised, open-label, phase 3 trial. Lancet Oncol. 2013;14:149-58.

[10] Haines IE, Stanley RM. Perspective on "Chemotherapy for advanced prostate cancer: 25 years later": is it a mirage or an oasis? J Clin Oncol. 2008;26:4049-50; author reply 51.

[11] Kelly WK, Curley T, Slovin S, Heller G, McCaffrey J, Bajorin D, et al. Paclitaxel, estramustine phosphate, and carboplatin in patients with advanced prostate cancer. J Clin Oncol. 2001;19:44-53.

[12] Michielsen DP, Braeckman JG, Denis L. Cabazitaxel for the treatment of prostate cancer. Expert Opin Pharmacother. 2011;12:977-82.

[13] Mahon KL, Henshall SM, Sutherland RL, Horvath LG. Pathways of chemotherapy resistance in castration-resistant prostate cancer. Endocr Relat Cancer. 2011;18:R103-23.

[14] Bergh M, Magnusson K, Nilsson JL, Karlberg AT. Contact allergenic activity of Tween 80 before and after air exposure. Contact Dermatitis. 1997;37:9-18.

[15] Persohn E, Canta A, Schoepfer S, Traebert M, Mueller L, Gilardini A, et al. Morphological and morphometric analysis of paclitaxel and docetaxel-induced peripheral neuropathy in rats. Eur J Cancer. 2005;41:1460-6.

[16] Coleman RE. Skeletal complications of malignancy. Cancer. 1997;80:1588-94.

[17] Galasko CS. Skeletal metastases. Clin Orthop Relat Res. 1986:18-30.

[18] Palmedo H. Radionuclide Therapy of Bone Metastases. In: Biersack H-J, Freeman L, editors. Clinical Nuclear Medicine: Springer Berlin Heidelberg; 2007. p. 433-42.

[19] Thompson K, Rogers MJ, Coxon FP, Crockett JC. Cytosolic entry of bisphosphonate drugs requires acidification of vesicles after fluid-phase endocytosis. Mol Pharmacol. 2006;69:1624-32.

[20] Fisher JE, Rogers MJ, Halasy JM, Luckman SP, Hughes DE, Masarachia PJ, et al. Alendronate mechanism of action: geranylgeraniol, an intermediate in the mevalonate pathway, prevents inhibition of osteoclast formation, bone resorption, and kinase activation in vitro. Proc Natl Acad Sci U S A. 1999;96:133-8.

[21] Luckman SP, Hughes DE, Coxon FP, Graham R, Russell G, Rogers MJ. Nitrogen-containing bisphosphonates inhibit the mevalonate pathway and prevent post-translational prenylation of GTP-binding proteins, including Ras. J Bone Miner Res. 1998;13:581-9.

[22] Coxon FP, Thompson K, Roelofs AJ, Ebetino FH, Rogers MJ. Visualizing mineral binding and uptake of bisphosphonate by osteoclasts and non-resorbing cells. Bone. 2008;42:848-60.

[23] Virtanen SS, Vaananen HK, Harkonen PL, Lakkakorpi PT. Alendronate inhibits invasion of PC-3 prostate cancer cells by affecting the mevalonate pathway. Cancer Res. 2002;62:2708-14.

[24] van der Pluijm G, Vloedgraven H, van Beek E, van der Wee-Pals L, Lowik C, Papapoulos S. Bisphosphonates inhibit the adhesion of breast cancer cells to bone matrices in vitro. J Clin Invest. 1996;98:698-705.

[25] Boissier S, Magnetto S, Frappart L, Cuzin B, Ebetino FH, Delmas PD, et al. Bisphosphonates inhibit prostate and breast carcinoma cell adhesion to unmineralized and mineralized bone extracellular matrices. Cancer Res. 1997;57:3890-4.

[26] Jagdev SP, Coleman RE, Shipman CM, Rostami HA, Croucher PI. The bisphosphonate, zoledronic acid, induces apoptosis of breast cancer cells: evidence for synergy with paclitaxel. Br J Cancer. 2001;84:1126-34.

[27] Senaratne SG, Pirianov G, Mansi JL, Arnett TR, Colston KW. Bisphosphonates induce apoptosis in human breast cancer cell lines. Br J Cancer. 2000;82:1459-68.

[28] Fournier P, Boissier S, Filleur S, Guglielmi J, Cabon F, Colombel M, et al. Bisphosphonates inhibit angiogenesis in vitro and testosterone-stimulated vascular regrowth in the ventral prostate in castrated rats. Cancer Res. 2002;62:6538-44.

[29] Stresing V, Fournier PG, Bellahcene A, Benzaid I, Monkkonen H, Colombel M, et al. Nitrogen-containing bisphosphonates can inhibit angiogenesis in vivo without the involvement of farnesyl pyrophosphate synthase. Bone. 2011;48:259-66.

[30] Senaratne S, Colston K. The role of bisphosphonates in breast cancer: Direct effects of bisphosphonates on breast cancer cells. Breast Cancer Res. 2002;4:18 - 23.

[31] Zeno Sparchez TMaPR. Old versus New – Tumor Ablation versus Tumor Nanoablation with Particular Emphasis on Liver Tumors, Recent Advances in Liver Diseases and Surgery: INTECH; 2015.

[32] Lindner U, Lawrentschuk N, Weersink RA, Davidson SR, Raz O, Hlasny E, et al. Focal laser ablation for prostate cancer followed by radical prostatectomy: validation of focal therapy and imaging accuracy. Eur Urol. 2010;57:1111-4.

[33] Brace CL. Radiofrequency and microwave ablation of the liver, lung, kidney, and bone: what are the differences? Curr Probl Diagn Radiol. 2009;38:135-43.

[34] Brunello F, Veltri A, Carucci P, Pagano E, Ciccone G, Moretto P, et al. Radiofrequency ablation versus ethanol injection for early hepatocellular carcinoma: A randomized controlled trial. Scand J Gastroenterol. 2008;43:727-35.

[35] Seror O. Percutaneous hepatic ablation: what needs to be known in 2014. Diagn Interv Imaging. 2014;95:665-75.

[36] Robinson JT, Welsher K, Tabakman SM, Sherlock SP, Wang H, Luong R, et al. High Performance In Vivo Near-IR (>1 mum) Imaging and Photothermal Cancer Therapy with Carbon Nanotubes. Nano Res. 2010;3:779-93.

[37] Leslie TA, Kennedy JE. High-intensity focused ultrasound principles, current uses, and potential for the future. Ultrasound Q. 2006;22:263-72.

[38] ter Haar G. High intensity ultrasound. Semin Laparosc Surg. 2001;8:77-89.

[39] Bobkova S, Gavrilov L, Khokhlova V, Shaw A, Hand J. Focusing of high-intensity ultrasound through the rib cage using a therapeutic random phased array. Ultrasound Med Biol. 2010;36:888-906.

[40] Pillai K, Akhter J, Chua TC, Shehata M, Alzahrani N, Al-Alem I, et al. Heat sink effect on tumor ablation characteristics as observed in monopolar radiofrequency, bipolar radiofrequency, and microwave, using ex vivo calf liver model. Medicine (Baltimore). 2015;94:e580.

[41] Okada A, Murakami T, Mikami K, Onishi H, Tanigawa N, Marukawa T, et al. A case of hepatocellular carcinoma treated by MR-guided focused ultrasound ablation with respiratory gating. Magn Reson Med Sci. 2006;5:167-71.

[42] Xu Z, Fowlkes JB, Ludomirsky A, Cain CA. Investigation of intensity thresholds for ultrasound tissue erosion. Ultrasound Med Biol. 2005;31:1673-82.

[43] Roberts WW, Hall TL, Ives K, Wolf JS, Jr., Fowlkes JB, Cain CA. Pulsed cavitational ultrasound: a noninvasive technology for controlled tissue ablation (histotripsy) in the rabbit kidney. J Urol. 2006;175:734-8.

[44] Maxwell AD, Cain CA, Hall TL, Fowlkes JB, Xu Z. Probability of cavitation for single ultrasound pulses applied to tissues and tissue-mimicking materials. Ultrasound Med Biol. 2013;39:449-65.

[45] Vlaisavljevich E, Kim Y, Allen S, Owens G, Pelletier S, Cain C, et al. Image-Guided Non-Invasive Ultrasound Liver Ablation using Histotripsy: Feasibility Study in an *In Vivo* Porcine Model. . Ultrasound Med Biol. 2013.

[46] Yuksel Durmaz Y, Vlaisavljevich E, Xu Z, ElSayed M. Development of nanodroplets for histotripsy-mediated cell ablation. Mol Pharm. 2014;11:3684-95.

[47] Winterroth F, Xu Z, Wang TY, Wilkinson JE, Fowlkes JB, Roberts WW, et al. Examining and analyzing subcellular morphology of renal tissue treated by histotripsy. Ultrasound Med Biol. 2011;37:78-86.

[48] Xu Z, Fowlkes JB, Cain CA. A new strategy to enhance cavitational tissue erosion using a high-intensity, Initiating sequence. IEEE Trans Ultrason Ferroelectr Freq Control. 2006;53:1412-24.

[49] Xu Z, Fowlkes JB, Rothman ED, Levin AM, Cain CA. Controlled ultrasound tissue erosion: the role of dynamic interaction between insonation and microbubble activity. J Acoust Soc Am. 2005;117:424-35.

[50] Hall TL, Hempel CR, Wojno K, Xu Z, Cain CA, Roberts WW. Histotripsy of the prostate: dose effects in a chronic canine model. Urology. 2009;74:932-7.

[51] Owens GE, Miller RM, Ensing G, Ives K, Gordon D, Ludomirsky A, et al. Therapeutic ultrasound to noninvasively create intracardiac communications in an intact animal model. Catheter Cardiovasc Interv. 2011;77:580-8.

[52] Szabo TL, ScienceDirect. Diagnostic ultrasound imaging: inside out. Amsterdam ; Burlington, MA: Elsevier Academic Press; 2004.

[53] King DA, University of Illinois at U-C. Collapse dynamics of ultrasound contrast agent microbubbles2012.

[54] Lencioni R, SpringerLink. Enhancing the role of ultrasound with contrast agents. Milan: Springer-Verlag; 2006.

[55] Gramiak R, Shah PM. Echocardiography of the aortic root. Invest Radiol. 1968;3:356-66.

[56] Feinstein SB, Cheirif J, Ten Cate FJ, Silverman PR, Heidenreich PA, Dick C, et al. Safety and efficacy of a new transpulmonary ultrasound contrast agent: initial multicenter clinical results. J Am Coll Cardiol. 1990;16:316-24.

[57] Spalding H, Martikainen H, Tekay A, Jouppila P. A randomized study comparing air to Echovist as a contrast medium in the assessment of tubal patency in infertile women using transvaginal salpingosonography. Hum Reprod. 1997;12:2461-4.

[58] Plew J, Sanki J, Young N, Gruenewald S, Dwyer R, Brancatisano R. Early experience in the use of Levovist ultrasound contrast in the evaluation of liver masses. Australas Radiol. 2000;44:28-31.

[59] Schutt EG, Pelura TJ, Hopkins RM. Osmotically stabilized microbubble sonographic contrast agents. Acad Radiol. 1996;3 Suppl 2:S188-90.

[60] Ibsen S, Schutt CE, Esener S. Microbubble-mediated ultrasound therapy: a review of its potential in cancer treatment. Drug Des Devel Ther. 2013;7:375-88.

[61] Cui W, Bei J, Wang S, Zhi G, Zhao Y, Zhou X, et al. Preparation and evaluation of poly(L-lactide-co-glycolide) (PLGA) microbubbles as a contrast agent for myocardial contrast echocardiography. J Biomed Mater Res B Appl Biomater. 2005;73:171-8.

[62] Niu C, Wang Z, Zuo G, Krupka TM, Ran H, Zhang P, et al. Poly(Lactide-co-glycolide) ultrasonographic microbubbles carrying Sudan black for preoperative and intraoperative localization of lymph nodes. Clin Breast Cancer. 2012;12:199-206.

[63] Fu H, Comer J, Cai W, Chipot C. Sonoporation at Small and Large Length Scales: Effect of Cavitation Bubble Collapse on Membranes. J Phys Chem Lett. 2015;6:413-8.

[64] Maeda H, Wu J, Sawa T, Matsumura Y, Hori K. Tumor vascular permeability and the EPR effect in macromolecular therapeutics: a review. J Control Release. 2000;65:271-84.

[65] Sirsi S, Borden M. Microbubble Compositions, Properties and Biomedical Applications. Bubble Sci Eng Technol. 2009;1:3-17.

[66] Sheeran PS, Wong VP, Luois S, McFarland RJ, Ross WD, Feingold S, et al. Decafluorobutane as a Phase-Change Contrast Agent for Low-Energy Extravascular Ultrasonic Imaging. Ultrasound in Medicine and Biology. 2011;37:1518-30.

[67] Wilson K, Homan K, Emelianov S. Biomedical photoacoustics beyond thermal expansion using triggered nanodroplet vaporization for contrast-enhanced imaging. Nature communications. 2012;3:618 (10 pp.).

[68] Rapoport N, Nam KH, Gupta R, Gao Z, Mohan P, Payne A, et al. Ultrasound-mediated tumor imaging and nanotherapy using drug loaded, block copolymer stabilized perfluorocarbon nanoemulsions. J Control Release. 2011;153:4-15.

[69] Kawabata Ki, Asami R, Azuma T, Umemura Si. Acoustic Response of Microbubbles Derived from Phase-change Nanodroplet. Japanese Journal of Applied Physics. 2010;49:07HF18 (9 pp.).

[70] Rapoport NY, Nam KH, Gao Z, Kennedy A. Application of ultrasound for targeted nanotherapy of malignant tumors. Acoustical Physics. 2009;55:594-601.

[71] Liberman A, Wu Z, Barback CV, Viveros RD, Wang J, Ellies LG, et al. Hollow iron-silica nanoshells for enhanced high intensity focused ultrasound. J Surg Res. 2014;190:391-8.

[72] Kopechek JA, Park EJ, Zhang YZ, Vykhodtseva NI, McDannold NJ, Porter TM. Cavitation-enhanced MR-guided focused ultrasound ablation of rabbit tumors in vivo using phase shift nanoemulsions. Phys Med Biol. 2014;59:3465-81.

[73] Mougenot C, Kohler MO, Enholm J, Quesson B, Moonen C. Quantification of near-field heating during volumetric MR-HIFU ablation. Med Phys. 2011;38:272-82.

[74] Perrier S, Jackson SG, Haddleton DM, Ameduri B, Boutevin B. Preparation of fluorinated methacrylic copolymers by copper mediated living radical polymerization. Tetrahedron. 2002;58:4053-9.

[75] Astafyeva K, Somaglino L, Desgranges S, Berti R, Patinote C, Langevin D, et al. Perfluorocarbon nanodroplets stabilized by fluorinated surfactants: characterization and potentiality as theranostic agents. Journal of Materials Chemistry B. 2015.

[76] Shen J, Piunova VA, Nutt S, Hogen-Esch TE. Blends of polystyrene and poly(n-butyl methacrylate) mediated by perfluorocarbon end groups. Polymer. 2013;54:5790-800.

[77] Janjic JM, Ahrens ET. Fluorine-containing nanoemulsions for MRI cell tracking. Wiley Interdiscip Rev Nanomed Nanobiotechnol. 2009;1:492-501.

[78] Nishihara M, Imai K, Yokoyama M. Preparation of Perfluorocarbon/Fluoroalkyl Polymer Nanodroplets for Cancer-targeted Ultrasound Contrast Agents. Chemistry Letters. 2009;38:556-7.

[79] Vlaisavljevich E, Durmaz YY, Maxwell A, Elsayed M, Xu Z. Nanodroplet-mediated histotripsy for image-guided targeted ultrasound cell ablation. Theranostics. 2013;3:851-64.

[80] Vlaisavljevich E, Aydin O, Yuksel Durmaz Y, Lin KW, Fowlkes B, ElSayed M, et al. Effects of Ultrasound Frequency on Nanodroplet-Mediated Histotripsy. Ultrasound Med Biol. 2015;41:2135-47.

[81] Vlaisavljevich E, Aydin O, Lin KW, Fowlkes B, El-Sayed M, Xu Z. Investigation of the role of ultrasound frequency and droplet composition in nanodroplet-mediated histotripsy. International Society for Therapeutic Ultrasound. Utrecht, Netherlands2015.

[82] Vlaisavljevich E, Aydin O, Durmaz YY, Lin K-W, Fowlkes B, Xu Z, et al. Effects of Droplet Composition on Nanodroplet-Mediated Histotripsy. Ultrasound Med Biol.

[83] Vlaisavljevich E, Aydin O, Lin KW, Durmaz YY, Fowlkes B, ElSayed M, et al. The role of positive and negative pressure on cavitation nucleation in nanodroplet-mediated histotripsy. Physics in medicine and biology. 2016;61:663-82.

[84] Bubendorf L, Schopfer A, Wagner U, Sauter G, Moch H, Willi N, et al. Metastatic patterns of prostate cancer: an autopsy study of 1,589 patients. Hum Pathol. 2000;31:578-83.

[85] Rana A, Chisholm GD, Khan M, Sekharjit SS, Merrick MV, Elton RA. Patterns of bone metastasis and their prognostic significance in patients with carcinoma of the prostate. Br J Urol. 1993;72:933-6.

[86] Mundy GR. Metastasis to bone: causes, consequences and therapeutic opportunities. Nat Rev Cancer. 2002;2:584-93.

[87] Bacac M, Stamenkovic I. Metastatic cancer cell. Annu Rev Pathol. 2008;3:221-47.

[88] John M. Chirgwin TAG. Cancer metastasis to bone. Science & Medicine. 2003;9.

[89] Yewle JN. BIFUNCTIONAL BISPHOSPHONATES FOR DELIVERING BIOMOLECULES TO BONE [Doctoral Dissertation]: University of Kentucky; 2012.

[90] Shen Y, Nilsson SK. Bone, microenvironment and hematopoiesis. Curr Opin Hematol. 2012;19:250-5.

[91] Stefanovic S, Schuetz F, Sohn C, Beckhove P, Domschke C. Bone marrow microenvironment in cancer patients: immunological aspects and clinical implications. Cancer Metastasis Rev. 2013;32:163-78.

[92] Stepensky D, Kleinberg L, Hoffman A. Bone as an effect compartment : models for uptake and release of drugs. Clin Pharmacokinet. 2003;42:863-81.

[93] Binkley N, Ramamurthy R, Krueger D. Low vitamin D status: definition, prevalence, consequences, and correction. Endocrinol Metab Clin North Am. 2010;39:287-301, table of contents.

[94] Rodan GA, Martin TJ. Therapeutic Approaches to Bone Diseases. Science. 2000;289:1508-14.

[95] Liao J, Schneider A, Datta NS, McCauley LK. Extracellular calcium as a candidate mediator of prostate cancer skeletal metastasis. Cancer Res. 2006;66:9065-73.

[96] Miwa S, Mizokami A, Keller ET, Taichman R, Zhang J, Namiki M. The bisphosphonate YM529 inhibits osteolytic and osteoblastic changes and CXCR-4-induced invasion in prostate cancer. Cancer Res. 2005;65:8818-25.

[97] Schneider A, Kalikin LM, Mattos AC, Keller ET, Allen MJ, Pienta KJ, et al. Bone turnover mediates preferential localization of prostate cancer in the skeleton. Endocrinology. 2005;146:1727-36.

[98] Keller ET, Brown J. Prostate cancer bone metastases promote both osteolytic and osteoblastic activity. J Cell Biochem. 2004;91:718-29.

[99] Takuwa Y, Masaki T, Yamashita K. The effects of the endothelin family peptides on cultured osteoblastic cells from rat calvariae. Biochem Biophys Res Commun. 1990;170:998-1005.

[100] Autzen P, Robson CN, Bjartell A, Malcolm AJ, Johnson MI, Neal DE, et al. Bone morphogenetic protein 6 in skeletal metastases from prostate cancer and other common human malignancies. Br J Cancer. 1998;78:1219-23.

[101] Cohen P, Peehl DM, Graves HC, Rosenfeld RG. Biological effects of prostate specific antigen as an insulin-like growth factor binding protein-3 protease. J Endocrinol. 1994;142:407-15.

[102] Fudge K, Wang CY, Stearns ME. Immunohistochemistry analysis of platelet-derived growth factor A and B chains and platelet-derived growth factor alpha and beta receptor expression in benign prostatic hyperplasias and Gleason-graded human prostate adenocarcinomas. Mod Pathol. 1994;7:549-54.

[103] Iwamura M, Hellman J, Cockett AT, Lilja H, Gershagen S. Alteration of the hormonal bioactivity of parathyroid hormone-related protein (PTHrP) as a result of limited proteolysis by prostate-specific antigen. Urology. 1996;48:317-25.

[104] Marquardt H, Lioubin MN, Ikeda T. Complete amino acid sequence of human transforming growth factor type beta 2. J Biol Chem. 1987;262:12127-31.

[105] Yin JJ, Mohammad KS, Kakonen SM, Harris S, Wu-Wong JR, Wessale JL, et al. A causal role for endothelin-1 in the pathogenesis of osteoblastic bone metastases. Proc Natl Acad Sci U S A. 2003;100:10954-9.

[106] Le Brun G, Aubin P, Soliman H, Ropiquet F, Villette JM, Berthon P, et al. Upregulation of endothelin 1 and its precursor by IL-1beta, TNF-alpha, and TGF-beta in the PC3 human prostate cancer cell line. Cytokine. 1999;11:157-62.

[107] Abu-Amer Y. IL-4 abrogates osteoclastogenesis through STAT6-dependent inhibition of NF-kappaB. J Clin Invest. 2001;107:1375-85.

[108] Boyce BF, Xing L. The RANKL/RANK/OPG pathway. Curr Osteoporos Rep. 2007;5:98-104.

[109] Lu Y, Cai Z, Xiao G, Keller ET, Mizokami A, Yao Z, et al. Monocyte chemotactic protein-1 mediates prostate cancer-induced bone resorption. Cancer Res. 2007;67:3646-53.

[110] Lam J, Takeshita S, Barker JE, Kanagawa O, Ross FP, Teitelbaum SL. TNF-alpha induces osteoclastogenesis by direct stimulation of macrophages exposed to permissive levels of RANK ligand. J Clin Invest. 2000;106:1481-8.

[111] Nakagawa M, Kaneda T, Arakawa T, Morita S, Sato T, Yomada T, et al. Vascular endothelial growth factor (VEGF) directly enhances osteoclastic bone resorption and survival of mature osteoclasts. FEBS Lett. 2000;473:161-4.

[112] Kingsley LA, Fournier PG, Chirgwin JM, Guise TA. Molecular biology of bone metastasis. Mol Cancer Ther. 2007;6:2609-17.

[113] Galasko CS. Skeletal metastases. Clin Orthop Relat Res. 1986:18-30.

[114] Damerla V, Packianathan S, Boerner PS, Jani AB, Vijayakumar S, Vijayakumar V. Recent developments in nuclear medicine in the management of bone metastases: a review and perspective. Am J Clin Oncol. 2005;28:513-20.

[115] Israeli RS. Managing bone loss and bone metastases in prostate cancer patients: a focus on bisphosphonate therapy. Reviews in urology. 2008;10:99-110.

[116] Ottewell PD, Monkkonen H, Jones M, Lefley DV, Coleman RE, Holen I. Antitumor effects of doxorubicin followed by zoledronic acid in a mouse model of breast cancer. J Natl Cancer Inst. 2008;100:1167-78.

[117] Kim SJ, Uehara H, Yazici S, He J, Langley RR, Mathew P, et al. Modulation of bone microenvironment with zoledronate enhances the therapeutic effects of STI571 and paclitaxel against experimental bone metastasis of human prostate cancer. Cancer research. 2005;65:3707-15.

[118] Lu S, Zhang J, Zhou Z, Liao ML, He WZ, Zhou XY, et al. Synergistic inhibitory activity of zoledronate and paclitaxel on bone metastasis in nude mice. Oncol Rep. 2008;20:581-7.

[119] Vordos D, Paule B, Vacherot F, Allory Y, Salomon L, Hoznek A, et al. Docetaxel and zoledronic acid in patients with metastatic hormone-refractory prostate cancer. BJU Int. 2004;94:524-7.

[120] Fleisch H, Russell RGG, Bisaz S, Casey PA, Mühlbauer RC. The influence of pyrophosphate analogues (diphosphonates) on the precipitation and dissolution of calcium phosphate in vitro and in vivo. Calcified Tissue Research.2:10-.

[121] Francis MD, Russell RG, Fleisch H. Diphosphonates inhibit formation of calcium phosphate crystals in vitro and pathological calcification in vivo. Science. 1969;165:1264-6.

[122] Russell RG, Watts NB, Ebetino FH, Rogers MJ. Mechanisms of action of bisphosphonates: similarities and differences and their potential influence on clinical efficacy. Osteoporos Int. 2008;19:733-59.

[123] Baron R, Neff L, Louvard D, Courtoy PJ. Cell-mediated extracellular acidification and bone resorption: evidence for a low pH in resorbing lacunae and localization of a 100-kD lysosomal membrane protein at the osteoclast ruffled border. J Cell Biol. 1985;101:2210-22.

[124] Blair HC, Teitelbaum SL, Ghiselli R, Gluck S. Osteoclastic bone resorption by a polarized vacuolar proton pump. Science. 1989;245:855-7.

[125] Thompson K, Rogers MJ, Coxon FP, Crockett JC. Cytosolic entry of bisphosphonate drugs requires acidification of vesicles after fluid-phase endocytosis. Mol Pharmacol. 2006;69:1624-32.

[126] Frith JC, Monkkonen J, Blackburn GM, Russell RG, Rogers MJ. Clodronate and liposome-encapsulated clodronate are metabolized to a toxic ATP analog, adenosine 5'-(beta, gamma-dichloromethylene) triphosphate, by mammalian cells in vitro. Journal of bone and mineral research : the official journal of the American Society for Bone and Mineral Research. 1997;12:1358-67.

[127] van Beek E, Pieterman E, Cohen L, Lowik C, Papapoulos S. Farnesyl pyrophosphate synthase is the molecular target of nitrogen-containing bisphosphonates. Biochemical and biophysical research communications. 1999;264:108-11.

[128] Weivoda MM, Oursler MJ. The Roles of Small GTPases in Osteoclast Biology. Orthop Muscular Syst. 2014;3.

[129] Luckman SP, Hughes DE, Coxon FP, Russell RGG, Rogers MJ. Nitrogen-Containing Bisphosphonates Inhibit the Mevalonate Pathway and Prevent Post-Translational Prenylation of GTP-Binding Proteins, Including Ras. Journal of Bone and Mineral Research. 1998;13:581-9.

[130] Clezardin P. Mechanisms of action of bisphosphonates in oncology: a scientific concept evolving from antiresorptive to anticancer activities. BoneKEy Rep. 2013;2.

[131] Wood J, Bonjean K, Ruetz S, Bellahcene A, Devy L, Foidart JM, et al. Novel antiangiogenic effects of the bisphosphonate compound zoledronic acid. J Pharmacol Exp Ther. 2002;302:1055-61.

[132] Molinuevo MS, Bruzzone L, Cortizo AM. Alendronate induces anti-migratory effects and inhibition of neutral phosphatases in UMR106 osteosarcoma cells. Eur J Pharmacol. 2007;562:28-33.

[133] So A, Chin J, Fleshner N, Saad F. Management of skeletal-related events in patients with advanced prostate cancer and bone metastases: Incorporating new agents into clinical practice. Can Urol Assoc J. 2012;6:465-70.

[134] Giger EV, Castagner B, Leroux JC. Biomedical applications of bisphosphonates. J Control Release. 2013;167:175-88.

[135] Cole LE, Vargo-Gogola T, Roeder RK. Targeted delivery to bone and mineral deposits using bisphosphonate ligands. Adv Drug Deliv Rev. 2016;99:12-27.

[136] Moradian-Oldak J, Frolow F, Addadi L, Weiner S. Interactions between acidic matrix macromolecules and calcium phosphate ester crystals: relevance to carbonate apatite formation in biomineralization. Proc Biol Sci. 1992;247:47-55.

[137] Addadi L, Weiner S. Interactions between acidic proteins and crystals: stereochemical requirements in biomineralization. Proceedings of the National Academy of Sciences of the United States of America. 1985;82:4110-4.

[138] Fujisawa R, Wada Y, Nodasaka Y, Kuboki Y. Acidic amino acid-rich sequences as binding sites of osteonectin to hydroxyapatite crystals. Biochimica et Biophysica Acta (BBA) - Protein Structure and Molecular Enzymology. 1996;1292:53-60.

[139] Addison WN, Miller SJ, Ramaswamy J, Mansouri A, Kohn DH, McKee MD. Phosphorylation-dependent mineral-type specificity for apatite-binding peptide sequences. Biomaterials. 2010;31:9422-30.

[140] Segvich S, Biswas S, Becker U, Kohn DH. Identification of peptides with targeted adhesion to bone-like mineral via phage display and computational modeling. Cells Tissues Organs. 2009;189:245-51.

[141] Segvich SJ, Smith HC, Kohn DH. The adsorption of preferential binding peptides to apatite-based materials. Biomaterials. 2009;30:1287-98.

[142] Ramaswamy J, Nam HK, Ramaraju H, Hatch NE, Kohn DH. Inhibition of osteoblast mineralization by phosphorylated phage-derived apatite-specific peptide. Biomaterials. 2015;73:120-30.

[143] Low SA, Kopecek J. Targeting polymer therapeutics to bone. Adv Drug Deliv Rev. 2012;64:1189-204.

[144] Murphy MB, Hartgerink JD, Goepferich A, Mikos AG. Synthesis and in vitro hydroxyapatite binding of peptides conjugated to calcium-binding moieties. Biomacromolecules. 2007;8:2237-43.

[145] Wang D, Miller S, Sima M, Kopeckova P, Kopecek J. Synthesis and evaluation of water-soluble polymeric bone-targeted drug delivery systems. Bioconjug Chem. 2003;14:853-9.

[146] Ross RD, Roeder RK. Binding affinity of surface functionalized gold nanoparticles to hydroxyapatite. J Biomed Mater Res A. 2011;99:58-66.

[147] Vinay R, KusumDevi V. Potential of targeted drug delivery system for the treatment of bone metastasis. Drug Deliv. 2016;23:21-9.

[148] Zhang G, Guo B, Wu H, Tang T, Zhang BT, Zheng L, et al. A delivery system targeting bone formation surfaces to facilitate RNAi-based anabolic therapy. Nat Med. 2012;18:307-14.

[149] Thamake SI, Raut SL, Gryczynski Z, Ranjan AP, Vishwanatha JK. Alendronate coated poly-lactic-co-glycolic acid (PLGA) nanoparticles for active targeting of metastatic breast cancer. Biomaterials. 2012;33:7164-73.

[150] Miller K, Clementi C, Polyak D, Eldar-Boock A, Benayoun L, Barshack I, et al. Poly(ethylene glycol)-paclitaxel-alendronate self-assembled micelles for the targeted treatment of breast cancer bone metastases. Biomaterials. 2013;34:3795-806.

[151] Clementi C, Miller K, Mero A, Satchi-Fainaro R, Pasut G. Dendritic poly(ethylene glycol) bearing paclitaxel and alendronate for targeting bone neoplasms. Molecular pharmaceutics. 2011;8:1063-72.

[152] Segal E, Pan H, Ofek P, Udagawa T, Kopeckova P, Kopecek J, et al. Targeting angiogenesis-dependent calcified neoplasms using combined polymer therapeutics. PLoS One. 2009;4:e5233.

[153] Wang G, Babadagli ME, Uludag H. Bisphosphonate-derivatized liposomes to control drug release from collagen/hydroxyapatite scaffolds. Molecular pharmaceutics. 2011;8:1025-34.

[154] Wang G, Mostafa NZ, Incani V, Kucharski C, Uludag H. Bisphosphonate-decorated lipid nanoparticles designed as drug carriers for bone diseases. J Biomed Mater Res A. 2012;100:684-93.

[155] Chaudhari KR, Kumar A, Khandelwal VKM, Mishra AK, Monkkonen J, Murthy RSR. Targeting Efficiency and Biodistribution of Zoledronate Conjugated Docetaxel Loaded Pegylated PBCA Nanoparticles for Bone Metastasis. Advanced Functional Materials. 2012;22:4101-14.

[156] Stamey TA, Caldwell M, McNeal JE, Nolley R, Hemenez M, Downs J. The prostate specific antigen era in the United States is over for prostate cancer: what happened in the last 20 years? J Urol. 2004;172:1297-301.

[157] Simma-Chiang V, Hom JJ, Simko JP, Chan JM, Carroll PR. Increased prevalence of unifocal prostate cancer in a contemporary series of radical prostatectomy specimens: Implications for focal ablation. J Urology. 2006;175:374-.

[158] Ohori M, Eastham JA, Koh H, Kuroiwa K, Slawin KM, Wheeler TM, et al. Is focal therapy reasonable in patients with early stage prostate cancer (CaP) - An analysis of radical prostatectomy (RP) specimens. J Urology. 2006;175:507-.

[159] Turkbey B, Pinto PA, Choyke PL. Imaging techniques for prostate cancer: implications for focal therapy. Nat Rev Urol. 2009;6:191-203.

[160] Parsons JE, Cain CA, Abrams GD, Fowlkes JB. Pulsed cavitational ultrasound therapy for controlled tissue homogenization. Ultrasound in Medicine and Biology. 2006;32:115-29.

[161] Hall TL, Kieran K, Ives K, Fowlkes JB, Cain CA, Roberts WW. Histotripsy of rabbit renal tissue in vivo: temporal histologic trends. J Endourol. 2007;21:1159-66.

[162] Vlaisavljevich E, Maxwell A, Mancia L, Johnsen E, Cain C, Xu Z. Visualizing the Histotripsy Process: Bubble Cloud-Cancer Cell Interactions in a Tissue-Mimicking Environment. Ultrasound in medicine & biology. 2016.

[163] Hempel CR, Hall TL, Cain CA, Fowlkes JB, Xu Z, Roberts WW. Histotripsy fractionation of prostate tissue: local effects and systemic response in a canine model. J Urol. 2011;185:1484-9.

[164] Maxwell AD, Owens G, Gurm HS, Ives K, Myers DD, Jr., Xu Z. Noninvasive treatment of deep venous thrombosis using pulsed ultrasound cavitation therapy (histotripsy) in a porcine model. J Vasc Interv Radiol. 2011;22:369-77.

[165] Owens GE, Miller RM, Ensing G, Ives K, Gordon D, Ludomirsky A, et al. Therapeutic ultrasound to noninvasively create intracardiac communications in an intact animal model. Catheter Cardiovasc Interv. 2011;77:580-8.

[166] Xu Z, Owens G, Gordon D, Cain C, Ludomirsky A. Noninvasive creation of an atrial septal defect by histotripsy in a canine model. Circulation. 2010;121:742-9.

[167] Styn NR, Wheat JC, Hall TL, Roberts WW. Histotripsy of VX-2 tumor implanted in a renal rabbit model. J Endourol. 2010;24:1145-50.

[168] Yuksel Durmaz Y, Vlaisavljevich E, Xu Z, ElSayed M. Development of nanodroplets for histotripsy-mediated cell ablation. Molecular pharmaceutics. 2014;11:3684-95.

[169] Vlaisavljevich E, Aydin O, Durmaz YY, Lin KW, Fowlkes B, Xu Z, et al. Effects of Droplet Composition on Nanodroplet-Mediated Histotripsy. Ultrasound in medicine & biology. 2016;42:931-46.

[170] Aydin O, Youssef I, Yuksel Durmaz Y, Tiruchinapally G, ElSayed ME. Formulation of Acid-Sensitive Micelles for Delivery of Cabazitaxel into Prostate Cancer Cells. Molecular pharmaceutics. 2016;13:1413-29.

[171] Lemmo S, Atefi E, Luker GD, Tavana H. Optimization of Aqueous Biphasic Tumor Spheroid Microtechnology for Anti-Cancer Drug Testing in 3D Culture. Cell Mol Bioeng. 2014;7:344-54.

[172] Parsons JE, Cain CA, Fowlkes JB. Cost-effective assembly of a basic fiber-optic hydrophone for measurement of high-amplitude therapeutic ultrasound fields. J Acoust Soc Am. 2006;119:1432-40.

[173] Vlaisavljevich E, Kim Y, Owens G, Roberts W, Cain C, Xu Z. Effects of tissue mechanical properties on susceptibility to histotripsy-induced tissue damage. Physics in medicine and biology. 2014;59:253-70.

[174] Vlaisavljevich E, Lin KW, Warnez MT, Singh R, Mancia L, Putnam AJ, et al. Effects of tissue stiffness, ultrasound frequency, and pressure on histotripsy-induced cavitation bubble behavior. Physics in medicine and biology. 2015;60:2271-92.

[175] Vlaisavljevich E, Maxwell A, Warnez M, Johnsen E, Cain CA, Xu Z. Histotripsy-induced cavitation cloud initiation thresholds in tissues of different mechanical properties. IEEE transactions on ultrasonics, ferroelectrics, and frequency control. 2014;61:341-52.

[176] Butler BD, Hills BA. The lung as a filter for microbubbles. J Appl Physiol Respir Environ Exerc Physiol. 1979;47:537-43.

[177] POLINMENI P, Bose D, Bose R, Otten M, Ottenbreit B. Drag-reducing polymers: a novel category of drugs potentially useful in cardiovascular disease? Journal of applied cardiology. 1988;3:57-66.

[178] Medina SH, Tiruchinapally G, Chevliakov MV, Durmaz YY, Stender RN, Ensminger WD, et al. Targeting hepatic cancer cells with pegylated dendrimers displaying N-acetylgalactosamine and SP94 peptide ligands. Adv Healthc Mater. 2013;2:1337-50.

[179] Al-Nasiry S, Geusens N, Hanssens M, Luyten C, Pijnenborg R. The use of Alamar Blue assay for quantitative analysis of viability, migration and invasion of choriocarcinoma cells. Hum Reprod. 2007;22:1304-9.

[180] Pazdur R, Kudelka AP, Kavanagh JJ, Cohen PR, Raber MN. The taxoids: paclitaxel (Taxol) and docetaxel (Taxotere). Cancer Treat Rev. 1993;19:351-86.

[181] Abal M, Andreu JM, Barasoain I. Taxanes: microtubule and centrosome targets, and cell cycle dependent mechanisms of action. Curr Cancer Drug Targets. 2003;3:193-203.

[182] Schwab CL, English DP, Roque DM, Santin AD. Taxanes: their impact on gynecologic malignancy. Anti-Cancer Drugs. 2014;25:522-35 10.1097/CAD.0000000000000057.

[183] FDA approves treatment IND protocol for taxol. Clin Pharm. 1992;11:912.

[184] Gill PS, Tulpule A, Espina BM, Cabriales S, Bresnahan J, Ilaw M, et al. Paclitaxel is safe and effective in the treatment of advanced AIDS-related Kaposi's sarcoma. J Clin Oncol. 1999;17:1876-83.

[185] Francis PA, Kris MG, Rigas JR, Grant SC, Miller VA. Paclitaxel (Taxol) and docetaxel (Taxotere): active chemotherapeutic agents in lung cancer. Lung Cancer. 1995;12 Suppl 1:S163-72.

[186] Tankanow RM. Docetaxel: a taxoid for the treatment of metastatic breast cancer. Am J Health Syst Pharm. 1998;55:1777-91.

[187] Belani CP, Eckardt J. Development of docetaxel in advanced non-small-cell lung cancer. Lung Cancer. 2004;46 Suppl 2:S3-11.

[188] Blagden SP, Kaye SB. Docetaxel in the management of ovarian cancer. Expert Rev Anticancer Ther. 2005;5:203-14.

[189] Hagiwara H, Sunada Y. Mechanism of taxane neurotoxicity. Breast Cancer. 2004;11:82-5.

[190] Markman M. Managing taxane toxicities. Support Care Cancer. 2003;11:144-7.

[191] Steele RH, Limaye S, Cleland B, Chow J, Suranyi MG. Hypersensitivity reactions to the polysorbate contained in recombinant erythropoietin and darbepoietin. Nephrology (Carlton). 2005;10:317-20.

[192] Gelderblom H, Verweij J, Nooter K, Sparreboom A. Cremophor EL: the drawbacks and advantages of vehicle selection for drug formulation. Eur J Cancer. 2001;37:1590-8.

[193] Gradishar WJ, Tjulandin S, Davidson N, Shaw H, Desai N, Bhar P, et al. Phase III trial of nanoparticle albumin-bound paclitaxel compared with polyethylated castor oil-based paclitaxel in women with breast cancer. J Clin Oncol. 2005;23:7794-803.

[194] Sempkowski M, Locke T, Stras S, Zhu C, Sofou S. Liposome-Based Approaches for Delivery of Mainstream Chemotherapeutics: Preparation Methods, Liposome Designs, Therapeutic Efficacy. 2014;19:177-221.

[195] Peng Z-H, Sima M, Salama ME, Kopečková P, Kopeček J. Spacer length impacts the efficacy of targeted docetaxel conjugates in prostate-specific membrane antigen expressing prostate cancer. Journal of Drug Targeting. 2013;21:968-80.

[196] Cabral H, Kataoka K. Progress of drug-loaded polymeric micelles into clinical studies. Journal of Controlled Release. 2014;190:465-76.

[197] Green MR, Manikhas GM, Orlov S, Afanasyev B, Makhson AM, Bhar P, et al. Abraxane, a novel Cremophor-free, albumin-bound particle form of paclitaxel for the treatment of advanced non-small-cell lung cancer. Ann Oncol. 2006;17:1263-8.

[198] Miele E, Spinelli GP, Miele E, Tomao F, Tomao S. Albumin-bound formulation of paclitaxel (Abraxane® ABI-007) in the treatment of breast cancer. International Journal of Nanomedicine. 2009;4:99-105.

[199] Singer JW. Paclitaxel poliglumex (XYOTAX, CT-2103): amacromolecular taxane. Journal of Controlled Release. 2005;109:120-6.

[200] Vrignaud P, Sémiond D, Lejeune P, Bouchard H, Calvet L, Combeau C, et al. Preclinical Antitumor Activity of Cabazitaxel, a Semisynthetic Taxane Active in Taxane-Resistant Tumors. Clinical Cancer Research. 2013;19:2973-83.

[201] de Bono JS, Oudard S, Ozguroglu M, Hansen S, Machiels JP, Kocak I, et al. Prednisone plus cabazitaxel or mitoxantrone for metastatic castration-resistant prostate cancer progressing after docetaxel treatment: a randomised open-label trial. Lancet. 2010;376:1147-54.

[202] Oudard S. TROPIC: Phase III trial of cabazitaxel for the treatment of metastatic castration-resistant prostate cancer. Future Oncol. 2011;7:497-506.

[203] Paller CJ, Antonarakis ES. Cabazitaxel: a novel second-line treatment for metastatic castration-resistant prostate cancer. Drug Des Devel Ther. 2011;10:117-24.

[204] Galletti E, Magnani M, Renzulli ML, Botta M. Paclitaxel and docetaxel resistance: molecular mechanisms and development of new generation taxanes. ChemMedChem. 2007;2:920-42.

[205] Afroz A. Cabazitaxel: A novel taxane for metastatic castration-resistant prostate cancer-current implications and future prospects. Journal of Pharmacology & Pharmacotherapeutics. 2013;4:230-7.

[206] Kocherlakota C, Banda N, Singh T, Vure P, BISWAS M, Bhagwatwar HP, et al. Pharmaceutical formulations of cabazitaxel. Google Patents; 2013.

[207] Sanofi-Aventis. JEVTANA® Prescribing Information. In: LLC S-AUS, editor. Bridgewater, NJMarch 2014.

[208] Norris LB, Qureshi ZP, Bookstaver PB, Raisch DW, Sartor O, Chen H, et al. Polysorbate 80 hypersensitivity reactions: a renewed call to action. Community Oncology. 2010;7:425-8.

[209] Matyjaszewski K, Xia J. Atom transfer radical polymerization. Chem Rev. 2001;101:2921-90.

[210] Durmaz H, Dag A, Altintas O, Erdogan T, Hizal G, Tunca U. One-Pot Synthesis of ABC Type Triblock Copolymers via in situ Click [3 + 2] and Diels−Alder [4 + 2] Reactions. Macromolecules. 2006;40:191-8.

[211] Broaders KE, Pastine SJ, Grandhe S, Frechet JMJ. Acid-degradable solid-walled microcapsules for pH-responsive burst-release drug delivery. Chemical Communications. 2011;47:665-7.

[212] Shim MS, Kwon YJ. Controlled Delivery of Plasmid DNA and siRNA to Intracellular Targets Using Ketalized Polyethylenimine. Biomacromolecules. 2008;9:444-55.

[213] Lim H, Noh J, Kim Y, Kim H, Kim J, Khang G, et al. Acid-Degradable Cationic Poly(ketal amidoamine) for Enhanced RNA Interference In Vitro and In Vivo. Biomacromolecules. 2012;14:240-7.

[214] Paramonov SE, Bachelder EM, Beaudette TT, Standley SM, Lee CC, Dashe J, et al. Fully Acid-Degradable Biocompatible Polyacetal Microparticles for Drug Delivery. Bioconjug Chem. 2008;19:911-9.

[215] Lee SJ, Min KH, Lee HJ, Koo AN, Rim HP, Jeon BJ, et al. Ketal Cross-Linked Poly(ethylene glycol)-Poly(amino acid)s Copolymer Micelles for Efficient Intracellular Delivery of Doxorubicin. Biomacromolecules. 2011;12:1224-33.

[216] Zhang A, Zhang Z, Shi F, Ding J, Xiao C, Zhuang X, et al. Disulfide crosslinked PEGylated starch micelles as efficient intracellular drug delivery platforms. Soft Matter. 2013;9:2224-33.

[217] Medina SH, Chevliakov MV, Tiruchinapally G, Durmaz YY, Kuruvilla SP, Elsayed ME. Enzyme-activated nanoconjugates for tunable release of doxorubicin in hepatic cancer cells. Biomaterials. 2013;34:4655-66.

[218] Russell PJ, Kingsley EA. Human prostate cancer cell lines. Methods Mol Med. 2003;81:21-39.

[219] Pagano RE, Ozato K, Ruysschaert JM. Intracellular distribution of lipophilic fluorescent probes in mammalian cells. Biochim Biophys Acta. 1977;465:661-6.

[220] Batrakova EV, Li S, Vinogradov SV, Alakhov VY, Miller DW, Kabanov AV. Mechanism of pluronic effect on P-glycoprotein efflux system in blood-brain barrier: contributions of energy depletion and membrane fluidization. J Pharmacol Exp Ther. 2001;299:483-93.

[221] Lin YL, Jiang G, Birrell LK, El-Sayed ME. Degradable, pH-sensitive, membrane-destabilizing, comb-like polymers for intracellular delivery of nucleic acids. Biomaterials. 2010;31:7150-66.

[222] Jurasz P, Alonso D, Castro-Blanco S, Murad F, Radomski MW. Generation and role of angiostatin in human platelets. Blood. 2003;102:3217-23.

[223] Radomski A, Stewart MW, Jurasz P, Radomski MW. Pharmacological characteristics of solid-phase von Willebrand factor in human platelets. Br J Pharmacol. 2001;134:1013-20.

[224] Radomski A, Jurasz P, Alonso-Escolano D, Drews M, Morandi M, Malinski T, et al. Nanoparticle-induced platelet aggregation and vascular thrombosis. Br J Pharmacol. 2005;146:882-93.

[225] Suk JS, Xu Q, Kim N, Hanes J, Ensign LM. PEGylation as a strategy for improving nanoparticle-based drug and gene delivery. Adv Drug Deliv Rev.

[226] Ge J, Neofytou E, Lei J, Beygui RE, Zare RN. Protein–Polymer Hybrid Nanoparticles for Drug Delivery. Small. 2012;8:3573-8.

[227] Bettencourt A, Almeida AJ. Poly(methyl methacrylate) particulate carriers in drug delivery. J Microencapsul. 2012;29:353-67.

[228] Chen L. Hydrogel/Polymer Micelles Composites Derived from Polymerization of Microemulsions for Oral Drug Delivery: University of Akron; 2013.

[229] Feng Z, Bo Y. Polymer Brushes on Surfaces. Self-Assembled Structures: CRC Press; 2010. p. 175-207.

[230] Lee R-S, Huang Y-T. Tuning the hydrophilic-hydrophobic balance of block-graft copolymers by click strategy: synthesis and characterization of amphiphilic PCL-b-(P[alpha]N3CL-g-PBA) copolymers. Polym J. 2010;42:304-12.

[231] Oerlemans C, Bult W, Bos M, Storm G, Nijsen JF, Hennink WE. Polymeric micelles in anticancer therapy: targeting, imaging and triggered release. Pharm Res. 2010;27:2569-89.

[232] Gillies ER, Jonsson TB, Frechet JM. Stimuli-responsive supramolecular assemblies of linear-dendritic copolymers. J Am Chem Soc. 2004;126:11936-43.

[233] Sackett DL, Wolff J. Nile red as a polarity-sensitive fluorescent probe of hydrophobic protein surfaces. Anal Biochem. 1987;167:228-34.

[234] Chen J, Qiu X, Ouyang J, Kong J, Zhong W, Xing MM. pH and reduction dual-sensitive copolymeric micelles for intracellular doxorubicin delivery. Biomacromolecules. 2011;12:3601-11.

[235] Lee SC, Huh KM, Lee J, Cho YW, Galinsky RE, Park K. Hydrotropic Polymeric Micelles for Enhanced Paclitaxel Solubility: In Vitro and In Vivo Characterization. Biomacromolecules. 2006;8:202-8.

[236] Wei R, Cheng L, Zheng M, Cheng R, Meng F, Deng C, et al. Reduction-responsive disassemblable core-cross-linked micelles based on poly(ethylene glycol)-b-poly(N-2-hydroxypropyl methacrylamide)-lipoic acid conjugates for triggered intracellular anticancer drug release. Biomacromolecules. 2012;13:2429-38.

[237] You J, Hu FQ, Du YZ, Yuan H. Polymeric micelles with glycolipid-like structure and multiple hydrophobic domains for mediating molecular target delivery of paclitaxel. Biomacromolecules. 2007;8:2450-6.

[238] Soleymani Abyaneh H, Vakili MR, Lavasanifar A. The effect of polymerization method in stereo-active block copolymers on the stability of polymeric micelles and their drug release profile. Pharm Res. 2014;31:1485-500.

[239] Yang C, Attia AB, Tan JP, Ke X, Gao S, Hedrick JL, et al. The role of non-covalent interactions in anticancer drug loading and kinetic stability of polymeric micelles. Biomaterials. 2012;33:2971-9.

[240] Read ES, Armes SP. Recent advances in shell cross-linked micelles. Chem Commun (Camb). 2007:3021-35.

[241] Shen Y. Functional polymers for nanomedicine. Cambridge: Royal Society of Chemistry; 2013.

[242] Fang J, Nakamura H, Maeda H. The EPR effect: Unique features of tumor blood vessels for drug delivery, factors involved, and limitations and augmentation of the effect. Adv Drug Deliv Rev. 2011;63:136-51.

[243] Montaudon D, Vrignaud P, Londos-Gagliardi D, Robert J. Fluorescence anisotropy of cell membranes of doxorubicin-sensitive and -resistant rodent tumoral cells. Cancer Res. 1986;46:5602-5.

[244] Fuchs P, Parola A, Robbins PW, Blout ER. Fluorescence polarization and viscosities of membrane lipids of 3T3 cells. Proc Natl Acad Sci U S A. 1975;72:3351-4.

[245] de Laat SW, van der Saag PT, Shinitzky M. Microviscosity modulation during the cell cycle of neuroblastoma cells. Proc Natl Acad Sci U S A. 1977;74:4458-61.

[246] Ramu A, Glaubiger D, Weintraub H. Differences in lipid composition of doxorubicin-sensitive and -resistant P388 cells. Cancer Treat Rep. 1984;68:637-41.

[247] Dobrovolskaia MA, Aggarwal P, Hall JB, McNeil SE. Preclinical studies to understand nanoparticle interaction with the immune system and its potential effects on nanoparticle biodistribution. Molecular pharmaceutics. 2008;5:487-95.

[248] Moghimi SM, Hunter AC, Murray JC. Long-circulating and target-specific nanoparticles: theory to practice. Pharmacol Rev. 2001;53:283-318.

[249] Kim D, El-Shall H, Dennis D, Morey T. Interaction of PLGA nanoparticles with human blood constituents. Colloids Surf B Biointerfaces. 2005;40:83-91.

[250] Gaw A. Clinical biochemistry: an illustrated colour text. Edinburgh ; New York: Churchill Livingstone; 2008.

[251] Paget S. Originally published as Volume 1, Issue 3421THE DISTRIBUTION OF SECONDARY GROWTHS IN CANCER OF THE BREAST. The Lancet. 1889;133:571-3.

[252] Ribatti D, Mangialardi G, Vacca A. Stephen Paget and the 'seed and soil' theory of metastatic dissemination. Clin Exp Med. 2006;6:145-9.

[253] Autio KA, Morris MJ. Targeting bone physiology for the treatment of metastatic prostate cancer. Clin Adv Hematol Oncol. 2013;11:134-43.

[254] Low SA, Kopecek J. Targeting polymer therapeutics to bone. Adv Drug Deliv Rev. 2012;64:1189-204.

[255] Sottnik JL, Zhang J, Macoska JA, Keller ET. The PCa Tumor Microenvironment. Cancer Microenviron. 2011;4:283-97.

[256] Clarke B. Normal bone anatomy and physiology. Clin J Am Soc Nephrol. 2008;3 Suppl 3:S131-9.

[257] Hendricks SB, Hill WL. The nature of bone and phosphate rock. Proceedings of the National Academy of Sciences of the United States of America. 1950;36:731-7.

[258] Kingsley LA, Fournier PGJ, Chirgwin JM, Guise TA. Molecular Biology of Bone Metastasis. American Association for Cancer Research. 2007;6:2609-17.

[259] Abal M, Andreu JM, Barasoain I. Taxanes: microtubule and centrosome targets, and cell cycle dependent mechanisms of action. Curr Cancer Drug Targets. 2003;3:193-203.

[260] Kaya E, Feuer D. Prostate cancer: palliative care and pain relief. Prostate Cancer Prostatic Dis. 2004;7:311-5.

[261] Ebetino FH, Hogan AM, Sun S, Tsoumpra MK, Duan X, Triffitt JT, et al. The relationship between the chemistry and biological activity of the bisphosphonates. Bone. 2011;49:20-33.

[262] Cotesta S, Jahnke W, Rondeau JM, Weiler S, Widler L. Phenylalkyl-imidazole-bisphosphonate compounds. Google Patents; 2011.

[263] Takeuchi M, Sakamoto S, Kawamuki K, Kurihara H, Nakahara H, Isomura Y. Studies on novel bone resorption inhibitors. II. Synthesis and pharmacological activities of fused aza-heteroarylbisphosphonate derivatives. Chem Pharm Bull (Tokyo). 1998;46:1703-9.

[264] Lin JH. Bisphosphonates: a review of their pharmacokinetic properties. Bone. 1996;18:75-85.

[265] Meads MB, Hazlehurst LA, Dalton WS. The bone marrow microenvironment as a tumor sanctuary and contributor to drug resistance. Clin Cancer Res. 2008;14:2519-26.

[266] Lipton A. New strategies to prevent and manage bone complications in cancer. Clinical advances in hematology & oncology : H&O. 2011;9:42-4.

[267] Lipton A. Implications of bone metastases and the benefits of bone-targeted therapy. Semin Oncol. 2010;37 Suppl 2:S15-29.

[268] Zhang S, Gangal G, Uludag H. 'Magic bullets' for bone diseases: progress in rational design of bone-seeking medicinal agents. Chem Soc Rev. 2007;36:507-31.

[269] Hsu WK, Virk MS, Feeley BT, Stout DB, Chatziioannou AF, Lieberman JR. Characterization of osteolytic, osteoblastic, and mixed lesions in a prostate cancer mouse model using 18F-FDG and 18F-fluoride PET/CT. J Nucl Med. 2008;49:414-21.

[270] Kaighn ME, Narayan KS, Ohnuki Y, Lechner JF, Jones LW. Establishment and characterization of a human prostatic carcinoma cell line (PC-3). Invest Urol. 1979;17:16-23.

[271] Pfitzenmaier J, Quinn JE, Odman AM, Zhang J, Keller ET, Vessella RL, et al. Characterization of C4–2 Prostate Cancer Bone Metastases and Their Response to Castration. Journal of Bone and Mineral Research. 2003;18:1882-8.

[272] Keller ET, Brown J. Prostate cancer bone metastases promote both osteolytic and osteoblastic activity. Journal of cellular biochemistry. 2004;91:718-29.

[273] Aydin O, Youssef I, Yuksel Durmaz Y, Tiruchinapally G, ElSayed MEH. Formulation of Acid-Sensitive Micelles for Delivery of Cabazitaxel into Prostate Cancer Cells. Molecular pharmaceutics. 2016;13:1413-29.

[274] Qiu L, Cheng W, Lin J, Luo S, Xue L, Pan J. Synthesis and biological evaluation of novel (99m)Tc-labelled bisphosphonates as superior bone imaging agents. Molecules. 2011;16:6165-78.

[275] Singh SK, Manne N, Ray PC, Pal M. Synthesis of imidazol-1-yl-acetic acid hydrochloride: a key intermediate for zoledronic acid. Beilstein J Org Chem. 2008;4:42.

[276] Kozloff KM, Volakis LI, Marini JC, Caird MS. Near-infrared fluorescent probe traces bisphosphonate delivery and retention in vivo. J Bone Miner Res. 2010;25:1748-58.

[277] Dai J, Zhang H, Karatsinides A, Keller JM, Kozloff KM, Aftab DT, et al. Cabozantinib inhibits prostate cancer growth and prevents tumor-induced bone lesions. Clin Cancer Res. 2014;20:617-30.

[278] Medina SH, Tiruchinapally G, Chevliakov MV, Durmaz YY, Stender RN, Ensminger WD, et al. Targeting hepatic cancer cells with pegylated dendrimers displaying N-acetylgalactosamine and SP94 peptide ligands. Adv Healthc Mater. 2013;2:1337-50.

[279] Dobrovolskaia MA, Patri AK, Simak J, Hall JB, Semberova J, De Paoli Lacerda SH, et al. Nanoparticle size and surface charge determine effects of PAMAM dendrimers on human platelets in vitro. Molecular pharmaceutics. 2012;9:382-93.

[280] Wang D, Miller SC, Shlyakhtenko LS, Portillo AM, Liu XM, Papangkorn K, et al. Osteotropic Peptide that differentiates functional domains of the skeleton. Bioconjug Chem. 2007;18:1375-8.

[281] de Miguel L, Noiray M, Surpateanu G, Iorga BI, Ponchel G. Poly(gamma-benzyl-L-glutamate)-PEG-alendronate multivalent nanoparticles for bone targeting. Int J Pharm. 2014;460:73-82.

[282] Stemmer U, Ramprecht C, Zenzmaier E, Stojcic B, Rechberger G, Kollroser M, et al. Uptake and protein targeting of fluorescent oxidized phospholipids in cultured RAW 264.7 macrophages. Biochimica et biophysica acta. 2012;1821:706-18.

[283] Kelly C, Jefferies C, Cryan SA. Targeted liposomal drug delivery to monocytes and macrophages. J Drug Deliv. 2011;2011:727241.

[284] Muralidharan A, Smith MT. Pathobiology and management of prostate cancer-induced bone pain: recent insights and future treatments. Inflammopharmacology. 2013;21:339-63.

[285] Jin JK, Dayyani F, Gallick GE. Steps in prostate cancer progression that lead to bone metastasis. Int J Cancer. 2011;128:2545-61.

[286] Lin DL, Tarnowski CP, Zhang J, Dai J, Rohn E, Patel AH, et al. Bone metastatic LNCaP-derivative C4-2B prostate cancer cell line mineralizes in vitro. Prostate. 2001;47:212-21.

[287] Vinogradov S, Warren G, Wei X. Macrophages associated with tumors as potential targets and therapeutic intermediates. Nanomedicine (Lond). 2014;9:695-707.

[288] Fischer C, Jonckx B, Mazzone M, Zacchigna S, Loges S, Pattarini L, et al. Anti-PlGF inhibits growth of VEGF(R)-inhibitor-resistant tumors without affecting healthy vessels. Cell. 2007;131:463-75.

[289] Steidl C, Lee T, Shah SP, Farinha P, Han G, Nayar T, et al. Tumor-associated macrophages and survival in classic Hodgkin's lymphoma. N Engl J Med. 2010;362:875-85.

[290] Tang X, Mo C, Wang Y, Wei D, Xiao H. Anti-tumour strategies aiming to target tumour-associated macrophages. Immunology. 2013;138:93-104.

[291] Rogers TL, Holen I. Tumour macrophages as potential targets of bisphosphonates. J Transl Med. 2011;9:177.

[292] Khan A. Bisphosphonate-associated osteonecrosis of the jaw. Can Fam Physician. 2008;54:1019-21.

[293] Bander NH, Trabulsi EJ, Kostakoglu L, Yao D, Vallabhajosula S, Smith-Jones P, et al. Targeting metastatic prostate cancer with radiolabeled monoclonal antibody J591 to the extracellular domain of prostate specific membrane antigen. J Urol. 2003;170:1717-21.

[294] Wu X, Ding B, Gao J, Wang H, Fan W, Wang X, et al. Second-generation aptamer-conjugated PSMA-targeted delivery system for prostate cancer therapy. International journal of nanomedicine. 2011;6:1747-56.

[295] Aggarwal S, Singh P, Topaloglu O, Isaacs JT, Denmeade SR. A dimeric peptide that binds selectively to prostate-specific membrane antigen and inhibits its enzymatic activity. Cancer research. 2006;66:9171-7.

[296] Bouchelouche K, Choyke PL, Capala J. Prostate specific membrane antigen- a target for imaging and therapy with radionuclides. Discov Med. 2010;9:55-61.

[297] Ghosh A, Heston WD. Tumor target prostate specific membrane antigen (PSMA) and its regulation in prostate cancer. Journal of cellular biochemistry. 2004;91:528-39.

[298] Wang C, Yan Q, Liu H-B, Zhou X-H, Xiao S-J. Different EDC/NHS Activation Mechanisms between PAA and PMAA Brushes and the Following Amidation Reactions. Langmuir. 2011;27:12058-68.

[299] Havens AM, Pedersen EA, Shiozawa Y, Ying C, Jung Y, Sun Y, et al. An in vivo mouse model for human prostate cancer metastasis. Neoplasia. 2008;10:371-80.

[300] Kalikin LM, Schneider A, Thakur MA, Fridman Y, Griffin LB, Dunn RL, et al. In vivo visualization of metastatic prostate cancer and quantitation of disease progression in immunocompromised mice. Cancer Biol Ther. 2003;2:656-60.

[301] Rehemtulla A, Stegman LD, Cardozo SJ, Gupta S, Hall DE, Contag CH, et al. Rapid and quantitative assessment of cancer treatment response using in vivo bioluminescence imaging. Neoplasia. 2000;2:491-5.

[302] Lin K-W, Hall TL, Xu Z, Cain CA. Histotripsy Lesion Formation Using an Ultrasound Imaging Probe Enabled by a Low-Frequency Pump Transducer. Ultrasound in Medicine and Biology.41:2148-60.

[303] Wang TY, Hall TL, Xu Z, Fowlkes JB, Cain CA. Imaging feedback of histotripsy treatments using ultrasound shear wave elastography. IEEE transactions on ultrasonics, ferroelectrics, and frequency control. 2012;59:1167-81.

[304] Roberts MJ, Bentley MD, Harris JM. Chemistry for peptide and protein PEGylation. Adv Drug Deliv Rev. 2002;54:459-76.

[305] Veronese FM. Peptide and protein PEGylation: a review of problems and solutions. Biomaterials. 2001;22:405-17.

[306] Corey E, Quinn JE, Bladou F, Brown LG, Roudier MP, Brown JM, et al. Establishment and characterization of osseous prostate cancer models: intra-tibial injection of human prostate cancer cells. Prostate. 2002;52:20-33.

[307] Zhang J, Dai J, Qi Y, Lin DL, Smith P, Strayhorn C, et al. Osteoprotegerin inhibits prostate cancer-induced osteoclastogenesis and prevents prostate tumor growth in the bone. J Clin Invest. 2001;107:1235-44.

[308] Medina SH, Tiruchinapally G, Chevliakov MV, Durmaz YY, Stender RN, Ensminger WD, et al. Targeting Hepatic Cancer Cells with PEGylated Dendrimers Displaying N-Acetylgalactosamine and SP94 Peptide Ligands. Adv Healthc Mater. 2013.

[309] Kozloff KM, Quinti L, Patntirapong S, Hauschka PV, Tung CH, Weissleder R, et al. Non-invasive optical detection of cathepsin K-mediated fluorescence reveals osteoclast activity in vitro and in vivo. Bone. 2009;44:190-8.

[310] Kozloff KM, Weissleder R, Mahmood U. Noninvasive optical detection of bone mineral. J Bone Miner Res. 2007;22:1208-16.

[311] Kozloff KM, Volakis LI, Marini JC, Caird MS. Near-infrared fluorescent probe traces bisphosphonate delivery and retention in vivo. J Bone Miner Res. 2010;25:1748-58.

[312] Pean E, Demolis P, Moreau A, Hemmings RJ, O'Connor D, Brown D, et al. The European Medicines Agency review of cabazitaxel (Jevtana(R)) for the treatment of hormone-refractory metastatic prostate

cancer: summary of the scientific assessment of the committee for medicinal products for human use. Oncologist. 2012;17:543-9.

[313] Parsons JE, Cain CA, Abrams GD, Fowlkes JB. Pulsed cavitational ultrasound therapy for controlled tissue homogenization. Ultrasound Med Biol. 2006;32:115-29.

[314] Parsons JE, Cain CA, Fowlkes JB. Spatial variability in acoustic backscatter as an indicator of tissue homogenate production in pulsed cavitational ultrasound therapy. IEEE Trans Ultrason Ferroelectr Freq Control. 2007;54:576-90.

[315] Xu Z, Fowlkes JB, Ludomirsky A, Cain CA. Investigation of intensity thresholds for ultrasound tissue erosion. Ultrasound Med Biol. 2005;31:1673-82.

[316] Vlaisavljevich E, Lin KW, Maxwell A, Warnez MT, Mancia L, Singh R, et al. Effects of Ultrasound Frequency and Tissue Stiffness on the Histotripsy Intrinsic Threshold for Cavitation. Ultrasound Med Biol. 2015.

[317] Vlaisavljevich E, Lin KW, Warnez MT, Singh R, Mancia L, Putnam AJ, et al. Effects of tissue stiffness, ultrasound frequency, and pressure on histotripsy-induced cavitation bubble behavior. Phys Med Biol. 2015;60:2271-92.

[318] Xu Z, Raghavan M, Hall TL, Chang CW, Mycek MA, Fowlkes JB, et al. High speed imaging of bubble clouds generated in pulsed ultrasound cavitational therapy--histotripsy. IEEE Trans Ultrason Ferroelectr Freq Control. 2007;54:2091-101.

[319] Hempel CR, Hall TL, Cain CA, Fowlkes JB, Xu Z, Roberts WW. Histotripsy fractionation of prostate tissue: local effects and systemic response in a canine model. J Urol. 2011;185:1484-9.

[320] Gao Z, Kennedy AM, Christensen DA, Rapoport NY. Drug-loaded nano/microbubbles for combining ultrasonography and targeted chemotherapy. Ultrasonics. 2008;48:260-70.

[321] Sheeran PS, Luois S, Dayton PA, Matsunaga TO. Formulation and acoustic studies of a new phase-shift agent for diagnostic and therapeutic ultrasound. Langmuir : the ACS journal of surfaces and colloids. 2011;27:10412-20.

[322] Vlaisavljevich E, Kim Y, Owens G, Roberts W, Cain C, Xu Z. Effects of tissue mechanical properties on susceptibility to histotripsy-induced tissue damage. Phys Med Biol. 2014;59:253-70.

[323] Vlaisavljevich E, Maxwell A, Warnez M, Johnsen E, Cain CA, Xu Z. Histotripsy-induced cavitation cloud initiation thresholds in tissues of different mechanical properties. IEEE Trans Ultrason Ferroelectr Freq Control. 2014;61:341-52.

[324] Vlaisavljevich E, Warnez M, Johnsen E, Singh R, Putnam A, Xu Z. Investigation of the role of tissue stiffness and ultrasound frequency in histotripsy-induced cavitation. . Symposium on Therapeutic Ultrasound. 2014.

[325] Masuzaki R, Tateishi R, Yoshida H, Sato T, Ohki T, Goto T, et al. Assessing liver tumor stiffness by transient elastography. Hepatol Int. 2007;1:394-7.

[326] Normand V, Lootens DL, Amici E, Plucknett KP, Aymard P. New insight into agarose gel mechanical properties. Biomacromolecules. 2000;1:730-8.

[327] Zhang M, Nigwekar P, Castaneda B, Hoyt K, Joseph JV, di Sant'Agnese A, et al. Quantitative characterization of viscoelastic properties of human prostate correlated with histology. Ultrasound Med Biol. 2008;34:1033-42.

[328] Lin KW, Duryea AP, Kim Y, Hall TL, Xu Z, Cain CA. Dual-beam histotripsy: a low-frequency pump enabling a high-frequency probe for precise lesion formation. IEEE Trans Ultrason Ferroelectr Freq Control. 2014;61:325-40.

[329] Hosmer DW, Lemeshow S. Confidence interval estimation of interaction. Epidemiology. 1992;3:452-6.

[330] Kripfgans OD, Fowlkes JB, Miller DL, Eldevik OP, Carson PL. Acoustic droplet vaporization for therapeutic and diagnostic applications. Ultrasound Med Biol. 2000;26:1177-89.

[331] Schad KC, Hynynen K. In vitro characterization of perfluorocarbon droplets for focused ultrasound therapy. Phys Med Biol. 2010;55:4933-47.

[332] Williams R, Wright C, Cherin E, Reznik N, Lee M, Gorelikov I, et al. Characterization of submicron phase-change perfluorocarbon droplets for extravascular ultrasound imaging of cancer. Ultrasound Med Biol. 2013;39:475-89.

[333] Li DS, Kripfgans OD, Fabiilli ML, Brian Fowlkes J, Bull JL. Initial nucleation site formation due to acoustic droplet vaporization. Appl Phys Lett. 2014;104:063703.

[334] Shpak O, Verweij M, Vos HJ, de Jong N, Lohse D, Versluis M. Acoustic droplet vaporization is initiated by superharmonic focusing. Proc Natl Acad Sci U S A. 2014;111:1697-702.

[335] Wang TY, Xu Z, Hall TL, Fowlkes JB, Cain CA. An efficient treatment strategy for histotripsy by removing cavitation memory. Ultrasound Med Biol. 2012;38:753-66.

[336] Roberts WW, Hall TL, Ives K, Wolf JS, Jr., Fowlkes JB, Cain CA. Pulsed cavitational ultrasound: a noninvasive technology for controlled tissue ablation (histotripsy) in the rabbit kidney. J Urol. 2006;175:734-8.

[337] Vlaisavljevich E, Lin KW, Maxwell A, Warnez M, Mancia L, Singh R, et al. Effects of Ultrasound Frequency and Tissue Stiffness on the Histotripsy Intrinsic Threshold for Cavitation. Ultrasound Med Biol. 2015.

[338] Vlaisavljevich E, Aydin O, Durmaz YY, Lin KW, Fowlkes JB, Elsayed M, et al. The Effects of Ultrasound Frequency on Nanodroplet-Mediated Histotripsy. Ultrasound Med Biol. 2015.

[339] Fabiilli ML, Haworth KJ, Fakhri NH, Kripfgans OD, Carson PL, Fowlkes JB. The role of inertial cavitation in acoustic droplet vaporization. IEEE Trans Ultrason Ferroelectr Freq Control. 2009;56:1006-17.

[340] Giesecke T, Hynynen K. Ultrasound-mediated cavitation thresholds of liquid perfluorocarbon droplets in vitro. Ultrasound Med Biol. 2003;29:1359-65.

[341] Rapoport NY, Kennedy AM, Shea JE, Scaife CL, Nam KH. Controlled and targeted tumor chemotherapy by ultrasound-activated nanoemulsions/microbubbles. Journal of Controlled Release. 2009;138:268-76.

[342] Sheeran PS, Luois S, Dayton PA, Matsunaga TO. Formulation and acoustic studies of a new phase-shift agent for diagnostic and therapeutic ultrasound. Langmuir. 2011;27:10412-20.

[343] Lin KW, Kim Y, Maxwell AD, Wang TY, Hall TL, Xu Z, et al. Histotripsy beyond the intrinsic cavitation threshold using very short ultrasound pulses: microtripsy. IEEE Trans Ultrason Ferroelectr Freq Control. 2014;61:251-65.

[344] Maxwell AD, Wang TY, Yuan LQ, Duryea AP, Xu Z, Cain CA. A Tissue Phantom for Visualization and Measurement of Ultrasound-Induced Cavitation Damage. Ultrasound Med Biol. 2010;36:2132-43.

[345] Vlaisavljevich E, Lin KW, Warnez M, Singh R, Mancia L, Putnam A, et al. Effects of Tissue Stiffness, Ultrasound Frequency, and Pressure on Histotripsy-induced Cavitation Bubble Behavior. Phys Med Biol. 2015.

[346] Fabiilli ML, Wilson CG, Padilla F, Martin-Saavedra FM, Fowlkes JB, Franceschi RT. Acoustic droplet-hydrogel composites for spatial and temporal control of growth factor delivery and scaffold stiffness. Acta Biomater. 2013;9:7399-409.

[347] Kim Y, Gelehrter SK, Fifer CG, Lu JC, Owens GE, Berman DR, et al. Non-invasive pulsed cavitational ultrasound for fetal tissue ablation: feasibility study in a fetal sheep model. Ultrasound in Obstetrics & Gynecology. 2011;37:450-7.

[348] Kim YH, Fifer CG, Gelehrter SK, Owens GE, Berman DR, Vlaisavljevich E, et al. Developmental Impact and Lesion Maturation of Histotripsy-Mediated Non-Invasive Tissue Ablation in a Fetal Sheep Model. Ultrasound in Medicine and Biology. 2013;39:1047-55.

[349] Arvengas A, Davitt K, Caupin F. Fiber optic probe hydrophone for the study of acoustic cavitation in water. Rev Sci Instrum. 2011;82:034904.

[350] Caupin F, Herbert E. Cavitation in water: a review. Comptes Rendus Physique. 2006;7:1000-17.

[351] Fisher JC. The Fracture of Liquids. Journal of Applied Physics. 1948;19:1062-7.

[352] Herbert E, Balibar S, Caupin F. Cavitation pressure in water. Phys Rev E Stat Nonlin Soft Matter Phys. 2006;74:041603.

[353] Kripfgans OD, Fabiilli ML, Carson PL, Fowlkes JB. On the acoustic vaporization of micrometer-sized droplets. J Acoust Soc Am. 2004;116:272-81.

[354] Sheeran PS, Dayton PA. Phase-change contrast agents for imaging and therapy. Curr Pharm Des. 2012;18:2152-65.

[355] Vlaisavljevich E, Aydin O, Lin KW, Fowlkes JB, ElSayed M, Xu Z. Investigation of the Role of Ultrasound Frequency and Droplet Composition in Nanodroplet-mediated Histotripsy. International Society for Therapeutic Ultrasound. Utrecht, Netherlands2015.

[356] Kawabata K, Asami R, Axuma T, Umemura S. Acoustic response of microbubbles derived from phase-change nanodroplet. Jpn J Appl Phys. 2010.

[357] Lin KW, Hall TL, McGough RJ, Xu Z, Cain CA. Synthesis of monopolar ultrasound pulses for therapy: the frequency-compounding transducer. IEEE Trans Ultrason Ferroelectr Freq Control. 2014;61:1123-36.

[358] Pettersen MS, Balibar S, Maris HJ. Experimental investigation of cavitation in superfluid 4He. Phys Rev B Condens Matter. 1994;49:12062-70.

[359] Reznik N, Shpak O, Gelderblom EC, Williams R, de Jong N, Versluis M, et al. The efficiency and stability of bubble formation by acoustic vaporization of submicron perfluorocarbon droplets. Ultrasonics. 2013;53:1368-76.

[360] Reznik N, Williams R, Burns PN. Investigation of Vaporized Submicron Perfluorocarbon Droplets as an Ultrasound Contrast Agent. Ultrasound in Medicine and Biology. 2011;37:1271-9.

[361] Doinikov AA, Sheeran PS, Bouakaz A, Dayton PA. Vaporization dynamics of volatile perfluorocarbon droplets: a theoretical model and in vitro validation. Med Phys. 2014;41:102901.

[362] Rapoport N, Nam K-H, Gupta R, Gao Z, Mohan P, Payne A, et al. Ultrasound-mediated tumor imaging and nanotherapy using drug loaded, block copolymer stabilized perfluorocarbon nanoemulsions. Journal of Controlled Release. 2011;153:4-15.

[363] Shpak O, Kokhuis TJ, Luan Y, Lohse D, de Jong N, Fowlkes B, et al. Ultrafast dynamics of the acoustic vaporization of phase-change microdroplets. J Acoust Soc Am. 2013;134:1610-21.

[364] Holland CK, Apfel RE. Thresholds for transient cavitation produced by pulsed ultrasound in a controlled nuclei environment. J Acoust Soc Am. 1990;88:2059-69.

[365] Miller DL, Thomas RM. Ultrasound contrast agents nucleate inertial cavitation in vitro. Ultrasound Med Biol. 1995;21:1059-65.